

# **STUDY OF ELECTRONIC STRUCTURE OF ORGANIC AND INORGANIC COMPLEXES**

Thesis submitted for the degree of  
Doctor of Philosophy (Science)

in

Physics (Theoretical)

by

**Hrishit Banerjee**

Department of Physics  
University of Calcutta  
June 2018

*To*

*my parents...*

# Acknowledgements

*At the completion of the longest, most arduous, and yet intellectually the most enriching phase of my life, I wish to acknowledge the contributions of all those who have supported and enhanced my efforts at what most people would call a maddening endeavour, known otherwise as a Ph.D.*

*Naturally, first of all I wish to express my sincere and humble gratitude to my respected supervisor Prof. Tanusri Saha-Dasgupta, and my co-supervisor Dr. Manoranjan Kumar. While it was the stern yet very valuable expert guidance, constant push, endless enthusiasm, prompt ideas of my supervisor that helped me finish off my thesis, my co-supervisor was always there to provide academic support at each and every point, whenever it seemed necessary. It has been my privilege to work with such scientifically driven honourable figures like my supervisor and my co-supervisor. The integral and enthusiastic view of Prof. Saha-Dasgupta on research have made a deep impact on me, while Dr. Kumar's rigorous attitude to understanding have made me a better researcher overall. I would like to thank Prof. Mohit Randeria of The Ohio State University, for his kind acceptance to work together in a very significant scientific project of my life. I would like to thank Prof. Karsten Held of Technische Universitat, Vienna for his wonderful support, help and hospitality during my stay in Vienna, Austria. It was a great and valuable experience for me to work with Prof. Held and learn the basics of Dynamical Mean Field Theory during my short stay at Vienna. I would also like to extend my gratitude towards Dr. Sumilan Banerjee of the Indian Institute of Science, Bangalore, for he has been a valued collaborator in some of my scientific projects. My heartfelt gratitude is extended to Dr. Sudip Chakraborty of the Uppsala University, with whom I collaborated on quite a few projects, and who has always been like an elder brother to me, giving his valuable advice and helping me through both academically and non-academically whenever there was any requirement on my part. I would like to thank Dr. Oleg Janson for all sorts of help in academic as well as non-academic matters in Vienna. I would also like to thank Prof. Peter Blaha for organising the departmental seminar that I delivered at his department at TU Vienna.*

*I have been quite active in the activities of "Muktangan" and the "Students' Advisory Committee" and I thank all my friends and companions who have been in*

---

*these committees and made it really easy to work and make our centre a better and more productive place not only in science but in other aspects as well. With this I would like to thank the S. N. Bose National Centre for Basic Sciences for the funding and the great working environment and academic ambience. I thank the director of our centre, the administrative departments and its officials who kept everything going, the Computer section which looked after the computational facilities and being a computational scientist, it was the need of the hour at any hour of the day! I thank the Thematic Unit of Excellence in Computational Material Science for the funding of our current computational facilities. I would like to thank the Department of Science and Technology for the funding of my research through the S. N. Bose National Centre for Basic Sciences, and also for funding my conference visit to Boston, USA, through the International Travel Scheme (ITS) grant of Science and Engineering Research Board (SERB).*

*I have been fortunate enough to have a great friend circle at our institute the Satyendranath Bose National Centre for Basic Sciences. Due to their presence the environment has always been very charming and joyful. It is my pleasure to have such group mates like; Soumyajit'da, Sudipta'da, Swarnakamal'da, Santu'da, Tilak'da, Aurab'da, Kartik, Poulami, Anita, Dhani, Ransell, and Shreya. Thanks to Anita for the painstaking job she did for me. Special thanks to Sudipta'da, for his continuous help and suggestions in any matter at any situation, even when abroad. Even though they weren't a part of our group when I joined I would still like to thank Hena'di, Swastika'di and Shreemoyee'di for all their advice and help at various times. I thank Sudip, Monalisa, Debasmita, Rakesh, and Aslam, who have been a part of my co-supervisor's group.*

*My time at the S. N. Bose Centre would not have been so great without a few trusted friends that I had here. I thank Arpan, Arpita, Karan, Ambalika, and Anindita, who have been the best of company for the last 5 years. I would like to add that my discussions and debates about all things which engages the mind have been with people like Arpan, Abhishek, Arnab, Pooja and so on. We had a really great music and arts group at the Centre. The times spent engaged in music with Pratik da, Ishita di, Ruma di, Shauri, Suchetana, Shaili, and so on have been very relaxing and enriching at the same time.*

*Utilizing this scope I would like to thank my school teachers and particularly my school, Dolna itself, for I am what I am because of that place. Of course no mention of my school is complete without mentioning the names of Mrs. Madhusree Dasgupta, Mrs. Madhura Bhattacharya, Mr. Jyotishka Dasgupta, Mrs. Neelanjana Dasgupta, Mrs. Gargi Roy, Mrs. Lata Banerjee, and Mr. Balaji Rajeen Iyer. They have been the moulding hands of my formative years. My closest friends from school of course have been the ideal companions to cheer me up whenever I have been down and it is with them that I have spent countless*

---

*weekends having a great time. It will be injustice if I do not thank Karthika, Avik, Pritha, Abhinandan, Ashesh, Kuntal, Debalina, Madhura, Papiya, Tarak, Srijani, Apalak and so on. I really cannot list our entire class but I wish I could. I would like to thank Prof. Jayashree Mukherjee of Bethune College for she was the person who got me interested in physics at the first place. The professors at my alma mater, Jadavpur University have been fantastic inspiration and through their constant encouragement have pushed me to explore physics and go into research. I would extend my thanks to fantastic friends at JU, who have been with me through thick and thin. Thank you, Sayanee, Oindrila, Deya, Anjan, Pranay, Archi, Avik, Sunetra, Sabana, Debjyoti, and Pragati. Thanks Pragati for hosting me during my academic visit to Europe. I would also like to thank Dr. Sandeep Choubey, who hosted me during my conference visit to Boston.*

*It is obvious that this long journey would not be possible without the unconditional support of my family throughout my life, in any situation at any cost. I have been down and depressed, hurt and ill, and yet it has been my parents who have got me through everything. It is said that we cannot thank our parents enough for everything. They gave us life and yet I would like to take this opportunity to express my biggest gratitude to my parents, my father Mr. Biswarup Banerjee, and my mother Mrs. Kalpana Banerjee, for understanding and tolerating me. It will be audacious if I try to express their contributions in my life. I would also like to mention that all of my family members have been extremely supportive of my ventures, and I am really grateful to each and every one of them. Here I would like to mention that the late Dr. Sisir Kanti Sur, my maternal uncle, was the first to inspire me to get into academics in the first place.*

*Finally I would like to thank everybody who played important role throughout my journey. I apologise if I missed anyone, who have helped me through these testing years.*

Hrishit Banerjee  
Kolkata, India  
June, 2018.

# List of Publications

1. Cooperativity in spin crossover transitions in metalorganic complexes : Interplay of magnetic and elastic interactions  
Hrishit Banerjee, Manoranjan Kumar, and Tanusri Saha-Dasgupta  
**Phys. Rev. B** **90** 174433 (2014)\*.
2. Electronic Structure of Oxide Interfaces: A Comparative Analysis of GdTiO<sub>3</sub>/SrTiO<sub>3</sub> and LaTiO<sub>3</sub>/SrTiO<sub>3</sub> Interfaces  
Hrishit Banerjee, Sumilan Banerjee, Mohit Randeria, Tanusri Saha-Dasgupta  
**Sci. Rep.** **5**, 18647, (2015)\*.
3. Cationic Effect on Pressure driven Spin-State Transition and cooperativity in Hybrid Perovskites  
Hrishit Banerjee, Sudip Chakraborty, Tanusri Saha-Dasgupta  
**Chemistry of Materials**, **28(22)**, 8379-8384 (2016)\*.
4. Design and Control of Cooperativity in Spin-Crossover in Metal-Organic Complexes: A Theoretical Overview  
Hrishit Banerjee, Sudip Chakraborty, Tanusri Saha-Dasgupta  
**Inorganics**, **5(3)**, 47 (2017)\*.
5. Understanding curious ferromagnetic insulating state of LaMnO<sub>3</sub> on SrTiO<sub>3</sub>  
Hrishit Banerjee, Oleg Janson, Karsten Held, Tanusri Saha-Dasgupta (under preparation) \*.

---

Publications marked with \* are reported in this thesis.

# Contents

<b>1</b>	<b>Introduction</b>	<b>1</b>
1.1	Metal-Organic Complexes . . . . .	4
1.1.1	Coordination Polymers . . . . .	5
1.1.2	Hybrid Perovskites . . . . .	8
1.2	Inorganic Oxide Heterostructures . . . . .	11
1.2.1	Oxides . . . . .	11
1.2.2	Heterostructures formed between Oxides . . . . .	15
1.3	Overview of present thesis . . . . .	19
<b>2</b>	<b>Theoretical methodology</b>	<b>27</b>
2.1	Introduction . . . . .	27
2.2	The many body Hamiltonian . . . . .	27
2.2.1	Born-Oppenheimer Approximation . . . . .	29
2.2.2	Classical Nuclei Approximation . . . . .	30
2.3	The Electronic Problem . . . . .	31
2.3.1	The Hartree approximation . . . . .	31
2.3.2	The Hartree-Fock approximation . . . . .	33
2.4	Density Functional Theory . . . . .	36
2.4.1	Reduced Density Matrices . . . . .	37
2.4.2	The Hohenberg-Kohn Theorems . . . . .	39
2.4.3	Energy Functional and Kohn-Sham Equations . . . . .	42
2.4.4	Interpretation of the Kohn-Sham equations . . . . .	45
2.5	Exchange and Correlation . . . . .	46
2.5.1	Local Density Approximation . . . . .	47
2.5.2	Generalized Gradient Approximation . . . . .	48
2.5.3	Hybrid Functionals . . . . .	49
2.6	Basis Sets . . . . .	50
2.6.1	Fixed basis set methods . . . . .	51
2.6.2	Partial wave basis set methods . . . . .	56
2.6.3	The Projector-Augmented-Wave (PAW) Formalism . . . . .	60
2.7	Ab initio Molecular Dynamics . . . . .	61
2.7.1	Ehrenfest Molecular Dynamics . . . . .	62
2.7.2	Born-Oppenheimer Molecular Dynamics . . . . .	63

2.7.3	Car-Parrinello Molecular Dynamics . . . . .	64
2.7.4	AIMD used in this thesis . . . . .	65
2.8	Monte Carlo simulation of model systems . . . . .	65
2.8.1	Metropolis Algorithm . . . . .	66
2.8.2	Simulation of the Ising Model . . . . .	66
<b>3</b>	<b>Cooperativity in Spin-crossover Transition in Metalorganic Complexes : Interplay of magnetic and elastic interactions</b>	<b>71</b>
3.1	Introduction . . . . .	71
3.2	Monte Carlo study of the Model Hamiltonian . . . . .	76
3.2.1	The Hamiltonian . . . . .	76
3.2.2	Results of Monte-Carlo simulations . . . . .	78
3.3	First principles study of Cooperativity in SCO of Fe-Triazole . . .	80
3.3.1	Electronic structure of Fe-triazole . . . . .	82
3.3.2	Monte Carlo results with material-specific parameters of Fe-triazole . . . . .	84
3.4	Finite temperature study with Ab initio molecular dynamics . . .	87
3.5	Conclusion . . . . .	89
3.6	Appendix . . . . .	90
<b>4</b>	<b>Cationic Effect on Pressure driven Spin-State Transition and cooperativity in Hybrid Perovskites</b>	<b>96</b>
4.1	Introduction . . . . .	96
4.2	Experimental studies on Hybrid Perovskites . . . . .	99
4.3	Motivation for studying Spin Crossover in hybrid perovskites . . .	100
4.4	Computational Methodology . . . . .	103
4.5	Crystal Structure of DMAFeF and HAFeF . . . . .	103
4.6	Spin-state transition under pressure and Cooperativity . . . . .	105
4.7	Microscopic understanding of Cooperativity . . . . .	108
4.8	Conclusions . . . . .	112
4.9	Appendix . . . . .	114
<b>5</b>	<b>Electronic Structure of Oxide Interfaces: A Comparative Analysis of GdTiO<sub>3</sub>/SrTiO<sub>3</sub> and LaAlO<sub>3</sub>/SrTiO<sub>3</sub> Interfaces</b>	<b>122</b>
5.1	Introduction . . . . .	122
5.1.1	Different kinds of Insulators . . . . .	124
5.1.2	Oxide Heterostructures . . . . .	128
5.1.3	Polar catastrophe hypothesis . . . . .	129
5.1.4	Existing studies on Oxide heterostructures . . . . .	130
5.2	Computational details . . . . .	132
5.3	Heterostructure Geometries . . . . .	133
5.4	Structure . . . . .	134

---

5.5	Electronic and Magnetic Structure . . . . .	135
5.6	Electronic reconstruction . . . . .	143
5.7	Conclusion . . . . .	146
<b>6</b>	<b>Understanding curious ferromagnetic insulating state of LaMnO<sub>3</sub> on SrTiO<sub>3</sub></b>	<b>151</b>
6.1	Introduction . . . . .	151
6.2	Computational Details . . . . .	153
6.3	Results . . . . .	154
6.3.1	Bulk Calculations . . . . .	154
6.3.2	Superlattice Calculations . . . . .	162
6.4	Conclusion . . . . .	165
<b>7</b>	<b>Conclusion</b>	<b>168</b>
7.1	Summary . . . . .	168
7.1.1	Summary of Chapter 3 . . . . .	168
7.1.2	Summary of Chapter 4 . . . . .	169
7.1.3	Summary of Chapter 5 . . . . .	170
7.1.4	Summary of Chapter 6 . . . . .	170
7.2	Outlook . . . . .	171
7.2.1	Metal-organic Complexes . . . . .	171
7.2.2	Inorganic Oxide heterostructures . . . . .	172

# List of Figures

1.1	Schematic representation of linear, 1-D coordination polymer (left panel) and hybrid perovskite (right panel). In case of linear, 1-D coordination polymer, chains of metals are linked by organic ligands. In the $ABX_3$ structure of hybrid perovskite, $BX_6$ forms octahedra with A cation sitting in the voids. B cation is a metal ion and A cation is an organic cation. $BX_6$ octahedra are also linked by organic linkers. Figure adapted from Banerjee et al [Inorganics, 5(3), 47 (2017)] . . . . .	6
1.2	Jahn-Teller breathing modes. Figure (a) on left panel shows the $Q_2$ breathing mode while figure (b) on right panel shows the $Q_3$ breathing mode. . . . .	12
1.3	A schematic diagram demonstrating the various properties of complex perovskite oxides. The green, blue, and red spheres forming the perovskite structure illustrated in the centre represent the A, B, and O atoms, respectively. Figure adapted from Triscone et al Annu. Rev. Condens.Matter Phys. 2011. 2:14165 . . . . .	14
1.4	Annular dark field (ADF) image of $LaTiO_3$ layers (bright) of varying thickness spaced by $SrTiO_3$ layers. The view is along the $[100]$ axis of the $SrTiO_3$ substrate. The growth sequence is $5 \times n$ (that is, 5 layers of $SrTiO_3$ and n layers of $LaTiO_3$ ), $20 \times n$ , $n \times n$ , and finally a $LaTiO_3$ capping layer. The numbers in the lower image indicate the number of $LaTiO_3$ unit cells in each layer. Field of view is 400 nm. Magnified view of the $5 \times 1$ series in the top panel. Figure is adapted from Ohtomo and Hwang Nature 419, 378, 2002	16
2.1	Algorithmic flowchart illustrating the Hartree–Fock method. . . .	36
2.2	Algorithmic flowchart illustrating the iterative procedure to solve the Kohn-sham equations. . . . .	44
2.3	Figure showing the Bloch function $\psi_k$ oscillating rapidly near atomic sites where the lattice potential is deep and attractive . . . . .	51
2.4	Comparison of a wave-function in the Coulomb potential of the nucleus (dashed) to the one in the pseudo-potential (solid). The real and the pseudo wave-function and potentials match above a certain cutoff radius. Figure adapted from Wikipedia. . . . .	54

2.5	Schematic diagram of potential inside real crystal and approximated potential considered in LMTO method. Potential is rapidly varying in the vicinity of core atomic region. In the interstitial region i.e. away from atom core region, the actual potential is approximated as a constant potential. . . . .	56
3.1	Molecular SCO showing a spin state change of the molecular SCO system driven by various external stimuli. Figure adapted from T. Saha-Dasgupta et al [1] . . . . .	72
3.2	SCO materials mostly belong to the first row of transition metal ions. . . . .	73
3.3	From Molecular SCO systems to connected systems like coordination polymers where cooperativity arises. . . . .	73
3.4	Figure showing the intra ionic transfer of electrons due to competition between crystal field splitting and Hund's rule coupling being driven by temperature or pressure. . . . .	75
3.5	Schematic diagram showing the different site labels of the interconnected chains and the respective interactions. . . . .	76
3.6	Figure showing the spin dependence of the intra chain elastic interaction. Figure adapted from K. Boukheddaden et al [20] . . . .	78
3.7	High spin fraction plotted as a function of increasing temperature (heating cycle) and decreasing temperature (cooling cycle), for (a) Ferroelastic intrachain coupling with magnetic coupling set to zero, (b) Ferroelastic intrachain coupling with finite, nonzero magnetic coupling, (c) Antiferroelastic intrachain coupling with magnetic coupling set to zero, and (d) Antiferroelastic intrachain coupling with finite, nonzero magnetic coupling. . . . .	79
3.8	Crystal structure of Fe-triazole complexes. (a) The synthesized compound $\text{Fe}[(\text{hyetrz})_3](4\text{-chlorophenylsulphonate})_2 \cdot 3\text{H}_2\text{O}$ . (b) The simplified computer designed complex. The medium sized blue, and black balls represent N and C, respectively. The small balls represent the H atoms, while the green medium sized balls denote counter-ion, $\text{F}^-$ . . . . .	81
3.9	GGA Fe-3d partial DOS. Top panel shows DOS for Fe-N bond-length=2.0Å and bottom panel shows DOS for Fe-N bond-length=2.2Å. Black shaded area shows the up spin channel and red shaded area shows the down spin channel. . . . .	83
3.10	GGA+U Fe-3d partial DOS. DOS plotted for Fe-N bond-length=2.2Å corresponding to the HS state. Black shaded area shows the up spin channel and red shaded area shows the down spin channel. . .	84

3.11	The variation of total energy as a function of variation of Fe-N bondlength about the equilibrium value, for three different configurations, LS-LS (circles), LS-HS (squares) and HS-HS (diamonds). Solid lines are fit to data points. . . . .	85
3.12	High spin fraction plotted as a function of increasing and decreasing temperature calculated with DFT derived elastic and magnetic interactions corresponding to that of Fe-triazole. The insets show the snap-shots of pseudo-spin configurations with LS (HS) state shown in black (yellow), at two different temperatures (80 K and 95 K) in cooling cycle, and two different temperatures (65 K and 80 K) in heating cycle. At $T = 80$ K, in the phase co-existence region, the configuration is HS or LS dominated, depending on the heating or cooling cycle. . . . .	86
3.13	Relative change in free energy plotted as a function magnetic moment in the cell for (a) $T = 10$ K, (b) $T = 80$ K, (c) $T = 200$ K. The relative change is measured with respect to the global minima of the free energy (F0). . . . .	88
4.1	Representation of Metal-organic frameworks. The left panel shows scanning electron microscope image of the seed inside a MOF crystal. The right panel shows the schematic representation of a MOF-76 crystal, where oxygen, carbon, and lanthanide atoms are represented by maroon, black, and blue spheres, respectively. Figures adapted from wikipedia. . . . .	97
4.2	Figure showing an example of a hybrid perovskite where the octahedra are connected by formate ligands and various different A site cations may occupy the $\text{ReO}_3$ type pseudocubic cavities. . . .	98
4.3	Schematic diagram demonstrating the cooperativity associated with spin crossover phenomena in hybrid perovskites. Figure shows the hysteresis in magnetic moment with change of pressure. The y axis shows the magnetic moment (M) and x axis represents pressure (P) increasing in the positive direction as shown in the figure. Upon decreasing P, a transition happens from LS $S=0$ state where all spins are paired up in the $t_{2g}$ states octahedrally coordinated $d^6$ Fe, to HS $S=2$ state where two of the electrons from $t_{2g}$ states are promoted to $e_g$ states. The reverse effect happens as demonstrated in the previous chapter on application of temperature. Due to the cooperativity between Fe(II) centres in the extended solid state geometry, hysteresis loop appears between cycles of exertion and release of pressure . . . . .	101

- 4.4 Computed crystal structures of DMAFeF [panel (a)] and HAFeF [panel (b)] in A-site ordered phase. The  $\text{FeO}_6$  octahedra are connected to each other by the formate ligands while the DMA or HA cations sit in the hollow formed by the octahedra. Various atoms have been marked. N-H $\cdots$ O and O-H $\cdots$ O bonds are represented by dashed lines, with thickness of lines indicating the strength of the bonds. . . . . 104
- 4.5 Projected density of states of DMAFeF and HAFeF at ambient and high pressure conditions. Panels (a) and (c) are for ambient pressure, while panels (b) and (d) are for high pressure. The DOS projected to Fe  $d$ , O  $p$ , C  $p$ , N  $p$  and H  $s$  are marked in red, cyan, black, green and blue, respectively. The zero of the energy is set at Fermi energy. . . . . 105
- 4.6 Computed magnetic moment per Fe atom plotted as a function of pressure for DMAFeF [panel (a)] and HAFeF [panel (b)]. The data are plotted for two different paths. The data points in blue denote the path following increasing pressure, starting from the HS state and the data points in red denote the path following decreasing pressure, starting from the LS state. HS  $\rightarrow$  LS transitions in both compounds exhibit interesting hysteresis effects. . . . . 106
- 4.7 Total energy versus volume of the unit cell for DMAFeF and HAFeF. Energy and volumes have been measured with respect to the equilibrium values,  $E_0$  and  $V_0$ , respectively. The symbols denote the DFT calculated data points. The lines depict that obtained from Murnaghan [57] equation of state fit. . . . . 108
- 4.8 Variation of total energy as a function of variation of Fe-O bond-length about the equilibrium value, for different spin-state configurations of neighbouring Fe atoms, LS-LS (diamond), LS-HS (square) and HS-HS (circle). Solid lines are fit to the data points. Bottom panel is same as top panel but for HAFeF. . . . . 109
- 5.1 Cubic and distorted perovskites. Figure (a) on the left panel shows a perfectly cubic perovskite structure with no distortion as found for example in  $\text{SrTiO}_3$ . Figure (b) on the right panel shows a perovskite structure with what is known as  $\text{GdFeO}_3$  type distortion where there is rotation of the octahedra in plane and tilt of the octahedra out of plane. . . . . 123
- 5.2 Schematic diagram showing tetragonal distortion (compression/elongation) for an octahedral complex. The top panel shows the compression and elongation effects. The bottom panel shows the effect of compression or elongation on the distribution of orbitals and the lift of degeneracy in energy of the orbitals. . . . . 124

- 5.3 A schematic diagram showing the difference in band structure between the two closely related systems of Mott insulators and charge transfer insulators. The left panel shows a schematic density of states (DOS) for a Mott insulator with the various energy scales marked and the right panel shows a similar schematic for that of a charge transfer insulator. . . . . 127
- 5.4 Diagram demonstrating the polar catastrophe hypothesis and the associated electronic reconstruction in an n-type interface. Figure adapted from J. Mannhart et al, MRS Bull. 33 1027 (2008) . . . . 130
- 5.5 The two geometries used in the present study, the superlattice (upper panel) and the thin film-substrate (lower panel) geometry. Shown are the representative cases of  $(\text{GTO})_{1.5}/(\text{STO})_{4.5}$  superlattice and  $(\text{GTO})_1/(\text{STO})_5$  thin film-substrate geometry, projected onto the  $ac$  plane. The large, medium and small balls represent Sr/Gd, Ti and O atoms, respectively. The interfaces, formed between GdO from GTO and  $\text{TiO}_2$  layers from STO, are marked. . . 134
- 5.6 The deviation of M-O-M angles from  $180^\circ$ ,  $\Delta(\phi_{M-O-M})$  and the difference of M-O lengths in the out-of-plane and inplane directions,  $\Delta(d_{M-O})$  plotted as function of  $\text{TiO}_2$  layers, for LAO/STO (right panels) and GTO/STO (left panels) in superlattice and thin film-substrate geometries. Top left:  $\Delta(\phi_{M-O-M})$  for GTO/STO, top right:  $\Delta(\phi_{M-O-M})$  for LAO/STO. Bottom left:  $\Delta(d_{M-O})$  for GTO/STO, bottom right:  $\Delta(d_{M-O})$  for LAO/STO. In case of superlattices, results for two system sizes are shown,  $(\text{LAO or GTO})_{4.5}/(\text{STO})_{1.5}$  (black symbols) and  $(\text{LAO or GTO})_{9.5}/(\text{STO})_{1.5}$  (red symbols). In case of thin film-substrate geometries, results are shown for  $(\text{GTO})_1/(\text{STO})_9$  (black symbols),  $(\text{GTO})_2/(\text{STO})_9$  (red symbols), and  $(\text{LAO})_1/(\text{STO})_9$  (black symbols),  $(\text{LAO})_5/(\text{STO})_9$  (red symbols). For LAO/STO, only the rotation angles are shown as circles, the tilt angles being zero. The rotation and the asymmetric tilts in  $+c$  and  $-c$  directions in GTO/STO are shown as circles, squares and diamonds, respectively. The x-axis marked in red on normal side corresponds to layer numbering of the larger systems (shown in red symbols) while the x-axis marked in black on opposite side corresponds to layer numbering of the smaller systems (shown in black symbols). . . . . 136

- 5.7 The density of states projected to  $xy$  (solid line),  $xz$  (shaded area),  $yz$  (dashed lines) orbitals of Ti, in different  $\text{TiO}_2$  layers of  $(\text{LAO})_{1.5}/(\text{STO})_{4.5}$  (right panels) and  $(\text{GTO})_{1.5}/(\text{STO})_{4.5}$  (left panels) superlattices. From top to bottom, different left panels refer to  $\text{TiO}_2$  in GTO,  $\text{TiO}_2$  at 1st IF, 1<sup>st</sup>, 2<sup>nd</sup> and 3<sup>rd</sup>  $\text{TiO}_2$  layers in STO block, and  $\text{TiO}_2$  at the 2nd IF in the cell. The cell is symmetric about the 2nd  $\text{TiO}_2$  layer in STO. Right hand panels refer to the same, except for the top most panel which refer to  $\text{AlO}_2$  layer in LAO, which shows no states in the chosen energy range. The zero of the energy is set at GGA+ $U$  Fermi energy. . . . . 138
- 5.8 The density of states projected to  $xy$  (solid line),  $xz$  (shaded area),  $yz$  (dashed lines) orbitals of Ti, in different  $\text{TiO}_2$  layers of LAO/STO and GTO/STO in thin film-substrate geometry. The panels from left to right show results for  $(\text{LAO})_1/(\text{STO})_9$ ,  $(\text{LAO})_5/(\text{STO})_9$  and  $(\text{GTO})_1/(\text{STO})_9$ . From top to bottom, different panels refer to  $\text{TiO}_2$  at IF,  $\text{TiO}_2$  layers belonging to STO block. The zero of the energy is set at  $E_F$ . . . . . 138
- 5.9 Spin-polarized DOS projected onto Ti d states for GTO/STO in superlattice (left and middle panels) and thin film-substrate geometry (right panel). For the thin film-substrate geometry, in the topmost  $\text{TiO}_2$  layer, which is the surface layer of GTO, the projection to two charge disproportionate Ti d states are shown in black and red lines. The zero of the energy is set at Fermi level. . . . . 139
- 5.10 Plot of orbital occupancies with number of STO layers. The left panel shows the occupancies for the superlattice geometry and the right panel shows that for the thin-film/substrate geometry. The orbital characters are marked with different colours as shown in the legends. In the superlattice geometry both  $(\text{STO})_{4.5}$  and  $(\text{STO})_{9.5}$  blocks are shown. For the case of thin-films, only  $(\text{STO})_9$  substrates are shown. . . . . 140
- 5.11 Conduction electron charge density plotted for  $(\text{LAO})_{1.5}/(\text{STO})_{4.5}$  (upper panel) and  $(\text{GTO})_{1.5}/(\text{STO})_{4.5}$  (lower panel) in the superlattice geometry, plotted for an energy window 0.5 eV below  $E_F$  to  $E_F$ . The colour coding of different contours are shown in side scale. The topmost  $\text{AlO}_2$  surface layer in LAO and the topmost  $\text{TiO}_2$  layer in GTO are both insulating. . . . . 141

- 5.12 Conduction electron charge density plotted for  $(\text{LAO})_5/(\text{STO})_9$  (upper panel) and  $(\text{GTO})_1/(\text{STO})_9$  (lower panel) in thin film-substrate geometry, plotted for an energy window 0.5 eV below  $E_F$  to  $E_F$ . The colour coding of different contours are shown in side scale. The topmost  $\text{AlO}_2$  surface layer in LAO is metallic while the topmost  $\text{TiO}_2$  layer in GTO is insulating. The latter is driven by the charge disproportionation which happens between two Ti atoms in the unit cell in the topmost layer, shown as inset in the lower panel. . . . . 141
- 5.13 The layer decomposed DFT density of states for  $(\text{LAO})_5/(\text{STO})_9$  (left panel) and  $(\text{GTO})_2/(\text{STO})_9$  (right panel) in thin film-substrate geometry, projected onto O  $p$  (brown shaded), Al  $p$  (green line), Ti  $d$  (black/red line) and Ga  $d$  (magenta) and La  $d$  (blue line) states. For GTO/STO projection to two charge disproportionated Ti atoms are shown as black and red lines, respectively, while for LAO/STO projection to Ti  $d$  is shown as black line.  $E_F$  is set at zero. From top to bottom, various panels show the surface layer, the LAO or GTO block, the IF and the STO block. . . . . 145
- 5.14 Band offset and electronic reconstruction in LAO/STO (left panels) and GTO/STO (right panels). The upper edge VB of LAO and STO are almost aligned derived from O  $p$  bands, thereby causing a large band bending required for conduction. The upper edge VB of GTO and STO, on the other hand are completely misaligned, one being Ti  $d$  lower Hubbard band (GTO), and another being O  $p$  band (LAO). This makes band bending required for conduction much smaller. . . . . 146
- 6.1 Figure showing the structures of unstrained and epitaxially strained LMO. The top panel shows how the LMO is strained to a square lattice. The middle panel shows the different epitaxial strains and corresponding values of the  $a$  lattice parameter. The bottom panel shows the rotation and tilt in the Mn-O octahedra and the corresponding Jahn Teller distortions at various values of strains. . . . 155
- 6.2 Figure showing the four Mn atoms in the unit cell, and the magnetic superexchange interactions  $J_1$  and  $J_2$  between them. The four Mn atoms are structurally equivalent, however they form two groups when treated within the regime of hybrid functional calculations, where each group is represented by  $\text{Mn}_1$ (yellow) and  $\text{Mn}_2$ (violet). . . . . 157

6.3	Energy differences $\Delta E = E_{FM} - E_{AFM}$ between FM and A-AFM configurations at various square matching epitaxial strain values for both GGA+ $U$ and HSE06, showing that the trend in magnetic ground state for both GGA+ $U$ and HSE06 are the same. . . . .	158
6.4	Projected Density of states (PDOS) for LMO strained to STO and band gaps for various epitaxial strains. The upper block shows the band gaps as calculated from both GGA+ $U$ (blue line) and HSE06 (red line) calculations. The lower block show PDOS using GGA+ $U$ and HSE06 at 25% HF exchange with $Mn_1-d$ (red), $Mn_2-d$ (green) and $O-p$ (brown). The zero of energy is set to Fermi energy. . . . .	159
6.5	Charge density for various epitaxial strain values in the orthorhombic geometry, calculated using the HSE06 functional. . . . .	161
6.6	Charge disproportionation using HSE06 functionals for various epitaxial strain values in the orthorhombic geometry. The histograms are calculated by measuring the difference between the magnetic moments of the two Mn atoms, with change in epitaxial strain. . . . .	163
6.7	Layer projected Density of States for $(LMO)_{4.5}/STO_{4.5}$ superlattice with states projected to $Mn_1-d$ (red), $Mn_2-d$ (green), Ti $d$ (blue), and O $p$ (cyan). The left panel shows the layer resolved DOS with the GGA+ $U$ functional compared to the right panel which shows the layer resolved DOS with HSE06 hybrid functional. The zero of energy is to Fermi energy. . . . .	164
6.8	Layerwise charge disproportionation for $(LMO)_{4.5}/STO_{4.5}$ superlattice calculated being taking difference in magnetic moment between $Mn_1d$ and $Mn_2d$ in each layer. . . . .	164

# List of Tables

4.1	Table summarising the elastic and magnetic exchanges. . . . .	111
5.1	The layer-wise contribution of the conduction electron in GTO/STO and LAO/STO in superlattice and thin film-substrate geometries. In case of superlattices, results for both (LAO or GTO) <sub>1.5</sub> /(STO) <sub>4.5</sub> and (LAO or GTO) <sub>1.5</sub> /(STO) <sub>9.5</sub> are shown. For thin film-substrate geometry, the results at minimum thickness of conductivity of LAO and GTO are shown, which are 5 u.c. and 1 u.c., respectively. . .	142
6.1	Lattice parameters ( $\text{\AA}$ ) of bulk LaMnO <sub>3</sub> from experiment and GGA+ $U$ calculations . . . . .	154
6.2	Properties of the ground-state and low-energy competing bulk phases in LaMnO <sub>3</sub> . . . . .	156
6.3	Electronic properties of ground state bulk A-AFM insulating phase of LaMnO <sub>3</sub> using GGA+ $U$ and hybrid functionals in comparison to experimentally measured values. . . . .	156

# Chapter 1

## Introduction

Materials science is an interdisciplinary science encompassing many different disciplines [1] [2] [3]. It is the horizon where physics meets chemistry and engineering. It is a subject which is of common interest to both the scientific community engaged in basic research and the engineering community trying to create new technological developments out of novel properties of materials.

Materials have been instrumental in the development of human civilization as a whole. Naming various pre-historic eras viz. *Stone age*, *Bronze age*, *Iron age* or *Steel age* after different materials is a clear indication of the extremely important role played by materials in the development of human societies and civilization. Even in the historic and modern eras, very important discoveries in the field of materials have marked the overall revolutions in human progress. From chinese lodestones for navigation by sailors to the entire silicon based industry which technically runs the modern World on the wings of computers and smartphones, every aspect of our life now has contributions from some fundamental research on materials in the last few hundred years. Therefore materials science research is irreplaceable to fulfill the growing demands of modern society. Recent times have seen various classic discoveries which are mainly material dependent.

Thus no doubt it will be, and as we have been seeing in the last few decades, it is one of the most exciting fields of research. *Novel phenomena* in materials is the route to newer technologies and advances for the human race. Thus it is essential to modify known materials in order to improve their properties and to discover, or even design, new materials with specific properties. Hence there is an ever increasing demand for materials with novel properties. These materials must be functional materials which possess certain unique properties which may be tunable. Such materials can be of the following broad classes:

- (i) Materials whose existing properties may be improved or enhanced to make the properties more accessible for practical uses. As an example we may consider the family of high  $T_C$  cuprate materials to fall in this category.

- 
- (ii) Materials that are not any extension or evolution of families or combination of other materials, but are distinct materials in their own right with very unique and interesting properties and configurations. Examples of such materials are carbon nano-tubes and fullerenes.
  - (iii) Composite materials where combination of two or more components lead to unexpected or unconventional properties. The class of materials like heterostructures, and hybrid systems of organic and inorganic components fall in this category.

In this thesis we have primarily concentrated on the third class of the materials among the list enumerated above. In this class we have studied two broad category of materials namely;

- (a) Metal-Organic Hybrid materials,
- (b) Inorganic Oxide Heterostructures.

A relatively new class of materials are composite organic-inorganic hybrid materials. An intriguing phenomena observed sometimes in these materials, especially those containing transition metal ions in the inorganic component is a spin crossover phenomena associated with hysteresis which one day may have huge applications in memory and display devices. Similarly oxide heterostructures, which are composites of known perovskite oxide materials, have shown tremendous application possibilities and may very well replace the silicon based electronics industry completely and we may one day live in the age of oxide electronics!

However, such materials are usually complex in structure and in behaviour, containing several atoms in the unit cell involving several different degrees of freedom. As a result, modeling of such complex materials plays an ever increasing role in the study of physical properties of those compounds. With the advent of computational materials science these materials can now be understood at the microscopic level. Such microscopic understanding is required for optimization of known materials, with the possibility of prediction of new materials. The proliferation of computing power is enabling exciting new approaches to the characterization and design of materials. Computational methods already play a central role in many materials studies and will only become more pervasive as computing power advances in the decades ahead. Thus computational materials science plays a two fold role in the development of this particular field of research. Microscopic understanding of observed novel phenomena can be obtained by simulating the behaviour of materials. This can provide very useful insight into how materials can be modified or designed to achieve properties which may be put to technological use. For example the understanding of the microscopic

---

behaviour of high  $T_C$  superconductors can help one to increase the critical temperature further and possibly design room temperature superconductors which understandably will have a huge impact on modern society transforming life itself on Earth. The second very important aspect of computational materials science is the aspect of prediction of properties and phenomena in materials which may be further tested in the laboratory. This aspect has been leading the community of scientists engaged in materials research to push further the boundaries of what can be achieved in the laboratory. Starting from describing transition phenomena to predicting the correct experimental conditions for growth of materials or onset of certain novel phenomena, this particular aspect of computational sciences have made leaps and bounds in advances in the synergistic approach of theory and experiments towards materials research. The purpose thus of this particular field of study in a nutshell is to simulate the properties of material to understand and complement the experiments, thus understanding and refining our materials model (generating the model), hence to use it to calculate different properties of that material under different conditions, and verifying the predictions through experiments (predicting and validating the model), leading to design of materials with specific properties on demand.

In the present thesis, we have investigated and understood the complex behaviour of some of these compounds in terms of suitable modeling, starting from first-principles electronic structure calculations, in general. Both zero temperature and finite temperature first principles electronic structure calculations have been carried out within the realm of Density Functional Theory (DFT) and Ab Initio Molecular Dynamics (AIMD). The advantages of first principles method is that, the only input required is the crystal structure with proper atomic information. These are very reliable, fast, accurate and parameter free approaches, and are able to capture the material dependent chemistry accurately. In addition to first principles methods classical model Hamiltonians have been studied and solved using techniques like classical Monte Carlo simulations.

In the next few sections we give a brief introduction to the materials studied in the current thesis.

## 1.1 Metal-Organic Complexes

Metal-organic complexes are a class of chemical compounds that contain metals and organic ligands, which confer solubility in organic solvents. Compounds with these attributes find multifarious applications. Metal organic complexes can be of various types. These materials may form dense systems, porous system, isolated molecular systems or extended network systems.

Among these types of materials, we primarily concentrate on coordination polymers and hybrid perovskites, and we study a phenomenon called Spin Crossover (SCO). SCO takes place in transition metal complexes, specially those consisting of transition metal ions and flexible organic ligands, wherein the spin state of the metal ion changes between low spin (LS) and high spin (HS) configuration under the influence of external perturbation [4]. The transition between high spin ( $S = 2$ ) and low spin ( $S = 0$ ) state of transition metal can be triggered by several different possibilities such as temperature, pressure, light irradiation etc [5]. Though this process, in principle, can be observed in any octahedrally or tetrahedrally coordinated transition metal complexes with transition metal ions in  $d^4$ - $d^7$  or  $d^3$ - $d^6$  electronic configurations, the most commonly observed cases are that of octahedrally coordinated iron(II) complexes with  $\text{Fe}^{2+}$  ions in  $3d^6$  electronic configuration. The SCO phenomenon deserves attention due to accompanying changes in magnetic and optical properties. Various different application possibilities have been suggested in information technology [6], as sensors [7], optical switches [8], display and memory devices. For device applications, it is important to induce cooperativity in the SCO phenomena implying spin transition rather than spin crossover, which may happen with associated hysteresis effect. The issue of cooperativity and associated hysteresis is important as it is expected to confer memory effect to the system.

In this context, in comparison to molecular assemblies or crystals with isolated molecular units connected by weak, van der Waals or hydrogen bonding, the extended network with repeating coordination entities having extended solid structures are better choices. We may broadly classify these systems into *coordinations polymers* which consist of a plethora of compounds that contain inorganic metallic centres connected via organic ligands or functional groups in various possible ways, or  $\text{ABX}_3$  type *hybrid perovskite* structures that are coordination frameworks with organic ligands containing potential voids, both of which have been studied in this thesis. The presence of chemical bridges, linking the SCO sites to each other, as in these compounds are expected to propagate the interac-

---

This section is based on "Design and Control of Cooperativity in Spin-Crossover in Metal-organic Complexes: A Theoretical Overview" *Hrishit Banerjee, Sudip Chakraborty, Tanusri Saha-Dasgupta Inorganics, 5(3), 47 (2017)*

tion between SCO centers more efficiently than that in molecular crystals. In spite of admitting the suitability of such compounds in exhibiting cooperativity there are several issues that need attention. The key questions are, (a) understanding the microscopic mechanism, i.e., what is the driving force for the cooperativity and the hysteresis; and (b) how the cooperativity can be tuned or modified to suit specific device application needs. These understandings are expected to provide an advancement of the field in terms of possible commercialization of this technologically important property which relies on critical parameters of crossover being close to ambient condition, and a large enough hysteresis width. Of prime importance in this case is the identification of materials able to show spin crossover associated with cooperativity.

Thus in the next sections, we give a brief general introduction to both coordination polymers and hybrid perovskites.

### 1.1.1 Coordination Polymers

Coordination polymers are organometallic polymeric structures having metal ion centers linked by organic ligands [9].

A typical example of such a polymeric compound, namely Fe-triazole is shown in the left panel of Figure 1.1. These are materials extending through repeating coordination entities, in 1 dimension, but with cross-links between two or more individual chains, and loops, while a coordination compound extends through repeating coordination entities in 1, 2 or 3 dimensions. The dimensionality of a coordination polymer is defined by the number of directions in space the array extends to. A one-dimensional structure extends in a straight line (for example along the x axis); a two-dimensional structure extends in a plane (two directions, x and y axes); and a three-dimensional structure extends in all three directions (x, y, and z axes) [11]. The work of Alfred Werner and his contemporary researchers laid the foundational groundwork for the study of coordination polymers. Terms unique to the field, such as coordination number, were coined by Werner. Werner et al categorized a lot of organometallic materials as coordination polymers. These include the cyanide complexes Prussian blue and Hofmann clathrates [12].

Metal centers, also called nodes, bond to a specific number of linkers at well defined angles. The number of linkers bound to a node is known as the coordination number, which, along with the angles they are held at, determines the dimensionality of the structure. The coordination number and coordination geometry of a metal center is determined by the nonuniform distribution of electron density around it, and in general the coordination number increases with cation size. Transition metals are commonly used as nodes. Partially filled  $d$  orbitals, can hybridize in different ways depending on environment. This electronic structure causes some of them to exhibit multiple coordination geometries,

particularly copper and gold ions which as neutral atoms have full  $d$ -orbitals in their outer shells. Alkali metals and alkaline earth metals exist as stable cations. Alkali metals readily form cations with stable valence shells, giving them different coordination behavior compared to transition metals. They are strongly affected by the counterion from the salt used in synthesis, which is difficult to avoid. Group II metals have also been used as nodes. In this case, the dimensionality of these structures increases as the radius of the metal increases down the group (e.g. from calcium to strontium to barium). In most coordination polymers, a

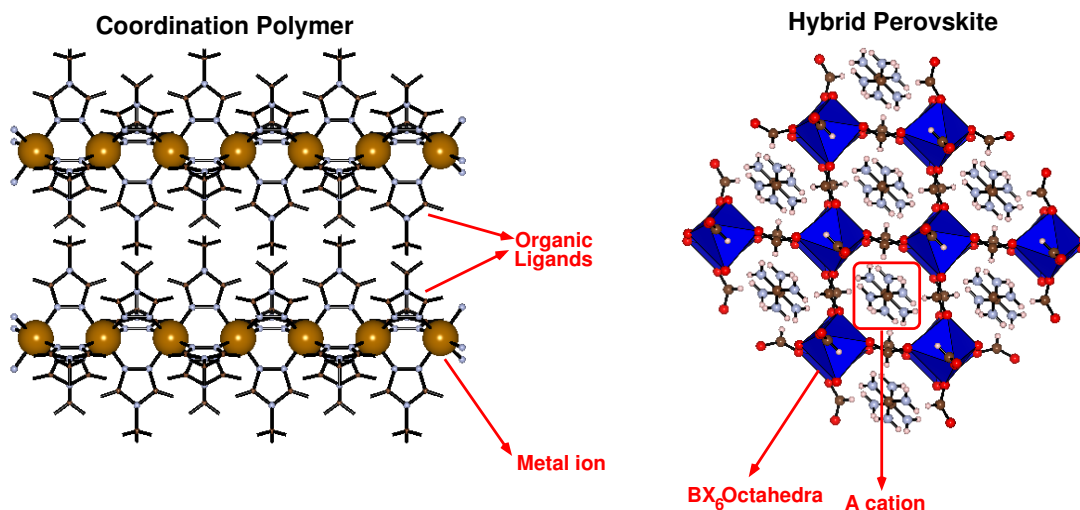


Figure 1.1: Schematic representation of linear, 1-D coordination polymer (left panel) and hybrid perovskite (right panel). In case of linear, 1-D coordination polymer, chains of metals are linked by organic ligands. In the  $ABX_3$  structure of hybrid perovskite,  $BX_6$  forms octahedra with A cation sitting in the voids. B cation is a metal ion and A cation is an organic cation.  $BX_6$  octahedra are also linked by organic linkers. Figure adapted from Banerjee et al [Inorganics, 5(3), 47 (2017)]

ligand (atom or group of atoms) will formally donate a lone pair of electrons to a metal cation and form a coordination complex via a Lewis acid/ base relationship. Coordination polymers are formed when a ligand has the ability to form multiple coordination bonds and act as a bridge between multiple metal centers. Ligands that can form one coordination bond are referred to as monodentate, but those which form multiple coordination bonds, which could lead to coordination polymers are called polydentate. Polydentate ligands are particularly important because it is through these ligands that connect multiple metal centers together, that an infinite array is formed. Polydentate ligands can also form multiple bonds to the same metal also known as chelation. Monodentate ligands are also referred to as terminal ligands because they do not offer a place for the network to con-

tinue. Often, coordination polymers will consist of a combination of poly- and monodentate, bridging, chelating, and terminal ligands.

Almost any type of atom with a lone pair of electrons can be used as a ligand. Ligands that are commonly found in coordination polymers include polypyridines, phenanthrolines, hydroxyquinolines and polycarboxylates. Oxygen and nitrogen atoms are commonly found to be the binding sites.

Besides the choice of metals and ligands, there are many other factors that affect the structure of coordination polymers. For example, one of the important factors which may affect properties of a coordination polymer is the counter ion. Other than this there are also guest molecules like water or other molecules which affect steric or other factors and may at times lead to Hydrogen bonding in these materials.

Coordination polymers have multifarious applications. The chief among these are molecular storage, where porous coordination polymers have potential as molecular sieves in parallel with porous carbon and zeolites [12], in luminescence [13], electrical conductivity [13], magnetism [13] and as sensors and memory devices.

The context of the study of coordination polymers in our case is to address the question of which are the materials which are suitable for cooperative SCO. As mentioned previously, 1, 2 or 3-dimensional coordination polymers, which are materials with repeating array of coordination entities, are suitable choices. The dimensionality of a coordination polymer is defined by the number of directions in space the array extends to. Most studied SCO materials showing cooperativity, so far are linear 1-dimensional coordination polymers which are compounds extending through repeating coordination entities in 1-dimension forming chain like structures, with weak links between individual chains [13], as shown in left panel of Figure 1.1. The other possibilities are coordination network solids [13], which are compounds extending through repeating coordination entities in 2 or even 3 dimensions. Strategic crystal engineering that makes use of multidentate ligands, connected by spacers, facilitates to increase the dimensionality from 1-D to 2-D or 3-D. Pressure-induced LS-HS transition in 2-D net was first reported for  $[\text{Fe}(\text{btr})_2(\text{NCS})_2]\text{H}_2\text{O}$  [14] [btr  $\rightarrow$  bis-triazole]. The compound consisted of Fe(II) ions linked by btr in two directions producing infinite layers which were connected by means of van der Waals or weak H bonds.  $[\text{Fe}(\text{btr})_3][(\text{ClO}_4)_2]$  [15] represents the first 3-D SCO coordination polymer.

For the sake of brevity, we will restrict ourselves to only linear or 1-D coordination polymers, and not extend our discussion to 2-D or 3-D polymers.

Among the linear coordination polymers, or 1-D chain compounds 4R-1,2,4-triazole based Fe(II) chain compounds have been in focus both in early studies and in recent developments.  $[\text{Fe}(\text{4R-1,2,4-triazole})_3]\text{A}_2.\text{solv}$ , where A is the counterion and *solv* denotes the solvent molecule, are made up of linear chains in which the adjacent Fe(II) ions in the chain are linked by three triazole ligands. The co-

ordination linkers, which are 1,2,4-triazole blocks, form efficient chemical bonds to transmit cooperative effect, leading to hysteresis loop of width ranging  $\approx 2$ -20 K. [16] Sometimes these hysteresis loops are also found to be centered at room temperature. [17] Bimetallic 1-D chain compounds like  $\text{Fe}(\text{aqin})_2(\mu_2\text{-M}(\text{CN})_4)$ ,  $\text{M}=\text{Ni}(\text{II})$  or  $\text{Pt}(\text{II})$ ,  $\text{aqin}$  = Quinolin-8-amine, have been recently synthesized which were found to show abrupt HS-LS SCO. [18] Novel 1-D Fe(II) SCO coordination polymers with 3,3'-azopyridine as axial ligand has been synthesized which were found to show kinetic trapping effects and spin transition above room temperature. [19] Combination of rigid links and a hydrogen bond network between 1-D Fe(II) chains has been recently shown as a promising tool to trigger SCO with hysteresis loops having widths as large as  $\approx 43$  K. [20]

### 1.1.2 Hybrid Perovskites

We will now focus on a new class of materials in context of SCO, namely hybrid perovskites. A subclass of coordination network solids are metal organic frameworks (MOFs) which are coordination networks with organic ligands containing potential voids [13], and thus can be labeled as porous coordination polymers. Most of the research on MOFs are related to porosity of the systems, however, recently attention has also been given to dense MOFs with limited porosity which show potential for applications in other areas like optical devices, batteries, and semiconductors.

Hybrid perovskites are a class of compounds with general formula  $\text{ABX}_3$  having long range connectivity that form a subclass of dense MOFs. The extended, 3-dimensional connectivity with limited void space, together with possibility of synthesizing hybrid perovskites containing transition metal ions have made these compounds also probable candidates for exhibiting cooperative SCO. While linear coordination polymers have already been explored to a large extent in search of cooperative SCO,  $\text{ABX}_3$  type hybrid perovskites, which though in attention in recent time, has not been explored for cooperative SCO.

Hybrid perovskites are actually counterparts of inorganic perovskites (discussed in detail in the next section) and have attracted a great deal of attention of the material chemists due to their varied technological applications and novel optical, dielectric, and multi-ferroic properties [21], [22], [23], [24], [40]. These materials have very useful applications in catalysis, [26] gas storage, [27] and thin film solar cells [28]. Their usage in chemical sensors [29] and luminescent materials have been known too to the scientific community. Combining some of these properties for their functionality like magnetism and optical properties, conductivity and magnetic properties, magnetism and porosity, or molecular motion and electric and magnetic properties has been interesting fields of study. Very interesting applications in the fields of drug delivery [30], methane storage [32], bio-mimetic mineralization [30], as semiconductors, [31] and in carbon capture [33] has also

been noted. The most famous applications for hybrid perovskites have been in the case of perovskite solar cells [28] which have enjoyed a huge success in design and implementation. These are primarily lead and tin halide based hybrids, which we shall discuss in detail shortly. These perovskite materials have been well known for many years, but the first incorporation into a solar cell was reported recently by Miyasaka et al. in 2009 [34].

In case of hybrid perovskites, while the B cation is a metal ion as in inorganic perovskites, both the A cation as well as the ligand can be organic. Lead halides hybrid perovskite [35,36] family having  $[AmH]MX_3$  composition, where  $AmH^+$  is the protonated amine part; M is either  $Sn^{2+}$  or  $Pb^{2+}$ , and  $X^-$  is the halogen part (Cl, Br, or I) have been shown to demonstrate high performance and efficiency in applications relating to design of mesostructural (and/or nanostructural) solar cells and other photovoltaic devices [34,37,38]. Easy processing techniques like spin-coating, dip-coating, and vapor deposition techniques have been known to be of advantage in this case [39,40].

Organic ligands like formate being simple enough have also been studied with varied A cations and metal ions primarily from the transition metal family. This class of materials have been shown to exhibit curious properties in the experimental literature, of which multiferroicity seems to be the most intriguing one. Computed crystal structures of representative compounds like dimethylammonium iron formate (DMAFeF) and hydroxylammonium iron formate (HAFeF) are shown in right panel of Figure 1.1. Studies have been carried out for transition metal atoms centres like Mn, Cu, Ni, Fe, Co [41] etc. In the crystal structure of these compounds, as shown schematically in right panel of Figure 1.1, formate bridges act as linkers that connect the  $BX_6$  octahedra, with the protonated amine cations situated at the hollow spaces formed by the linked octahedra. These hollow spaces act as pseudo-cubic  $ReO_3$  type cavities.

Some of these compounds are canted weak ferromagnets with small values of  $T_C$ , and have shown hysteresis loops below their critical temperatures. It has been seen from model calculations with these materials that the dominant superexchange mechanism in them is antiferromagnetic. It has been suggested that it is possible to synthesize other weak ferromagnets by changing the central A amine cation. This class of materials has been shown to exhibit curious properties, of which multiferroicity seems to be an intriguing one [42–44]. Ferroelectricity and especially multiferroicity in these materials has been extensively studied by Stroppa and coworkers mostly from a DFT based first principles perspective and at times combined with experimental studies [45–49]. Structural details and effects due to structural phase transitions, strain tuning of various effects like polarisation, and magnetic structure has also been studied [50–53]. It has also been seen that these materials undergo structural order-disorder phase transitions. This phase change is often associated with a dielectric anomaly when cooling. When compared to the phase transition on heating, a clear hysteresis of

a reasonable width was observed.

As mentioned previously, the presence of transition metal in these compounds together with its octahedral environment makes them suited also for exhibiting SCO behavior and possibly also cooperativity due to dense nature of framework, which would provide another dimension to functionality of these interesting class of compounds. This aspect of this interesting class of compounds has remained unexplored, until our recent theoretical proposal [54].

## 1.2 Inorganic Oxide Heterostructures

### 1.2.1 Oxides

Complex oxides represent a class of materials with a plethora of fascinating physical properties. The intriguing interplay of charge, spin, and orbital ordering in these systems coupled with lattice effects opens up a scientifically rewarding playground for both fundamental and application-oriented research. In particular transition metal oxides (TMO) continue to attract a great deal of attention both experimentally and theoretically spanning over many decades, due to their several interesting properties, e.g. Mott transition, High-Tc superconductivity, ferromagnetism, antiferromagnetism, low-spin/high-spin transition, ferroelectricity, antiferroelectricity, colossal magnetoresistance, charge ordering etc.

The basic structural unit of this class of materials is metal-oxygen polyhedra ( $\text{MO}_n$ , where M is the Transition Metal (TM) atom, O is the oxygen and  $n$  is an integer) such as octahedra, square pyramid, square planar, tetrahedra, pentagonal bipyramid, trigonal bipyramid etc. The strong tendency of surrounding oxygen atoms towards negative valency, remove the  $s$  electrons from the TM atom and subject the  $d$  orbitals of TM ions to an anisotropic field, known as crystal field. Under the influence of this field each  $d$  orbital is affected differently and how a particular  $d$  orbital will be affected depends upon the geometry of the oxygen surrounding. This results in splitting of the energy levels of the five fold degenerate (including spin, 10- fold degenerate)  $d$  orbitals in the atomic limit. The strength of this splitting, known as crystal field splitting, depends on the following factors:

- Geometry of the oxygen polyhedra.
- Strength of TM-O covalency

The most common geometry is the octahedral geometry, where six oxygen ligands form an octahedron around the metal ion. For a cubic symmetry the  $d$ -orbitals split into two sets : a higher energy level of two-fold (including spin, fourfold) degenerate  $e_g$  orbitals and a lower energy level of three-fold (including spin, six-fold) degenerate  $t_{2g}$  orbitals. For a perfect octahedral symmetry, the lobes of the  $e_g$  orbitals, formed by  $d_{x^2-y^2}$  and  $d_{3z^2}$  orbitals, are pointed directly towards the oxygen atoms and therefore feel stronger electrostatic field than the  $t_{2g}$  orbitals, which are constituted by  $d_{xy}$ ,  $d_{yz}$  and  $d_{xz}$  orbitals with lobes directed in between two oxygen atoms. If the degenerate  $e_g$  states are occupied partially, it generally leads to further lifting of degeneracy of the ground state. The perfect octahedral geometry distort spontaneously driven by the combined effect of two phonon modes  $Q_2$  and  $Q_3$ . The modes are defined as

$$Q_2 = \frac{1}{\sqrt{2}}(X_1 - X_4 - Y_2 + Y_5), \quad (1.1)$$

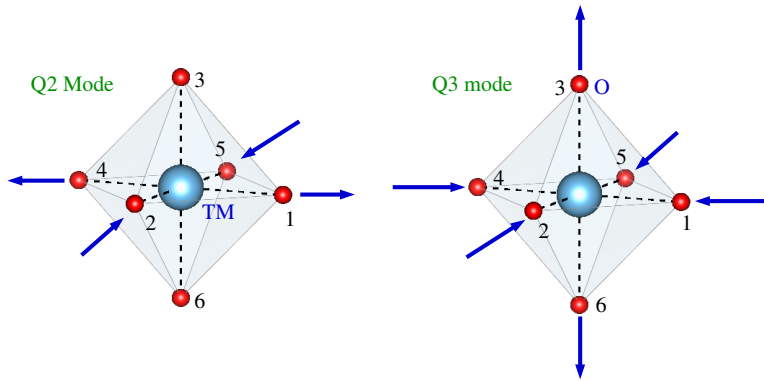


Figure 1.2: Jahn-Teller breathing modes. Figure (a) on left panel shows the  $Q_2$  breathing mode while figure (b) on right panel shows the  $Q_3$  breathing mode.

$$Q_3 = \frac{1}{\sqrt{6}}(2Z_3 - 2Z_6 - X_1 + X_4 - Y_2 + Y_5). \quad (1.2)$$

This spontaneous distortion removes the degeneracy and reduce the energy of the system to stable states. This effect is known as Jahn-Teller effect as demonstrated in Figure 1.2, named after Hermann Jahn and Edward Teller, who first gave the full explanation of this effect [59]. In Figure 1.2 the  $Q_2$  and  $Q_3$  Jahn Teller breathing modes are shown. The left panel shows the  $Q_2$  breathing mode where one pair of the two in-plane O atoms move towards each other and the other pair moves away from each other. In the right panel the  $Q_3$  breathing mode is shown where the in plane oxygen atoms all move towards each other and the out of plane oxygen atoms move away from each other. In TMOs, as the direct overlap between TM  $d$  orbitals is negligibly small, the  $d$  electrons can move only through hybridization with oxygen  $2p$ -bands. The magnitude of this indirect overlap depends on the following factors such as, the orientation of the  $d$  orbitals with respect to the connecting O  $p$  orbitals, that are responsible for the low energy phenomenon, and, the relative position of oxygen  $p$ -levels ( $\epsilon_p$ ) and transition metal  $d$ -levels ( $\epsilon_d$ ), i.e. the value of charge transfer energy

$$\Delta = \epsilon_d - \epsilon_p. \quad (1.3)$$

In case of some  $3d$  transition metal (Ti, V, Cr, Mn) oxides having octahedral surrounding of oxygen ions the Fermi level lies in the manifold of  $t_{2g}$  bands. Therefore the net overlap between two adjacent TM  $d$  orbital takes place through the hybridization between  $t_{2g}$  bands and oxygen  $2p$  bands. As the  $t_{2g}$  orbitals point away from the oxygen  $2p$  orbitals, it forms weak  $\pi$  hybridization with oxygen. Furthermore, low nuclear charge of early TM, makes the relative energy difference of  $d$  and  $p$  bands large. On the other hand in case of late  $3d$  TM (Fe, Co, Ni, Cu) based oxides, for the same octahedral symmetry, as the  $t_{2g}$  levels are completely occupied,  $e_g$  levels play the main role to create varied interesting physical

phenomenon. Owing to the favorable geometric orientation of the  $e_g$  orbitals with respect to oxygen  $2p$  orbital, the hybridization is stronger. Additionally, the larger charge on the TM nuclei decreases the chemical potential of  $d$  electrons and thus the relative energy difference of  $d$  and  $p$  bands.

Metal oxide perovskites constitute one of the largest class of oxide materials. First perovskite based mineral  $\text{CaTiO}_3$  was discovered in 1839 in the Ural mountains by geologist Guastav Rose and the name given in the honor of famous Russian mineralogist Count Lev Alexevich Perovski. [60] It lends its name to the class of compounds which have the same type of crystal structure as  $\text{CaTiO}_3$  known as the perovskite structure [55]. The perovskite crystal structure was first described by Victor Goldschmidt in 1926 [61]. The general formula of any perovskite is  $\text{ABX}_3$ , where B atom is surrounded by X in a 6 coordinated environment whereas A atom is surrounded in a 12 coordinated environment by X atom. Perovskite materials  $\text{MgSiO}_3$  and  $\text{FeSiO}_3$  are the most abundant compounds in the Earths crust.

The general formula for perovskite based transition metal oxides is  $\text{ABO}_3$ , where A is a rare earth or alkaline earth element and B is a transition metal. B site ions sit at the center of the lattice, and could be  $3d$ ,  $4d$ , and  $5d$  transition metal elements. Generally the structure consists of an array of corner shared  $\text{BO}_6$  octahedral units with large A cations sitting at the void spaces in between the octahedral units. The structure of these perovskite oxides are mainly derived from cubic structure. However many compounds at low temperatures often exist with lower symmetry structures such as in tetragonal, orthorhombic or hexagonal symmetries.

Among the complex oxides, the  $\text{ABO}_3$  perovskites and related layered compounds stand out. The subtle interplay between competing energy scales result in a variety of orderings of the spin, charge, and orbital degrees of freedom. It endows these materials with a broad spectrum of functional properties; for instance, charge transport can exhibit colossal magnetoresistance, metal-to-insulator transitions, or insulator-to-superconductor transitions (for strongly correlated compounds). Cooperative alignment of electric dipoles or spins lead to ferroelectricity or ferromagnetism, respectively. Tilting and buckling of oxygen octahedra, which result in antiferrodistortive (AFD) structural ordering, can couple to other modes in the system, driving structural and electronic phase transitions.

A large number of metallic elements are stable in the perovskite structure, if the tolerance factor  $t$  is in the range of 0.75-1.0, where  $t$  may be defined as [57],

$$t = \frac{R_A + R_O}{\sqrt{2}(R_B + R_O)} \quad (1.4)$$

Here  $R_A$ ,  $R_B$  and  $R_O$  are the ionic radii of A and B site elements and oxygen, respectively.

In the idealized cubic unit cell of such a compound, type 'A' atom sits at cube

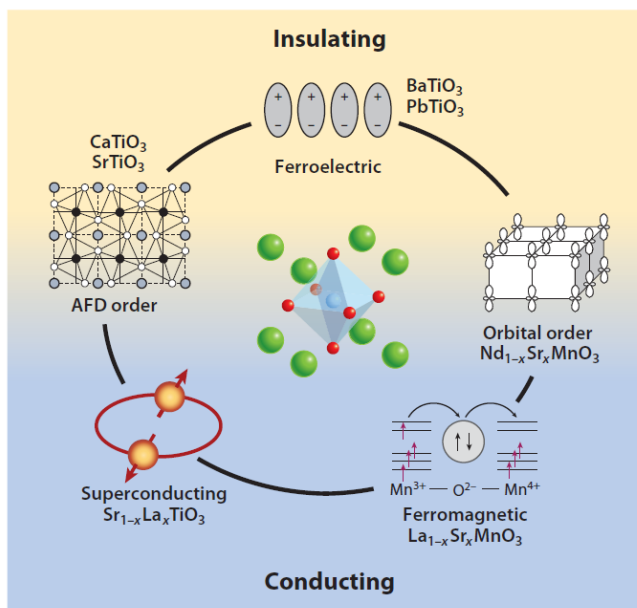


Figure 1.3: A schematic diagram demonstrating the various properties of complex perovskite oxides. The green, blue, and red spheres forming the perovskite structure illustrated in the centre represent the A, B, and O atoms, respectively. Figure adapted from Triscone et al *Annu. Rev. Condens.Matter Phys.* 2011. 2:14165

corner positions  $(0, 0, 0)$ , type 'B' atom sits at body centre position  $(1/2, 1/2, 1/2)$  and oxygen atoms sit at face centred positions  $(1/2, 1/2, 0)$ . As shown in Figure 1.3. the green balls are the A atoms, the light blue ball in the middle of the shaded octahedra is the B atoms and the small red balls are the O atoms. Figure 1.3 also showcases the various interesting properties of perovskite oxides.

The relative ion size requirements for stability of the cubic structure are quite stringent, so slight buckling and distortion can produce several lower-symmetry distorted versions, in which the coordination numbers of A cations, B cations or both are reduced. Tilting of the  $\text{BO}_6$  octahedra reduces the coordination of an undersized A cation from 12 to as low as 8. Conversely, off-centering of an undersized B cation within its octahedron allows it to attain a stable bonding pattern. The resulting electric dipole is responsible for the property of ferroelectricity shown by perovskites such as  $\text{BaTiO}_3$  that distort in this fashion.

The orthorhombic and tetragonal phases are most common non-cubic variants of perovskite oxides.

Complex perovskite structures contain two different B-site cations. This results in the possibility of ordered and disordered variants.

Perovskites may be structured in layers, with the above  $\text{ABO}_3$  structure sep-

arated by thin sheets of other materials. Different forms of intrusions, based on the chemical composition of the intrusion or interpenetration, are defined as [58]:

- Ruddlesden-Popper phase: This phase happens to be the simplest of all the three different phases. Here the intercalating layer occurs between every one ( $n = 1$ ) or two ( $n = 2$ ) layers of the  $ABO_3$  lattice. Ruddlesden-Popper phases have a similar relationship to perovskites in terms of atomic radii of elements with A being quite large (such as La or Sr) and the B ion in comparison being a much smaller transition metal ion (such as Mn, Co or Ni).
- Aurivillius phase: In this phase the inter-penetrating layer is composed of a  $[Bi_2O_2]^{2+}$  ion, occurring every  $n$   $ABO_3$  layers, leading to an overall chemical formula of  $[Bi_2O_2]^- A_{(n-1)} B_2 O_7$ . The oxide ion-conducting properties of materials belonging to this phase were first discovered in the 1970s by Takahashi et al., and they have been used for this purpose ever since.
- Dion-Jacobson phase: In this particular phase interpenetrating layer is composed of an alkali metal (M) for every  $n$   $ABO_3$  layers, giving the overall composite formula to be  $M^{10+} A_{(n-1)} B_n O_{(3n+1)}$

Perovskite materials exhibit many interesting and intriguing properties from both the theoretical and the application point of view. Colossal magnetoresistance, ferroelectricity, superconductivity, charge ordering, spin dependent transport, high thermopower and the interplay of structural, magnetic and transport properties are commonly observed features in this family. These compounds are used as sensors and catalyst electrodes in certain types of fuel cells and are candidates for memory devices and spintronics applications.

Many superconducting ceramic materials (the high temperature superconductors) have perovskite-like structures, often with 3 or more metals including copper, and some oxygen positions left vacant. One prime example is yttrium barium copper oxide which can be insulating or superconducting depending on the oxygen content.

### 1.2.2 Heterostructures formed between Oxides

Developments in recent experimental methods like molecular beam epitaxy (MBE) or pulsed laser deposition (PLD) have lead to the possibility of layer by layer growth of perovskite oxides on one another. Such layered structures with more than one oxide compound in the structure are called oxide heterostructures as shown in the experimental annular dark field image in Figure 1.4. The pioneering work by Ohtomo & Hwang [62] established that a two dimensional electron gas (2DEG) of high carrier density and high mobility is formed at the interface (IF) of two perovskite oxides, like  $LaAlO_3$ (LAO) and  $SrTiO_3$ (STO), both of which are

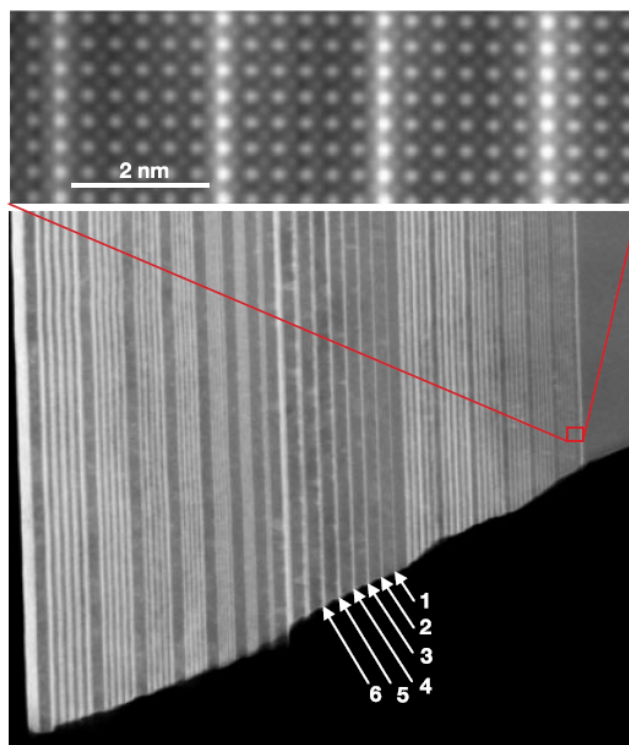


Figure 1.4: Annular dark field (ADF) image of  $\text{LaTiO}_3$  layers (bright) of varying thickness spaced by  $\text{SrTiO}_3$  layers. The view is along the  $[100]$  axis of the  $\text{SrTiO}_3$  substrate. The growth sequence is  $5 \times n$  (that is, 5 layers of  $\text{SrTiO}_3$  and  $n$  layers of  $\text{LaTiO}_3$ ),  $20 \times n$ ,  $n \times n$ , and finally a  $\text{LaTiO}_3$  capping layer. The numbers in the lower image indicate the number of  $\text{LaTiO}_3$  unit cells in each layer. Field of view is 400 nm. Magnified view of the  $5 \times 1$  series in the top panel. Figure is adapted from Ohtomo and Hwang Nature 419, 378, 2002

band insulators, and [63] neither of which share the properties seen at the interface. Interfaces can exhibit electrical conductivity [62], superconductivity [64], ferromagnetism [65], large negative in-plane magnetoresistance [66], and giant persistent photoconductivity [67].

Under the right conditions, the  $\text{LaAlO}_3/\text{SrTiO}_3$  interface is electrically conductive, like a metal. The angular dependence of Shubnikov-de Haas oscillations indicate that the conductivity is two-dimensional, leading to its reference as a two-dimensional electron gas (2DEG) [68]. Two-dimensional does not mean that the conductivity has zero thickness, but rather that the electrons are confined to only move in two directions.

However not all  $\text{LaAlO}_3/\text{SrTiO}_3$  interfaces are conductive. Typically, conductivity is achieved only when:

- The LaAlO<sub>3</sub>/SrTiO<sub>3</sub> interface is along the [001], [110] and [111] crystallographic directions,
- The LaAlO<sub>3</sub> and SrTiO<sub>3</sub> are crystalline and epitaxial,
- The SrTiO<sub>3</sub> side of the interface is TiO<sub>2</sub>-terminated (causing the LaAlO<sub>3</sub> side of the interface to be LaO-terminated) [62], which is known as an n-type interface,
- The LaAlO<sub>3</sub> layer is at least 4 unit cells thick (this however is not the case with other interfaces, like for example in interfaces between Mott insulators and band insulators where there is no critical or cutoff thickness for conduction). [71]

Conductivity may also be achieved when the SrTiO<sub>3</sub> is doped with oxygen vacancies; however, in that case, the interface is technically LaAlO<sub>3</sub>/SrTiO<sub>3-x</sub> instead of LaAlO<sub>3</sub>/SrTiO<sub>3</sub>.

The source of conductivity at the LaAlO<sub>3</sub>/SrTiO<sub>3</sub> interface has been debated for years. SrTiO<sub>3</sub> is a wide-band gap semiconductor that can be doped n-type in a variety of ways. Clarifying the mechanism behind the conductivity is a major goal of current research. Four leading hypotheses in this context are:

1. Polar catastrophe
2. Oxygen vacancies
3. Intermixing of cations
4. Structural distortions

The most prevalent hypothesis is the Polar Catastrophe Hypothesis which we shall discuss in detail in the relevant chapter.

We could similarly have various types of interfaces between Mott insulators and band insulators or Jahn Teller insulators and band insulators and see how the property of the interfaces change! A large number of both conducting and insulating interfaces have been identified . Some of the conducting interfaces are, GdTlO<sub>3</sub>/SrTiO<sub>3</sub>, LaTiO<sub>3</sub>/SrTiO<sub>3</sub>, LaVO<sub>3</sub>/SrTiO<sub>3</sub>, LaGaO<sub>3</sub>/SrTiO<sub>3</sub>, PrAlO<sub>3</sub>/SrTiO<sub>3</sub>, NdAlO<sub>3</sub>/SrTiO<sub>3</sub>, NdGaO<sub>3</sub>/SrTiO<sub>3</sub>, GdAlO<sub>3</sub>/SrTiO<sub>3</sub>, Al<sub>2</sub>O<sub>3</sub>/SrTiO<sub>3</sub>, YAlO<sub>3</sub>/SrTiO<sub>3</sub>, La<sub>0.5</sub>Al<sub>0.5</sub>Sr<sub>0.5</sub>Ti<sub>0.5</sub>O<sub>3</sub>/SrTiO<sub>3</sub>, DyScO<sub>3</sub>/SrTiO<sub>3</sub>, KTaO<sub>3</sub>/SrTiO<sub>3</sub>, CaZrO<sub>3</sub>/SrTiO<sub>3</sub>, while the insulating interfaces are, LaCrO<sub>3</sub>/SrTiO<sub>3</sub>, LaMnO<sub>3</sub>/SrTiO<sub>3</sub>, La<sub>2</sub>O<sub>3</sub>/SrTiO<sub>3</sub>, Y<sub>2</sub>O<sub>3</sub>/SrTiO<sub>3</sub>, LaYO<sub>3</sub>/SrTiO<sub>3</sub>, EuAlO<sub>3</sub>/SrTiO<sub>3</sub>, BiMnO<sub>3</sub>/SrTiO<sub>3</sub>. The most intriguing property [69] among those shown by interfaces seem to be the puzzling existence of both ferromagnetism and superconductivity!

In case of LAO/STO carrier densities are found [70] to be an order of magnitude smaller than  $(e/2)$  which is expected out of polar catastrophe model. Moreover the IFs have been reported to be insulating below a critical thickness of

LAO layers [71]. Recently superlattices & heterostructures consisting of  $\text{GdTiO}_3$  (GTO) which is a Mott insulator and  $\text{SrTiO}_3$  which is a band insulator have been grown [72] which show 2DEG densities of  $3.3 \times 10^{14} \text{cm}^{-2}$  in accordance with polar catastrophe model irrespective of layer thickness.

Among the various novel properties of heterointerfaces, a lot of effort has been made to control and utilize magnetic properties as well for e.g. the magneto-electric coupling, the magnetic ordering modification, and the charge-transfer effect were observed by using manganese oxides as a constituent layer within oxide heterostructures. In this context,  $\text{LaMnO}_3$  (LMO), a Jahn Teller Insulator, based layers have been widely adopted to employ magnetism to the oxide heterostructures. The primary advantage of using LMO is that its magnetic and electric phases can be modified diversely by a small amount of doping. Stoichiometric LMO is an A-type antiferromagnet and is a good insulator. The system can be doped by cautiously controlling its stoichiometry and can become a ferromagnetic metal. On the other hand, such a doping effect can also be a major disadvantage in identifying a system. The delicate effect of doping requires the careful characterization of LMO, especially when it is used in a heterostructure. Numerous experimental studies have been undertaken to identify the nature of the LMO/STO interfaces and it was found that the electronic structure of the LMO/STO interface depends strongly on the relative thickness of LMO and STO and in which geometry it is being studied. Having been studied in both superlattice and thin-films geometry, the interfaces also show strong dependence on the type of geometry in which it is studied. In the superlattice geometry, it is seen that when LMO much thicker than STO one obtains a ferromagnetic metal, however when LMO and STO have comparable thickness one obtains experimentally a ferromagnetic insulator. There is however no consistent satisfactory explanation of this FM insulating state! In the thin-film/substrate geometry for thickness of  $\text{LMO} \leq 5$  unit cells, LMO is AFM. However when thickness of  $\text{LMO} \geq 6$  unit cells, LMO is FM and in these cases FM state is usually accompanied with insulating behaviour above the critical thickness.

Huge number of applications have been predicted for interfaces of these complex oxides. Some of these applications have been included in field-effect devices, sensors, photodetectors, and thermoelectrics and in functional solar cells. Thus oxide electronics is thought to one day replace for the better the silicon semiconductor industry as we know it today. Just as Nobel laureate Herbert Kroemer mentioned in his Nobel lecture "the interface is the device" [73], it indeed seems to be the way to look to the future.

In this part of the thesis we study 3 different interfaces,  $\text{LaAlO}_3/\text{SrTiO}_3$ ,  $\text{GdTiO}_3/\text{SrTiO}_3$ ,  $\text{LaMnO}_3/\text{SrTiO}_3$ , and try to look at interesting features and properties of these interfaces which shall be dealt with in the subsequent chapters.

## 1.3 Overview of present thesis

It is apparent from the several examples presented in the previous sections that diverse classes of systems show a variety of properties which are not completely understood at the microscopic level. Thus first principles calculations on these compounds have been the most obvious choice, in terms of making accurate predictions at the microscopic level. It is abundantly clear that impressive improvements in computational techniques and resources have made it easier to reach this point. First principles calculations assist in understanding the structure and various intriguing and interesting properties of these compounds, which at a glance seems to be very complex with a wide gamut of degrees of freedom. The understanding at the microscopic level opens up new avenues for the design of novel functional materials. A better understanding of the interplay between the different ordering like magnetic, charge and orbital degrees of freedom may lead to the identification of materials with desirable functional properties. Parallel to this, first principles calculations are capable of making more precise connection between real systems and simplified models to understand the underlying physics of the materials leading to conceptual advances and a stronger feedback between theory and experiment.

In this thesis six different compounds have been studied belonging to two different classes of materials. Thus the thesis may be thought of to be divided into two parts: The first part dealing with novel properties derived from the phenomena of spin crossover in metal organic complexes and the second part dealing with the exciting field of 2-dimensional electron gases at the interfaces between inorganic oxides heterostructures. Among metal organic complexes a detailed study has been made of Fe-triazole polymeric chain compounds, followed by metal organic frameworks taking the example of hybrid perovskites like Dimethylammonium Iron formate (DMAFeF) and Hydroxylamine Iron Formate (HAFeF). Among inorganic oxide hetero-interfaces, three different types of heterostructures have been studied, (a) the interface between two band insulators taking the example of the interface between Lanthanum Aluminate  $\text{LaAlO}_3$  (LAO), and Strontium Titanate  $\text{SrTiO}_3$  (STO), (b) the interface between a band insulator STO and a Mott insulator, Gadolinium Titanate  $\text{GdTiO}_3$  (GTO) and finally, (c) the Interface between a band insulator STO and a Jahn-Teller insulator Lanthanum Manganate  $\text{LaMnO}_3$  (LMO).

First principles calculations based on advanced Density Functional Theory techniques, at times in conjunction with finite temperature techniques like Ab initio molecular dynamics (AIMD) and model Hamiltonian approaches have been performed on these materials to understand from microscopic point of view the exciting properties exhibited by them. The contents of the various chapters discussed in the present thesis have been organized as follows :

- **Chapter 2:** In this chapter, we discuss the theoretical methodology of

our calculations. This includes both the theoretical background of Density Functional Theory (DFT) and applying the same, how in practice one can solve a many electron Hamiltonian. In addition to this we discuss the different basis sets which we have considered during the course of calculation, depending upon the properties we have studied. We discuss the construction of low energy model Hamiltonian of such complex materials starting from first-principles calculations. We also discuss few tools beyond the zero temperature DFT such as Ab-initio molecular dynamics (AIMD), and classical Monte Carlo simulations.

- **Chapter 3:** In this chapter a study of the origin of cooperativity associated with the spin crossover phenomena has been undertaken. A model Hamiltonian was developed and solved using Monte Carlo techniques to study the effect of various interaction parameters on cooperativity in SCO materials in general. Taking a real life example of Fe-triazole the advent of hysteresis was shown to be driven by magnetic interactions primarily and the experimental  $T_C$  and width of hysteresis was reproduced using the DFT derived model Hamiltonian. Furthermore AIMD calculations were undertaken to actually demonstrate a bistability and hence the presence of hysteresis region at the critical transition temperature.
- **Chapter 4:** In this chapter an extensive study of pressure dependent spin crossover phenomena was made in MOF systems taking hybrid perovskites like DMAFeF and HAFeF. Crystal structures of these materials were predicted by first principles methods. SCO driven by pressure was seen to arise in these two materials albeit at different  $P_C$  owing to their differing mechanical strengths as demonstrated by their different bulk moduli. On reversal of pressure the materials were shown to demonstrate a hysteresis effect which implies the presence of cooperativity in the materials. The widths of hysteresis were found to be tunable by chemical means through change of the A-site cation. The hysteresis was found to be driven primarily by elastic interactions.
- **Chapter 5:** This particular chapter deals with a comparative analysis of the interfaces between two band insulators LAO and STO and a Mott insulator GTO with a band insulator STO. A complete study of both the experimentally observed superlattice and thin-film/substrate configurations were undertaken. Though the two interfaces were found to behave similarly in the superlattice geometry, a large qualitative and quantitative difference in properties was observed in case of the film/substrate geometry. Band bending and polar catastrophe was seen to be the driving reasons for the generation of the 2D electron gas in case of the overlayer/substrate geometry. A correlation driven charge disproportionated state was discovered

which was found to be responsible for driving the surface layer to be insulating in case of GTO/STO which is otherwise found to be metallic in LAO/STO.

- **Chapter 6:** This particular chapter studies the properties of strained Jahn Teller insulator  $\text{LaMnO}_3$ , along with its interface with the band insulator STO. The effect of square planar strain which is induced by matching of LMO lattice constants to cubic STO lattice constants is the important issue. The electronic and magnetic properties of these systems have been studied with different techniques with varying degrees of sophistication in handling electron electron exchange correlation effects like GGA+U and hybrid functionals. This multi-pronged approach reveals that the curious state of ferromagnetic insulator of LMO, as observed experimentally, may be driven by electronic instability towards charge disproportionation.
- **Chapter 7:** This chapter deals with summary of the results of study on the various different organic and inorganic compounds at one place. Possibilities of future work has also been discussed here.

# Bibliography

- [1] Rustum Roy (1979) interdisciplinary science on campus, pages 161-196 in *Interdisciplinarity and Higher Education*, J.J. Kockelmans editor, Pennsylvania State University Press
- [2] Eddy, Matthew Daniel (2008). *The Language of Mineralogy: John Walker, Chemistry and the Edinburgh Medical School 1750-1800*. Ashgate.
- [3] Smith, Cyril Stanley (1981). *A Search for Structure*. MIT Press. ISBN 0262191911.
- [4] Saha-Dasgupta, T.; Oppeneer, P.M. *MRS Bull.* 2014, 39, 614-620.
- [5] Olguín, J.; Brooker, *Chem. Rev.* 2011, 255, 203-240.
- [6] Létard, J.-F.; Guionneau, P.; Goux-Capes, L. *Spin Crossover in Transition Metal Compounds I-III*; Gütlich, P., Goodwinpp, H., Eds.; Springer: Berlin, Germany, 2004; pp. 221-249
- [7] Linares, J.; Codjovi, E.; Garcia, Y. *Sensors* 2012, 12, 4479-4492.
- [8] Cobo, S.; Molnár, G.; Real, J.A.; Bousseksou, A. *Angew. Chem. Int. Ed.* 2006, 45, 5786-5789.
- [9] Batten, Stuart R.; Champness, Neil R.; Chen, Xiao-Ming; Garcia-Martinez, Javier; Kitagawa, Susumu; Öhrström, Lars; O’Keeffe, Michael; Suh, Myunghyun P.; Reedijk, Jan (2013). *Pure and Applied Chemistry*. IUPAC. 85 (8): 1715.
- [10] C. N. R. Rao, A. K. Cheetham and A. Thirumurugan, *J. Phys. Condens. Matter* 20, 083202 (2008).
- [11] Chen, X; Ye, B.; Tong, M. (2005). *Coord. Chem. Rev.* Elsevier. 249 (5-6): 545-565.
- [12] Kitagawa, S.; Kitaura, R.; Noro, S. I. (2004). *Angewandte Chemie International Edition*. 43 (18): 2334.

- [13] Batten, Stuart R. (2008). RSC Publishing. pp. 297-307, 396-407.
- [14] Ozarowski, A.; Shunzhong, Y.; McGarvey, B.R.; Mislankar, A.; Drake, J.E. *Inorg. Chem.* 1991, 30, 3167-3174.
- [15] Yann Garcia, N.N.A.; Naik, A.D. *Chimia* 2013, 67, 411-418.
- [16] Garcia, Y.; Niel, V.; Muñoz, M.C.; Real, J.A., ; Gütllich, P.; Goodwin, H., Eds.; Springer Berlin Heidelberg: Berlin, Heidelberg, 2004; pp. 229–257.
- [17] Krober, J.; Codjovi, E.; Kahn, O.; Groliere, F.; Jay, C. *Journal of the American Chemical Society* **1993**, 115, 9810–9811,
- [18] Setifi, F.; Milin, E.; Charles, C.; Thétiot, F.; Triki, S.; Gómez-García, C.J. *Inorganic Chemistry* **2014**, 53,97–104,
- [19] Schonfeld, S.; Lochenie, C.; Thoma, P.; Weber, B. *CrystEngComm* **2015**, 17, 5389–5395.
- [20] Bauer, W.; Lochenie, C.; Weber, B. *Dalton Trans.* **2014**, 43, 1990–1999.
- [21] Wang et al, PRB 87, 224406 (2013)
- [22] Jain et al, J. Am. Chem. Soc. 131, 13625-13627(2009)
- [23] Hagen et al, J. Am. Chem. Soc. 131, 7516-7517 (2009)
- [24] Li et al, J. Am. Chem. Soc. 136, 7801-7804 (2014)
- [25] Liu et al, Inorg. Chem. 51, 13363-13372 (2012)
- [26] Czaja, A.U.; Trukhan, N.; Muller, U. *Chem. Soc. Rev.* 2009, 38, 1284-1293.
- [27] Morris, R.; Wheatley, P. Gas Storage in Nanoporous Materials. *Angew. Chem. Int. Ed.* 2008, 47, 4966-4981.
- [28] Manser, Joseph S. and Christians, Jeffrey A. and Kamat, Prashant V. (2016). *Chemical Reviews*. 116 (21): 12956-13008.
- [29] Kreno, L.E.; Leong, K.; Farha, O.K.; Allendorf, M.; Van Duyne, R.P.; Hupp, J.T. *Chem. Rev.* 2012, 112, 1105-1125,
- [30] Horcajada, P.; Chalati, T.; Serre, C.; Gillet, B.; Sebrie, C.; Baati, T.; Eubank, J.F.; Heurtaux, D.; Clayette, P.; Kreuz, C.; et al. *Nat. Mater.* 2010, 9, 172-178.
- [31] Cheetham, A.K.; Rao, C.N.R. *Science* 2007, 318, 58-59

- [32] Mendoza-Cortes, Jose L.; Pascal, Tod A.; Goddard Wa, William A. (2011). *The Journal of Physical Chemistry A*. 115 (47): 13852-7.
- [33] Choi, Sunho; Drese, Jeffrey H.; Jones, Christopher W. (2009-09-21). *ChemSusChem*. 2 (9): 796-854.
- [34] Kojima, Akihiro; Teshima, Kenjiro; Shirai, Yasuo; Miyasaka, Tsutomu (May 6, 2009). *Journal of the American Chemical Society*. 131 (17): 6050-6051.
- [35] Mitzi, D.B.; Feild, C.A.; Harrison, W.T.A.; Guloy, A.M. *Nature* 1994, 369, 467-469.
- [36] Náfrádi, B.; Szirmai, P.; Spina, M.; Lee, H.; Yazyev, O.V.; Arakcheeva, A.; Chernyshov, D.; Gibert, M.; Forró, L.; Horváth, E. *Nat. Commun.* 2016, 7, 13406.
- [37] Zhou, H.; Chen, Q.; Li, G.; Luo, S.; Song, T.B.; Duan, H.S.; Hong, Z.; You, J.; Liu, Y.; Yang, Y. *Science* 2014, 345, 542-546.
- [38] Heo, J.H.; Song, D.H.; Han, H.J.; Kim, S.Y.; Kim, J.H.; Kim, D.; Shin, H.W.; Ahn, T.K.; Wolf, C.; Lee, T.W.; et al. *Adv. Mater.* 2015, 27, 3424-3430.
- [39] Burschka, J.; Pellet, N.; Moon, S.J.; Humphry-Baker, R.; Gao, P.; Nazeeruddin, M.K.; Gratzel, M. *Nature* 2013, 499, 316-319.
- [40] Liu, M.; Johnston, M.B.; Snaith, H.J. *Nature* 2013, 501, 395-398
- [41] Wang, Z.; Hu, K.; Gao, S.; Kobayashi, H. *Adv. Mater.* 2010, 22, 1526-1533.
- [42] Jain, P.; Dalal, N.S.; Toby, B.H.; Kroto, H.W.; Cheetham, A.K. *J. Am. Chem. Soc.* 2008, 130, 10450-10451.
- [43] Jain, P.; Ramachandran, V.; Clark, R.J.; Zhou, H.D.; Toby, B.H.; Dalal, N.S.; Kroto, H.W.; Cheetham, A.K. *J. Am. Chem. Soc.* 2009, 131, 13625-13627,
- [44] Weng, D.F.; Wang, Z.M.; Gao, S. *Chem. Soc. Rev.* 2011, 40, 3157-3181.
- [45] Stroppa, A.; Jain, P.; Barone, P.; Marsman, M.; Perez-Mato, J.M.; Cheetham, A.K.; Kroto, H.W.; Picozzi, S. *Angew. Chem. Int. Ed.* 2011, 50, 5847-5850
- [46] Di Sante, D.; Stroppa, A.; Jain, P.; Picozzi, S. *J. Am. Chem. Soc.* 2013, 135, 18126-18130.

- [47] Stroppa, A.; Barone, P.; Jain, P.; Perez-Mato, J.M.; Picozzi, S. *Adv. Mater.* 2013, 25, 2284-2290.
- [48] Jain, P.; Stroppa, A.; Nabok, D.; Marino, A.; Rubano, A.; Paparo, D.; Matsubara, M.; Nakotte, H.; Fiebig, M.; Picozzi, S.; et al. *Npj Quant. Mater.* 2016, 1, 16012.
- [49] Tian, Y.; Stroppa, A.; Chai, Y.; Yan, L.; Wang, S.; Barone, P.; Picozzi, S.; Sun, Y. *Sci. Rep.* 2014. 4, 6062.
- [50] Gómez-Aguirre, L.C.; Pato-Doldán, B.; Stroppa, A.; Yáñez-Vilar, S.; Bayarjargal, L.; Winkler, B.; Castro-García, S.; Mira, J.; Sánchez-Andújar, M.; Searís-Rodríguez, M.A. *Inorg. Chem.* 2015, 54, 2109-2116.
- [51] Kamminga, M.E.; Stroppa, A.; Picozzi, S.; Chislov, M.; Zvereva, I.A.; Baas, J.; Meetsma, A.; Blake, G.R.; Palstra, T.T.M. *Inorg. Chem.* 2017, 56, 33-41.
- [52] Ghosh, S.; Di Sante, D.; Stroppa, A. *J. Phys. Chem. Lett.* 2015, 6, 4553-4559.
- [53] Mazzuca, L.; Cañadillas-Delgado, L.; Rodríguez-Velamazán, J.A.; Fabelo, O.; Scarrozza, M.; Stroppa, A.; Picozzi, S.; Zhao, J.P.; Bu, X.H.; Rodríguez-Carvajal, J. *Inorg. Chem.* 2017, 56, 197-207.
- [54] Banerjee, H.; Chakraborty, S.; Saha-Dasgupta, T. *Chemistry of Materials* **2016**, 28, 8379–8384.
- [55] Wenk, Hans-Rudolf; Bulakh, Andrei (2004). *Minerals: Their Constitution and Origin*. New York, NY: Cambridge University Press. p. 413.
- [56] Goldschmidt, V. M. (1926). "Die Gesetze der Krystallochemie". *Die Naturwissenschaften*. 21 (21): 477-485.
- [57] Peña, M. A.; Fierro, J. L. (2001). *Chemical Reviews*. 101 (7): 1981-2017.
- [58] Cava, Robert J. "Cava Lab: Perovskites". Princeton University. Retrieved 13 November 2013.
- [59] H. Jahn and E. Teller, *Phys. Rev.* 49, 874 (1936)
- [60] D. G. Marc and M. E. McHenry, *Structure of Materials: an introduction to crystallography, diffraction and symmetry*, Cambridge University Press (2007).
- [61] Victor M. Goldschmidt, "Die Gesetze der Krystallochemie". *Die Naturwissenschaften*, 21, 477- 485, (1926), Xiang Chun Liu, Rongzi Hong and Changsheng Tian, *Journal of Materials Science: Materials in Electronics*, 20, 323-327 (2012)

- [62] A. Ohtomo and H. Y. Hwang, *Nature (London)* 427, 423 (2004).
- [63] J. Mannhart et al., *MRS Bull.*, 33, 1027 (2008); A. Hujiben et al., *Adv. Mater.* 21, 1665 (2009).
- [64] Gariglio, S.; Reyren, N.; Caviglia, A. D.; Triscone, J.-M. (31 March 2009). *Journal of Physics: Condensed Matter.* 21 (16): 164213.
- [65] Bert, Julie A.; Kalisky, Bell; Kim, Hikita; Hwang, Moler (4 September 2011). *Nature Physics.* 7 (10): 767-771.
- [66] Ben Shalom, M.; Sachs, Rakhmilevitch; Palevski, Dagan (26 March 2010) *Physical Review Letters.* 104 (12).
- [67] Tebano, Antonello; E Fabbri; D Pergolesi; G Balestrino; E Traversa (19 January 2012). *ACS Nano.* 6 (2): 1278-1283.
- [68] Caviglia, A. D.; Gariglio, Cancellieri; Sacepe, Fete; Reyren, Gabay; Morpurgo, Triscone (1 December 2010). *Physical Review Letters.* 105 (23).
- [69] A. Brinkman et al, *Nat. Mater.* 6, 493 (2007); N. Reyren et al, *Science* 317, 1196 (2007); I. Li et al., *Nat. Phys.* 7, 762 (2011).
- [70] W. Siemons et al., *Phys. Rev. Lett.*, 98, 196802 (2007); M. Bastetic et al., *Nat. Mater.* 7, 621 (2008).
- [71] S. Thiel et al, *Science* 313, 1942 (2006).
- [72] P. Moetakef et al., *Appl. Phys. Lett* 99, 232116 (2011); T. A. Cain et al., *Appl. Phys. Lett* 101, 111604 (2012); P. Moetakef et al., *Appl. Phys. Lett* 101, 151604 (2012).
- [73] Herbert Kroemer, "Quasi electric fields and band offsets: Teaching electrons new tricks.", Nobel Lecture December 8 2000

# Chapter 2

## Theoretical methodology

### 2.1 Introduction

In this chapter I shall discuss the various methods and techniques that have been used to study the electronic structure of materials and their novel properties. We have used both  $T=0K$  conventional ab-initio techniques as well as its extension to finite temperature within the framework of ab initio molecular dynamics. We have also carried out classical statistical mechanical calculations like Monte Carlo Simulation of model Hamiltonian. We start this section by stating the many body Hamiltonian which is the fundamental Hamiltonian describing atoms, molecules, clusters, and bulk systems. We then get into various approximations adopted to solve this many body Hamiltonian. Following this, we discuss the finite temperature extension. Finally we discuss the Monte Carlo (MC) simulation of the model Hamiltonian.

### 2.2 The many body Hamiltonian

The microscopic description of the physical and chemical properties of matter is a complex problem. Matter is a collection of interacting atoms. This ensemble of particles may be in the gas phase (molecules and clusters) or in a condensed phase. They could be solids or liquids, crystalline or amorphous, homogeneous or heterogeneous. However, in all these cases one can without any ambiguity describe the system as a collection of nuclei and electrons interacting through Coulombic (electrostatic) forces. Thus the many body Hamiltonian for any such system can be written in a generalized form as,

$$H = - \sum_{I=1}^P \frac{\hbar^2}{2M_I} \nabla_I^2 - \sum_{i=1}^N \frac{\hbar^2}{2m_i} \nabla_i^2 + \frac{e^2}{2} \sum_{I=1}^P \sum_{J \neq I}^P \frac{Z_I Z_J}{|\mathbf{R}_I - \mathbf{R}_J|}$$

$$+\frac{e^2}{2} \sum_{i=1}^N \sum_{j \neq i}^N \frac{1}{|\mathbf{r}_i - \mathbf{r}_j|} - e^2 \sum_{I=1}^P \sum_{i=1}^N \frac{Z_I}{|\mathbf{R}_I - \mathbf{r}_i|}, \quad (2.1)$$

where,  $\mathbf{R} = \{ \mathbf{R}_I \}$ ,  $I=1, \dots, P$ , are  $P$  nuclear coordinates, and  $\mathbf{r} = \{ \mathbf{r}_i \}$ ,  $i=1, \dots, N$ , are a set of  $N$  electronic coordinates.  $Z_I$  and  $M_I$  are the  $P$  nuclear charges and masses respectively.  $m_i$  are the  $N$  electronic masses each of charge  $e$ .

Electrons are fermions, and thus the total electronic wave function must be anti-symmetric, with respect to exchange of two electrons. Nuclei can be bosons, fermions or even distinguishable particles, according to the concerned problem. Thus it appears that all the components are perfectly known, and, in principle, all the properties can be obtained by solving the many body Schrödinger's Equation,

$$H\Psi_i(\mathbf{r}, \mathbf{R}) = E_i\Psi_i(\mathbf{r}, \mathbf{R}). \quad (2.2)$$

However in reality, this problem is almost impossible to solve in a full quantum mechanical framework. The possibility of finding exact analytical solutions is limited to very few potentials even for a single particle, and hence one has to resort to approximate techniques, such as variational principle or perturbative treatments. In an alternate approach, one may in principle attempt a direct numerical solution. However the difficulty arises due to the sheer number of variables ( $3N$ ) involved in the wave-function  $\Psi(\mathbf{r}_1, \mathbf{r}_2, \dots, \mathbf{r}_N)$ , as has been best described by D.R.Hartree: "It has been said that the tabulation of a function of one variable requires a page, of two variables a volume, and of three variables a library; but the full specification of a single wave function of neutral Fe is a function of seventy-eight variables. It would be rather crude to restrict to ten the number of values of each variable at which to tabulate this function, but even so, full tabulation of it would require  $10^{78}$  entries, and even if this number could be reduced somewhat from considerations of symmetry, there would still not be enough atoms in the whole solar system to provide the material for printing such a table". Added on to this are the problems of interpretation. In the words of R. P. Feynman, "The trouble with quantum mechanics is not only in solving the equations, but in understanding what the solutions mean."

Thus different factors contribute to this problem. First, this is a multi-component many body system, where each component obeys its own statistics. Second, the complete wave function cannot be factorized due to Coulomb correlations, and one has to deal with  $(3N+3P)$  coupled degrees of freedom. Thus usually one resorts to some sensible approximations. Most calculations presented in literature are based on:

- (1) Born Oppenheimer or Adiabatic Approximation, and,
- (2) Classical Nuclei Approximation.

### 2.2.1 Born-Oppenheimer Approximation

The first step towards the simplification of the problem was the Born-Oppenheimer (B-O) approximation(1927). [1] The timescale associated with the motion of the nuclei is usually much slower than that associated with electrons. The negligible mass of the electrons compared to the protons (a ratio of 1 in 1836) implies that their velocity is much larger. Thus it is generally accepted that the electrons can be adequately described as following the motion of the nuclei instantaneously, while maintaining the same stationary state of the electronic Hamiltonian. This stationary state varies in time because of the Coulombic coupling of the two sets of degrees of freedom. Thus as the nuclei follow their dynamics, the electrons instantaneously adjust their wave function in accordance with the nuclear wave function.

Thus a possibility of factorizing the full wave function and decoupling the nuclear and electronic motion arises. One may write without much loss of generality,

$$\Psi(\mathbf{R}, \mathbf{r}, t) = \Theta_m(\mathbf{R}, t)\Phi(\mathbf{R}, \mathbf{r}), \quad (2.3)$$

where the electronic wave function  $\Phi_m(\mathbf{R}, \mathbf{r})$  [normalized wave-function for every  $\mathbf{R}$ ] is the  $m^{th}$  stationary state of the electronic Hamiltonian,

$$H_e = T_e + U_{ee} + V_{ne} = H - T_n - U_{nn}, \quad (2.4)$$

where,  $T_n$ , and  $U_{nn}$  are the nuclear kinetic and potential operators, respectively,  $T_e$ , and  $U_{ee}$  are the same for the electronic case, and,  $V_{ne}$  the electron-nuclear interaction.

The electronic energy eigenvalues are  $\epsilon_m(\mathbf{R})$ . In electronic (stationary) Schrödinger's equation, the nuclear coordinates  $\mathbf{R}$  are merely parameters, while the nuclear wave-function  $\Theta_m(\mathbf{R}, t)$  obeys the time dependent Schrödinger's equation,

$$i\hbar \frac{\partial}{\partial t} [\Theta_m(\mathbf{R}, t)] = [T_n + U_{nn} + \epsilon_m] \Theta_m(\mathbf{R}, t), \quad (2.5)$$

or the stationary version

$$[T_n + U_{nn} + \epsilon_m] \Theta_m(\mathbf{R}) = E_m \Theta_m(\mathbf{R}). \quad (2.6)$$

Inspite of the fact that  $m$  can be any eigenstate,  $m = 0$ , the ground state is most prevalent in literature focusing on these phenomena.

### 2.2.2 Classical Nuclei Approximation

Solving any of the last two equations (2.5) or (2.6) is still a formidable task for primarily two reasons. Firstly, it is a many body equation in 3P nuclear coordinates, the interaction potential being given in an implicit form. Secondly, determination of the potential energy surface for all possible nuclear configurations involve solving  $M^{3P}$  times the electronic equation, where M is the number of grid points. Not more than 6 nuclear degrees of freedom can be handled using non-stochastic methods.

In most cases, however it turns out that solving the quantum nuclear equation is redundant. The rationale for this being:

(i) The thermal wavelength for a particle of mass M is

$$\lambda_T = \frac{h}{2\pi\sqrt{Mk_B T}}$$

, and regions of space separated by distance more than  $\lambda_T$  do not show quantum phase coherence. Even for the largest  $\lambda_T \approx 0.4\text{\AA}$  for hydrogen, inter-atomic distances are  $\approx 1\text{\AA}$ .

(ii) Nuclear wave functions are mostly localized due to the fact that potential energy surfaces are generally quite stiff in typical bonding environments.

Though quantum nuclear effects are not unheard of in certain systems of interest, in the majority of systems, nuclear wave packets are well localized and might in most cases be replaced by Dirac's  $\delta$  functions. The centers of these  $\delta$  functions are then by definition, the classical positions  $\mathbf{R}^{cl}$ .

Ehrenfest's theorem [2] for mean values of position and momentum operators paves the way for connection between classical and quantum mechanics. The quantum mechanical analogue to Newton's equations yields,

$$M_I \frac{d^2}{dt^2} \langle \mathbf{R}_I \rangle = -\langle \nabla_{\mathbf{R}_I} \epsilon_n(\mathbf{R}) \rangle, \quad (2.7)$$

where we deal with quantum expectation values. The classical nuclei approximation identifies  $\langle \mathbf{R}_I \rangle$  with  $\mathbf{R}_I^{cl}$ . Thus,

$$\langle \nabla \epsilon_m(\mathbf{R}) \rangle = \nabla \epsilon_m(\mathbf{R}_{cl}), \quad (2.8)$$

is valid for  $\delta$  functions or harmonic potentials, the error term being proportional to the an-harmonicity of the potential and the spatial extension of the wave-function.

Thus with the above two approximations in place and the problem of many electron and many nuclear Hamiltonian being effectively reduced to a many electron Hamiltonian, one must proceed to solving the many body electronic Schrödinger's equation for a set of fixed nuclear positions.

To solve the many electron problem two different approaches are generally taken:

- (i) The wave-function based approach as implemented by the Hartree and the Hartree Fock Approximations, and,
- (ii) The density based approach as implemented by the Density Functional Theory.

In the next section, we discuss the two wave-function based approaches, and in the subsequent sections to follow we devote our attention to the density based approach.

## 2.3 The Electronic Problem

The primary problem in the structure of matter is to solve the Schrödinger equation for a system of  $N$  interacting electrons in the Coulombic field created by a collection of atomic nuclei. It is a very difficult problem in many-body theory and, in fact, the exact solution is known only in case of the uniform electron gas, for atoms with a small number of electrons and for a few small molecules. These exact solutions are always numerical. At the analytic level, one always has to resort to approximations. However, the effort of devising schemes to solve this problem is really worthwhile because the knowledge of the electronic ground state of a system gives access to many of its important properties.

### 2.3.1 The Hartree approximation

The many body Hamiltonian for a system of  $N$  interacting electrons in presence of nuclei fixed in selected configuration can be written as,

$$H_e = T_e + V_{ne} + U_{ee} = \sum_{i=1}^N h(\mathbf{r}_i) + \frac{1}{2} \sum_{i \neq j}^N \frac{e^2}{r_{ij}}, \quad (2.9)$$

writing  $|\mathbf{r}_i - \mathbf{r}_j| = r_{ij}$ ,

where,

$$h(\mathbf{r}) = -\frac{\hbar^2}{2m} \nabla^2 + V_{ne} = \frac{p^2}{2m} + V_{ne}, \quad (2.10)$$

and the many body eigenvalue problem written as,

$$H_e \Psi(\mathbf{r}_1 \sigma_1, \mathbf{r}_2 \sigma_2, \dots, \mathbf{r}_N \sigma_N) = E \Psi(\mathbf{r}_1 \sigma_1, \mathbf{r}_2 \sigma_2, \dots, \mathbf{r}_N \sigma_N), \quad (2.11)$$

where  $\mathbf{r}_i \sigma_i$  are the space and spin variables for the  $i^{\text{th}}$  electron.

The first approach to solve eqn.(2.11) was the Hartree Theory (1928) [3] where the total N electron ground state is represented by the simple product of N one-electron spin orbitals.

Thus one considers a complete set of orthonormal one-electron orbitals  $\{\phi_i(\mathbf{r})\}$ . From this a complete set of orthonormal spin orbitals  $\{\psi_i(\mathbf{r}\sigma)\} = \phi_i(\mathbf{r})\chi_i(\sigma)$  are formed, where  $\phi_i(\mathbf{r})$  and  $\chi_i(\sigma)$  are spatial orbitals and spin functions respectively, and  $\sigma$  could be either spin up  $\alpha$  or spin down  $\beta$ .

Therefore, in Hartree theory, the ground state wave-function of the many body system can be expressed as a simple product of orthonormal one-electron spin orbitals of the form,

$$\Psi(\mathbf{r}_1 \sigma_1, \mathbf{r}_2 \sigma_2, \dots, \mathbf{r}_N \sigma_N) = \psi_1(\mathbf{r}_1 \sigma_1) \psi_2(\mathbf{r}_2 \sigma_2) \dots \psi_N(\mathbf{r}_N \sigma_N). \quad (2.12)$$

Here any given electron is assigned to some given spin orbital. However it is very apparent that the simplistic Hartree product (2.12) does not have the required anti-symmetric character for interchange of space and spin coordinates of any two electrons. Also this product completely neglects any correlation in the position of electrons and Pauli's exclusion principle is built in by hand avoiding multiple occupancy of spin orbitals. Thus in present time Hartree theory is merely of historical significance.

The electronic charge density  $\rho(\mathbf{r})$  corresponding to the Hartree wave-function (2.12) is given by,

$$\rho(\mathbf{r}) = -e \sum_j^{occ} \phi_j^*(\mathbf{r}) \phi_j(\mathbf{r}), \quad (2.13)$$

where the sum runs over all occupied spin orbitals, entering the ground state  $\Psi$ . The Coulomb or Hartree Potential corresponding to the electronic charge density (2.12) is

$$V_{coul}(\mathbf{r}) = \sum_j^{occ} \int \phi_j^*(\mathbf{r}') \frac{e^2}{|\mathbf{r} - \mathbf{r}'|} \phi_j(\mathbf{r}') dr'. \quad (2.14)$$

We note that  $V_{Coul}(\mathbf{r}) = V_i^H(\mathbf{r})$ , where  $V_i^H(\mathbf{r})$  is the Hartree Potential which is

defined as the electrostatic potential from the electron charge density and must be calculated from the Poisson equation:

$$\nabla^2 V_H[n](\mathbf{r}) = -4\pi n(\mathbf{r}).$$

In Hartree self consistent approximation, it is generally assumed that each electron moves in the effective field corresponding to the Coulomb potential generated by the charge distribution of all the other (N-1) electrons; the effective field for any electron is given by the Hartree Potential. Thus the spin-orbitals entering in the product wave-function satisfy the Hartree equations.

$$\left[\frac{\mathbf{p}^2}{2m} + V_{ne} + V_i^H(\mathbf{r})\right]\psi_i = \epsilon_i\psi_i. \quad (2.15)$$

Here Hartree potential is defined in terms of the occupied orbitals  $\psi_i$  and therefore must be determined in a self consistent method. From a certain initial guess of the functions  $\psi_1, \psi_2, \dots, \psi_N$  one evaluates the space charge distribution (2.13), and the corresponding Hartree Potential (2.14). A new set of improved wave-functions are then calculated by solving Hartree equations (2.15). The corresponding Hartree Potential is used to again start a new cycle. This iterative process is repeated upto self consistency of input and output functions and potentials.

### 2.3.2 The Hartree-Fock approximation

The next level of sophistication was then introduced by Fock in 1930, [4] incorporating the fermionic nature of electrons in the many body wave-function  $\Psi(\{\mathbf{r}_i\})$ . To achieve this one may choose a wave-function which is a properly anti-symmetrized form of the Hartree wave-function which changes sign when the coordinates of two electrons are interchanged. For the sake of convenience one may neglect the spin degrees of freedom of electrons and keep only the spatial degrees of freedom. This does not have any serious implication since at the Hartree-Fock level one may include explicitly the spin degrees of freedom, by consideration that electrons with up and down spins are at position  $\mathbf{r}$ . Thus taking together the Hartree type wave-functions to form a properly anti-symmetrized wave function for the system, we may write,

$$\Psi^{HF}(\{\mathbf{r}_i\}) = A\{\phi_1(\mathbf{r}_1)\phi_2(\mathbf{r}_2)\dots\phi_N(\mathbf{r}_N)\}, \quad (2.16)$$

where A is the anti-symmetrization operator,

$$A = \frac{1}{\sqrt{N!}} \sum_{i=1}^N (-1)^{p_i} P_i, \quad (2.17)$$

The sum extends over all the  $N!$  permutations  $P_i$  of the electronic coordinates and  $(-1)^{p_i}$  equals +1 or -1 for permutations of even or odd class with respect to

the fundamental one.  $\Psi^{HF}$  is normalized to one provided the composing orbitals are orthonormal. Putting expression (2.17) into (2.16)  $\Psi^{HF}$  can be conveniently written in the determinantal form suggested by Slater,

$$\Psi^{HF}(\{\mathbf{r}_i\}) = \frac{1}{\sqrt{N!}} \begin{vmatrix} \phi_1(\mathbf{r}_1) & \phi_1(\mathbf{r}_2) & \cdots & \phi_1(\mathbf{r}_N) \\ \phi_2(\mathbf{r}_1) & \phi_2(\mathbf{r}_2) & \cdots & \phi_2(\mathbf{r}_N) \\ \vdots & \vdots & \ddots & \vdots \\ \phi_N(\mathbf{r}_1) & \phi_N(\mathbf{r}_2) & \cdots & \phi_N(\mathbf{r}_N) \end{vmatrix}$$

where,  $N$  is the total number of electrons. This has the required property, since interchanging the position of two electrons is equivalent to interchanging the corresponding columns in the determinant, which changes its sign. It also shows that any two electrons with the same spin cannot be in the same spatial position, since the nodes of  $\Psi^{HF}$  occur whenever,

$$\mathbf{r}_i \equiv \mathbf{r}_j.$$

The total energy with the Hartree-Fock wave-function is

$$E^{HF} = \langle \Psi^{HF} | H_e | \Psi^{HF} \rangle,$$

$$E^{HF} = \sum_i^N \langle \phi_i | -\frac{\hbar^2 \nabla^2}{2m} + V_{ne}(\mathbf{r}) | \phi_i \rangle + \frac{e^2}{2} \sum_{i \neq j}^N \langle \phi_i \phi_j | \frac{1}{|\mathbf{r} - \mathbf{r}'|} | \phi_i \phi_j \rangle - \frac{e^2}{2} \sum_{i \neq j}^N \langle \phi_i \phi_j | \frac{1}{|\mathbf{r} - \mathbf{r}'|} | \phi_j \phi_i \rangle, \quad (2.18)$$

and the single particle Hartree-Fock equations, obtained by a variational calculation are,

$$\left[ -\frac{\hbar^2 \nabla^2}{2m} + V_{ne}(\mathbf{r}) + V_i^H(\mathbf{r}) \right] \phi_i(\mathbf{r}) - e^2 \sum_{j \neq i}^N \langle \phi_j | \frac{1}{|\mathbf{r} - \mathbf{r}'|} | \phi_i \rangle \phi_j(\mathbf{r}) = \epsilon_i \phi_i(\mathbf{r}). \quad (2.19)$$

Thus we observe that this equation has one extra term compared to the Hartree equation, the last term, which is called the "exchange" term. This exchange term describes the effects of exchange between electrons which we introduce in the Hartree-Fock many particle wave-function by construction. However this term cannot be written simply as  $V_i^X(\mathbf{r}_i) \phi_i(\mathbf{r}_i)$ .

Here we first try to express the Hartree term differently, writing the single particle and total densities as,

$$\rho_i(\mathbf{r}) = |\phi_i(\mathbf{r})|^2,$$

$$\rho(\mathbf{r}) = \sum_i^N \rho_i(\mathbf{r}),$$

Thus the Hartree term takes the form,

$$V_i^H(\mathbf{r}) = \sum_{j \neq i} \int \rho_j(\mathbf{r}') \frac{e^2}{|\mathbf{r} - \mathbf{r}'|} d\mathbf{r}' = e^2 \int \frac{\rho(\mathbf{r}') - \rho_i(\mathbf{r}')}{|\mathbf{r} - \mathbf{r}'|} d\mathbf{r}', \quad (2.20)$$

In the previous step, we take the sum of  $\rho_j(\mathbf{r}')$  over all  $j$ 's except the  $i^{\text{th}}$  coordinate. Now, taking the sum of  $\rho_j(\mathbf{r}')$  over all  $j$  gives  $\rho(\mathbf{r}')$  as shown in the previous step. However, since this is a restricted sum we must exclude the  $i^{\text{th}}$   $\rho(\mathbf{r}')$  and thus we would obtain the value of the sum as  $\rho(\mathbf{r}') - \rho_i(\mathbf{r}')$ . It is worth noting here that the sum and the integral are independent of each other.

Constructing the single particle density as,

$$\rho_i^X(\mathbf{r}, \mathbf{r}') = \sum_{j \neq i} \frac{\phi_i(\mathbf{r}') \phi_i^*(\mathbf{r}) \phi_j(\mathbf{r}) \phi_j^*(\mathbf{r}')}{\phi_i(\mathbf{r}) \phi_i^*(\mathbf{r})}, \quad (2.21)$$

Hence the single particle Hartree-Fock equations take the form,

$$\left[ -\frac{\hbar^2 \nabla^2}{2m} + V_{ne}(\mathbf{r}) + V_i^H(\mathbf{r}) + V_i^X(\mathbf{r}) \right] \phi_i(\mathbf{r}) = \epsilon_i \phi_i(\mathbf{r}). \quad (2.22)$$

Thus the exchange potential, drawing analogy to the Hartree Potential, is given by,

$$V_i^X(\mathbf{r}) = -e^2 \int \frac{\rho_i^X(\mathbf{r}, \mathbf{r}')}{|\mathbf{r} - \mathbf{r}'|} d\mathbf{r}'. \quad (2.23)$$

The Hartree and exchange potentials together yield the following potential for electron-electron interaction in the Hartree-Fock approximation,

$$V_i^{HF}(\mathbf{r}) = e^2 \int \frac{\rho(\mathbf{r}')}{|\mathbf{r} - \mathbf{r}'|} d\mathbf{r}' - e^2 \int \frac{\rho_i^X(\mathbf{r}, \mathbf{r}') + \rho_i(\mathbf{r}')}{|\mathbf{r} - \mathbf{r}'|} d\mathbf{r}', \quad (2.24)$$

which can be written with the help of Hartree-Fock density,

$$\rho_i^{HF}(\mathbf{r}, \mathbf{r}') = \sum_j \frac{\phi_i(\mathbf{r}') \phi_i^*(\mathbf{r}) \phi_j(\mathbf{r}) \phi_j^*(\mathbf{r}')}{\phi_i(\mathbf{r}) \phi_i^*(\mathbf{r})}, \quad (2.25)$$

as the following expression for electron-electron interaction potential,

$$V_i^{HF}(\mathbf{r}) = e^2 \int \frac{\rho(\mathbf{r}')}{|\mathbf{r} - \mathbf{r}'|} d\mathbf{r}' - e^2 \int \frac{\rho_i^{HF}(\mathbf{r}, \mathbf{r}')}{|\mathbf{r} - \mathbf{r}'|} d\mathbf{r}'. \quad (2.26)$$

The first term is the total Coulombic repulsion common for all states  $\phi_i(\mathbf{r})$ , while the second term is the effect of fermionic exchange, and is different for each state  $\phi_i(\mathbf{r})$ . The flow chart for the algorithm of Hartree-Fock self consistent method, is shown in Figure 2.1.

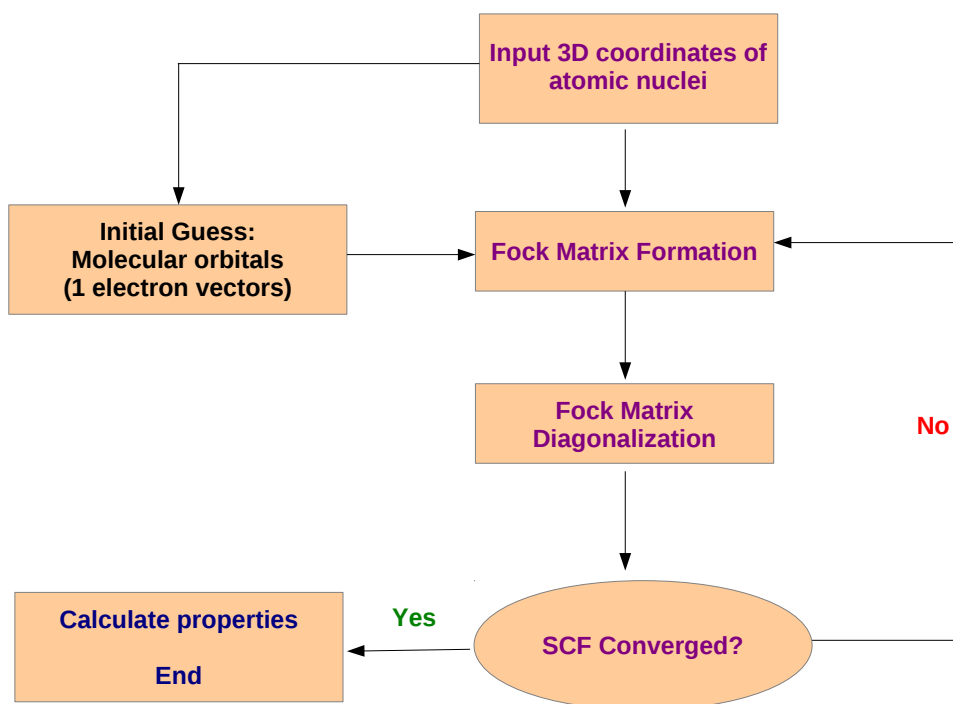


Figure 2.1: Algorithmic flowchart illustrating the Hartree–Fock method.

## 2.4 Density Functional Theory

Parallel to the wave-function based approaches, a different line of thought based on reduction of the problem to lower dimensions led L.H.Thomas and E.Fermi to propose, at about the same time as Hartree, that the full electronic density was the fundamental variable of the many body problem. Starting from this very idea they derived a differential equation for the density without any reference to the one electron orbitals (Thomas 1927, Fermi 1928) [5]. The Thomas Fermi approximation however was too crude, primarily because the approximation used for the kinetic energy of the electrons was unable to sustain bound states, but it had paved the way for the later development of Density Functional Theory (DFT) by Hohenberg and Kohn in 1964 [6] to deal with many electron problems more efficiently, and has been till date the way of choice for electronic structure calculations in condensed matter physics. In more recent times, it has also been accepted by the quantum chemistry community due to its computational advantages compared to post Hartree-Fock methods of comparable quality.

The primary advantages of taking electronic density as the basic variable are:

- (i) it is a function of 3 variables, unlike the wave-function which is a function of  $3N$  variables, and is simpler to tabulate and plot,
- (ii) it is a function in 3D space in which we live and perceive,
- (iii) it provides better visualization, and,
- (iv) it is an experimental variable.

However one must also ensure that,

- (i) density contains sufficient information,
- (ii) it is possible to develop a procedure for direct calculation of density, and,
- (iii) calculations of energy and other physical quantities are possible from density alone.

In the next section we discuss the reduced density matrices and hence develop the mathematical formalism required for density functional theory.

### 2.4.1 Reduced Density Matrices

Here we write the electronic Hamiltonian as

$$H_e = -\frac{1}{2} \sum_i \nabla_i^2 + \sum_i v(\mathbf{r}_i) + \frac{1}{2} \sum_i \frac{1}{\mathbf{r}_{ij}}, \quad (2.27)$$

in atomic units for convenience. Although the many particle wave-function  $\Psi(\mathbf{r}_1, \mathbf{r}_2, \dots, \mathbf{r}_N)$  is a function of  $3N$  variables, the expectation value of any operator  $\langle \Theta \rangle = \langle \Psi | \Theta | \Psi \rangle$  may be calculated by means of other derived quantities depending on lesser number of variables, if  $\Theta$  is a sum of one- or two- particle operators, as is the case for many electron Hamiltonian. Therefore for the nuclear-electron potential energy comprising of the one-particle terms one has,

$$\begin{aligned} \langle V_{ne} \rangle &= \int \Psi^*(\mathbf{r}_1, \mathbf{r}_2, \dots, \mathbf{r}_N) \sum_i v(\mathbf{r}_i) \Psi(\mathbf{r}_1, \mathbf{r}_2, \dots, \mathbf{r}_N) d\mathbf{r}_1 d\mathbf{r}_2 \dots d\mathbf{r}_N, \\ &= N \int d\mathbf{r}_1 v(\mathbf{r}_1) \int \Psi^*(\mathbf{r}_1, \mathbf{r}_2, \dots, \mathbf{r}_N) \Psi(\mathbf{r}_1, \mathbf{r}_2, \dots, \mathbf{r}_N) d\mathbf{r}_2 d\mathbf{r}_3 \dots d\mathbf{r}_N, \end{aligned} \quad (2.28)$$

and thus the result that emerges,

$$\langle V_{ne} \rangle = \langle \Psi | \sum_i v(\mathbf{r}_i) | \Psi \rangle = \int d\mathbf{r} v(\mathbf{r}) \rho(\mathbf{r}), \quad (2.29)$$

which is valid in general for any single-particle multiplicative operator, where the single particle density is defined as,

$$\rho(\mathbf{r}_1) = N \int \Psi^*(\mathbf{r}_1, \mathbf{r}_2, \dots, \mathbf{r}_N) \Psi(\mathbf{r}_1, \mathbf{r}_2, \dots, \mathbf{r}_N) d\mathbf{r}_2 d\mathbf{r}_3 \dots d\mathbf{r}_N, \quad (2.30)$$

In a similar manner one may proceed to write for two particle multiplicative operators, as for example for the electron- electron repulsion,

$$\langle V_{ee} \rangle = \langle \Psi | \frac{1}{2} \sum_{i,j} \frac{1}{r_{ij}} | \Psi \rangle = \frac{1}{2} \int d\mathbf{r}_1 d\mathbf{r}_2 \frac{\Gamma_2(\mathbf{r}_1, \mathbf{r}_2)}{r_{12}}, \quad (2.31)$$

where the two-particle density is defined as,

$$\Gamma_2(\mathbf{r}_1, \mathbf{r}_2) = N(N-1) \int \Psi^*(\mathbf{r}_1, \mathbf{r}_2, \dots, \mathbf{r}_N) \Psi(\mathbf{r}_1, \mathbf{r}_2, \dots, \mathbf{r}_N) d\mathbf{r}_3 d\mathbf{r}_4 \dots d\mathbf{r}_N, \quad (2.32)$$

The reduced density functions may also be written as the expectation values of the corresponding density operators, viz.,

$$\rho(\mathbf{r}_1) = \langle \Psi | \sum_i \delta(\mathbf{r} - \mathbf{r}_i) | \Psi \rangle, \quad (2.33)$$

$$\Gamma_2(\mathbf{r}_1, \mathbf{r}_2) = \langle \Psi | \sum_{i \neq j} \delta(\mathbf{r}_1 - \mathbf{r}_i) \delta(\mathbf{r}_2 - \mathbf{r}_j) | \Psi \rangle. \quad (2.34)$$

For the kinetic energy term comprising of differential operators one may write,

$$\begin{aligned} T &= -\langle \Psi | \frac{1}{2} \sum_i \nabla_i^2 | \Psi \rangle, \\ &= -\frac{1}{2} N \int \Psi^*(\mathbf{r}_1, \mathbf{r}_2, \dots, \mathbf{r}_N) \nabla_1^2 \Psi(\mathbf{r}_1, \mathbf{r}_2, \dots, \mathbf{r}_N) d\mathbf{r}_1 d\mathbf{r}_2 \dots d\mathbf{r}_N, \\ &= -\frac{1}{2} N \int [\nabla_1^2 \Psi^*(\mathbf{r}'_1, \mathbf{r}_2, \dots, \mathbf{r}_N) \Psi(\mathbf{r}_1, \mathbf{r}_2, \dots, \mathbf{r}_N)]_{\mathbf{r}_1=\mathbf{r}'_1} d\mathbf{r}_1 d\mathbf{r}_2 \dots d\mathbf{r}_N, \\ &= -\frac{1}{2} \int d\mathbf{r}_1 [\nabla_1^2 \gamma(\mathbf{r}_1, \mathbf{r}'_1)]_{\mathbf{r}_1=\mathbf{r}'_1}, \end{aligned} \quad (2.35)$$

with the first order reduced density matrix defined as,

$$\gamma(\mathbf{r}_1, \mathbf{r}'_1) = N \int \Psi^*(\mathbf{r}'_1, \mathbf{r}_2, \dots, \mathbf{r}_N) \Psi(\mathbf{r}_1, \mathbf{r}_2, \dots, \mathbf{r}_N) d\mathbf{r}_2 d\mathbf{r}_3 \dots d\mathbf{r}_N. \quad (2.36)$$

For spin-polarized situation, one has to include spin dependence, viz.,

$$\begin{aligned} \rho(x_1) &\equiv \rho(\mathbf{r}_1 \sigma_1), \\ \int dx &\rightarrow \sum_{\sigma} \int d\mathbf{r}, \\ \rho(\mathbf{r}_1) &= \int \rho(x_1) d\sigma_1, \end{aligned}$$

$$\begin{aligned}\rho(\mathbf{r}) &= \rho_{\uparrow}(\mathbf{r}) + \rho_{\downarrow}(\mathbf{r}), \\ \sigma(\mathbf{r}) &= \rho_{\uparrow}(\mathbf{r}) - \rho_{\downarrow}(\mathbf{r}),\end{aligned}$$

The total energy can thus be expressed in terms of the Reduced Density Matrices (RDM) as,

$$E[\rho, \gamma, \Gamma_2] = T[\gamma(\mathbf{r}_1, \mathbf{r}'_1)] + V_{ne}[\rho(\mathbf{r})] + V_{ee}[\Gamma_2(\mathbf{r}_1, \mathbf{r}_2)], \quad (2.37)$$

and this leads to the possibility of developing a quantum mechanical formalism of many electron systems in reduced space in terms of RDMs bypassing the wave-function formalism. A pre-requisite of the formalism is the possibility of directly determining the RDMs by minimizing the energy with respect to the RDMs for which the Pauli exclusion principle must be built into the RDMs. Also the existence of an anti-symmetric wave-function  $\Psi$  from which the RDMs can be constructed has to be guaranteed. This problem known as the N-representability problem must be solved by imposing necessary and sufficient conditions on  $\gamma(\mathbf{r}_1, \mathbf{r}'_1)$  and  $\Gamma_2(\mathbf{r}_1, \mathbf{r}_2)$  which are yet unknown. The N-representability condition on  $\rho(\mathbf{r})$  is given as,

$$\int \rho(\mathbf{r}) d\mathbf{r} = N, \rho(\mathbf{r}) \geq 0 \quad (2.38)$$

Thus the single particle density (simplest reduced quantity) emerges as a promising candidate for the formulation of quantum mechanics in reduced space.

Next we discuss the theorems proposed by Hohenberg and Kohn which are the basic postulates of density functional theory.

## 2.4.2 The Hohenberg-Kohn Theorems

### Theorem 1

The external potential is unequivocally determined by electronic density, and an additive constant.

### Corollary 1

$\rho(\mathbf{r})$  also determines ground state wave function, which can be obtained by solving the full many body Schrödinger's equation.

### Theorem 2

A universal functional for the energy  $E[\rho]$  in terms of density  $\rho(\mathbf{r})$  can be defined, valid for any external potential. For any particular external potential, the exact ground state energy of the system is the global minimum value of this functional, and the density that minimizes the functional is the exact ground state density.

### Corollary 2

The functional  $E[\rho]$  alone is sufficient to determine the exact ground state energy and density. In general excited states of the electrons must be determined by other processes.

### Proof of Theorem 1

Let the ground state of two  $N$ -electron systems characterized by two different external potentials (differing by more than an additive constant)  $v_1(\mathbf{r})$  and  $v_2(\mathbf{r})$  with the corresponding Hamiltonians and Schrödinger's equations given by,

$$H_1 = T + U + \sum_i v_1(\mathbf{r}_i),$$

$$H_2 = T + U + \sum_i v_2(\mathbf{r}_i),$$

$$T = -\frac{1}{2} \sum_i \nabla_i^2,$$

$$U = \frac{1}{2} \sum_{i \neq j} \frac{1}{r_{ij}},$$

$$H_1 \Psi_1 = E_1 \Psi_1,$$

$$H_2 \Psi_2 = E_2 \Psi_2,$$

A pre-assumption that the two wave-functions  $\Psi_1$  and  $\Psi_2$  yield the same density as given by,

$$\rho(\mathbf{r}_1) = N \int \Psi^*(\mathbf{r}_1, \mathbf{r}_2, \dots, \mathbf{r}_N) \Psi(\mathbf{r}_1, \mathbf{r}_2, \dots, \mathbf{r}_N) d\mathbf{r}_2 d\mathbf{r}_3 \dots d\mathbf{r}_N. \quad (2.39)$$

One may make use of the variational principle and write the energy expressions as,

$$E_1 = \langle \Psi_1 | H_1 | \Psi_1 \rangle < \langle \Psi_2 | H_1 | \Psi_2 \rangle, \quad (2.40)$$

$$\langle \Psi_2 | H_1 | \Psi_2 \rangle = \langle \Psi_2 | H_2 | \Psi_2 \rangle + \langle \Psi_2 | H_1 - H_2 | \Psi_2 \rangle = E_2 + \int d\mathbf{r} \rho(\mathbf{r}) [v_1(\mathbf{r}) - v_2(\mathbf{r})]. \quad (2.41)$$

Hence one obtains,

$$E_1 < E_2 + \int d\mathbf{r} \rho(\mathbf{r}) [v_1(\mathbf{r}) - v_2(\mathbf{r})], \quad (2.42)$$

on interchanging the suffices, one has,

$$E_2 < E_1 + \int d\mathbf{r} \rho(\mathbf{r}) [v_2(\mathbf{r}) - v_1(\mathbf{r})]. \quad (2.43)$$

Summation of these two leads to a contradiction,

$$E_1 + E_2 < E_2 + E_1. \quad (2.44)$$

Thus one may arrive at the conclusion that the assumption of identical density arising from two different external potentials is wrong. Hence a given  $\rho(\mathbf{r})$  corresponds to only one  $v(\mathbf{r})$  and since  $v(\mathbf{r})$  is fixed, the Hamiltonian and hence the wave-function are also fixed by the density.

### Proof of Theorem 2

Since the wave-function is a functional of density, the energy functional  $E_v[\rho]$  for a given external potential  $v(\mathbf{r})$  is a unique functional of density. From here one must prove that this functional assumes a minimum value for the true density, i.e.,

$$E_0 < E_v[\tilde{\rho}],$$

where  $\tilde{\rho}(\mathbf{r})$  is a non-negative density normalized to  $N$ , for,

$$E_v[\tilde{\rho}] = F[\tilde{\rho}] + \int \tilde{\rho}(\mathbf{r})v(\mathbf{r})d\mathbf{r},$$

where,

$$H = T + U + V,$$

and,

$$F[\tilde{\rho}] = \langle \Psi[\tilde{\rho}] | T + U | \Psi[\tilde{\rho}] \rangle.$$

Thus we have,

$$\langle \Psi[\tilde{\rho}] | H | \Psi[\tilde{\rho}] \rangle = F[\tilde{\rho}] + \int \tilde{\rho}(\mathbf{r})v(\mathbf{r})d\mathbf{r} = E_v[\tilde{\rho}] \geq E_v[\rho] = E_0 = \langle \Psi | H | \Psi \rangle. \quad (2.45)$$

The above inequality follows from Rayleigh-Ritz variational principle for the wave-function but applied to the electronic density. Therefore the variational principle gives,

$$\delta\{E_v[\rho] - \mu(\int \rho(\mathbf{r})d\mathbf{r} - N)\} = 0, \quad (2.46)$$

and from this a generalized equation is obtained,

$$\mu = \frac{\partial}{\partial \rho} E_v[\rho] = v(\mathbf{r}) + \frac{\partial}{\partial \rho} F[\rho]. \quad (2.47)$$

The crux of the problem now is to obtain an expression for the energy functional in terms of density which brings us to the next section.

### 2.4.3 Energy Functional and Kohn-Sham Equations

The equations of Kohn and Sham, published in 1965, turn DFT into a practical tool. [7]

The energy functional in terms of density has thus the generalized form,

$$E_v[\rho] = F[\rho] + \int \rho(\mathbf{r})v(\mathbf{r})d\mathbf{r}, \quad (2.48)$$

where  $F[\rho]$  is a universal functional of density.

Comparing with Energy functional in terms of RDMs which is,

$$E_v[\rho, \gamma, \Gamma_2] = T[\gamma] + \int v(\mathbf{r})\rho(\mathbf{r})d\mathbf{r} + \frac{1}{2} \int \int \frac{\Gamma_2(\mathbf{r}_1, \mathbf{r}_2)}{\mathbf{r}_{12}} d\mathbf{r}_1 d\mathbf{r}_2, \quad (2.49)$$

and assuming a decomposition of  $\Gamma_2$  of the form,

$$\Gamma_2(\mathbf{r}_1, \mathbf{r}_2) = \rho(\mathbf{r}_1)\rho(\mathbf{r}_2)[1 - f(\mathbf{r}_1, \mathbf{r}_2)], \quad (2.50)$$

where  $f(\mathbf{r}_1, \mathbf{r}_2)$  is the correlation function, and one may separate out from the electron-electron repulsion term  $V_{ee}[\rho]$ , the classical electrostatic contribution.

$$E_{coul}[\rho] = \frac{1}{2} \int \int \frac{\rho(\mathbf{r}_1)\rho(\mathbf{r}_2)}{\mathbf{r}_{12}} d\mathbf{r}_1 d\mathbf{r}_2. \quad (2.51)$$

The exact kinetic energy functional  $T[\rho]$  is usually replaced by the kinetic energy of a system of non interacting particles  $T_s[\rho]$  and the contribution  $V_{ee}[\rho] - E_{coul}[\rho]$  together with  $T[\rho] - T_s[\rho]$  comprise of what is in general called the exchange-correlation (XC) energy functional  $E_{XC}[\rho]$ . Hence one may write,

$$E_v[\rho] = \int v(\mathbf{r})\rho(\mathbf{r})d\mathbf{r} + E_{coul}[\rho] + \{T_s[\rho] + E_{XC}[\rho]\}. \quad (2.52)$$

The procedure for obtaining the non-interacting K.E. functional  $T_s[\rho]$  for a certain  $\rho(\mathbf{r})$  is through the solution of the one particle Schrödinger's equations,

$$[-\frac{1}{2}\nabla^2 + \lambda(\mathbf{r})]\psi_i = \epsilon_i\psi_i, \quad (2.53)$$

for a suitable chosen  $\lambda(\mathbf{r})$  so that the resulting orbitals yield the density as,

$$\rho(\mathbf{r}) = \sum_{\mathbf{i}} |\psi_i|^2,$$

and henceforth the functional may be evaluated as,

$$T_s[\rho] = \sum_i \epsilon_i - \int d\mathbf{r} \lambda(\mathbf{r})\rho(\mathbf{r}). \quad (2.54)$$

The energy functional to be minimized for determining equilibrium density may then be written as,

$$E_v[\rho] = \sum_i \epsilon_i - \int d\mathbf{r} \lambda(\mathbf{r}) \rho(\mathbf{r}) + \int v(\mathbf{r}) \rho(\mathbf{r}) d\mathbf{r} + E_{coul}[\rho] + E_{XC}[\rho], \quad (2.55)$$

which leads to the variational condition,

$$\delta E_v[\rho] = 0 = \sum_i \delta \epsilon_i - \int d\mathbf{r} \delta \lambda(\mathbf{r}) \rho(\mathbf{r}) + \int \delta \rho(\mathbf{r}) [-\lambda(\mathbf{r}) + v(\mathbf{r}) + \frac{\delta E_{coul}[\rho]}{\delta \rho(\mathbf{r})} + \frac{\delta E_{XC}[\rho]}{\delta \rho(\mathbf{r})}]. \quad (2.56)$$

Now since,

$$\epsilon_i = -\langle \psi_i | \frac{1}{2} \nabla^2 | \psi_i \rangle + \langle \psi_i | \lambda(\mathbf{r}) | \psi_i \rangle, \quad (2.57)$$

one has, taking differentials of the above equation,

$$\begin{aligned} \delta \epsilon_i &= \langle \delta \psi_i | \frac{1}{2} \nabla^2 | \psi_i \rangle + \langle \delta \psi_i | \lambda(\mathbf{r}) | \psi_i \rangle + \mathbf{c.c.} + \mathbf{c.c.} + \langle \psi_i | \delta \lambda(\mathbf{r}) | \psi_i \rangle, \\ \delta \epsilon_i &= \epsilon_i \delta \langle \psi_i | \psi_i \rangle + \langle \psi_i | \delta \lambda(\mathbf{r}) | \psi_i \rangle, \\ \delta \langle \psi_i | \psi_i \rangle &= 0, \end{aligned}$$

and, hence the result,

$$\sum_i \delta \epsilon_i = \int d\mathbf{r} \delta \lambda(\mathbf{r}) \rho(\mathbf{r}), \quad (2.58)$$

which when combined with the variational condition leads to,

$$\delta E_v[\rho] = 0 = \int \delta \rho(\mathbf{r}) [-\lambda(\mathbf{r}) + v(\mathbf{r}) + \frac{\delta E_{coul}[\rho]}{\delta \rho(\mathbf{r})} + \frac{\delta E_{XC}[\rho]}{\delta \rho(\mathbf{r})}]. \quad (2.59)$$

Since the variation of  $\delta \rho(\mathbf{r})$  is arbitrary, the bracketed quantity must be zero and hence one obtains,

$$\lambda(\mathbf{r}) = v(\mathbf{r}) + \frac{\delta E_{coul}[\rho]}{\delta \rho(\mathbf{r})} + \frac{\delta E_{XC}[\rho]}{\delta \rho(\mathbf{r})}. \quad (2.60)$$

This clearly shows that if one chooses  $\lambda(\mathbf{r})$  given by this expression, the single particle Schrödinger's equation leads to the correct density for the system. Hence one arrives at the basis for the Kohn-Sham (KS) density functional scheme which involves solution of a set of N-nonlinear integro-differential equations called the *Kohn-Sham equations*,

$$[-\frac{1}{2} \nabla^2 + v_{eff}(\mathbf{r}; \rho)] \psi_i = \epsilon_i \psi_i, \quad (2.61)$$

with the effective potential given by,

$$v_{eff}(\mathbf{r}) = v(\mathbf{r}) + \int \frac{\rho(\mathbf{r}')}{|\mathbf{r} - \mathbf{r}'|} d\mathbf{r}' + \frac{\delta E_{XC}}{\delta \rho(\mathbf{r})} = \phi_{es}(\mathbf{r}) + \frac{\delta E_{XC}}{\delta \rho(\mathbf{r})}, \quad (2.62)$$

where  $\nabla^2 \phi_{es}(\mathbf{r}) = 4\pi\rho(\mathbf{r})$  and the density is calculated as,

$$\rho(\mathbf{r}) = \sum_i |\psi_i|^2. \quad (2.63)$$

The energy functional in this theory developed is hence calculated as,

$$E_v[\rho] = \sum_i \epsilon_i - \frac{1}{2} \int \int \frac{\rho(\mathbf{r})\rho(\mathbf{r}')}{|\mathbf{r} - \mathbf{r}'|} d\mathbf{r}d\mathbf{r}' + E_{XC}[\rho(\mathbf{r})] - \int d\mathbf{r}\rho(\mathbf{r}) \frac{\delta E_{XC}}{\delta \rho(\mathbf{r})}. \quad (2.64)$$

The Kohn-sham equations may be solved using a self consistent numerical method as shown in Figure 2.2

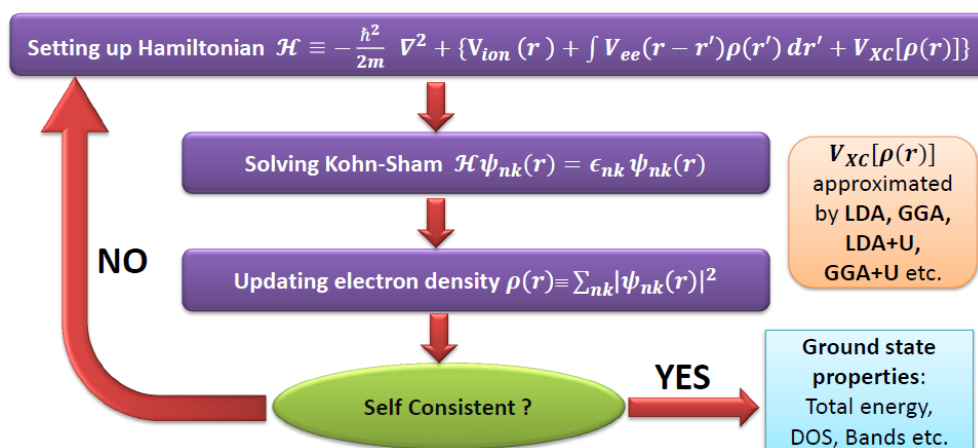


Figure 2.2: Algorithmic flowchart illustrating the iterative procedure to solve the Kohn-sham equations.

For the spin-polarized cases, one may include the spin components of density as the basic variables, and write,

$$E_v[\rho_\alpha, \rho_\beta] = T_s + \int v(\mathbf{r})\rho(\mathbf{r})d\mathbf{r} + E_{coul}[\rho] + E_{XC}[\rho_\alpha, \rho_\beta], \quad (2.65)$$

and the Kohn-sham equations are given by,

$$\left[-\frac{1}{2}\nabla^2 + v_{eff}(\mathbf{r}; \rho_\sigma)\right]\psi_{k\sigma} = \epsilon_{k\sigma}\psi_{k\sigma}, \quad (2.66)$$

with an effective potential,

$$v_{eff,\sigma}(\mathbf{r}) = v(\mathbf{r}) + \int \frac{\rho(\mathbf{r}')}{|\mathbf{r} - \mathbf{r}'|} d\mathbf{r}' + \frac{\delta E_{XC}[\rho_\alpha, \rho_\beta]}{\delta \rho(\mathbf{r})}, \quad (2.67)$$

and densities given by

$$\rho_\sigma(\mathbf{r}) = \sum_k |\psi_{k\sigma}|^2. \quad (2.68)$$

Although the Kohn-Sham theory has been quite successful, its limitations arise from the fact that:

- (i) it gives only ground state  $\rho(\mathbf{r})$  and  $E_\rho$ , but no wave-function can be constructed from the orbitals,
- (ii) the expectation values of only single particle operators are obtainable and approximations are required for two particle or differential operators, and,
- (iii) there is no simple interpretations of the energy eigenvalues.

#### 2.4.4 Interpretation of the Kohn-Sham equations

On introducing the non-interacting reference system, one is able to take into account the most important part of the kinetic energy. The missing part (correlations) is due to the fact that the full many body wave-function is not the single Slater determinant, otherwise Hartree-Fock theory would be exact. If one thinks of a true non-interacting system then the KS scheme is exact.

The price one must pay for having a good description of kinetic energy is that, instead of solving a single equation for the density, one has to deal with a system of  $N$  Euler equations. The primary difference between the Kohn-Sham and Hartree equations is that the effective potential now includes exchange and correlation. Hence the computational effort is of the same order as Hartree but much less than Hartree-Fock, which includes exact non-local exchange.

Hence the density functional theory is able to solve the complicated many body electronic ground state problem by mapping exactly the many body Schrödinger's equation onto a set of  $N$  coupled single particle equations. Hence with a given external potential one is in a position to find the electronic density, the energy, and any desired ground state property. The density of the non-interacting system is equal to that of the true interacting system. Till this point one has an exact theory, and there is no approximation involved in the electronic problem. All the unknown terms in the many-electron Hamiltonian has been relegated to the exchange-correlation functional term, while remaining terms are well known. A further investigation into the nature of  $T[\rho]$  and  $T_s[\rho]$  reveals that both are expectation values of kinetic energy but in different states, with the non-interacting

one corresponding to the expectation value in the ground state of the kinetic operator, while the interacting one to that of the full Hamiltonian, and hence  $T_s[\rho] \leq T[\rho]$  with a positive contribution to the correlation term.

## 2.5 Exchange and Correlation

Although DFT is exact in principle, the crux of the matter lies in the fact that exact expressions for the XC energy and potential are yet unknown and these quantities are generally approximated. In practice the utility of the theory lies on the approximations used for  $E_{XC}[\rho]$ .

As derived previously,

$$E_{XC}[\rho] = \{V_{ee} - E_{coul}[\rho]\} + \{T[\rho] - T_s[\rho]\}.$$

It can be shown that kinetic contribution to correlation energy (kinetic contribution to exchange is Pauli's exclusion principle, which is present in  $T_s[\rho]$ , and in the density when adding up the contributions of  $N$  lowest eigenstates ) can be taken into account by averaging the pair correlation function  $f(\mathbf{r}, \mathbf{r}')$  over the strength of the electron-electron interaction, i.e.,

$$E_{XC}[\rho] = \frac{1}{2} \int \int \frac{\rho(\mathbf{r})\rho(\mathbf{r}')}{|\mathbf{r} - \mathbf{r}'|} [f(\mathbf{r}, \mathbf{r}') - 1] d\mathbf{r}d\mathbf{r}', \quad (2.69)$$

where,  $\tilde{f}(\mathbf{r}, \mathbf{r}') = \int_0^1 f_\lambda(\mathbf{r}, \mathbf{r}') d\lambda$ , and  $f_\lambda(\mathbf{r}, \mathbf{r}')$ , is the pair correlation function corresponding to the Hamiltonian  $H = T + V + \lambda U_{ee}$ . Separating the exchange and correlation contributions, one obtains,

$$\tilde{f}(\mathbf{r}, \mathbf{r}') = 1 - \frac{\sum_\sigma |\rho_\sigma(\mathbf{r}, \mathbf{r}')|^2}{\rho(\mathbf{r})\rho(\mathbf{r}')} + \tilde{f}_c(\mathbf{r}, \mathbf{r}'), \quad (2.70)$$

with  $\rho_\sigma$  being the spin-up and spin-down components of the one body matrix, which in general is a non-diagonal operator.

The exchange-correlation hole is defined in the following form,

$$E_{XC}[\rho] = \frac{1}{2} \int \int \frac{\rho(\mathbf{r})\tilde{\rho}_{XC}(\mathbf{r}, \mathbf{r}')}{|\mathbf{r} - \mathbf{r}'|} d\mathbf{r}d\mathbf{r}', \quad (2.71)$$

$$\tilde{\rho}_{XC}(\mathbf{r}, \mathbf{r}') = \rho(\mathbf{r}')\{1 - \tilde{f}(\mathbf{r}, \mathbf{r}')\}, \quad (2.72)$$

Hence  $E_{XC}[\rho]$  could be written as the interaction between the electronic charge distribution that has been displaced by exchange and correlation effects, i.e., by the fact that the presence of an electron at  $\mathbf{r}$  reduces the possibility for a second electron to be at  $\mathbf{r}'$ , in the vicinity of  $\mathbf{r}$ . The displaced electron comes exclusively from the exchange part, and the correlation hole integrates to zero. The different approximate functionals for exchange-correlation are discussed next.

### 2.5.1 Local Density Approximation

The Local Density Approximation (LDA) has been for a long time the most widely used approximation to the exchange correlation energy. The primary idea is to consider generally in-homogeneous electron systems as locally homogeneous, and then to use the exchange-correlation hole corresponding to the homogeneous electron gas for which there are good approximations as well as exact numerical (quantum Monte-Carlo) results. LDA postulates that the exchange correlation functional has the following form,

$$E_{XC}^{LDA} = \int \rho(\mathbf{r}) \epsilon_{XC}[\rho(\mathbf{r})] d\mathbf{r}, \quad (2.73)$$

where, under the local density approximation,  $\epsilon_{XC}[\rho(\mathbf{r})]$  is assumed to be the exchange-correlation energy density of the homogeneous electron gas of density  $\rho(\mathbf{r})$ . Within the LDA,  $\epsilon_{XC}[\rho(\mathbf{r})]$  is a function of only the local value of density. It can be separated into exchange and correlation contributions,

$$\epsilon_{XC}[\rho(\mathbf{r})] = \epsilon_X[\rho(\mathbf{r})] + \epsilon_C[\rho(\mathbf{r})]. \quad (2.74)$$

In LDA, the exchange energy is given by the Dirac expression,

$$E_X[\rho(\mathbf{r})] = -C_X \int \rho^{\frac{4}{3}}(\mathbf{r}) d\mathbf{r}, \quad (2.75)$$

or the corresponding spin-polarized expressions,

$$E_X[\rho_\alpha, \rho_\beta] = -2^{\frac{1}{3}} C_X \int [\rho_\alpha^{\frac{4}{3}}(\mathbf{r}) + \rho_\beta^{\frac{4}{3}}(\mathbf{r})] d\mathbf{r}. \quad (2.76)$$

For the LDA exchange-only situation, the Kohn-Sham exchange potential as obtained through functional derivative of the LDA exchange energy is, [8] [9]

$$v_x[\rho] = -\frac{4}{3} C_X \rho^{\frac{1}{3}}; C_X = \frac{3}{4} \left(\frac{3}{\pi}\right)^{\frac{1}{3}}. \quad (2.77)$$

The Kohn-Sham theory treats the non-interacting kinetic energy exactly through the LDA.

The kinetic energy density in LDA is given by the Thomas-Fermi approximations, as,

$$E_{kin} = C_k \int d\mathbf{r} \rho^{\frac{5}{3}}(\mathbf{r}); C_k = \frac{3}{10} (3\pi^2)^{\frac{2}{3}}. \quad (2.78)$$

The energy functional within the LDA is expressed as,

$$E_v[\rho] = -C_k \int \rho^{\frac{5}{3}}(\mathbf{r}) d\mathbf{r} + \int v(\mathbf{r}) \rho(\mathbf{r}) d\mathbf{r} + E_{coul}(\rho) - C_X \int \rho^{\frac{4}{3}}(\mathbf{r}) d\mathbf{r} + E_C(\rho), \quad (2.79)$$

which on minimization subject to the constraint of fixed number of particles yields the Euler equation for density,

$$\mu = \frac{\delta E_v}{\delta \rho(\mathbf{r})} = \frac{5}{3}C_k \rho^{\frac{2}{3}}(\mathbf{r}) + v(\mathbf{r}) + \frac{\delta E_{coul}}{\delta \rho(\mathbf{r})} - \frac{4}{3}C_X \rho^{\frac{1}{3}}(\mathbf{r}) + \frac{\delta E_C}{\delta \rho(\mathbf{r})}. \quad (2.80)$$

The functional form for E is unknown, and has been simulated for the homogeneous electron gas in numerical quantum Monte-Carlo calculations which yield essentially exact results. [10] The resultant XC energy has been fitted by a number of analytic forms [11] [12] [13] all of which yield exact results and are collectively referred to as LDA functionals.

## 2.5.2 Generalized Gradient Approximation

Generalized Gradient Approximations (GGA) [14] constitutes the next step towards the improvement of LDA wherein the information on how the density  $\rho(\mathbf{r})$  varies spatially is included in the functional. The primary idea of GGAs is to express the exchange-correlation energy in the following generalized form,

$$E_{XC}[\rho] = \int \rho(\mathbf{r})\epsilon_{XC}[\rho(\mathbf{r})]d\mathbf{r} + \int F_{XC}[\rho(\mathbf{r}), \nabla\rho(\mathbf{r})]d\mathbf{r}, \quad (2.81)$$

where the functional  $F_{XC}$  is required to satisfy a number of formal conditions for the exchange-correlation hole, such as, sum rules, long range decay and so on. Different GGAs differ in the choice of the functional  $F_{XC}$ . A few of them are Langreth-Mehl(LM) [15], Perdew-Wang (PW'86 and PW'91) [16] [17], Becke '88 (B88) [18] exchange functional, Lee-Yang-Parr (LYP) correlation functional, [19] Perdew-Burke-Ernzerhof (PBE) [20]exchange-correlation etc. Among these PBE is the most widely used.

**PBE exchange-correlation functional:** In case of PBE exchange correlation functional, first the enhancement factor  $F_{XC}$  over the local exchange is defined as,

$$E_{XC}[\rho] = \int \rho(\mathbf{r})\epsilon_X^{LDA}[\rho(\mathbf{r})]F_{XC}(\rho, \zeta, s), \quad (2.82)$$

where  $\rho$  = local density,  $\zeta$  =relative spin-polarization, and,

$$s = \frac{|\nabla\rho(\mathbf{r})|}{2k_F\rho},$$

is the dimensionless density gradient.

$$F_{XC}(s) = 1 + \kappa - \frac{\kappa}{1 + \mu s^2/\kappa},$$

$\kappa$  and  $\mu$  are empirically fitted to a database of ionization energies. The correlation energy is written as,

$$E_C^{GGA} = \int \rho(\mathbf{r})[\epsilon_C^{LDA}(\rho, \zeta) + H(\rho, \zeta, t)], \quad (2.83)$$

with,

$$H[\rho, \zeta, t] = \left(\frac{e^2}{a_0}\right)\gamma\phi^3 \ln\left\{1 + \frac{\beta\gamma^2}{t} \left[\frac{1 + At^2}{1 + At^2 + At^4}\right]\right\}, \quad (2.84)$$

here,

$$t = \frac{|\nabla\rho(\mathbf{r})|}{2\phi k_s \rho},$$

is the dimensional density gradient, and,

$$k_s = \left(\frac{4k_F}{\pi a_0}\right),$$

is the Thomas Fermi screening wave number, and,

$$\phi(\zeta) = [(1 + \zeta)^{\frac{2}{3}} + (1 - \zeta)^{\frac{2}{3}}]/2,$$

is a spin scaling factor.

The function A has the form,

$$A = \frac{\beta}{\gamma} [\exp -\epsilon_C^{LDA}[\rho]/(\gamma\phi^3 e^2/a_0) - 1]^{-1}. \quad (2.85)$$

This GGA retains the correct features of LDA and combines them with the inhomogeneity features that are most important energetically.

### 2.5.3 Hybrid Functionals

In spite of the more or less accurate performance of LDA and different GGAs, the search for more accurate functionals go on and various beyond GGA functionals have appeared. Examples are hybrid functionals which incorporate a portion of exact exchange from Hartree-Fock theory with exchange and correlation from other sources (such as LDA). Few of the most popular forms of hybrid functionals are B3LYP (Becke, three-parameter, Lee-Yang-Parr) and HSE (Heyd-Scuseria-Ernzerhof) [21], etc. In this section we briefly describe various hybrid functionals.

The hybrid approach to constructing density functional approximations was introduced by Becke in 1993. Hybridization with Hartree-Fock (exact) exchange

provides a simple scheme for improving the calculations of many molecular properties, such as atomization energies, bond lengths and vibration frequencies, which tend to be poorly described with simple ab initio functionals.

A hybrid exchange-correlation functional is usually constructed as a linear combination of the Hartree-Fock exact exchange functional,  $E_X^{HF}$ , where,

$$E_X^{HF} = -\frac{1}{2} \sum_{ij} \int \int \psi_i^*(r_1) \psi_j^*(r_1) \frac{1}{r_{12}} \psi_i(r_2) \psi_j(r_2) dr_1 dr_2,$$

(here the wavefunctions  $\psi$  are as has been defined before for the Hartree Fock formalism) and any number of exchange and correlation explicit density functionals.

The HSE (Heyd-Scuseria-Ernzerhof) [21] exchange-correlation functional uses an error function screened Coulomb potential to calculate the exchange portion of the energy in order to improve computational efficiency,

$$E_{XC}^{HSE}(\omega) = \alpha E_X^{HF,SR}(\omega) + (1 - \alpha) E_X^{PBE,SR}(\omega) + E_X^{PBE,LR}(\omega) + E_C^{PBE},$$

where  $\alpha$  is the mixing parameter and  $\omega$  is an adjustable parameter controlling the short-rangeness of the interaction. Standard value of  $\omega=0.2$  (usually referred to as HSE06) along with varying values of  $\alpha$  from 0.15 to 0.35 were used in our calculations.  $E_X^{HF,SR}(\omega)$  is the short range Hartree-Fock exact exchange functional,  $E_X^{PBE,SR}(\omega)$  and  $E_X^{PBE,LR}(\omega)$  are the short and long range components of the PBE exchange functional, and  $E_C^{PBE}(\omega)$  is the PBE correlation functional.

## 2.6 Basis Sets

Numerous methods to solve the Kohn-Sham equations have been introduced, However one must choose an appropriate basis set to expand the single particle wave functions. The choice of the basis set depends on the specification of a given problem, such as the crystal symmetry, the nature of the involved elements of the periodic table. Several basis methods have been developed in last four decades and are widely used for band structure calculations of solids. Depending on the choice of basis functions these methods can be broadly classified into two categories, (i)fixed basis set method and (ii)partial wave basis set method.

The fixed basis set method is based on energy independent basis sets or fixed basis sets, like tight binding method using linear combination of atomic orbitals (LCAO) type basis [22], orthogonalized plane wave (OPW) method within a pseudopotential scheme [25] [26] using plane waves orthogonalized to core states as the basis set.

Considering the partial wave basis sets the crucial approximation that these methods are based on is the Muffin-tin (MT) sphere approximation. These methods include Linear Muffin-Tin orbital method (LMTO) [23], Linearised Augmented plane wave based method (LAPW) [29]

Finally, we have the Projector Augmented Wave (PAW) [27] [28] method which is a general approach for the all electron solution, proposed by Blöchl [28]. The unique feature of this method is the combination of the formal simplicity of plane wave pseudopotential approach and the versatility of the LAPW method.

In this thesis we have primarily used the partial wave basis set methods like LMTO (as implemented in the TB-LMTO-ASA code) and LAPW (as implemented in the Wien2K code) and the generalised PAW method (as implemented in the Vienna ab initio Simulation Package (VASP) code) In this section we discuss these above-mentioned basis sets.

### 2.6.1 Fixed basis set methods

#### Orthogonalized Plane Waves (OPW)-Pseudopotential Method

Plane wave expansions are required to accommodate two very different features of Bloch functions. Inside the core of the atoms, the potential is spherically symmetric and  $\psi_k$  has rapid oscillations and angular dependence of atomic wave functions. In the region between ion cores, the potential is nearly flat and  $\psi_k$  is slowly varying in the manner of plane waves. The atomic levels are classified

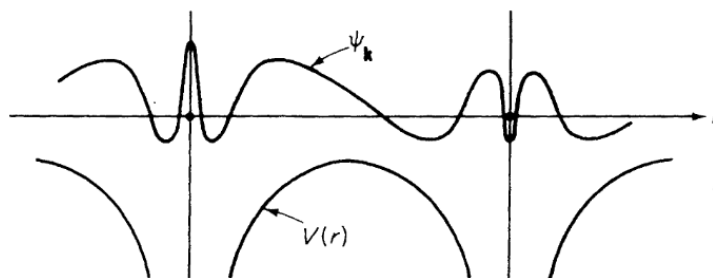


Figure 2.3: Figure showing the Bloch function  $\psi_k$  oscillating rapidly near atomic sites where the lattice potential is deep and attractive

into valance levels and ion cores. Orthogonalized plane waves or OPWs are quite literally plane waves that have been made orthogonal to occupied ion core orbitals. This is demonstrated in Figure 2.3.

Considering Bloch functions constructed out of core states,

$$b_{tk} = \sum_l \exp(i\mathbf{k}\cdot\mathbf{l})b_{tk}(\mathbf{r} - \mathbf{l}), \quad (2.86)$$

where core orbitals which are a combination of degenerate one electron states, each corresponding to localization of the electron on a particular atom, and  $b_{tk}$

are solutions of Schrodinger equation of whole crystal corresponding to the core levels  $\xi_t$ .

Higher states which are solutions of same Schrodinger equation all orthogonal to  $b_{tk}$ ,

$$\langle \psi_k | b_{tk} \rangle = 0, \quad (2.87)$$

one may consider,

$$\chi_k = \exp(i\mathbf{k}\cdot\mathbf{r}) - \sum_t \beta_t b_{tk},$$

as possible wave functions for one of the higher states, choosing  $\beta_t$  such that  $\chi_k$  satisfies the orthogonality condition.

Thus one may make  $\chi_k$  an OPW,

$$\chi_k = \exp(i\mathbf{k}\cdot\mathbf{r}) - \sum_t \langle b_{tk} | \exp(i\mathbf{k}\cdot\mathbf{r}) b_{tk} \rangle = 0. \quad (2.88)$$

One may now use the OPWs as basis sets for the wave functions, considering

$$\psi_k = \sum_k \alpha_{\mathbf{k}-\mathbf{K}} \chi_{\mathbf{k}-\mathbf{K}}, \quad (2.89)$$

as a solution of the Schrodinger equation.

One may use the variational principle to minimize energy and determine  $\alpha_{\mathbf{k}-\mathbf{K}}$ . This process converges very rapidly, and often a single OPW is sufficient to represent the wave function. To justify this, one may consider the wave function  $\chi_k$  as exact with definite  $\alpha_{\mathbf{k}-\mathbf{K}}$ . Let,

$$\phi = \sum_k \alpha_{\mathbf{k}-\mathbf{K}} \exp(i(\mathbf{k}-\mathbf{K})\cdot\mathbf{r}). \quad (2.90)$$

Then

$$\psi = \phi - \sum_t \langle b_t | \phi \rangle b_t,$$

omitting the  $k$  index. Substituting in the Schrodinger equation,

$$\begin{aligned} H\psi &= \xi\psi, \\ \implies H\phi - \sum_t \langle b_t | \phi \rangle Hb_t &= \xi\phi - \sum_t \langle b_t | \phi \rangle \xi b_t, \\ \implies H\phi - \sum_t \langle b_t | \phi \rangle \xi_t b_t + \xi \sum_t \langle b_t | \phi \rangle b_t &= \xi\phi, \end{aligned} \quad (2.91)$$

$b_t$  is also an eigenstate of  $H$  with energy  $\xi_t$ ,

$$H\phi + \sum_t (\xi - \xi_t) b_t \langle b_t | \phi \rangle = \xi\phi. \quad (2.92)$$

The above equation looks almost like a new Schrodinger's equation,

$$(H + V_R)\phi = \xi\phi,$$

where,

$$V_R\phi = \sum_t (\xi - \xi_t)b_t\langle b_t|\phi\rangle. \quad (2.93)$$

The smoothened out wave-function  $\phi$  satisfies a new equation of which the Hamiltonian is,

$$H + V_R = -\frac{\hbar^2}{2m} + U + V_R. \quad (2.94)$$

As if one had to find plane wave solution for eigenfunctions in the pseudo potential,

$$\Gamma = U + V_R, \quad (2.95)$$

where  $V_R$  is the non-localized operation

$$V_R = \sum_t (\xi - \xi_t)|b_t\rangle\langle b_t|, \quad (2.96)$$

$\phi$  is the pseudo wave-function, and satisfies Schrodinger's equation in which effective potential is relatively weak.

$$V_R(\mathbf{r} - \mathbf{r}') = \sum_t (\xi - \xi_t)b_t(\mathbf{r})b_t^*(\mathbf{r}'), \quad (2.97)$$

such that,

$$V_R\phi = \int V_R(\mathbf{r}, \mathbf{r}')\phi(\mathbf{r}')\mathbf{d}\mathbf{r}'. \quad (2.98)$$

$U$  being the attractive potential of an atom is negative, but  $V_R$  containing  $(\epsilon - \epsilon_t)$  and the square of the core orbitals is positive. Thus there is some cancellation between them reducing the value of  $v_{eff}$ .

The whole process of constructing  $V_R$  is not unique. One may show that the valence eigenfunctions of the Hamiltonian  $(H + V_R)$  are the same for any operator of the form  $V_R\phi = \sum_t \langle F_t|\phi\rangle b_t$ , where  $F_t$  are completely arbitrary functions.

$$F_t = -Ub_t, \Gamma\phi = (U + V_R)\phi = U\phi - \sum_t \langle Ub_t|\phi\rangle. \quad (2.99)$$

One may subtract from  $V$  any part that can be expanded as a sum of core functions. This is because  $V_R$  always projects onto the manifold of the core states. But the valence eigenfunction is orthogonal to this manifold. So addition of  $V_R$  to  $H$  makes no difference to the eigenvalue problem in the space of valence eigenfunctions.

Cancellation between true attractive potential and repulsive orthogonalization term may be viewed as a manifestation of Pauli's Exclusion Principle, which require the valence electrons (Bloch functions) to be orthogonal to core orbitals. Requirement of orthogonality is expressed through the rapid oscillations of true wave-function in core region where true potential is deep and attractive. Rapid oscillations give rise to high kinetic energy of valence electrons, which behaves as repulsive potential in ion core region. Hence as a result valence electrons tend to face only a net weak potential called pseudo-potential. Effective electronic wave-function corresponding to the replacement of the true potential by the pseudo-potential does not have all the rapid oscillations of the true wave-function. This is the pseudo wave-function. A graphical representation of the pseudo potential and the pseudo wave function are provided in Figure 2.4.

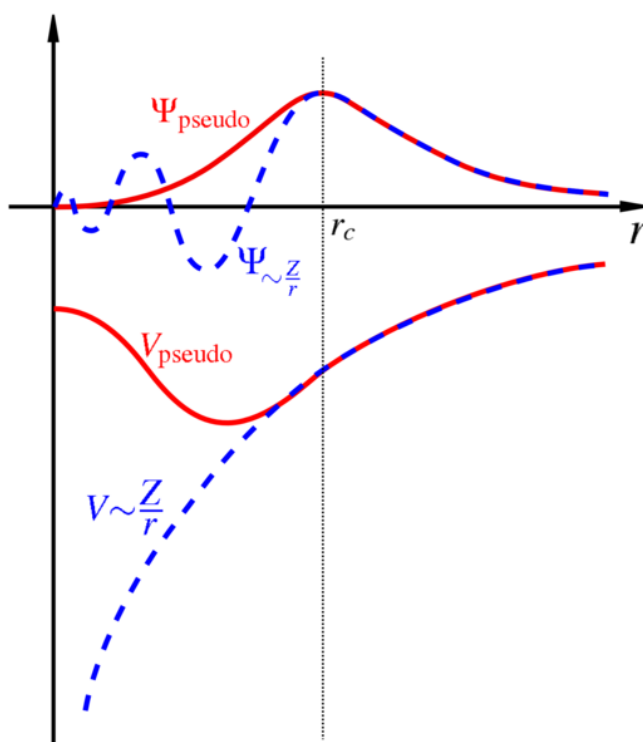


Figure 2.4: Comparison of a wave-function in the Coulomb potential of the nucleus (dashed) to the one in the pseudo-potential (solid). The real and the pseudo wave-function and potentials match above a certain cutoff radius. Figure adapted from Wikipedia.

However even after the huge utility of the pseudo-potential method it's not free of its fair share of failures. The failure of this method is primarily due to the fact that it depends too much on energy and angular momentum. It is not a true

local potential and it can not deal elegantly with d-bands.

### Norm Conserving Pseudo Potentials (NC-PP)

Norm conserving pseudopotentials (NCPP) are constructed with an extra constraint that the pseudo-wave function must ensure that the charge within the core radius is same for the pseudo and all-electron wave function, i.e.,

$$\int |\phi_{AE}^{nl}(\mathbf{r})|^2 d\mathbf{r} = \int |\phi_{ps}^{nl}(\mathbf{r})|^2 d\mathbf{r},$$

where  $\phi_{AE}^{nl}(\mathbf{r})$  is the all electron wave function and  $\phi_{ps}^{nl}(\mathbf{r})$  is the pseudo wave function.

NCPP works well for most elements except for some first period 2p and 3d elements. In these cases the pseudo and the all-electron wave functions are almost identical. In norm-conserving pseudo-potential scheme, inside some core radius, the all electron (AE) wave function is replaced by a soft nodeless pseudo (PS) wave function, subject to the condition that within the chosen core radius the norm of the PS wave function has to be the same with the AE wave function and outside the core radius both the wave functions are identical. However, the charge distribution and moments of AE wave function are well reproduced by the PS wave function only when the core radius is taken around the outer most maximum of AE wave function. This in practice makes the situation for strongly localized orbitals like 3d and rare-earth elements, complicated as the resulting pseudo-potentials require a large plane-wave basis set. This situation was remarkably improved by Vanderbilt by introduction of ultra-soft pseudo-potential.

### Ultrasoft Pseudopotentials (US-PP)

According to the scheme proposed by David Vanderbilt the norm conservation constraint was relaxed and localized atom centered augmentation charges were introduced to make up for the charge deficit. These augmentation charges are defined as the charge density difference between the AE and the PS wavefunction. Only for the augmentation charges, a small cutoff radius must be used to restore the moments and the charge distribution of the AE wavefunction accurately. But the success of this particular approach is partly hampered by rather difficult construction of the pseudo potential. As the name suggests, ultrasoft pseudo potentials attain much smoother (softer) pseudo wave-functions so considerably fewer plane-waves for calculations of the same accuracy may be used. This is achieved by relaxing the norm-conservation constraint, which offers greater flexibility in the construction of the pseudo-wave-functions. In this scheme the total valence density  $\rho(\mathbf{r})$  is partitioned into so-called hard and soft contributions,

$$\rho(\mathbf{r}) = \sum_n [|\phi_n(\mathbf{r})|^2 + \sum_{ij} Q_{ij} \langle \phi_n | \beta_j \rangle \langle \beta_i | \phi_n \rangle], \quad (2.100)$$

where  $\beta_i$  are projector functions that depend on the ionic positions, and the augmentation function  $Q_{ij}$  is given by,

$$Q_{ij}(\mathbf{r}) = \psi_i^*(\mathbf{r})\psi_j(\mathbf{r}) - \phi_i^*(\mathbf{r})\phi_j(\mathbf{r}), \quad (2.101)$$

$\psi_j(\mathbf{r})$  are the all-electron wave-functions,  $\phi_j(\mathbf{r})$  and are ultrasoft wave-functions constructed without satisfying the norm-conservation condition  $Q_{ij}(\mathbf{r}) = 0$ . The plane wave code VASP uses ultra-soft potentials to describe the interaction between ions and electrons as one of the many basis sets.

## 2.6.2 Partial wave basis set methods

### Linear Muffin-Tin Orbital method (LMTO)

The linear muffin-tin orbital method is a good choice to evaluate the correct eigenstates of the many electron Hamiltonian subject to a real crystal potential in a computationally more "efficient" and less "expensive" method. It is based on the tight binding model. In this method, the muffin-tin approximation is used, in which the actual crystal potential is approximated in the following way (as shown in Figure 2.5)

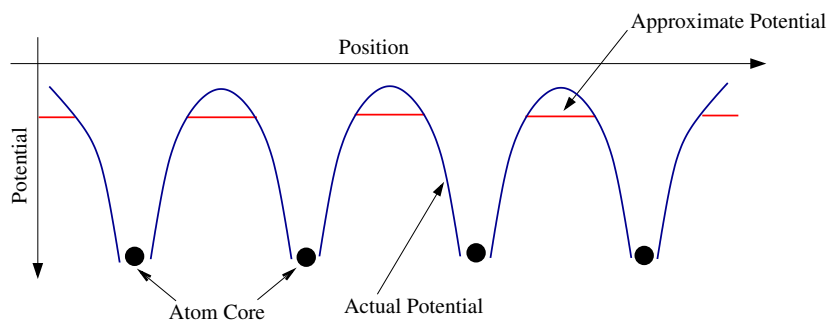


Figure 2.5: Schematic diagram of potential inside real crystal and approximated potential considered in LMTO method. Potential is rapidly varying in the vicinity of core atomic region. In the interstitial region i.e. away from atom core region, the actual potential is approximated as a constant potential.

In this approximation, the space inside the crystal is considered to be divided into two parts, atom-centered muffin tin spheres and the rest region as interstitial. The potential around each atom is treated as spherically symmetric within a radius  $S_R$  and in the interstitial region the potential is considered to be constant. Hence the potential is of the following form,

$$v(\vec{r}_R) = \begin{cases} v(r_R) & r_R \leq S_R, \vec{r}_R = |\vec{r} - \vec{R}| \\ -v_0 & r_R > S_R \end{cases}$$

Inside the spherically symmetric muffin tin sphere the rapidly varying part of wave-function is represented by the radial solution of Schrödinger equation times spherical harmonics, known as partial waves, which is given as,

$$\phi(\mathbf{r}_R) = \theta(\hat{r}_R, \epsilon) Y_L(\hat{r}_R). \quad (2.102)$$

Here  $L$  denotes the angular momentum labels  $(l, m)$ ,  $Y_L(\hat{r}_R)$  are the spherical harmonics functions and  $\hat{r}_R$  are the angular variables associated with the vector  $\mathbf{r}_R$ . This solution is regular at  $\mathbf{r} = \mathbf{R}$  and behaves like  $r_R^l$  at  $r_R \rightarrow 0$ . Outside the muffin-tin region the potential is assumed to be constant, and therefore the radial equation with a constant  $v_{r_R} = v_0$  takes the form,

$$\left[ \frac{d^2}{dr_R^2} + \frac{l(l+1)}{r_R^2} - \kappa^2 \right] r_R \theta_{RL}(r_R, \epsilon) = 0, \quad (2.103)$$

where  $\kappa^2 = \epsilon - v_0$ .

Thus in the interstitial region the solution is plane waves, which can be expanded in terms of spherical Neumann and Bessel functions. It is needless to mention that, the solutions must be continuous and smooth at the sphere boundary in order to have a well-behaved wave-function. This particular method relies on atomic sphere approximation (ASA) which replaces the muffin tin spheres by space-filling atomic spheres, called Wigner-Seitz (WS) spheres. Including this approximation, the information needed to set up the Hamiltonian can be divided into two independent parts. One part contains the structure matrix which depends only on the structure and the positions of the atoms and not on the type of atoms occupying the sites. The solution of the Schrödinger's equation inside each inequivalent WS sphere with appropriate boundary conditions form the other part of the information. Finally following Andersens approach of linearization, the LMTO basis functions within ASA can be expressed as,

$$\chi_{RL}^\alpha = \phi_{RL}(r_R) + \sum_{R'L'} \dot{\phi}_{R'L'}^\alpha(r_{R'}) h_{R'L',RL}^\alpha, \quad (2.104)$$

where  $\phi$ s are the partial waves inside the WS sphere centered at  $\mathbf{R}$  for a energy of linearization  $\epsilon_{RL}$ . The functions  $\dot{\phi}^\alpha$  are the linear combinations of the  $\phi$ s and their energy derivatives  $\dot{\phi}$ s. The matrix  $h^\alpha$  is given by,

$$h^\alpha = C^\alpha - \epsilon_v + (\Delta^\alpha)^{\frac{1}{2}} S^\alpha (\Delta^\alpha)^{\frac{1}{2}}, \quad (2.105)$$

where  $C$  and  $\Delta$  are the diagonal potential matrices. They depend on the potential inside the sphere,  $\alpha$  and on sphere radii.  $C$  and  $\Delta$  are commonly known as band center parameter and band width.  $S$  is the structure matrix depending on the representation and the geometrical arrangement of the atomic sites.

An improved LMTO method called  $N^{\text{th}}$  **order LMTO** or **NMTO** method [30] was developed. The characteristics of the method are:

- (1) It still has muffin tin potential.
- (2) It still uses partial waves in atomic spheres.
- (3) Instead of Neumann functions, screened spherical waves (SSW) are used in the interstitial regions.
- (4) Kinked partial waves (KPWs) are defined out of partial waves and screened spherical waves.
- (5) Energy dependent NMTOs are constructed which are superposition of KPWs at  $(N+1)$  energy points.

### Linearised Augmented Plane Wave (LAPW) method

Keeping in mind the fact that pseudo potential methods are extremely useful, if one is interested in information that is inherently contained in the region near the nucleus, pseudo potential methods may not be a reasonable choice. In such cases Augmented Plane Wave (APW) basis set can be more useful. In the region far away from the nuclei, the electrons are relatively delocalized and thus can be described by plane waves. On the other hand, close to the nuclei, the electrons behave in a localized manner confined in an isolated atom. In such case atomic like functions can describe the behaviour of the electrons more efficiently. Therefore the space can be treated as divided into two regions, as was discussed for LMTO method previously. Around each atom a sphere of radius  $r_0$  is considered and such spheres are usually referred to as muffin tin spheres. The remaining space is known as interstitial region. The potential is that of a free ion at the core, and is strictly constant outside the core. The wave function for the wave vector  $\mathbf{k}$  is taken to be  $\psi_{\mathbf{k}}(r)$  where  $r_0$  is the core radius. Outside the core, the function is a plane

$$\psi_{\mathbf{k}}(\mathbf{r}) = \begin{cases} e^{i\mathbf{k}\cdot\mathbf{r}} & \text{when } |\mathbf{r} - \mathbf{R}| \geq r_0 \\ \text{atomicfunction} & \text{when } |\mathbf{r} - \mathbf{R}| < r_0 \end{cases}$$

wave because the potential is constant there. Inside the core the function is atom-like, and is found by solving the appropriate free-atom Schrödinger equation. The well-known condition for well-behaved wave-function is that the solution must be

continuous at the boundary and the atomic function must be chosen in such a way that it joins continuously to the plane wave at the surface of the sphere forming the core (this is the boundary condition here). However this is not an obvious thing, since a plane wave is oscillating in nature and has a unique direction built in. Therefore to match it with another function based on spherical harmonics over the entire surface of a sphere, is not straightforward. One may use a very large number of the constants included in the atomic functions to create a good matching between the two functions.

Up till this point the basis set functions are dependent on energy  $E$ . Linearization of APW method ie. Linearized Augmented Plane Wave (LAPW) [31] helps to get rid of this problem.

The linearized version of Augmented Plane Wave (LAPW) basis, following Andersen's linearization approach, is expressed as,

$$\chi_{\mathbf{q}}(\mathbf{r}, \epsilon) = \begin{cases} \sum_{l,m} \left( A_{lm,R}^q \phi_{LR}(r_R, \epsilon_\nu) + B_{lm,R}^q \dot{\phi}_{LR}(r_R, \epsilon_\nu) \right) & \text{for } r_R \leq S_R \\ e^{i(\mathbf{q} \cdot \mathbf{r})} & \text{for } r_R > S_R \end{cases}$$

where the coefficients  $A_{lm,R}^q$  and  $B_{lm,R}^q$  can be determined by matching these solutions in magnitude and slope at the sphere boundary. To do so the plane wave solution in the interstitial is required to expand in terms of Bessel functions  $j_l(r_R; q)$ . In principle a large number of  $l$  values are required for exact matching, but to keep the problem tractable one truncates this number at some value  $l_{max}$ . Therefore in band structure calculations based on LAPW basis set a crucial parameter is  $l_{max}$  for which a reasonable choice is needed. The condition that allows a good choice of  $l_{max}$  is :

$$R_i K_{max} = l_{max}$$

where  $R_i$  is the radius of  $i^{th}$  MT sphere and  $K_{max}$  determines the cut-off for the plane waves. The accuracy of the basis is controlled by the quantity  $R_i^{min} K_{max}$ , where  $R_i^{min}$  is the smallest MT sphere radius in the unit cell.

In this method the core states, those do not participate in chemical bonding, are treated as in free atoms, but subject to the potential due to the valence states. The problem arises in order to treat the semi-core states, which lie in between core and valence states. In order to solve this problem an additional set of basis functions can be added. They are called "local orbitals" and consist of a linear combination of two radial functions at two different energies and one energy derivative at one of these energies:

$$\phi_{lm}^{LO} = A_{lm,R} \phi_{LR}(r_R; \epsilon_{\nu 1}) + B_{lm,R} \dot{\phi}_{LR}(r_R; \epsilon_{\nu 1}) + C_{lm,R} \phi_{LR}(r_R; \epsilon_{\nu 2})$$

The coefficients are determined by the requirements that  $\phi^{LO}$  should be normalized and should have zero value and slope at the sphere boundary. Though

adding local orbitals increases the LAPW basis set size, still their number is quite small compared to typical LAPW basis set size of a few hundred functions. The problem with the APW method was the energy dependence of the basis set, which is removed in the LAPW+LO method, however at the cost of a somewhat larger basis set size.

### 2.6.3 The Projector-Augmented-Wave (PAW) Formalism

The projector-augmented-wave (PAW) method was developed by P.E. Blöchl in 1994. This method turned out to be computationally elegant, transferable and accurate method for electronic structure calculation, and facilitates density functional theory calculations to be performed with greater computational efficiency. Later Kresse and Joubert modified this PAW method and implemented it within the plane wave code of Vienna Ab-initio Simulation Package(VASP). Here also valence wave-functions tend to have rapid oscillations near ion cores due to the requirement that they be orthogonal to core states; this situation is problematic because it requires many Fourier components to describe the wave-functions accurately. The PAW approach addresses this issue by transforming these rapidly oscillating wave-functions into smooth wave-functions (by a linear transformation) which are more computationally convenient. This approach is somewhat reminiscent of a change from the Schrödinger picture to the Heisenberg picture. In this formalism, the AE wave-function  $\Psi_n$  is derived from the PS wave-function  $\tilde{\Psi}_n$  by means of a linear transformation:

$$|\Psi_n\rangle = |\tilde{\Psi}_n\rangle + \sum_i (|\phi_i\rangle - |\tilde{\phi}_i\rangle) \langle \tilde{p}_i | \tilde{\Psi}_n \rangle \quad (2.106)$$

The index  $i$  is a shorthand for the atomic site at  $\mathbf{R}_i$ . The all electron partial waves  $\phi_i$  are the solutions of the radial Schrödinger equation for the isolated atom. The PS partial waves  $\tilde{\phi}_i$  are equivalent to the AE partial waves outside a core radius  $r_c$ . Of course these two wave-functions match both in value and slope at the boundary  $r_c^l$ . The projector function  $p_i$  for each PS partial wave localized within the core radius, obeys the relation  $\langle \tilde{p}_i | \tilde{\phi}_j \rangle = \delta_{ij}$ .

The AE charge density in PAW method can be written as,

$$\rho = \tilde{\rho} + \rho^l - \tilde{\rho}^l \quad (2.107)$$

where  $\tilde{\rho}$  is the soft pseudo-charge density calculated directly from the pseudo wave-functions on a plane wave grid. The on-site charge densities  $\rho^l$  and  $\tilde{\rho}^l$  are treated on radial support grids localized around each atom. It must be stated that the charge density  $\tilde{\rho}^l$  is exactly the same as  $\rho^l$  within the augmentation spheres around each atom. In PAW approach, an additional density, called compensation charge density is added to both auxiliary densities  $\tilde{\rho}^l$  and  $\rho^l$  so that

the multi-pole moments of the terms  $\rho^l - \tilde{\rho}^l$  vanish. Thus the electrostatic potential due to these terms vanishes outside the augmentation spheres around each atom. Like density, the energy can also be written as a sum of three terms and by functional derivatives of the total energy, one can derive the expressions of Kohn-Sham equations. The PAW method is typically combined with the frozen core approximation, in which the core states are assumed to be unaffected by the ions' environment. There are several online repositories of pre-computed atomic PAW data.

## 2.7 *Ab initio Molecular Dynamics*

Conventional DFT formalism has certain shortcomings. For example, it can not take care of time variation, i.e, the dynamics in the system. Therefore apart from above mentioned basic electronic structure methods, in the present thesis we have employed a few advanced techniques. Among these Molecular Dynamics (MD) forms a primary part of the study. Molecular dynamics is a computer simulation method for studying the physical movements of atoms and molecules, and is thus a type of N-body simulation. The atoms and molecules are allowed to interact for a fixed period of time, giving a view of the dynamic evolution of the system. In the most common version, the trajectories of atoms and molecules are determined by numerically solving Newton's equations of motion for a system of interacting particles, where forces between the particles and their potential energies are calculated using interatomic potentials or molecular mechanics force fields. The method was originally developed within the field of theoretical physics in the late 1950s but is applied today mostly in chemical physics, materials science and the modelling of biomolecules.

Molecular Dynamics (MD) of a many body system is a method which describe the dynamical evolution of the system at a microscopic level. For solid state systems molecular dynamics generates configurations from dynamical evolution of atoms.

The prime objective of any molecular dynamics method is to solve primarily the Newtons equations of motion which are of the form;

$$M\ddot{\mathbf{R}}(t) = F(t) = -\nabla V(\mathbf{R}(t)),$$

where  $\ddot{\mathbf{R}}(t)$  is the double time derivative of ionic coordinates, which can be related to the gradient of effective potential field in which the system evolves.

In the last few decades enormous number of studies have been done on how to describe more efficiently and reliably the potential for multi-atom systems. In principle, potential energy landscape may be calculated from full quantum mechanical calculations. However, in reality, it is not possible. The traditional method of approximating the potential is to determine the potential in advance.

In this method the full many body interaction can be split into different parts in different ways depending on the number of terms and also on the basis of long range-short range interaction. Taking into account this intuitive information, the potentials are represented by suitable empirical functional forms. Using this empirical potential energy landscape the dynamics of the system is determined. In spite of huge success [32] of the empirical potential MD method in various cases like liquids, gas phases etc, it fails in a number of cases [33,34]. These predefined empirical model potentials MD fails where electronic degrees of freedom plays a very crucial role in the description of the system. Therefore it was imperative to develop a new route to handle the above mentioned shortcomings, by coupling the traditional MD with the ab-initio electronic structure calculations named as "Ab-initio Molecular Dynamics" (AIMD). The basic idea of ab-initio MD is to calculate the forces on the nuclei from the electronic structure calculations for the generated dynamical configurations of nuclei, by treating electronic degrees of freedom quantum mechanically and ionic degrees of freedom classically.

Therefore in this method the electronic degrees of freedom are treated actively, which capture the details of all electronic behavior as well as all sorts of chemical complexity derived by electronic level. In literature mainly three types of AIMD have been reported based on the way of generating the quantum many body potential by solving quantum electronic structure calculation. These methods are:

1. Ehrenfest MD
2. Born-Oppenheimer MD
3. Car-Parrinello MD

We shall describe each of these methods in some detail.

### 2.7.1 Ehrenfest Molecular Dynamics

The many body Hamiltonian contains both ionic and electronic degrees of freedom. In this scheme [35] using the technique of separation of variables the ionic and electronic degrees of freedom are separated out. For the electronic part we solve the time dependent Schrödinger equation for a particular configuration of nuclei, which may be expressed as,

$$i\hbar\frac{\partial\psi}{\partial t} = H_e(\mathbf{r}, \mathbf{R})\psi(\mathbf{r}, \mathbf{R}, \mathbf{t}), \quad (2.108)$$

where,  $H$  is the complete many body Hamiltonian with the K.E part of nuclei and  $\psi(\mathbf{r}, \mathbf{R}, t)$  is the electronic part of the full wave function. The nuclear motion

is treated classically in the field created by the quantum mechanical dynamics of electrons and it may be expressed as,

$$M\ddot{\mathbf{R}}(t) = -\nabla \langle H_e \rangle . \quad (2.109)$$

Hence the salient features of Ehrenfest MD method may be summarized as follows :

- (i) The electronic Hamiltonian  $H_e$  depends parametrically on the instantaneous nuclear position  $\mathbf{R}$ , and it is time dependent via nuclear propagation  $\mathbf{R}(t)$ .
- (ii) The connection between classical and quantum mechanical degrees of freedom are established in a mean field way.
- (iii) Time evolution of nuclei are dictated by Newton's law of motion in a mean field created by the electron whereas the electrons evolve according to time dependent Schrödinger's equation.
- (iv) It is a hybrid method of classical and quantum mechanical approach.

### 2.7.2 Born-Oppenheimer Molecular Dynamics

Born and Oppenheimer proposed an alternative way [1] to solve coupled electron-nuclei wave equation by treating electrons completely time independently at each time configuration of nuclei. That means we have to solve the time independent Schrödinger's equation for electrons at each molecular dynamics step of time varying nuclear positions. Mathematically it can be written as,

$$H_e \Psi_0 = E_0(\mathbf{R}) \Psi_0, \quad (2.110)$$

$$M\ddot{\mathbf{R}}(t) = -\nabla \min \langle \Psi_0 | H_e | \Psi_0 \rangle .$$

Hence we might conclude,

- (i) The effective potential energy is obtained from the time independent electronic part for a particular nuclei configuration.
- (ii) Here  $\psi$  is no longer intrinsically time dependent. It is assumed that electronic degrees of freedom follow adiabatically the classical nuclear motion.

In Born-Oppenheimer MD (BO-MD) the electronic wave function of the Schrödinger's equation is calculated at each ionic configuration and the force at each step is calculated by minimizing the Hamiltonian  $H_e$  with respect to the exact eigen

functions. Hence any unwanted contribution in the force are eliminated automatically in Born-Oppenheimer MD.

In the case of DFT based AIMD within the formalism given by Born-Oppenheimer, the Hamiltonian  $H_e$  is replaced with the Kohn-Sham Hamiltonian  $H_e^{KS}$ . Thus we get the energy eigenvalues as the Kohn-Sham eigenvalues,  $E_0^{KS}$ , and the wave functions are simply the Kohn-Sham orbitals.

### 2.7.3 Car-Parrinello Molecular Dynamics

Car-Parrinello MD (CP-MD) [36, 37] is a combined approach of both Ehrenfest MD and BO-MD scheme. In CP-MD we have to solve the nuclear motion classically over a large time scale set by the time of nuclear motion. On top of that we have to take onto account evolution of intrinsic quantum mechanical electronic part. In order to handle this mixed quantum/classical problem the route is to map this two component problem into one component problem with two different energy scales. Instead of Hamiltonian in the previous cases, in this method we deal with the corresponding Lagrangian involving both nuclear and electronic part,

$$L = \sum (1/2)M\dot{\mathbf{R}}^2 + \sum_i \mu_i \langle \dot{\psi}_i | \dot{\psi}_i \rangle - \langle \Psi_0 | H_e | \Psi_0 \rangle + \sum_{ij} \Lambda_{ij} (\langle \psi_i | \psi_i \rangle - \delta_{ij}), \quad (2.111)$$

where, the first two terms of eqn. (2.122) are the K.E of nuclear and electronic part respectively, the third term is the potential energy and the fourth term is the constraint involved in the Lagrangian. Here  $\mu$  is the fictitious mass associated with electronic degrees of freedom. The corresponding Lagrange's equation of motion for nuclear part thus becomes,

$$M\ddot{\mathbf{R}}(t) = -\frac{\partial}{\partial \mathbf{R}} \langle \Psi | H_e | \Psi \rangle, \quad (2.112)$$

and the electronic part becomes,

$$\mu_i \ddot{\psi}_i(t) = -\frac{\delta}{\delta |\psi_i \rangle} \langle \Psi_0 | H_e | \Psi_0 \rangle + \sum_j \Lambda_{ij} \psi_j. \quad (2.113)$$

The primary disadvantage of Car Parrinello MD lies in the fact that the calculation of force acting on the nuclei is taken into account. The force acting on the nuclei may be calculated by Hellmann-Feynman theorem of the form [39],

$$F^{HF} = - \langle \Psi_0 | \nabla H_e | \Psi_0 \rangle,$$

where,  $\Psi_0$  is an exact eigen function corresponding to the Hamiltonian  $H_e$ . In case of Car Parrinello MD the expectation values of the Hamiltonian  $H_e$  are not

minimized with respect to the wave function, which is also a problem with the previously described Ehrenfest MD too. Thus in both of these cases the force is calculated with respect to the non self consistent wave function, which leads to additional non self consistent force terms in the calculation.

### 2.7.4 AIMD used in this thesis

In both Ehrenfest MD and CP-MD one has to simultaneously integrate over the coupled equations of motion of electrons and nuclei, whereas in the case of Born-Oppenheimer MD there are no explicit electron dynamics, so one needs to integrate over one time scale dictated by the nuclear motion. This is a huge advantage of Born-Oppenheimer method over the other two methods. In respect of computational time, Born-Oppenheimer MD may be made as fast as CP-MD at the expense of energy conservation. However by suitable choice of ensemble the problem of energy conservation can be avoided and as far as the convergence of wave function and energy is concerned this problem is not so serious.

In this thesis we adopted the Born-Oppenheimer approach to include the finite temperature effect in our calculations. For implementation of the above scheme in practice, the primary task is to separate the nuclear and electronic motion. The basic requirement is that the fictitious temperature associated with the electronic motion should remain low compared to the nuclear motion. This may be achieved by proper choice of time steps and thermostats in the simulation. Various thermostats like Berendsen thermostat or Nosé-Hoover thermostat are available for this purpose.

In the case of DFT based AIMD within the formalism given by Born-Oppenheimer the equations for Born-Oppenheimer MD takes the forms,

$$H_e^{KS}\Psi_0 = E_0^{KS}(\mathbf{R})\Psi_0,$$

$$M\ddot{\mathbf{R}}(t) = -\nabla \min \langle \Psi_0 | H_e^{KS} | \Psi_0 \rangle .$$

## 2.8 Monte Carlo simulation of model systems

Not all calculations in this thesis are based purely on Density functional theory or its extensions thereof. Calculations employing model Hamiltonians developed specifically to address the requirements of the system, were solved using Monte Carlo algorithms, often in conjunction with Density functional theory calculations. Here we give a brief overview of the Monte Carlo methods employed in this thesis.

Monte Carlo methods are in general a broad class of computational algorithms that rely on repeated random sampling to obtain numerical results. Their essential idea is using randomness to solve problems that might be deterministic in

principle. They are often used in physical and mathematical problems and are most useful when it is difficult or impossible to use other approaches. Monte Carlo methods are mainly used in three distinct problem classes [38]: optimization, numerical integration, and generating draws from a probability distribution.

### 2.8.1 Metropolis Algorithm

The Metropolis-Hastings algorithm is a Markov chain Monte Carlo (MCMC) method for obtaining a sequence of random samples from a probability distribution for which direct sampling is difficult. This sequence can be used to approximate the distribution (e.g., to generate a histogram), or to compute an integral (such as an expected value). Metropolis-Hastings and other MCMC algorithms are generally used for sampling from multi-dimensional distributions, especially when the number of dimensions is high. For single-dimensional distributions, other methods are usually available (e.g. adaptive rejection sampling) that can directly return independent samples from the distribution, and are free from the problem of autocorrelated samples that is inherent in MCMC methods.

### 2.8.2 Simulation of the Ising Model

Our model Hamiltonian developed was based on the simple ideas of an Ising model. With the brief introduction to importance sampling and Metropolis algorithm we now use these techniques in developing a simple algorithm for simulation of an Ising like Hamiltonian. We consider here a single spin flip Ising model simulation.

First we need to specify the type and size of lattice and the boundary conditions which may be used. For all practical purposes in real systems we are required to model a 3D Ising spin chain. Here a simple cubic lattice of size  $L \times L \times L$  is considered, with all linear dimensions being equal and periodic boundary conditions. Next an initial spin configuration is chosen, e.g. all spins may be initially pointing up or down. Hence the following steps are repeated until a self-consistency condition is reached [40].

1. Selecting one lattice site  $i$ , at which the spin  $S_i$  is considered for flipping ( $S_i \rightarrow -S_i$ )
2. Computing the energy change  $\delta E$  associated with that spin flip.
3. Calculating the transition probability  $\tau_S W$  for that spin flip.
4. A random number  $Z$  uniformly distributed between zero and unity is drawn.
5. If  $Z < \tau_S W$  the spin flip is allowed, otherwise the spin flip is not allowed. In any case the configuration of the spins obtained in this way at the end of step 5 is counted as a new configuration.

6. The resulting configuration is analyzed as desired, its properties are stored to calculate the necessary averages. If one is for e.g. just interested in the un-normalized magnetization  $M_{tot}$ , one may update it replacing  $M_{tot}$  by  $M_{tot} + 2S_i$ .

# Bibliography

- [1] M. Born and J. R. Oppenheimer, *Ann. Physik* 84, 457 (1927)
- [2] Messiah, A. (1961) *Quantum Mechanics*, Vol.1, North-Holland, Amsterdam.
- [3] D. R. Hartree, *Mathematical Proceedings of the Cambridge Philosophical Society* 24, 426-437 (1928).
- [4] V. Fock, *Z. Phys.* 61 (1930).
- [5] March, N.H. (1983) in *Theory of the Inhomogeneous Electron Gas*, eds S. Lundqvist and N.H. March, Plenum Publishing, New York
- [6] P. Hohenberg and W. Kohn, *Phys. Rev.* 136, B864-B871 (1964).
- [7] W. Kohn and L. J. Sham, *Phys. Rev.* 140, A1133-A1138 (1965).
- [8] R. M. Dreizler and E. K. U. Gross, *Density Functional Theory* (Springer, Berlin, 1990).
- [9] R. G. Parr and W. Yang, *Density-Functional Theory of Atoms and Molecules* (Oxford University Press, Oxford, 1989).
- [10] D. M. Ceperley and B. J. Alder, *Phys. Rev. Lett.* 45, 566-569 (1980).
- [11] J. P. Perdew and A. Zunger, *Phys. Rev. B* 23, 5048-5079 (1981)
- [12] U. v. Barth and L. Hedin, *J. Phys. C: Solid State Phys.* 5, 1629-1642 (1972).
- [13] S. H. Vosko, L. Wilk, and M. Nusair, *Canadian Journal of Physics* 58, 1200-1211 (1980).
- [14] J. P. Perdew and W. Yue, *Phys. Rev. B* 33, 8800-8802 (1986).
- [15] Langreth, D.C. and Mehl, M.J. (1981) *Phys. Rev. Lett.*, 47, 446.
- [16] Perdew, J.P. and Wang, Y. (1986) *Phys. Rev. B*, 33, 8800, 8822.
- [17] Perdew, J.P. and Wang, Y. (1991) *Phys. Rev. B*, 45, 13 244

- [18] Becke, A.D. (1988) *Phys. Rev. A*, 38, 3098.
- [19] Lee, C., Yang, W., and Parr, R.G. (1988) *Phys. Rev. B*, 37, 785
- [20] J. P. Perdew, K. Burke, and M. Ernzerhof, *Phys. Rev. Lett.* 77, 3865-3868 (1996)
- [21] J. Heyd, G. E. Scuseria, and M. Ernzerhof, *The Journal of Chemical Physics* 118, 8207-8215 (2003).
- [22] J. C. Slater and G. F. Koster, *Phys. Rev.* 94, 1498-1524 (1954).
- [23] O. K. Andersen and O. Jepsen, *Phys. Rev. Lett.* 53, 2571-2574 (1984).
- [24] J. C. Phillips and L. Kleinman, *Phys. Rev.* 116, 287-294 (1959).
- [25] D. Vanderbilt, *Phys. Rev. B* 41, 7892 (1990).
- [26] G. Kresse and J. Hafner, *J. Phys.: Condens. Matter* 6, 8245 (1994).
- [27] G. Kresse and D. Joubert, *Phys. Rev. B* 59, 1758 (1999).
- [28] P. E. Blöchl, *Phys. Rev. B* 50, 17953 (1994).
- [29] T. L. Loucks, *Augmented plane wave method* (W.A. Benjamin, New York, 1967).
- [30] O. K. Andersen and T. Saha-Dasgupta, *Phys. Rev. B* 62, R16219-R16222 (2000).
- [31] O. Jepsen, J. Madsen, and O. K. Andersen, *Phys. Rev. B* 18, 605-615 (1978).
- [32] G. C. Schatz, *Rev. Mod. Phys.* 61, 669 (1989), C. G. Gray and K. E. Gubbins, *Theory of Molecular Fluids Vol. 1* (Oxford, Clarendon, 1984), M. Sprik, in *Computer Simulation in Chemical Physics*, eds. M. P. Allen and D. J. Tildesley (Kluwer, Dordrecht, 1993).
- [33] D. K. Remler and P. A. Madden, *Molec. Phys.* 70, 921 (1990).
- [34] M. C. Payne, M. P. Teter, D. C. Allan, T. A. Arias, and J. D. Joannopoulos, *Rev. Mod. Phys.* 64, 1045 (1992).
- [35] P. Ehrenfest, *Z. Phys.* 45, 455 (1927).
- [36] R. Car and M. Parrinello, *Phys. Rev. Lett.* 55, 2471 (1985), R. Car and M. Parrinello, *Solid State Commun.* 62, 403 (1987).

- 
- [37] R. Car, M. Parrinello, and M. Payne, *J. Phys.: Condens. Matter* 3, 9539 (1991), R. Car, in *Monte Carlo and Molecular Dynamics of Condensed Matter Systems*, Chapt. 23, p. 601, eds. K. Binder and G. Ciccotti (Italian Physical Society SIF, Bologna, 1996).
- [38] Kroese, D. P.; Brereton, T.; Taimre, T.; Botev, Z. I. (2014) *WIREs Comput Stat.* 6: 386-392
- [39] R. P. Feynman, *Phys. Rev.* 56, 340 (1939); H. Hellmann, *Z. Phys.* 85, 180 (1933)
- [40] K. Binder, and D. W. Heermann, *Monte Carlo Simulation in Statistical Physics*, 1988

# Chapter 3

## Cooperativity in Spin-crossover Transition in Metalorganic Complexes : Interplay of magnetic and elastic interactions

### 3.1 Introduction

Spin Crossover (SCO) is a phenomena which may take place in certain transition metal (TM) complexes, especially in metalorganic molecules or molecular assemblies, wherein the spin state of the metal ion changes between low spin (LS) and high spin (HS) configurations under the influence of external perturbations such as temperature, pressure, light irradiation, magnetic field etc. as shown in Figure 3.1 [1]

Though this phenomena, in principle, may be observed in octahedrally coordinated transition metal complexes with TM ions in  $d^4-d^8$  electronic configurations (c.f. Figure 3.2), the most commonly observed cases are that of octahedrally coordinated iron(II) complexes with  $\text{Fe}^{2+}$  ions in  $3d^6$  electronic configuration. [2] The SCO phenomenon deserves attention due to accompanying changes in magnetic and optical properties, which opens up their application possibilities as optical switches, sensors or memory devices. [3]

To be useful as devices, it is desirable to make the SCO phenomena cooperative implying a spin transition rather than spin crossover, which may happen with

---

This chapter is based on "Cooperativity in spin crossover transition in metalorganic complexes : Interplay of magnetic and elastic interactions" - *Hrishit Banerjee*, Manoranjan Kumar, and Tanusri Saha-Dasgupta, **Phys Rev. B**, **90**, 174433 (2014)

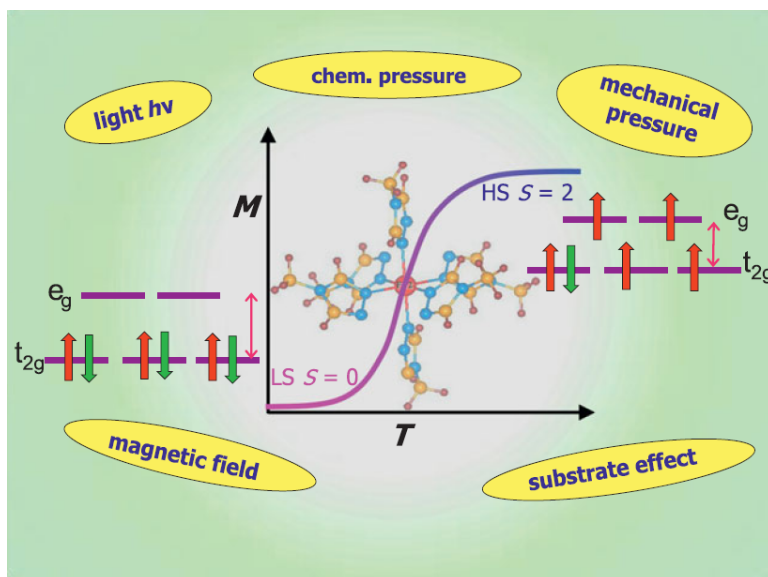


Figure 3.1: Molecular SCO showing a spin state change of the molecular SCO system driven by various external stimuli. Figure adapted from T. Saha-Dasgupta et al [1]

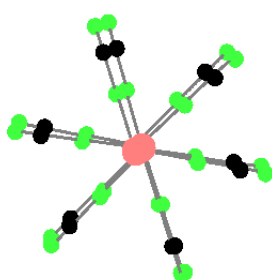
associated hysteresis effect. Cooperativity is a phenomenon displayed by certain systems involving identical or near-identical elements, which act dependently of each other, relative to a hypothetical standard non-interacting system in which the individual elements are acting independently. The hysteresis effect associated with this cooperativity is of immense importance as this confers memory effect to the system. Thus much attention has been paid to the issue of cooperativity in SCO phenomena. In this respect, SCO polymers or 3D coordination compounds are better choices compared to molecular assemblies with isolated molecular units, which even from a purely geometric point of view, are expected to favour long range interaction, increasing cooperativity as seen from Figure 3.3. [4]. Coordination polymeric compounds with repeating coordination entities having extended solid structures are thus assumed to be better choices. The presence of chemical bridges, linking the SCO sites to each other, as in coordination polymers are expected to propagate the interaction between SCO centers more efficiently than that in molecular crystals. In spite of recognising the suitability of such compounds in exhibiting cooperativity there are however several issues that need attention. The prime questions are, (a) understanding the microscopic mechanism *i.e.* what is the driving force for the cooperativity and the hysteresis, and (b) how the cooperativity can be tuned or modified to suit specific device needs. These understandings are expected to provide an advancement to the field in terms of possible commercialization of this technologically important property

1 H																	2 He
3 Li	4 Be											5 B	6 C	7 N	8 O	9 F	10 Ne
11 Na	12 Mg											13 Al	14 Si	15 P	16 S	17 Cl	18 Ar
19 K	20 Ca	21 Sc	22 Ti	23 V	24 Cr	25 Mn	26 Fe	27 Co	28 Ni	29 Cu	30 Zn	31 Ga	32 Ge	33 As	34 Se	35 Br	36 Kr
37 Rb	38 Sr	39 Y	40 Zr	41 Nb	42 Mo	43 Tc	44 Ru	45 Rh	46 Pd	47 Ag	48 Cd	49 In	50 Sn	51 Sb	52 Te	53 I	54 Xe
55 Cs	56 Ba	57-71	72 Hf	73 Ta	74 W	75 Re	76 Os	77 Ir	78 Pt	79 Au	80 Hg	81 Tl	82 Pb	83 Bi	84 Po	85 At	86 Rn
87 Fr	88 Ra	89-103	104 Rf	105 Db	106 Sg	107 Bh	108 Hs	109 Mt	110 Ds	111 Rg	112 Cn	113 Uut	114 Fl	115 Uup	116 Lv	117 Uus	118 Uuo
57 La	58 Ce	59 Pr	60 Nd	61 Pm	62 Sm	63 Eu	64 Gd	65 Tb	66 Dy	67 Ho	68 Er	69 Tm	70 Yb	71 Lu			
89 Ac	90 Th	91 Pa	92 U	93 Np	94 Pu	95 Am	96 Cm	97 Bk	98 Cf	99 Es	100 Fm	101 Md	102 No	103 Lr			

Figure 3.2: SCO materials mostly belong to the first row of transition metal ions.

which relies on critical parameters of cross-over being close to ambient condition, and a large enough hysteresis width.

### Molecular Materials



### Connected Systems

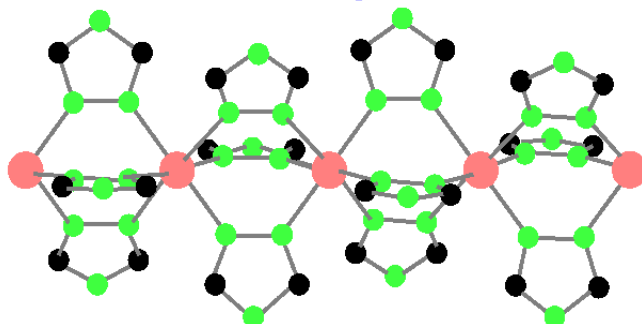


Figure 3.3: From Molecular SCO systems to connected systems like coordination polymers where cooperativity arises.

The above issues are very intimately connected to the materials issue, namely what are the materials to look for which might display cooperative SCO. Indeed a large number of polymeric SCO materials have been synthesized [5] which are found to show cooperativity at the HS-LS transition accompanied by hysteresis effect. 1, 2 or 3-dimensional coordination polymers, which are materials with repeating arrays of coordination entities, are the suitable choices. The dimensionality of a coordination polymer is defined by the number of directions in space the array extends to. Most studied SCO materials showing cooperativity, so far are linear 1-dimensional coordination polymers which are compounds extending through repeating coordination entities in 1-dimension forming chain like

structures, with weak links between individual chains, [6] as shown in right panel of Figure 3.3. The other possibilities are coordination network solids, [6] which are compounds extending through repeating coordination entities in 2 or even 3 dimensions. Strategic crystal engineering makes use of multidentate ligands, connected by spacers, which facilitate to increase the dimensionality from 1-D to 2-D or 3-D. Pressure-induced LS-HS transition in 2-D net was first reported for  $[\text{Fe}(\text{btr})_2(\text{NCS})_2]\cdot\text{H}_2\text{O}$ . [7] The compound consisted of Fe(II) ions linked by btr ( $\rightarrow 4,4'$ -bis-1,2,4-triazole) in two directions producing infinite layers which were connected by means of van der Waals or weak H bonds.  $[\text{Fe}(\text{btr})_3][(\text{ClO}_4)_2]$  [8] represents the first 3-D SCO coordination polymer. [8].

In this chapter we will restrict ourselves to only linear or 1-D coordination polymers, and not extend our discussion to 2-D or 3-D polymers of type  $[\text{Fe}(\text{btr})_2(\text{NCS})_2]\cdot\text{H}_2\text{O}$  or  $[\text{Fe}(\text{btr})_3][(\text{ClO}_4)_2]$ . The case of metal-organic frameworks(MOFs) and hybrid perovskites which may prove to be a promising candidate for showing cooperativity shall be taken up in the next chapter.

Among the linear coordination polymers, or 1-d chain compounds 4R-1,2,4-triazole based Fe(II) chain compounds have been in focus both in early studies and in recent developments.  $[\text{Fe}(4\text{R}-1,2,4\text{-triazole})_3]\text{A}_2.\text{solv}$ , where A is the counterion, and *solv* denotes the solvent molecule, are made up of linear chains in which the adjacent Fe(II) ions in the chain are linked by three triazole ligands. The coordination linkers, which are 1,2,4-triazole blocks form efficient chemical bonds to transmit cooperative effect, leading to hysteresis loop of width ranging  $\approx 2\text{-}20$  K. [9] Sometimes these hysteresis loops are also found to be centered at room temperature. [4] Bimetallic 1-d chain compounds like  $\text{Fe}(\text{aqin})_2(\mu_2\text{-M}(\text{CN})_4)$ ,  $\text{M}=\text{Ni}(\text{II})$  or  $\text{Pt}(\text{II})$ , *aqin*  $\rightarrow$  quinoline-8-amine, have been recently synthesized which were found to show abrupt HS-LS SCO. [10] Novel 1-d Fe(II) SCO coordination polymers with 3,3'-azopyridine as axial ligand has been synthesized which were found to show kinetic trapping effects and spin transition above room temperature. [11] Combination of rigid links and a hydrogen bond network between 1-d Fe(II) chains has been recently shown as a promising tool to trigger SCO with hysteresis loops having widths as large as  $\approx 43$  K. [12]

It is rather easy to understand what drives the spin crossover in the molecular materials. As can be seen from Figure 3.4 there may be an intra ionic transfer of two electrons (taking  $\text{Fe}^{2+}$  as an example) between the  $t_{2g}$  and  $e_g$  orbitals, accompanied by a spin flip due to competition between crystal field splitting  $\Delta$  and Hund's Rule coupling  $J_H$ .

One of the key questions behind the microscopic understanding of SCO in polymeric metalorganic compounds, is what drives the cooperativity and the hysteresis at the intermolecular level of the extended polymeric system. This understanding is important, as this is expected to lead to designing of SCO polymers with improved properties, *i.e.* large hysteresis effect at room temperature - a challenge to meet. There has been attempts by different research groups to

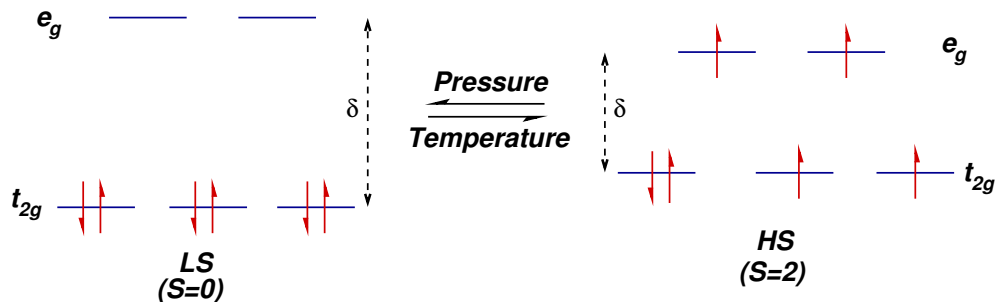


Figure 3.4: Figure showing the intra ionic transfer of electrons due to competition between crystal field splitting and Hund’s rule coupling being driven by temperature or pressure.

account for and explain the origin of this transition and its cooperativity. [13–16] The most prevailing concept is that the responsible factor driving the cooperativity is the long range elastic interaction arising due to interaction between local lattice distortions at each molecular unit. [17] This approach however ignores completely the importance of the long range magnetic interaction that may build up between transition metal ions via super-exchange interaction mediated through the organic ligands connecting the metal centers. The importance of magnetic interaction has been pointed out only recently in a density functional theory based study [18] which estimated the strength of magnetic exchange interaction in a Fe-triazole compound, and found it to be of the same order of magnitude as that of elastic exchange, estimated in similar compounds. To the best of our knowledge, no systematic study exists taking together the effect of magnetic and elastic interactions to study the interplay of the two in development of cooperativity.

In the present chapter, we first study the interplay of the two possible driving mechanisms of cooperativity, namely elasticity and magnetism, employing Monte-Carlo simulation in context of a general model Hamiltonian. Following this, we consider the specific example of Fe-triazole compound, which forms quasi 1-dimensional polymeric structure. Extracting the material specific inputs from DFT, and plugging them into the model Hamiltonian, we further find that the hysteresis at the LS-HS transition in this specific case, is driven entirely by the magnetic super-exchange. Finally we show that the finite temperature ab-initio molecular dynamics calculations within the framework of DFT on this compound, can successfully reproduce the bistable behavior of the compound at the HS-LS transition. The transition temperature is found to be in very good agreement with experimentally measured temperature, establishing the efficiency of DFT method in capturing the material specific details associated with the transition. Our study underlines the significance of magnetic super-exchange in cooperativity in SCO,

which should be treated with equal importance as elastic interaction. In certain cases the magnetic exchange interaction can influence the qualitative description of the cooperativity, not merely the quantitative description.

## 3.2 Monte Carlo study of the Model Hamiltonian

### 3.2.1 The Hamiltonian

There have been a number of studies using model Hamiltonian approaches to study the collective behavior of SCO. These studies primarily focus on the evaluation of thermodynamic quantities like HS fraction. In the first category of the calculations, [19–21] Ising type Hamiltonians, describing the elastic interaction between spin states, LS or HS, in terms of pseudo spin operators  $\sigma_i = -1$  ( $+1$ ) for LS(HS) that interact via the nearest neighbour coupling, were considered. The coupling constants were parameters of the theory. In the second category of calculations, [13–15] free energy of SCO systems have been calculated based on anisotropic sphere model describing the volume and shape changes of the lattice at the transition. Calculations have also been carried out considering a spin-state independent elastic interaction and Ising-like magnetic interaction. [22]

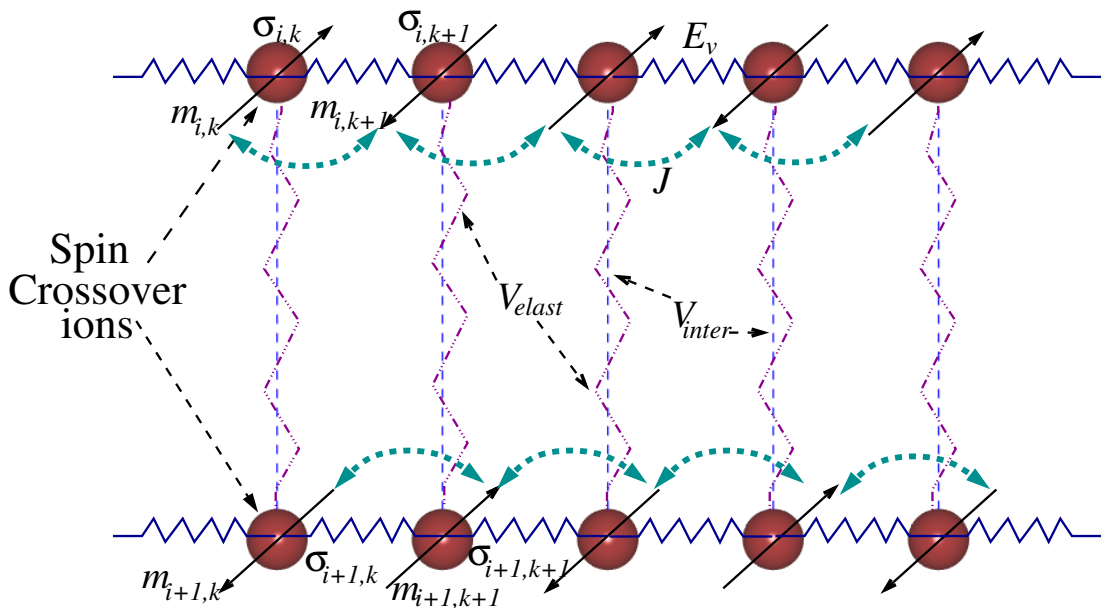


Figure 3.5: Schematic diagram showing the different site labels of the interconnected chains and the respective interactions.

For our study, we used model Hamiltonian set up in the basis of pseudo-spin, describing the elastic part of the interaction and the actual spin, describing the magnetic interaction.

The system consists of linked chains of spin crossover centers labeled with indices  $i$  and  $k$ ,  $i$  denoting the chain number and  $k$  denoting the site number in a given chain (c.f. Figure 3.5). Thus,  $i$  and  $i \pm 1$  denote two neighbouring chains, while  $(i, k)$  and  $(i, k \pm 1)$  denote two neighbouring sites within the same chain  $i$ . The SCO ions in a chain are connected by intra-chain elastic interactions that depend on their spin states given by  $E_v(\sigma_{i,k}, \sigma_{i,k+1})$ , where  $\sigma$  denotes the pseudo-spin describing the spin state of SCO ion,  $\sigma = -1(1)$  for LS(HS). The spin-dependent rigidity of the lattice introduces the spin-phonon coupling in the system, making the elastic interactions dependent on the spin-state of the site. These elastic interactions are assumed to be simple harmonic. Given the highly anisotropic nature of the SCO polymers, the magnetism is described by Ising spin  $S$ , where  $m_{i,k} = S_{i,k}$  with  $m_{i,k} = 0$  for  $\sigma_{i,k} = -1$  (LS state) and  $m_{i,k} = -2, \dots, 2$  for  $\sigma_{i,k} = 1$ , corresponding to the HS  $\text{Fe}^{2+}$  state. The energy of the HS state is assumed to be higher compared to LS state, by an energy difference of  $\Delta$ . The inter-chain interactions, though expected to be weaker compared to intra-chain interactions are crucial for the description of cooperativity in SCO as strict 1-dimensional system cannot support phase transition. Indeed quasi 1-D polymeric SCO chains are not isolated, rather the presence of counter-ions or non-bonded water molecules generate steric as well as electrostatic interactions among the neighbouring chains, which needs to be taken into account in the model Hamiltonian. [20] Thus, the model Hamiltonian taking together the effect of lattice and the spin can be written as,

$$\begin{aligned}
 H = & - \sum_k E_v(\sigma_{i,k}, \sigma_{i,k+1}) \sigma_{i,k} \sigma_{i,k+1} + \Delta \sum_{i,k} \sigma_{i,k} \\
 & - \sum_{i,k} [V_{\perp} \sigma_{i,k} \sigma_{i+1,k} + V_{\parallel} (\sigma_{i,k} + \sigma_{i+1,k})] \\
 & + J \sum_k m_{i,k} m_{i,k+1}
 \end{aligned}$$

where,  $E_v(\sigma_{i,k}, \sigma_{i,k+1}) = \frac{e_{k,k+1}}{2} q_i^2$ ,  $q_i$  being a small displacement, and  $e_{k,k+1} = e_{--}$  for both  $k$  and  $k + 1$  sites in LS,  $= e_{++}$  for both sites in HS, and  $= e_{-+}$  for  $k$  site in LS and  $k + 1$  in HS, or vice-versa (c.f. Figure 3.6). The experimental literature on SCO polymers [23–25] shows  $e_{--} > e_{++}$  which is essentially driven by the size change of the SCO molecular unit upon changing temperature. The nature of the elastic interaction, however, crucially depends on the value of  $e_{-+}$ , which is expected to lie in between  $e_{--}$  and  $e_{-+}$ . The effective elastic interaction turns out to be [20] of ferroelastic nature for  $e_{-+} > \sqrt{e_{++} \times e_{--}}$

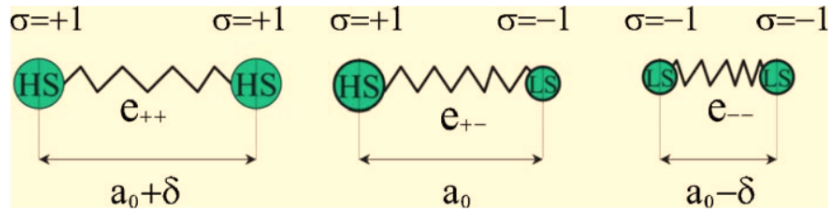


Figure 3.6: Figure showing the spin dependence of the intra chain elastic interaction. Figure adapted from K. Boukheddaden et al [20]

and of antiferroelastic nature for  $e_{+-} < \sqrt{e_{++} \times e_{--}}$ , which is found to have a direct influence on the cooperativity.  $V_{\perp}$  ( $=V_{inter}$  in Figure 3.5) and  $V_{\parallel}$  ( $=V_{elast}$  in Figure 3.5) represent inter-chain interactions arising out of electrostatic and steric interactions, respectively, as discussed in Ref. [20](cf Appendix for full derivation). The Hamiltonian consisting of the first three terms, which involves ligand field energy, and the spin-dependent elastic interaction has been studied in Ref. [20] using transfer matrix technique for the one dimensional intra-chain problem, and treating the inter-chain interactions in a mean field way. The study, however, did not include the magnetic interaction, given by the fourth term of the Hamiltonian, which involves Ising-like antiferromagnetic super-exchange interaction  $J$  acting between two  $\text{Fe}^{2+}$  ions with spin  $S = 2$ . This as pointed out earlier, may play an equally important role as the elastic interaction.

### 3.2.2 Results of Monte-Carlo simulations

The constructed Hamiltonian is solved using Monte Carlo simulation based on standard Metropolis algorithm. Through Monte-Carlo simulation the degeneracies of the spin states are explicitly taken into account in the calculation, taking the approach of a Potts model rather than the simpler Ising case, and definitely not in a mean-field manner in the Hamiltonian as done in most of the other related studies reported in the literature. [16, 20, 22] Finite size scaling in the Monte Carlo simulation results has been checked and a system containing 50 chains, each chain of 50 sites has been found to be large enough to avoid finite size effects.

The Monte Carlo simulations were carried out in the parameter space of  $\Delta$ ,  $e_{++}$ ,  $e_{--}$ ,  $e_{+-}$ ,  $J$ ,  $V_{\parallel}$  and  $V_{\perp}$ . While ideally all these parameters are material-specific and therefore should be extracted from a material-specific quantum-chemical or density functional theory based calculation, at the level of model study, the parameters,  $\Delta$ ,  $e_{--}$ ,  $e_{++}$  were fixed to some typical values,  $\Delta = 20$  K,  $e_{++} = 1$  and  $e_{--} = 20$ . The change in the values of  $\Delta$ ,  $e_{--}$  and  $e_{++}$  does not affect the qualitative behavior, though the quantitative numbers, specially the transition temperature is strongly influenced. The value of  $e_{+-}$  was varied

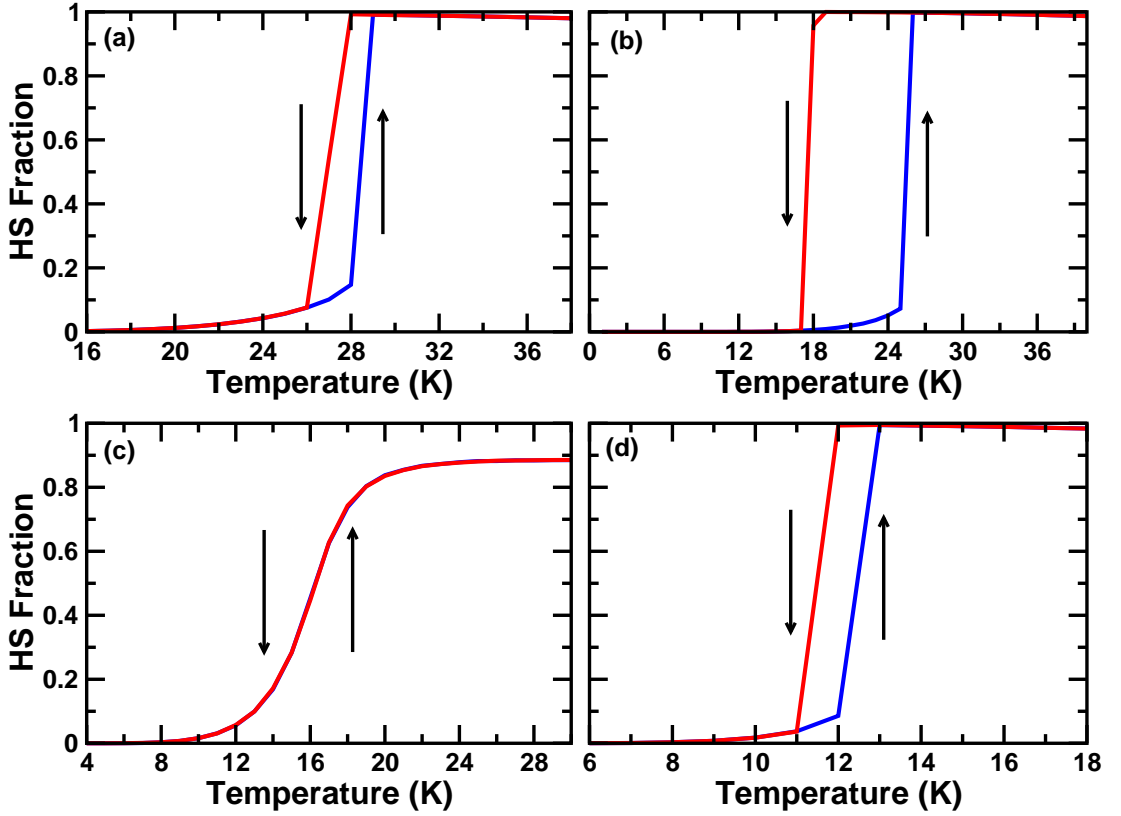


Figure 3.7: High spin fraction plotted as a function of increasing temperature (heating cycle) and decreasing temperature (cooling cycle), for (a) Ferroelastic intrachain coupling with magnetic coupling set to zero, (b) Ferroelastic intrachain coupling with finite, nonzero magnetic coupling, (c) Antiferroelastic intrachain coupling with magnetic coupling set to zero, and (d) Antiferroelastic intrachain coupling with finite, nonzero magnetic coupling.

to simulate the ferroelastic and antiferroelastic regimes respectively. The effect of variation in the strength in interchain interactions has been also studied, they have been found to affect the cooperativity once it sets in. The central quantity, computed to study the SCO transition is the HS fraction, defined as  $\frac{n_{HS}}{N}$ , where  $N$  is the total number of lattice sites, and  $n_{HS}$  is the number of the sites in HS state, averaged over several Monte Carlo sweeps after thermal equilibration. Figure 3.7 summarizes the results of the Monte Carlo study. Figure 3.7(a) shows the results without magnetic term of the Hamiltonian  $H$  with  $e_{+-} = 20$ , which makes the system fall in ferroelastic regime. The system shows hysteresis in the temperature dependence of the HS fraction, with a difference in HS-LS transition temperature between the cooling and heating cycle. The choice of inter-chain interactions  $V_{\perp}$ ,  $V_{\parallel}$  of 10, gives a hysteresis width of  $\approx 1 - 2$  K. Introduction of

magnetic interaction of  $J = 1.375$  K, is found to enhance the width of hysteresis significantly to about 7 K, with shift in transition temperature,  $T_{1/2}$ , where  $T_{1/2}$  is the mid point of the hysteresis region, by  $\approx 5$  K, as shown in Figure 3.7(b). The behavior of the system changes drastically upon changing the value of  $e_{+-}$  to 2, thereby changing to antiferroelastic regime, which is found to kill the hysteresis behavior completely, making the transition more gradual, shown in Figure 3.7(c). The transition temperature is found to decrease from  $\approx 27$  K to  $\approx 16$  K. Remarkably with the choice of  $e_{+-} = 2$ , *i.e.* with antiferroelastic interactions, turning on the super-exchange driven magnetic interaction,  $J$ , brings back the hysteresis. For choice of  $J = 2$  K, the width of the hysteresis is found to be  $\approx 1$  K (cf Figure 3.7(d)). Increase of  $J$  value is found to increase the width of the hysteresis further, following the expectation.

The above results lead us to conclude that for polymeric compounds with antiferroelastic interactions, the cooperative behavior is solely determined by the magnetic super-exchange between the TM ions. In the following, we find that this is indeed the case for a typical Fe-triazole system under study.

### 3.3 First principles study of Cooperativity in SCO of Fe-Triazole

Establishing a general idea for the interactions that might possibly give rise to cooperativity in SCO materials we set out to examine the interactions which may be important in case of a real material from materials specific first principles calculations, There are of course various challenges for this kind of calculations which include

- Strong electron-electron correlation in the open d-shell of the metal center,
- The very complex geometry of these metal organic complexes and the lack of enough crystal structure data,
- Ability to capture electronic and structural changes in these materials under external perturbation.

Our proposed methodology to deal with these challenges to the materials specific calculations is using density functional theory methods combined with the strong correlation problem being addressed by Hubbard  $U$ , and the problem of external perturbation such as temperature being treated using Ab-initio molecular dynamics calculations within the framework of DFT.

For our calculations we choose Fe-triazole polymeric complexes which are a very popular class of SCO materials, which consist of Fe(II) centers, neighbouring Fe's connected through three pyrazole bridges, forming a chain like structure. This creates an octahedral environment of six nitrogen atoms surrounding

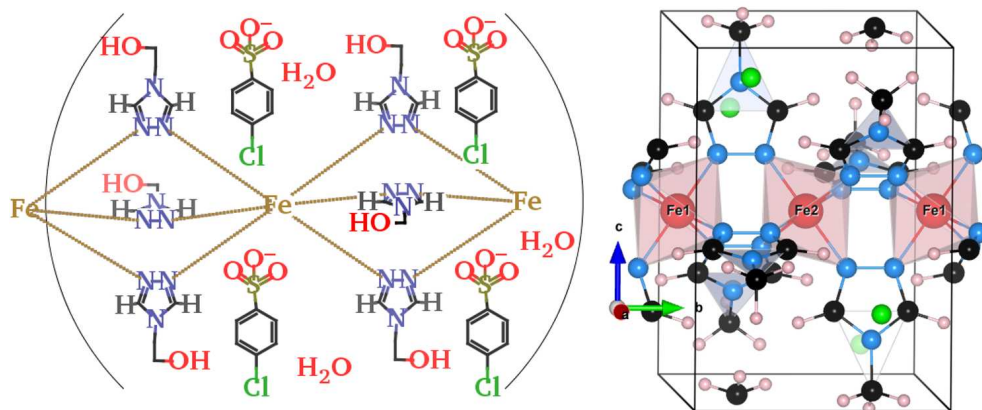


Figure 3.8: Crystal structure of Fe-triazole complexes. (a) The synthesized compound  $\text{Fe}[(\text{hyetrz})_3](4\text{-chlorophenylsulphonate})_2 \cdot 3\text{H}_2\text{O}$ . (b) The simplified computer designed complex. The medium sized blue, and black balls represent N and C, respectively. The small balls represent the H atoms, while the green medium sized balls denote counter-ion,  $\text{F}^-$ .

each Fe center. The counter-ions and non-bonded water molecules separate the chains. A typical example for the  $\text{Fe}[(\text{hyetrz})_3](4\text{-chlorophenylsulphonate})_2 \cdot 3\text{H}_2\text{O}$  (hyetrz denotes 4-(2'-hydroxyethyl)-1,2,4-triazole) complex [26] is shown in left panel of Figure 3.8. The SCO transitions are observed for a wide range of variation in choice of counter-ions and the substituents in pyrazole ring. Unfortunately, hardly any crystal structure data is available due to the nature of the samples, which are polymeric powder insoluble in water and organic solvents. Computational modeling of such complexes, is therefore a challenge. A simplified computer designed crystal structure was used in the DFT study in Ref. [18], in which fluorine was used as counter-ion and the substituent was chosen as  $\text{CH}_3$ . The structure is shown in right panel of Figure 3.8. This computer-designed structure which keeps the local environment of Fe same as the  $\text{Fe}[(\text{hyetrz})_3](4\text{-chlorophenylsulphonate})_2 \cdot 3\text{H}_2\text{O}$  complex, was found to reproduce the SCO behavior of the  $\text{Fe}[(\text{hyetrz})_3](4\text{-chlorophenylsulphonate})_2 \cdot 3\text{H}_2\text{O}$  complex rather well. [18] In absence of other crystal structure data, we used the same crystal structure in our DFT study, as used in Ref. [18] This structure has  $\text{P2}_1/\text{m}$  symmetry with two formula units per unit cell. All the Fe(II) ions are crystallographically equivalent and the Fe-N octahedra are arranged with alternating orientations along the chain direction.

For the DFT calculations, we used the plane wave based basis set with the all-electron potential given by Projector Augmented Wave (PAW) method [27] included by fitting the pseudo-potential, as implemented in the Vienna Ab-initio Simulation Package (VASP). [28] The exchange correlation functional was chosen

to be that of generalized gradient approximation (GGA) implemented following the method of Perdew-Burke-Ernzerhof(PBE). [29] For the plane wave calculation 500 eV plane wave cutoff was used. A k-point mesh of  $2 \times 4 \times 2$  in the Brillouin zone was used for self-consistent calculations. The plane wave cutoff and the k-point mesh have been checked for convergence of obtained results. In order to have a correct description of the insulating solution, specially in high-spin state, the missing correlation beyond GGA was included in the form of GGA+ $U$  calculation, [30] with choice of  $U = 4$  eV and  $J_H = 0.8$  eV. The variation within  $3 \text{ eV} \leq U \leq 6 \text{ eV}$  is found to keep the qualitative result the same.

### 3.3.1 Electronic structure of Fe-triazole

From the LMTO calculations carried out previously in our group [1] thermally frozen structures of this Fe- triazole compound was constructed and two different spin states corresponding to two different Fe-N bond-lengths were identified. It was observed that for the structure with Fe-N bond-length = $2.0\text{\AA}$  the magnetic state of the system is the low spin (LS) state, and for the structure with Fe-N bond-length = $2.2\text{\AA}$  the magnetic state of the system is the high spin (HS) state.

Here we calculate by an ab-initio approach within the framework of density functional theory, the Density of States(DOS) for the two different structures one with Fe-N bond-length= $2.0\text{\AA}$  and another with Fe-N bond-length= $2.2\text{\AA}$ . From the non spin-polarized DOS (not shown here for the sake of brevity) it is seen in both the structures that near the Fermi level the major contribution to the density of states is from the Fe- $3d$  orbitals, with an admixture of contributions from F- $p$ , N- $p$  and C- $p$  orbitals. However non spin-polarised calculations do not offer any information as regards the spin state of the system.

In case of the spin polarised partial DOS showing Fe- $3d$  orbitals for the structure with Fe-N bond-length= $2.0\text{\AA}$  (top panel Figure 3.9) we see that in the two different spin channels the DOS are exactly identical. Also it is seen from the spin-polarised self consistent field calculations that the total magnetic moment in this case turns out to be equal to  $0\mu_B$ , thus confirming in this case, the system is in the low spin (S=0) state.

In case of the DOS for the structure with Fe-N bond-length= $2.2\text{\AA}$  (bottom panel Figure 3.9) we see that in the two different spin channels the DOS have a considerable splitting. This structure therefore, can be confirmed to be in the magnetic state, and from the spin-polarized self consistent field calculations, total magnetic moment of the system is observed to be equal to  $8\mu_B$  and thus we can conclude that Fe(II) ion is in the high spin state S=2, with two Fe(II) ions in the unit cell.

The major contribution to the splitting in total DOS is by Fe (since Fe is the magnetic element in the compound) with lesser but finite contributions from other

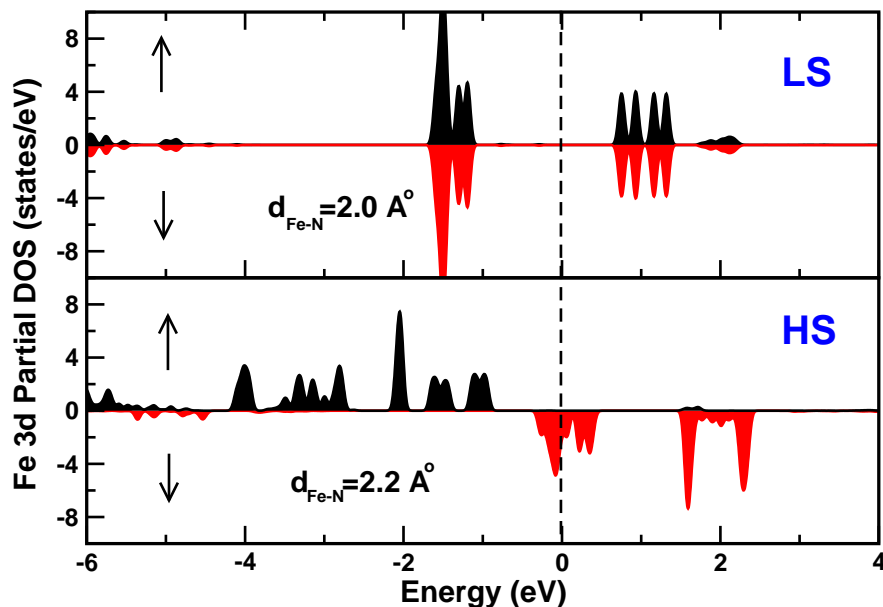


Figure 3.9: GGA Fe-3d partial DOS. Top panel shows DOS for Fe-N bond-length=2.0Å and bottom panel shows DOS for Fe-N bond-length=2.2Å. Black shaded area shows the up spin channel and red shaded area shows the down spin channel.

elements too. We, however, notice that this calculation leads to a half metallic situation, with finite (zero) DOS at Fermi energy in down (up) spin channel while in reality the compound is insulating.

To rectify this, subsequent calculations (Figure 3.10) were performed for Fe-N bond-length=2.2Å with Hubbard  $U$  included in the calculations. The Hubbard  $U$  is required in case of strongly correlated electron systems. For Fe-3d orbitals the electrons are strongly correlated electrons and without inclusion of the Hubbard  $U$  correct ground state electronic structure cannot be obtained. The inclusion of Hubbard  $U$  is not required in case of the LS state structure since it behaves as an insulator already at the level of GGA calculation (hence LS DOS with GGA+ $U$  is not shown here). The band gap in LS and HS configuration are found to be  $\sim 2.1$  eV and  $\sim 1.6$  eV respectively.

Thus we see a spin state change happens with change in Fe-N bondlength which is driven by temperature.

Given the experimental observation of cooperativity in the experimentally studied Fe-triazole complex, the natural questions to ask are, what is the primary driving force behind cooperativity in this system? Is it driven by conventional elastic interactions? What is the role of magnetic super-exchange interactions, which is estimated [18] to be large ( $\approx 22$  K) in this complex.

In the next step, we therefore extracted the elastic as well as magnetic inter-

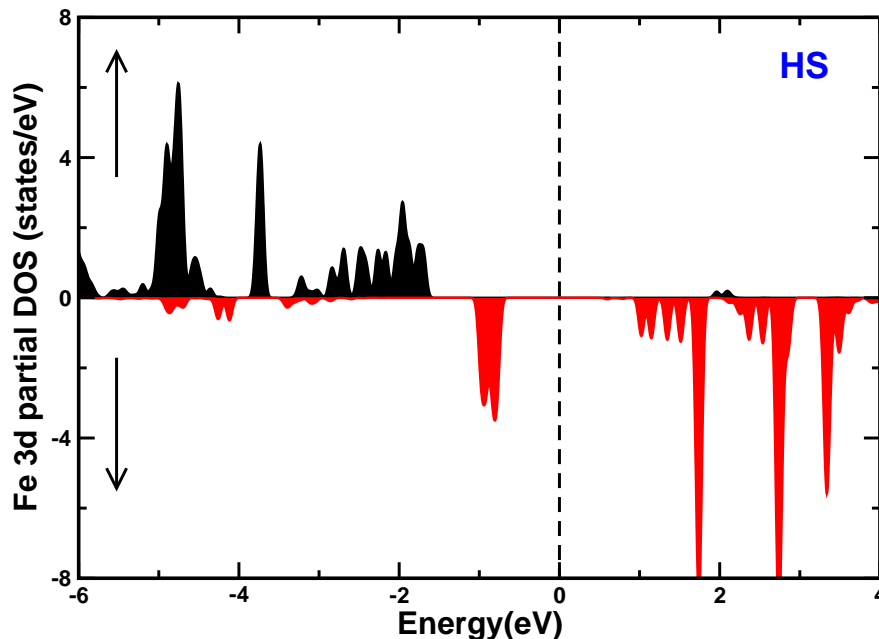


Figure 3.10: GGA+ $U$  Fe-3d partial DOS. DOS plotted for Fe-N bond-length=2.2Å corresponding to the HS state. Black shaded area shows the up spin channel and red shaded area shows the down spin channel.

actions of the studied complex from DFT calculations, and carried out the Monte Carlo study plugging in these parameters in the model Hamiltonian.

### 3.3.2 Monte Carlo results with material-specific parameters of Fe-triazole

One of the crucial parameters in the model Hamiltonian study, is the spin-state dependent elastic interaction. To estimate the spin-state dependent elastic interactions, the following steps were followed. Analysis of the optimized crystal structure data shows that the LS state is stabilized for average Fe-N bondlength of 2.0 Å or less, while the HS state is stabilized for Fe-N bondlength of 2.2 Å or more. Following this, model structures were constructed by considering regular FeN<sub>6</sub> octahedra and setting the Fe-N bondlength at 2.0 Å and 2.2 Å to mimic the LS-LS and HS-HS state of neighbouring FeN<sub>6</sub> units, respectively. To model the LS-HS situation, chains of alternating FeN<sub>6</sub> octahedra with Fe-N bondlengths of 2.0 Å and 2.2 Å, was created. Considering these three model structures, the Fe-N bondlength was varied by small amount around the equilibrium bondlength, maintaining the harmonic oscillation limit. The obtained energy versus displacement curves for the three cases are shown in Figure 3.11. A parabolic fit through the data points provide the estimates of the elastic interactions. Setting the

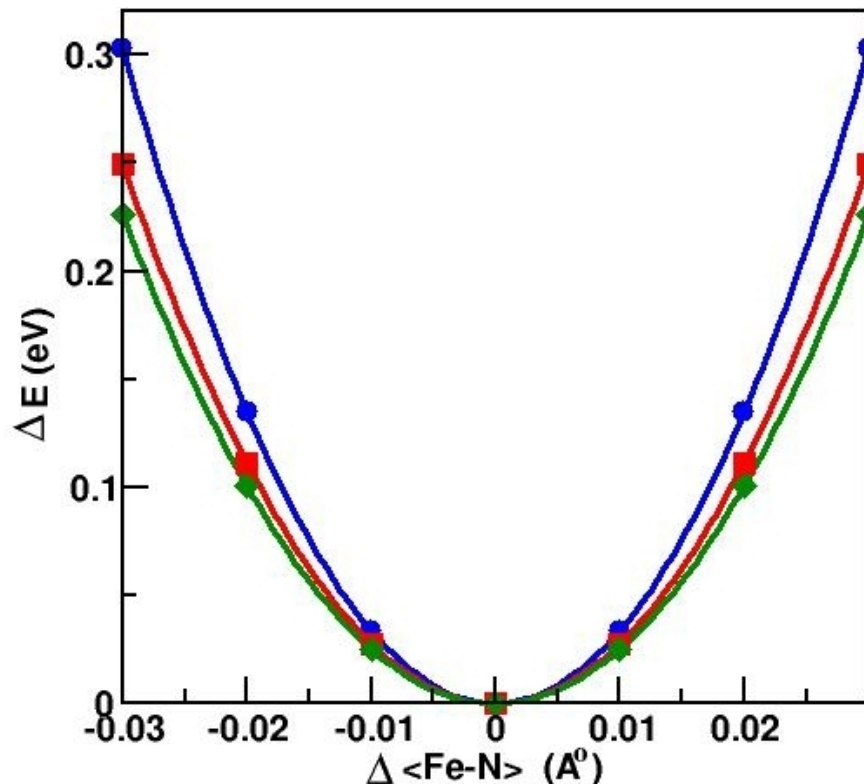


Figure 3.11: The variation of total energy as a function of variation of Fe-N bondlength about the equilibrium value, for three different configurations, LS-LS (circles), LS-HS (squares) and HS-HS (diamonds). Solid lines are fit to data points.

small displacement,  $q$  as  $0.005 \text{ \AA}$ , this gives  $E_v(++ ) = 72 \text{ K}$ ,  $E_v(-- ) = 101 \text{ K}$  and  $E_v(+ - ) = 80 \text{ K}$ . As mentioned before, it is known from experimental literature [23–25] that the lattice is more rigid in the low temperature phase (LS) than at high temperature (HS) phase. The ab-initio estimates of elastic interactions for Fe-triazole reconfirms this trend, establishing the confidence in the followed procedure. Very interestingly we note that the value of  $E_v(+ - )$  turns out to be such that it makes the effective elastic interaction to be of antiferroelastic type. This makes us conclude that the observed cooperativity in this real system, is driven entirely by magnetic interactions.

The Fe-Fe magnetic exchange interactions were obtained by carrying out GGA+ $U$  total energy calculations of parallel and antiparallel orientations of Fe spin considering the high spin crystal structure. The energy difference between the two spin configurations gave rise to an antiferromagnetic super-exchange interaction of magnitude 18 K, in good agreement with the values reported previously. [18] While the DFT calculation captures the elastic and magnetic properties

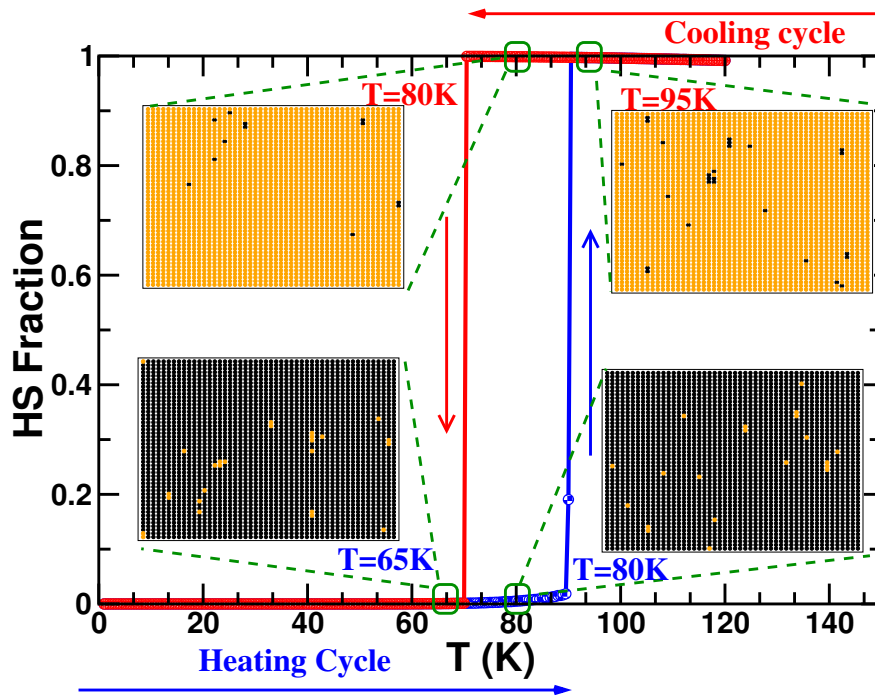


Figure 3.12: High spin fraction plotted as a function of increasing and decreasing temperature calculated with DFT derived elastic and magnetic interactions corresponding to that of Fe-triazole. The insets show the snap-shots of pseudo-spin configurations with LS (HS) state shown in black (yellow), at two different temperatures (80 K and 95 K) in cooling cycle, and two different temperatures (65 K and 80 K) in heating cycle. At  $T = 80$  K, in the phase co-existence region, the configuration is HS or LS dominated, depending on the heating or cooling cycle.

rather well, the accurate estimate of the energy difference between LS and HS state of an isolated molecular unit is a challenge due to poor representation of the excited state properties within DFT, which is well known in literature. A possible remedy would be to use time-dependent DFT [33] or quantum-chemical calculations based on multi-determinantal wavefunctions, [34] both of which are computationally very expensive and beyond the scope of the present study on an extended polymeric system. The parameter,  $\Delta$  was therefore chosen to have a typical value of 130 K, estimated in literature in similar systems from heat capacity measurements. [35] The inter-chain interactions are kept as a fraction of  $\Delta$  in accordance with model study described in section 3.2. The measured susceptibility in  $\text{Fe}[(\text{hyetrz})_3](4\text{-chlorophenylsulphonate})_2 \cdot 3\text{H}_2\text{O}$  complex showed a hysteresis of width 20 K and a transition temperature of 80 K. We find that calculation of temperature dependent HS fraction plugging in the material specific parameters obtained from the DFT calculation of the simplified computer

designed Fe-triazole complex, gives rise to a very similar scenario, as shown in Figure 3.12. The insets in Figure 3.12 show the snapshots of the MC runs of the simulations along the heating and cooling cycle, at temperatures 65 K and 80 K for heating path and at temperatures 95 K and 80 K for the cooling path. At the temperature of 80 K, the snapshot configuration of pseudo-spins shows sites with primarily HS (LS) configurations for the cooling (heating) cycle, proving the signature of bistability in this material and hence also showing that there indeed is a hysteresis loop in the physical properties like magnetic susceptibility in these materials.

### 3.4 Finite temperature study with Ab initio molecular dynamics

In order to further probe and establish from a purely first principles basis, the presence of the hysteresis region by showing a certain bistability exists in the temperature driven SCO in the above mentioned Fe-triazole compounds, we carried out rigorous Ab initio Molecular Dynamics (AIMD) calculations as implemented in VASP. [28] Ideally, given the problem, the calculations should be carried out in NPT ensemble. However, for technical reason, we decided to carry out the calculations in NVT ensemble. For this purpose, the structures were initially optimized at 0 K at different volumes which correspond to the thermal expansion of Fe-triazole at the studied temperatures in AIMD study. Starting from the  $T = 0\text{K}$  optimized structures, the temperature was increased using a Berendsen thermostat [31] with a time step of 1 fs for each molecular dynamics step and 600 temperature steps between the 0 K and the final temperature. At the final step the system was thermalized using an NVT ensemble for a time duration of 1 ps. A canonical ensemble is simulated in this case using the algorithm of Nosé. The Nosé mass controls the frequency of the temperature oscillations during the simulation. In our calculation a Nosé-mass corresponding to period of 40 time steps was chosen. The Nosé-mass was set such that the induced temperature fluctuation show approximately the same frequencies as the typical 'phonon'-frequencies for our specific system. The frequency of the approximate temperature fluctuations induced by the Nosé-thermostat is calculated. At the end, a NVE ensemble thermalization was carried out to accurately determine the free energy of the system at the final temperature. The free energy here is calculated in this microcanonical ensemble. This is a constant energy molecular dynamics simulation. The computed Feynman-Hellman forces serve as an acceleration acting on the ions. The total free energy including the free electronic energy + Madelung energy of ions + kinetic energy of ions is calculated. The above mentioned calculations were carried out constraining the total moment of the system, corresponding to LS state ( $0 \mu_B$ ) and the HS state ( $8 \mu_B$  corresponding to two  $\text{Fe}^{2+}$  ions in the unit

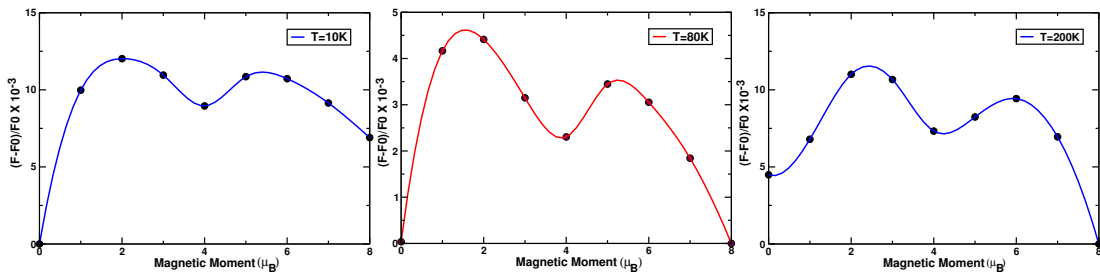


Figure 3.13: Relative change in free energy plotted as a function magnetic moment in the cell for (a)  $T = 10\text{K}$ , (b)  $T = 80\text{K}$ , (c)  $T = 200\text{K}$ . The relative change is measured with respect to the global minima of the free energy ( $F_0$ ).

cell each having a HS magnetic moment of  $4 \mu_B$ ), and seven different intermediate spin states. In each of the calculations, the positions of all unconstrained atoms were relaxed within AIMD until the forces became less than  $0.01 \text{ eV}/\text{\AA}$ , and the change in bond lengths less than  $10^{-3} \text{ \AA}$ .

The temperatures at which AIMD calculations were carried out, were chosen to be 10 K, 80 K and 200 K. This choice was driven by the measured susceptibility on  $\text{Fe}[(\text{hyetrz})_3](4\text{-chlorophenylsulphonate})_2 \cdot 3\text{H}_2\text{O}$  complex, which showed a SCO transition at a temperature of  $\approx 80 \text{ K}$  with a width of  $\approx 20 \text{ K}$ . The AIMD calculations at three different temperatures, fixing the total magnetic moment, resulted in three different free energy profiles, as a function of varying magnetic moments in the unit cell. The results are summarized in Figure 3.13. We find that all three free energy profiles exhibit minima either at total magnetic moment of  $0 \mu_B$ , corresponding to LS state of the system, or at  $8 \mu_B$ , corresponding to HS state of the system. We find that at  $T = 10 \text{ K}$ , the LS state is a global minima while the HS state is a local minima, the reverse being true for  $T = 200 \text{ K}$ , supporting the temperature induced spin state transition in this complex. Interestingly, at  $T = 80\text{K}$ , we find both LS and HS states to be having same free energies, *proving the existence of bistability* in this compound. Remarkably, we find that our AIMD results are in very good agreement with the experimental scenario, though the calculations have been carried out in a simplified crystal structure. This in turn, proves the efficiency of the AIMD in capturing correctly the temperature driven SCO transitions, together with the cooperativity. Interestingly in all the studied temperatures, the free energy profile shows a local minima at a total magnetic moment of  $4 \mu_B$  with  $2 \mu_B$  moment contributed by each of the two  $\text{Fe}^{2+}$  ions in the unit cell. This corresponds to intermediate spin state of  $\text{Fe}^{2+}$  with  $S=1$ . Tuning the value of  $E_v(+)$  it might be possible to achieve intermediate spin (IS) state as the minimum energy state at an intermediate temperature range. This would make the SCO transition a two-step transition from  $\text{LS} \rightarrow \text{IS} \rightarrow \text{HS}$ , as reported for Fe-Nb based coordination polymer under pressure [32]. Thus, it

might be worthwhile to study the SCO transition in Fe-triazole complexes under pressure.

### 3.5 Conclusion

In conclusion, our MC study based on model Hamiltonian firmly establishes the important role of magnetic super-exchange interaction acting between the TM ion centers in the cooperativity in spin transition in polymeric metalorganic complexes. They turn out to be equally important as the elastic interaction, popularly accepted as the main cause of cooperativity in polymeric SCO systems. Depending on the nature of the spin-dependent elastic interaction, which depends on the nature of the spin-phonon coupling, the magnetic interaction can contribute to the development of cooperativity in a quantitative or a qualitative manner. In case of ferro type elastic interaction, the magnetic interaction helps in enhancing the hysteresis effect, set-up already by the elastic interaction, thus being important for the quantitative description of the cooperativity in SCO. In case of antiferro nature of elastic interaction, the magnetic interaction plays the deciding role in driving the hysteresis the system, putting the elastic interaction to a back seat. Taking the real example of a Fe-triazole complex, we demonstrate the existence of bistability in this compound through Ab-initio Molecular Dynamics simulation, which is known from experimental measurement on similar compounds. [18] This establishes the capability of ab-initio technique to capture the bistability accurately. Extraction of the material specific parameters for this Fe triazole complex, shows the elastic interaction to be of antiferroelastic nature. The observed bistability in this system, is therefore totally driven by the magnetic exchange interaction. The computed transition temperature, and the width of the hysteresis are found to be in reasonable agreement with that of the measured susceptibility reported for the similar compound. [18] Our study highlights the microscopic role of magnetic exchange interaction in cooperativity and bistability in the class of Fe-triazole SCO polymers. Similar study may be extended to other coordination metalorganic compounds to find out the applicability of magnetic interaction driven cooperativity in a general class of metalorganic polymeric materials.

## 3.6 Appendix

**Intra-chain Elastic Interactions** A model consisting of two-level atoms and elastic interaction between them is considered. The two levels of the atom are expressed by fictitious spins  $\sigma = \pm 1$ . The state  $\sigma = 1$  denotes the HS state, which is  $g_H$ -fold degenerate, and the state  $\sigma = -1$  denotes the LS state, which is  $g_L$ -fold degenerate,

$$H^{spin} = \sum_{i=0}^{N+1} \frac{\Delta_{eff}}{2} \sigma_i, \quad (3.1)$$

where  $\Delta_{eff} = \Delta k_B T \ln(g)$ . Here,  $g = \frac{g_H}{g_L}$  is the degeneracy ratio,  $\Delta$  is the ligand field energy, and  $T$  is the temperature.

In the case of intra-chain interactions, the fictitious spins are coupled by spin-dependent intra-chain elastic interactions, given by the Hamiltonian,

$$H^{phonon} = \sum_{i=0}^N \frac{e_{i,i+1}}{2} (u_{i+1} - u_i)^2, \quad (3.2)$$

where  $u_i = x_i - x_i^0$  is the deviation from equilibrium position,  $x_i$  is the position of the  $i^{th}$  spin,  $x_i^0$  is the equilibrium position, and,

$$x_j^0 = \sum_{j=0}^{i-1} (a_0 + \frac{\delta}{2} [\sigma_j + \sigma_{j+1}]), \quad (3.3)$$

where  $\delta$  is the difference in HS and LS volume, and  $a_0$  is the average distance between neighbouring HS-LS molecules.

To include the spin dependence of the elastic interaction the following expression was considered,

$$e_{i,i+1} = A + B(\sigma_i + \sigma_{i+1}) + C, (\sigma_i \sigma_{i+1}) \quad (3.4)$$

where,

$$A = \frac{1}{4}(e_{++} + 2e_{+-} + e_{--}),$$

$$B = \frac{1}{4}(e_{++} - e_{--}),$$

$$C = \frac{1}{4}(e_{++} - 2e_{+-} + e_{--}),$$

which yield with the values of A,B,C plugged into the equation, the proper spin dependence of the elastic interaction, i.e., when

$e_{i,i+1} = e_{++}$  for HS-HS interaction,

$e_{i,i+1} = e_{+-}$  for HS-LS interaction,

$e_{i,i+1} = e_{--}$  for LS-LS interaction.

Thus the Hamiltonian becomes:

$$H^{phonon} = \frac{1}{2} \sum_{i=0}^N [A + B(\sigma_i + \sigma_{i+1}) + C(\sigma_i \sigma_{i+1})] q_i^2, \quad (3.5)$$

where  $q_i = u_{i+1} - u_i$ .

The kinetic energy part of the Hamiltonian is given by,

$$H^{KE} = \sum_{i=0}^{N+1} \frac{p_i^2}{2m_a}, \quad (3.6)$$

where  $m_a$  is the atom mass, which will be taken as equal to 1 in all the calculations. So the Total Hamiltonian is

$$\mathcal{H} = H^{spin} + H^{phonon} + H^{KE}. \quad (3.7)$$

Solving we obtain the effective Hamiltonian in the form of an Ising Hamiltonian as,

$$\tilde{\mathcal{H}} = -\tilde{J} \sum_{i=0}^N \sigma_i \sigma_{i+1} - \frac{\tilde{h}}{2} \sum_{i=0}^N (\sigma_i + \sigma_{i+1}) + \left[ \frac{\Delta_{eff}}{4} \times (\sigma_0 + \sigma_{N+1}) \right] + E_0, \quad (3.8)$$

where,

$$\tilde{J} = k_B T \times K,$$

$$\tilde{h} = -\frac{\Delta_{eff}}{2} + 2Lk_B T,$$

and

$$E_0 = k_B T \ln(2\pi I^2 k_B T).$$

Here I, K, and L are given respectively by the expressions,

$$I = \sqrt{2\pi k_B T} (e_{++} \times e_{--} \times e_{+-}^2), \quad (3.9)$$

$$K = \frac{1}{8} \ln\left(\frac{e_{+-}^2}{e_{++} \times e_{--}}\right), \quad (3.10)$$

$$L = \frac{1}{8} \ln\left(\frac{e_{--}}{e_{++}}\right). \quad (3.11)$$

Using the coupling  $e_{+-}$  as a variable to tune the coupling parameter, with  $e_{++} \leq e_{+-} \leq e_{--}$ , it appears that the effective interaction is such as,

$$-\frac{k_B T}{4} \ln \sqrt{\frac{e_{--}}{e_{++}}} \leq \tilde{J} \leq \frac{k_B T}{4} \ln \sqrt{\frac{e_{--}}{e_{++}}}. \quad (3.12)$$

The effective elastic interaction turns out to be of ferroelastic nature for  $e_{+-} > \sqrt{e_{++} \times e_{--}}$  and of antiferroelastic nature for  $e_{+-} < \sqrt{e_{++} \times e_{--}}$ .

**Inter-chain Elastic interaction** In some cases it happens at times that in SCO polymers, the chains are not isolated, and steric or/and electrostatic interactions are present between neighbouring chains. As for example in Fe-triazoles water molecules and counter anions are present between the polymeric chains. These are responsible for the steric or/and electrostatic interactions. The Hamiltonian is then written in the following form:

$$\mathcal{H} = \sum_{i=1}^N \mathcal{H}_i^{\text{phonon}} + \sum_{i,k}^N \mathcal{H}_{i,k}^{\text{phonon-inter}}, \quad (3.13)$$

where  $\mathcal{H}_{i,k}^{\text{phonon-inter}}$  is given by,

$$\mathcal{H}_{i,k}^{\text{phonon-inter}} = \frac{E_{\text{inter}}}{2} (u_{i+1,k} - u_{i,k})^2, \quad (3.14)$$

where  $i$  denotes the index of the chain and  $k$  denote the specific atom in the  $i^{\text{th}}$  chain. Here spin dependence of elastic inter-chain interaction is not considered. However the form of equation (3) is used in this case neglecting the constant term A. B is rewritten as  $e_{\perp}$  and C is rewritten as  $J_{\perp}$ . Thus we arrive at the form,

$$E_{\text{inter}} = e_{\perp}(\sigma_{i,k} + \sigma_{i+1,k}) + J_{\perp}\sigma_{i,k}\sigma_{i+1,k} \quad (3.15)$$

Thus the Hamiltonian has the form,

$$\mathcal{H}^{\text{phonon-inter}} = \frac{1}{2} \sum_{i,k}^N [e_{\perp}(\sigma_{i,k} + \sigma_{i+1,k}) + J_{\perp}\sigma_{i,k}\sigma_{i+1,k}](u_{i+1,k} - u_{i,k})^2, \quad (3.16)$$

or,

$$\mathcal{H}^{\text{phonon-inter}} = \frac{1}{2} \sum_{i,k}^N [e_{\perp}(\sigma_{i,k} + \sigma_{i+1,k}) + J_{\perp}\sigma_{i,k}\sigma_{i+1,k}]q_{i,k}^2, \quad (3.17)$$

where  $q_{i,k} = u_{i+1,k} - u_{i,k}$ .

For the weak inter-chain interaction where spin dependence is not explicitly considered we have taken this form of the Hamiltonian when developing our code mapping  $e_{\perp} \rightarrow V_{\text{elast}}$  and  $J_{\perp} \rightarrow V_{\text{inter}}$ . Thus in our case since for the inter chain interaction part we are not following the previous scheme for spin dependence and taking the Hamiltonian of the form of eqn. 3.8. Here for us  $e_{\perp} \rightarrow V_{\parallel}$  is the interchain elastic constant which takes care of the steric strains between the two chains, and  $J_{\perp} \rightarrow V_{\perp}$  is the electronic interaction between two atoms belonging to neighbouring chains which takes care of the electrostatic interactions between two polymeric chains.

# Bibliography

- [1] T. Saha-Dasgupta and P. Oppeneer, *MRS Bulletin* **39**, 614 (2014).
- [2] S. Brooker, J. A. Kitchen, *Dalton Trans.* **36** 7331, (2009); S.-I. Ohkoshi , K. Imoto , Y. Tsunobuchi , S. Takano , H. Tokoro , *Nat. Chem.***3**, 564 (2011); G. J. Halder , C. J. Kepert , B. Moubaraki , K. S. Murray , C. S. Cashion , *Science* **298**, 1762 (2002).
- [3] S. Cobo *et al.*, *Angew. Chem.* **45**, 5786 (2006).
- [4] O. Kahn and C Jay Martinez, *Science* **44**, 279 (1998).
- [5] P. Gütlich ,A. Hauser and H. Spiering, *Angew. Chem. Int. Ed. Engl.* **33**, 2024 (1994).
- [6] Batten, S.R.; Champness, N.R.; Chen, X.M.; Garcia-Martinez, J.; Kitagawa, S.; Ohrstorm, L.; O’Keeffe, M.; Suh, M.P.; Reedijk, J. Terminology of metal-organic frameworks and coordination polymers (IUPAC Recommendations 2013), 2013-07-29.
- [7] Ozarowski, A.; Shunzhong, Y.; McGarvey, B.R.; Mislankar, A.; Drake, J.E. *Inorganic Chemistry* **1991**, *30*, 3167–3174.
- [8] Yann-Garcia, N.N.A.; Naik, A.D. *Chimia* **2013**, *67*, 411–418.
- [9] Garcia, Y.; Niel, V.; Muñoz, M.C.; Real, J.A., In *Spin Crossover in Transition Metal Compounds I*; Gütlich, P.; Goodwin, H., Eds.; Springer Berlin Heidelberg: Berlin, Heidelberg, 2004; pp. 229–257.
- [10] Setifi, F.; Milin, E.; Charles, C.; Thetiot, F.; Triki, S.; Gomez-Garca, C.J. *Inorganic Chemistry* **2014**, *53*,97-104.
- [11] Schonfeld, S.; Lochenie, C.; Thoma, P.; Weber, B. *CrystEngComm* **2015**, *17*,5389-5395.
- [12] Bauer, W.; Lochenie, C.; Weber, B. *Dalton Trans.* **2014**, *43*, 1990–1999.

- [13] N. Willenbacher and H. Spiering, *J. Phys. C: Solid State Phys.* **21**, 1423 (1988).
- [14] H. Spiering and N. Willenbacher, *J. Phys.: Condens. Matter* **1**, 10089, (1989).
- [15] H. Spiering, K. Boukheddaden, J. Linares and F Varret, *Phys. Rev. B* **70**, 184106 (2004).
- [16] M. Nishino, K. Boukheddaden, Y. Konishi and S. Miyashita, *Phys. Rev. Lett.* **98**, 247203 (2007).
- [17] H. Spiering *et al.* *Chem. Phys.* **68**, 65 (1982).
- [18] Harald O Jeschke, L Andrea Salguero, Badiur Rahaman, Christian Buchsbaum, Volodymyr Pashchenko, Martin U Schmidt, Tanusri Saha-Dasgupta, and Roser Valenti *New Journal of Physics* **9**, 448 (2007).
- [19] J. Wajnflasz and R. Pick, *J. Physique IV* **32**, C1 (1971).
- [20] K. Boukheddaden, S. Miyashita and M. Nishino, *Phys. Rev. B* **75**, 094112 (2007).
- [21] K. Boukheddaden, J. Linares, R. Tanasa and C. Chong, *J. Phys.: Condens. Matter* **19**, 106201 (2007).
- [22] C. Timm, *Phys. Rev. B* **73**, 014423 (2006).
- [23] E. König, *Struct. Bonding Berlin* **76**, 51 (1991).
- [24] A. Hauser *et al.*, *Coord. Chem. Rev.* **471**, 190 (1999).
- [25] R. Zimmermann and E. König, *J. Phys. Chem. Solids* **38**, 779 (1977).
- [26] Y. Garcia, V. Niel, M. Muñoz and J. Real, *Top. Curr. Chem.* **233**, 229 (2004).
- [27] P. E. Blöchl, *Phys. Rev. B* **50**, 17953 (1994).
- [28] G. Kresse and J. Furthmuller, *Phys. Rev. B* **54**, 11169 (1996).
- [29] J. P. Perdew, K. Burke, and M. Ernzerhof, *Phys. Rev. Lett.* **77**, 3865 (1996).
- [30] V.I. Anisimov , J. Zaanen , O.K. Andersen , *Phys. Rev. B: Condens. Matter* **44**, 943 (1991).
- [31] H. J. C Berendsen, J. P. M. Postma, W. F. van Gunsteren, A. DiNola, J. R. Haak, *Journal of Chemical Physics* **81**, 3684 (1984).

- 
- [32] K. Tarafder, S. Kanungo , P.M. Oppeneer , T. Saha-Dasgupta , Phys. Rev. Lett. **109**, 077203 ( 2012 ).
- [33] Y. Qu, Inter. J. Quan. Chem. **113**, 943 (2013).
- [34] M. Kepenekian, B. Le Guennic, V. Robert, J. Am. Chem. Soc. **131**, 11498 (2009); M. Kepenekian, J. Snchez Costa, B. Le Guennic, P. Maldivi, S. Bonnet, J. Reedijk, P. Gamez, V. Robert, Inorg. Chem. **49**, 11057 (2010).
- [35] A. Sava *et al.* Adv. Mater. **5**, 977 (2003).

# Chapter 4

## Cationic Effect on Pressure driven Spin-State Transition and cooperativity in Hybrid Perovskites

### 4.1 Introduction

Metal organic framework (MOF) complexes, built from inorganic and organic components, form a vibrant area of research which has undergone a rapid and immense growth in the last decade. [1, 2] In Figure 4.1 in the left panel a Scanning Electron Microscope (SEM) image of a MOF crystal is seen. From the right panel of the same figure which shows the schematic diagram of a MOF crystal it is seen that MOFs can be of many types and various different connectivity ranging from node connectivity, to long rods in 1 dimension and complete networks in 3 dimensions. Most of the study in this field are focused on open systems with large porous regions [3–5] having potential applications in gas storage, [6] chemical sensing, [7] catalysis [8], drug delivery [9], bio mimetic mineralization [9] etc. In recent times however much of the attention has been directed towards dense hybrid frameworks with limited porosity. Some of these dense hybrid compounds adopt the celebrated perovskite geometry of general formula  $ABX_3$ . [10] This has opened up an emerging research area on hybrid perovskites, parallel to the well-established field of inorganic perovskite oxides. Hybrid perovskites

---

This chapter is based on "Cationic Effect on Pressure driven Spin-State Transition and cooperativity in Hybrid Perovskites", *Hrishit Banerjee*, Sumilan Banerjee, Sudip Chakraborty, Tanusri Saha-Dasgupta, **Chemistry of Materials**, **28(22)**, **8379-8384 (2016)**

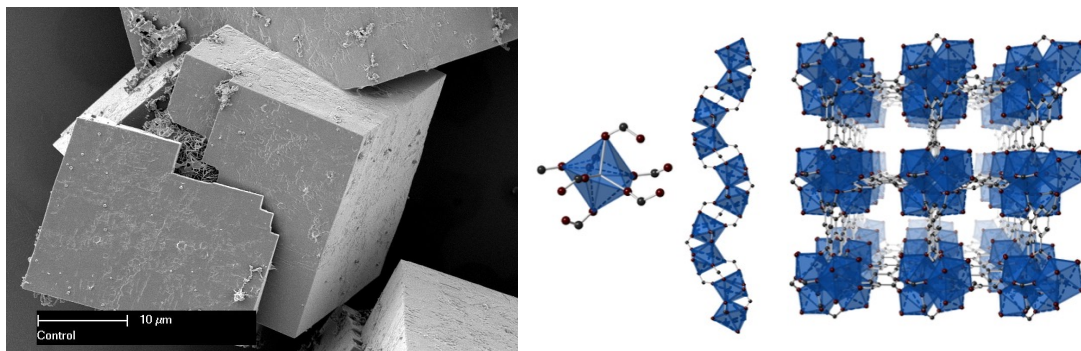


Figure 4.1: Representation of Metal-organic frameworks. The left panel shows scanning electron microscope image of the seed inside a MOF crystal. The right panel shows the schematic representation of a MOF-76 crystal, where oxygen, carbon, and lanthanide atoms are represented by maroon, black, and blue spheres, respectively. Figures adapted from wikipedia.

are a class of compounds with general formula  $ABX_3$  having long range connectivity that form a subclass of dense MOFs. The synergistic effect between inexpensive synthesised organic cation and mechanically stable inorganic anion in hybrid perovskites have enabled these materials to emerge with superior physical and chemical properties in recent decades. The halide hybrid perovskites of general composition,  $[AmH]MX_3$  ( $AmH^+ =$  protonated amine,  $M = Sn^{2+}$  or  $Pb^{2+}$ , and  $X = Cl^-$  or  $Br^-$  or  $I^-$ ) have already attracted a great deal of attention due to their potential use in solar cell applications [11] and have been shown to demonstrate high performance and efficiency in applications relating to design of both mesostructural (and/or nanostructural) solar cells and other photovoltaic devices [12–14] like Light Emitting Diodes (LEDs) [15,16] and spintronics [17–19]. Their efficiency as LED materials is due to the compatible ionization potential and electron affinity of such perovskites as compared to other organic systems. They have also become strong candidates for low-cost LEDs with comparable energy levels similar to organic semiconductors by overcoming the luminescence quenching at room temperature. The hybrid perovskites are organic counterparts of inorganic  $ABO_3$  perovskite oxides. The inherent high carrier mobility of the inorganic part in hybrid perovskites is suitable for various nano-electronic devices. Easy processing techniques like spin-coating, dip-coating and vapor deposition techniques have been known to be of advantage in this case [20,21]. These materials have been investigated intensely in photovoltaic community to acquire high absorption coefficient, reasonable carrier mobility with smaller exciton binding energy and longer exciton diffusion length. There is a humongous effort to study these materials from different perspectives like stability, efficiency, hysteresis with different possible combinations of organic, metallic, and halogen parts.

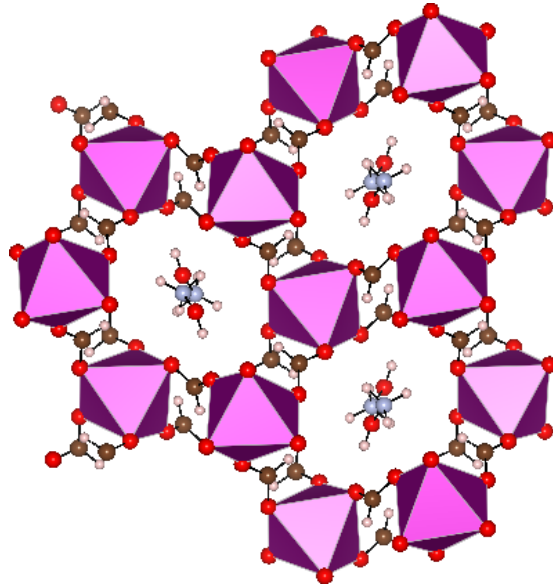


Figure 4.2: Figure showing an example of a hybrid perovskite where the octahedra are connected by formate ligands and various different A site cations may occupy the  $\text{ReO}_3$  type pseudocubic cavities.

The other class of hybrid perovskites discussed in very recent times due to their attractive ferroic properties, [22–27] are transition metal formates  $[\text{AmH}]\text{M}(\text{HCOO})_3$  ( $\text{M} = \text{Mn}, \text{Cu}, \text{Ni}, \text{Fe}, \text{Co}$ ), where  $\text{MO}_6$  octahedra are linked via formate bridges, and the protonated amine molecules sit in the hollow cavity formed by the octahedral framework, establishing hydrogen bonding with formates. [28] These hollow spaces act as pseudo-cubic  $\text{ReO}_3$  type cavities. Organic ligands like formates being simple enough have been mostly studied with varied A cations, as shown in Figure 4.2.

This class of materials has been shown to exhibit curious properties, of which multiferroicity seems to be an intriguing one [29–31]. Ferroelectricity and especially multiferroicity in these materials has been extensively studied by Stroppa and coworkers mostly from a DFT based first principles perspective and at times combined with experimental studies [32–38]. Structural details and effects due to structural phase transitions, strain tuning of various effects like polarisation, and magnetic structure has also been studied by the same groups [39–43]. Interestingly, in these materials due to the non-centrosymmetric nature of the formate linkers, spin canting has been observed and structural order-disorder phase transition accompanied by hysteresis is observed as well. The variation of specific heat with respect to temperature reflects the aspect of prominent dielectric anomalies at two temperatures with a hysteresis width. These anomalies can be correlated to a transition leading to magnetic and electrical ordering. At present, there are no extensive theoretical or experimental studies available to our knowledge

for specifically probing the underlying reason behind such exciting hysteresis and phase transition phenomena.

## 4.2 Experimental studies on Hybrid Perovskites

As mentioned previously, a number of experimental investigations have been conducted with the focus of synthesis and characterization of metal-organic complexes in the last few years. The works of Jain and co-workers [29, 30] are few among many such experimental investigations of hybrid perovskites that consist of Dimethylammonium (DMA) metal formates with the variation of metal ions as Zn, Mn, Fe, Co and Ni. They have found an exciting phase transition in dielectric constant with a hysteresis width of about 10K, and a dielectric anomaly around 160K in Dimethylammonium Zn formate, which shows antiferroelectric behaviour while cooling below 160K temperature. Additionally, a specific heat anomaly has been observed around 156K along with an order-disorder phase transition and electrical ordering, that is shown at the same temperature. The DMA cation at the centre of the  $\text{ReO}_3$  type cavity is found to be disordered at room temperature and Mn, Co and Ni based compounds show ordering at  $T_C=8.5\text{K}$ ,  $14.9\text{K}$ , and  $35.6\text{K}$  respectively with corresponding magnetic exchange coupling values of  $J= -0.32$ ,  $-2.3$ ,  $-4.85$ . All the three compounds exhibit canted weak ferromagnetism with a hysteresis loop below  $T_C$ . The AFM super-exchange and spin canting originate from the non-centrosymmetric character of the atoms forming the  $\text{HCOO}^-$  bridge.  $\text{DMAFeF}$  shows ferromagnetism below 20K with a corresponding phase change that has been associated with a dielectric constant anomaly. The anomaly occurred at 185K, accompanied by a hysteresis of width  $\sim 10\text{K}$ , and a paraelectric to anti-ferroelectric phase transition, which corresponds to a structural phase transition. The corresponding  $T_C$  values for Fe, Co, and Ni based hybrid perovskites are 160K, 165K and 180K respectively. The specific heat anomaly in  $\text{DMAMnF}$  is found to occur at 183K with the associated electrical and magnetic ordering at 8.4K. All four compounds are multiferroic metal organic frameworks with a complex transition as compared to a straight-forward three fold order-disorder model. DMA cation is found to be dynamically disordered in the rhombohedral paraelectric phase with a corresponding transition to monoclinic anti-ferroelectric phase that involves H bonded ordered DMA cations. The magnetic ordering can be achieved through magnetic cooling and one can observe the co-existence of antiferroelectric ordering along with weak ferromagnetic ordering. The experimental demonstration of hysteresis associated with order-disorder phase transitions in this system is indicative of the fact that these systems are capable of undergoing other kinds of phase transitions associated with hysteresis effects.

It has been found in a recent study [44] that a large spontaneous electric polarization below the Curie point accompanied with a colour change exists in

case of electrically polar and magnetic, halide based hybrid perovskites. The system has also been found to be ferroelectric, with large remnant polarization. The origin of this multiferroicity has been attributed to hydrogen-bond ordering of the organic ligands. It has been shown that in these classes of hybrid perovskites the underlying hydrogen bonding is easily tunable via the availability of a plethora of organic building blocks in combination with the 3d transition-metal octahedral geometries. This shall be shown to be particularly useful in subsequent sections.

### 4.3 Motivation for studying Spin Crossover in hybrid perovskites

The presence of transition metal in these compounds together with its octahedral environment makes these materials also well suited for exhibiting spin crossover (SCO) behavior and possibly also cooperativity due to dense nature of framework, which would provide another dimension to functionality of these interesting class of compounds. The presence of organic components in the structure offers greater structural flexibility, and thus better tunability of properties by external means, as compared to that of inorganic perovskites. The flexibility of hybrid perovskites to undergo large structural changes in response to external stimuli has already been reported. [45] Furthermore, it is possible to tailor properties by changing the amine molecule, thereby changing the strength and cross-linking of hydrogen bondings in the structure, yet maintaining the basic topology. [46] Needless to say, much remains to be explored in terms of functionalities that can be achieved in this new class of perovskite materials.

Here we focus on this unexplored area of hybrid perovskites, namely the external stimuli driven spin-crossover. The tremendous flexibility of the organic linkers makes the transition metal based formate hybrid perovskites ideally suited for triggering spin-crossover from a high-spin (HS) to low-spin (LS) state at the transition metal site by external perturbation. A much discussed aspect in this context is the issue of cooperativity in SCO phenomena. [47] The cooperativity in SCO phenomena makes it a spin transition rather than spin-crossover, which may show up with associated hysteresis, as shown in of Figure 4.3, having important implications in designing memory devices. [48] For device applications, the challenges primarily are;

1. to achieve a large hysteresis width which would enable the memory effect to be observable over a wide range of external stimuli,
2. facilitating the transition to occur at a value of the stimuli that can be reached readily.

In this respect, commonly the explored candidates are SCO polymers or 3D coordination compounds which are expected to provide better connectivity compared

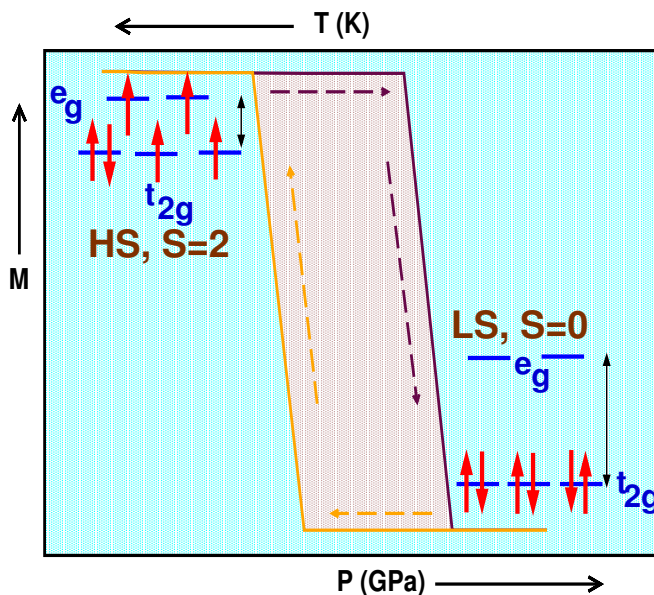


Figure 4.3: Schematic diagram demonstrating the cooperativity associated with spin crossover phenomena in hybrid perovskites. Figure shows the hysteresis in magnetic moment with change of pressure. The y axis shows the magnetic moment (M) and x axis represents pressure (P) increasing in the positive direction as shown in the figure. Upon decreasing P, a transition happens from LS  $S=0$  state where all spins are paired up in the  $t_{2g}$  states octahedrally coordinated  $d^6$  Fe, to HS  $S=2$  state where two of the electrons from  $t_{2g}$  states are promoted to  $e_g$  states. The reverse effect happens as demonstrated in the previous chapter on application of temperature. Due to the cooperativity between Fe(II) centres in the extended solid state geometry, hysteresis loop appears between cycles of exertion and release of pressure

to molecular crystals with isolated molecular units. [49] Considering the dense topology of the newly discussed hybrid perovskites, they can be a potential alternative to SCO polymers or 3D coordination compounds in exhibiting cooperative spin-state transitions. This will add a new functionality to this interesting class of compounds. The extended, 3-dimensional connectivity with limited void space, together with possibility of synthesizing hybrid perovskites containing transition metal ions have made these compounds excellent probable candidates for exhibiting cooperative SCO.

In light of the above, we venture onto the study of SCO properties of transition metal based formate hybrid perovskites, through first-principles calculations.

Although the inorganic part of a hybrid perovskite is mechanically stable, but the organic linker is sensitive enough to external pressure and temperature to

undergo morphological transformation (/structural transition). This was brought to the attention of scientific community by Kieslich and co-workers [50], where they showed a drastic change in mechanical properties, particularly in rigidity modulus while changing the amine with other cations of different effective radii  $r_{A_{eff}}$  and consequent effect in hydrogen bonding mode alteration. The effective radii of the molecular cation  $r_{A_{eff}}$  can be expressed as

$$r_{A_{eff}} = r_{mass} + r_{ion},$$

where  $r_{mass}$  is the distance between the molecular centre of mass and furthest atom from the centre of mass and  $r_{ion}$  is the corresponding ionic radius of the atom. The hydrogen atoms generally are not considered while determining  $r_{A_{eff}}$ . This work has encouraged us to investigate for profound understanding the organic cationic effect on spin state transition and the elastic interaction in the constant anionic environment and how they can be tuned under external pressure with associated hysteresis.

In particular we consider  $\text{Fe}^{2+}$  based hybrid perovskites. The choice is prompted by the fact that SCO transitions in Fe(II)-based compounds, having 6 *d*-electrons in Fe(II) ion, and showing a transition from a LS ( $S = 0$ ) to a HS ( $S = 2$ ) state are pronounced and abrupt, making them suitable for applications. In our study, we consider hydrostatic pressure as an external stimuli. To the best of our knowledge, no study exists so far on the pressure effect on hybrid perovskites, although hydrostatic pressure is considered as one of the effective means to tune properties in inorganic perovskites. [51] Additionally, to study the influence of changing the primary organic component, namely the amine cation, located in the perovskite cavity, we consider two different cations, Dimethyl-ammonium ( $\text{CH}_3\text{NH}_2\text{CH}_3$ ), and Hydroxylammonium ( $\text{NH}_3\text{OH}$ ). It is worth noting that our conscious choice of these two different molecular cations, leads to a change in the tolerance factor of the Fe formate perovskite structures, as the effective molecular radii for Dimethyl-ammonium and Hydroxylammonium are different, being 272 pm and 215 pm, respectively. As previously mentioned a change in mechanical properties, particularly in rigidity can be achieved by changing cations of different effective molecular radius.

Our density functional theory (DFT) based computational study that takes into account all structural and chemical aspects in full rigor, shows that pressure induced spin-state transitions are achieved in both Dimethyl-ammonium Iron Formate (DMAFeF) and Hydroxylammonium Iron Formate (HAFeF) for modest critical pressure range of 2-7 GPa, associated with large hysteresis of 2-5 GPa. The latter implies that these compounds should exhibit spin-switchability over a wide range of operating pressure. Our findings highlight the possible technical use of spin-switching functionalities of hybrid perovskite compounds with accompanied changes in electronic, magnetic and optical properties, in sensors and memory devices. Interestingly, the flexibility in choice of the A site cation,

*i.e.* the protonated amine molecule adds another dimension, namely the tuning and modulation of spin-switching properties.

## 4.4 Computational Methodology

Our first-principles calculations were carried out in the plane wave basis as implemented in the Vienna Ab-initio Simulation Package (VASP) [52, 53] with projector-augmented wave (PAW) [54] potential. The exchange-correlation functional was chosen to be that of generalized gradient approximation (GGA) implemented following the Perdew-Burke-Ernzerhof [55] prescription. For ionic relaxations, internal positions of the atoms were allowed to relax until the forces became less than  $0.005 \text{ eV}/\text{\AA}$ . Energy cutoff of 500 eV, and  $4 \times 4 \times 2$  Monkhorst-Pack k-points mesh were found to provide a good convergence of the total energy in self-consistent field calculations. To take into account of the correlation effect at Fe sites beyond GGA, which turned out to be crucial for the correct description of the electronic and magnetic properties, calculations with supplemented Hubbard  $U$  (GGA +  $U$ ) a la Liechtenstein et al [56] were carried out, with the choice of  $U = 4 \text{ eV}$  and Hund's coupling parameter  $J_H = 1 \text{ eV}$ . In order to study the effect of hydrostatic pressure, calculations were done by first changing the volume of the unit cell isotropically and then relaxing the shape of the cell together with the ionic positions for each of the modified volume. The estimate of applied hydrostatic pressure for each compressed volume was obtained from the knowledge of the calculated bulk modulus. The bulk modulus was calculated by varying the volume of the unit cell and relaxing the ionic positions at each volume. Accurate self-consistent-field calculations were carried out to obtain the total energy of the systems at each volume. The energy versus volume data was fitted to the third order Birch-Murnaghan isothermal equation of state [57], given by,

$$E(V) = E_0 + \frac{9V_0B_0}{16} \left\{ \left[ \left( \frac{V_0}{V} \right)^{2/3} - 1 \right]^3 B'_0 + \left[ \left( \frac{V_0}{V} \right)^{2/3} - 1 \right]^2 [6 - 4 \left( \frac{V_0}{V} \right)^{2/3}] \right\}$$

where  $V_0$  is the equilibrium volume,  $B_0$  is the bulk modulus and is given by  $B_0 = -V(\delta P/\delta V)_T$  evaluated at volume  $V_0$ .  $B'_0$  is the pressure derivative of  $B_0$  also evaluated at volume  $V_0$ .

## 4.5 Crystal Structure of DMAFeF and HAFeF

An essential pre-requisite for the first-principles study is the accurate information of the crystal structure. An interesting feature of  $[\text{AmH}]\text{M}(\text{HCOO})_3$  compounds is the order-disorder transition of the A-site amine cations through ordering of hydrogen bonds. [28] While the crystal structure data for disordered phase of

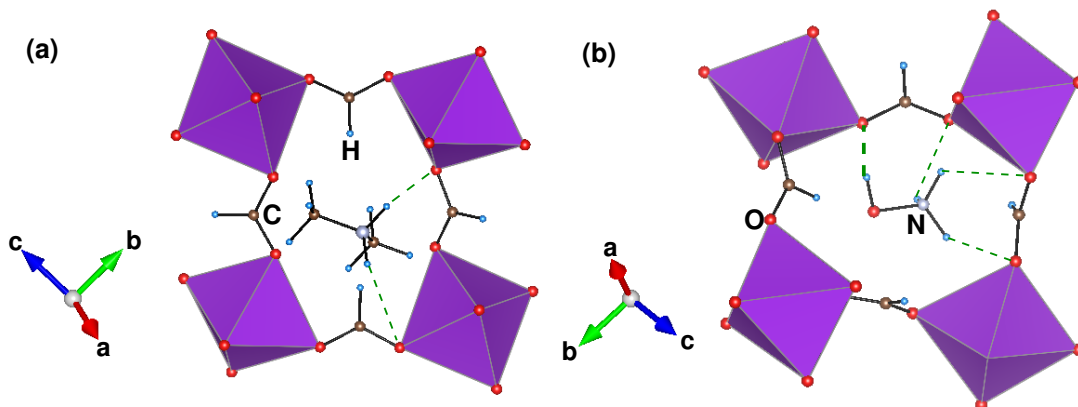


Figure 4.4: Computed crystal structures of DMAFeF [panel (a)] and HAFeF [panel (b)] in A-site ordered phase. The  $\text{FeO}_6$  octahedra are connected to each other by the formate ligands while the DMA or HA cations sit in the hollow formed by the octahedra. Various atoms have been marked. N-H $\cdots$ O and O-H $\cdots$ O bonds are represented by dashed lines, with thickness of lines indicating the strength of the bonds.

DMAFeF [28] is available, no such data exists for the corresponding ordered phase. Moreover, in case of HAFeF, no crystal structure data has been reported till date. Therefore we started with crystal structure data for the ordered phases of DMAMnF [58] and HAMnF [59], the Mn analogues of DMAFeF and HAFeF. We relaxed the structure completely after replacing Mn atoms with Fe atoms, which gave the first-principles predicted ordered structures of DMAFeF and HAFeF. Mn being next to Fe in the periodic table, this forms a legitimate approach. We carried out a complete structural relaxation, which involved relaxation of the unit cell volume and shape, as well as atomic positions. We found that though the symmetries do not change between Fe compounds and their corresponding Mn counterparts, there is appreciable change in the volume of the unit cells, as expected. DMAFeF and HAFeF crystallize in two different monoclinic space groups, DMAFeF being in  $Cc$  space group and HAFeF being in  $P2_1$  space group. The lattice constants for DMAFeF are found to be,  $a=14.464\text{\AA}$ ,  $b=8.355\text{\AA}$ ,  $c=8.975\text{\AA}$ , with the angle  $\gamma = 119.8^\circ$ , whereas for HAFeF the lattice constants are found to be  $a=7.812\text{\AA}$ ,  $b=7.961\text{\AA}$ ,  $c=13.173\text{\AA}$ , with angles  $\alpha = \beta = \gamma = 90^\circ$ .

The calculated crystal structures as cif files can be found in the Appendix.

As shown in Figure 4.4, in both the framework compounds each  $\text{FeO}_6$  octahedra is connected to neighbouring  $\text{FeO}_6$  octahedra via  $\text{HCOO}^-$  ligand bridges. This forms a three-dimensional  $\text{ReO}_3$ -type network, with Dimethyl-ammonium or Hydroxylammonium, cations occupying the centers of the  $\text{ReO}_3$ -type cavities. In DMAFeF, two bridging N-H $\cdots$ O hydrogen bonds from each DMA cation are

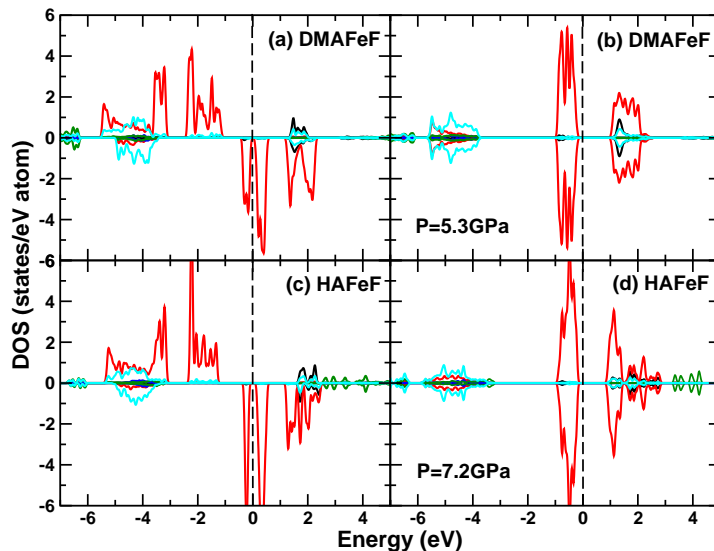


Figure 4.5: Projected density of states of DMAFeF and HAFeF at ambient and high pressure conditions. Panels (a) and (c) are for ambient pressure, while panels (b) and (d) are for high pressure. The DOS projected to Fe  $d$ , O  $p$ , C  $p$ , N  $p$  and H  $s$  are marked in red, cyan, black, green and blue, respectively. The zero of the energy is set at Fermi energy.

formed, while in HAFeF, three N-H $\cdots$ O hydrogen bonds, and a O-H $\cdots$ O hydrogen bond are formed from each HA cation. The nature of hydrogen bondings is expected to be different between N-H $\cdots$ O and O-H $\cdots$ O due to the less polar nature of N-H bond as compared to O-H bond. Thus the O-H $\cdots$ O hydrogen bond is stronger than N-H $\cdots$ O hydrogen bond. The lattice for HAFeF is therefore expected to be more rigid compared to the lattice for DMAFeF, having important bearing on SCO phenomena as we will be discussing in the following sections.

## 4.6 Spin-state transition under pressure and Cooperativity

In order to determine the spin-states of the Fe atoms in DMAFeF and HAFeF, we calculated the spin-polarized electronic structures. The spin-polarized density of states at ambient pressure condition for DMAFeF and HAFeF are shown in panels (a) and (c) of Figure 4.5, respectively. The states close to Fermi level ( $E_F$ ) are dominantly of Fe  $d$  character, which are found to be strongly spin-polarized. The octahedral coordination of oxygen atoms around Fe, groups the Fe  $d$  states into states of  $e_g$  and  $t_{2g}$  symmetries. The Fe  $d$  states are found to be completely occupied in the majority spin channel, with empty Fe  $e_g$  states, and partially filled

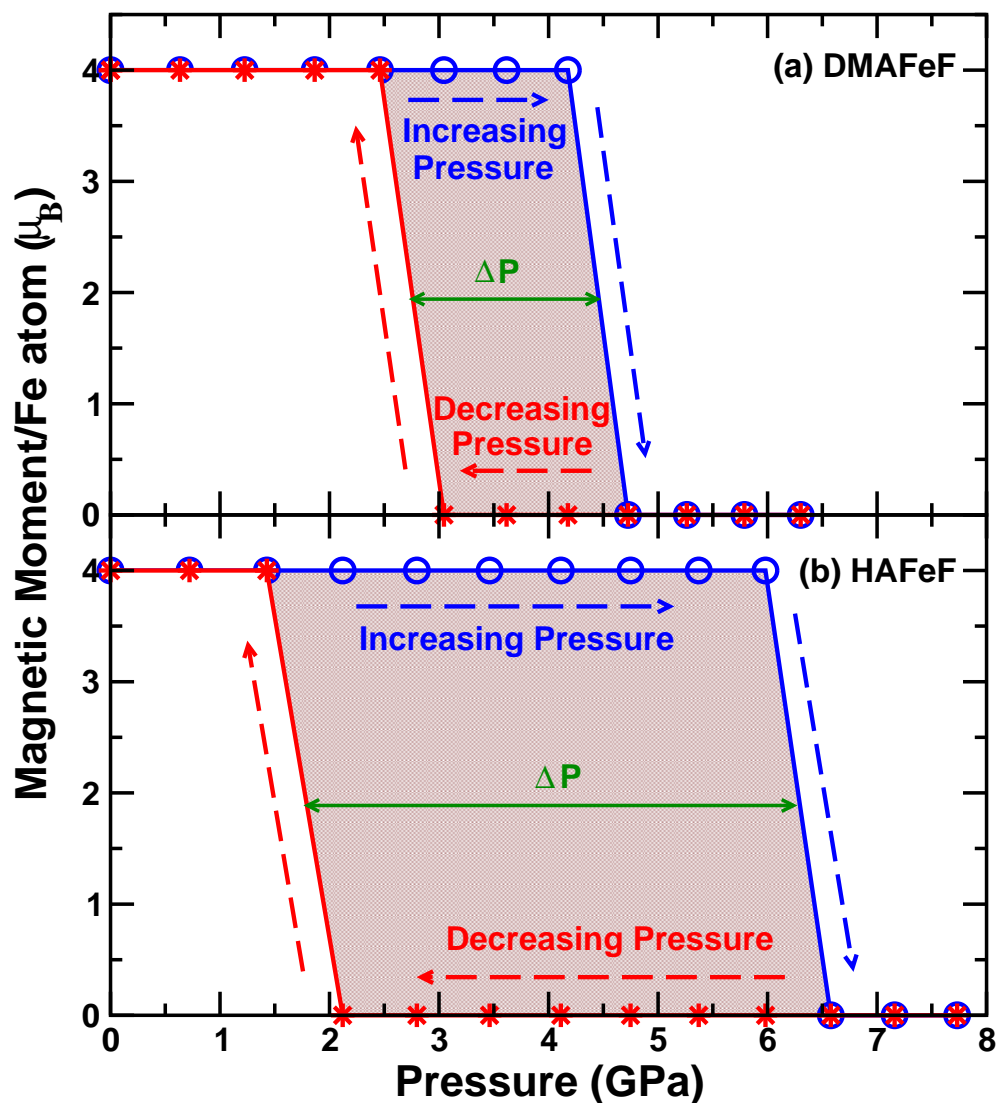


Figure 4.6: Computed magnetic moment per Fe atom plotted as a function of pressure for DMAFeF [panel (a)] and HAFeF [panel (b)]. The data are plotted for two different paths. The data points in blue denote the path following increasing pressure, starting from the HS state and the data points in red denote the path following decreasing pressure, starting from the LS state. HS  $\rightarrow$  LS transitions in both compounds exhibit interesting hysteresis effects.

Fe  $t_{2g}$  states in the minority spin channel. The distortion in the FeO<sub>6</sub> octahedra causes further splitting within states of Fe  $t_{2g}$ , leading to a small gap at the Fermi region in the minority spin channel. Insulating solution is obtained for both compounds at ambient condition, with a large band gap ( $\approx 2$  eV) between occupied Fe  $d$  and empty C  $p$  states in majority spin channel and a tiny band gap ( $\approx 0.1$  eV) within the Fe  $t_{2g}$  states in the minority spin channel. This suggests at ambient condition spin-state of Fe in both DMAFeF and HAFeF to be HS. The calculated total magnetic moment (M) turned out to be  $4 \mu_B$  per Fe atom, for both the compounds, in conformity with the stabilization of HS (S=2) state of Fe. Panels (b) and (d) of Figure 4.5 show the spin-polarized density of states for DMAFeF and HAFeF at high pressure condition. We find the exerting pressure (P) in the range of  $\approx 5-7$  GPa causes drastic change in the electronic structure. First of all, for both the compounds the ground states turned out to be non spin-polarized, with calculated magnetic moments of  $0 \mu_B$ . This confirms a spin-state transition from HS (S=2) state to LS (S=0) state, obtained by application of pressure. In the high-pressure LS state a large band gap of  $\approx 1$  eV opens up between the fully occupied Fe  $t_{2g}$  states, and completely empty Fe  $e_g$  states. The spin-state transition thus should be accompanied by a significant change in the overall band gap, which should be manifested in corresponding change in optical response.

In the next step, in order to find out the critical pressure where such spin-state transition happens for the two compounds, we increased the pressure in steps of 0.6-0.7 GPa, starting from the ambient pressure condition. As shown in the plot of the magnetic moment (M) versus pressure (P) in Figure 4.6, we find a spin-state transition from HS with a total magnetic moment of  $4 \mu_B/\text{Fe}$  to LS with a total moment of  $0 \mu_B/\text{Fe}$  at pressure ( $P_c \uparrow$ ) of 4.7 GPa for DMAFeF and 6.6 GPa for HAFeF. This implies a strong influence of the choice of A cation on the optimal pressure needed for spin-state transition. We then decreased the pressure starting from the highest applied pressure. Interestingly we find the optimal pressure required for the transition from LS with a total moment of  $0 \mu_B/\text{Fe}$  to HS with total magnetic moment of  $4 \mu_B/\text{Fe}$ , happens at a different pressure ( $P_c \downarrow$ ) compared to  $P_c \uparrow$ , having values 2.5 GPa for DMAFeF and 1.4 GPa for HAFeF. This is reflected as significant hysteresis effect in M-P data in case of both compounds, with width of hysteresis being 2.2 GPa for DMAFeF as compared to 5.2 GPa for HAFeF, the former being more than a factor of 2 smaller than the latter. Therefore, the choice of A cation has a significant influence on spin-switching properties. This constitutes the key finding of our investigation. We note that both  $P_c \uparrow$  and  $P_c \downarrow$  are of moderate values for both compounds, that can be generated in a laboratory set-up.

Additionally, we have calculated the energies (E) upon varying the cell volume (V) within the scheme of fixed moment calculations, once fixing the moment to HS state and another fixing the moment to LS state. The generated E-V curve

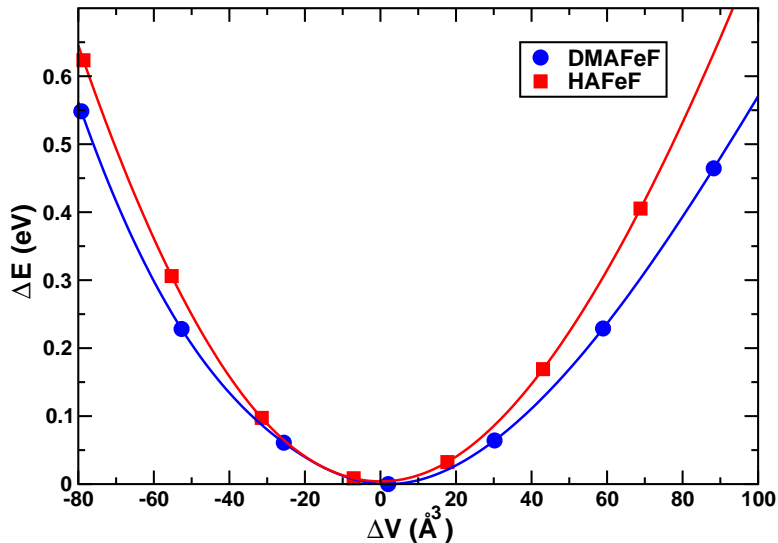


Figure 4.7: Total energy versus volume of the unit cell for DMAFeF and HAFeF. Energy and volumes have been measured with respect to the equilibrium values,  $E_0$  and  $V_0$ , respectively. The symbols denote the DFT calculated data points. The lines depict that obtained from Murnaghan [57] equation of state fit.

showed the strong hysteresis effect, confirming our finding in the above.

## 4.7 Microscopic understanding of Cooperativity

In order to understand the microscopic origin of the quantitative differences in response of the two formate frameworks considered in this study to the applied pressure, we firstly calculated the mechanical strengths of the two compounds. As mentioned previously due to the differential nature of H bonding, the lattice for HAFeF is expected to be more rigid compared to that of DMAFeF. This is confirmed by the magnitudes of the calculated bulk moduli of the two systems. The fit of the DFT total energy versus volume data to the Birch-Murnaghan equation of state, [57] as shown in Figure 4.7, gave the bulk modulus to be 21.55 GPa for DMAFeF, and 24.27 GPa for HAFeF, with  $B'_0 = 5.39$  and 1.84, respectively. This would in turn imply that the critical pressure needed to cause spin-switching through change in Fe-O bond-length to be larger in the significantly more rigid lattice of HAFeF compared to that in comparatively less rigid lattice of DMAFeF, as reflected in different values of  $P_c \uparrow$  in two compounds.

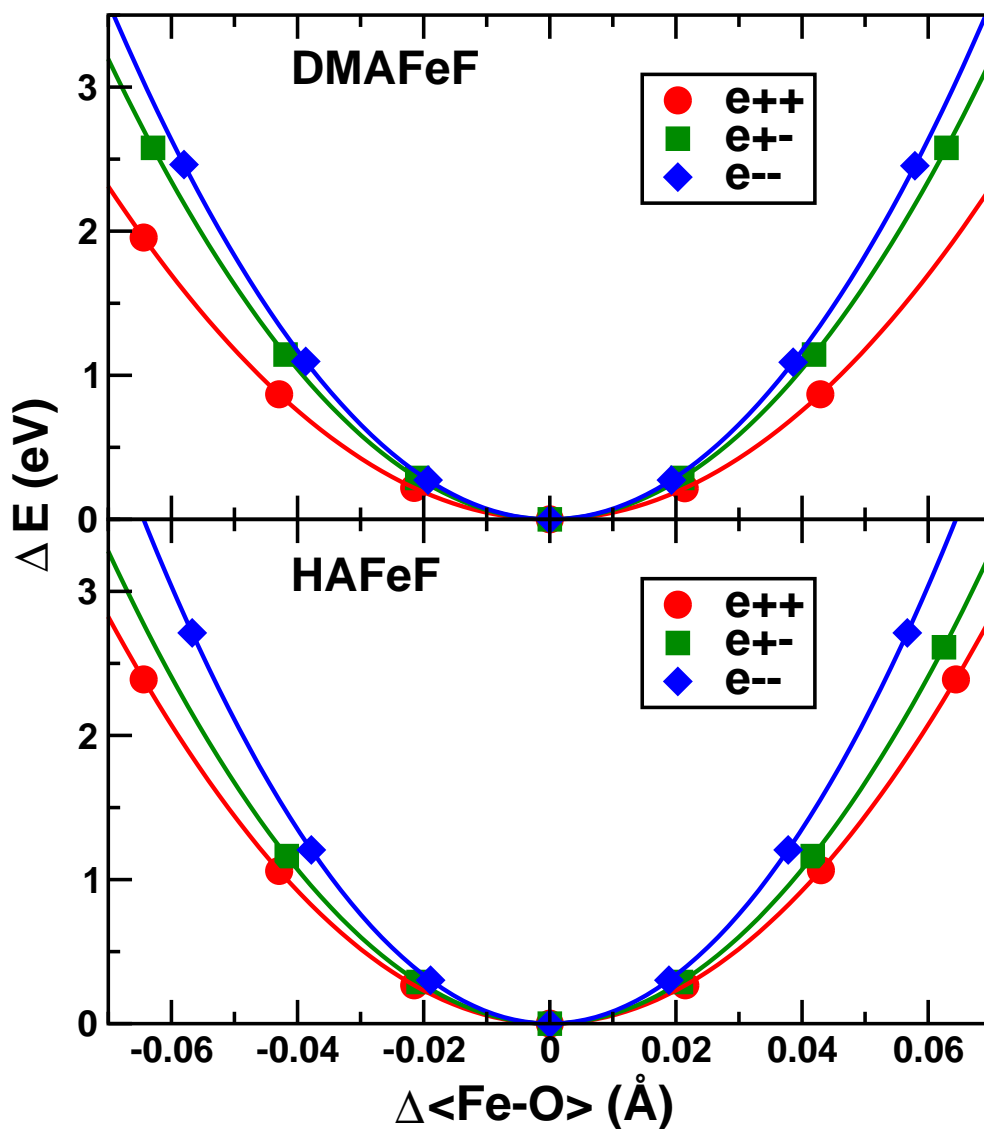


Figure 4.8: Variation of total energy as a function of variation of Fe-O bond-length about the equilibrium value, for different spin-state configurations of neighbouring Fe atoms, LS-LS (diamond), LS-HS (square) and HS-HS (circle). Solid lines are fit to the data points. Bottom panel is same as top panel but for HAFeF.

Further to elucidate the mechanism by which the cooperativity, manifested in the form of hysteresis in the M-P plot, develops in these materials we computed the elastic and magnetic exchange interactions. The most prevalent idea in this context attributes the microscopic origin of cooperativity to the elastic interaction between local distortions at the SCO centers. [60] However in our very recent work, as described in Chapter 3, the importance of magnetic super-exchanges in driving cooperativity was uncovered. [47] Depending on the sign of the spin-dependent elastic interaction, which is dictated by the nature of the spin-phonon coupling in the material, the magnetic interaction was found to influence the hysteresis in a quantitative or qualitative way. As was found in our previous work in Chapter 3, [47] the interplay between elastic and magnetic interaction in building up cooperativity, crucially relies on the spin-dependent rigidity of the lattice. Depending on the spin-state of the spin-crossover ion, which is Fe in the present case, the elastic interaction between two neighbouring Fe ions can be different, which are labeled as  $e_{++}$  ( $e_{--}$ ) for both neighbouring sites in HS (LS) state, and  $e_{-+}$  for one site in LS and another in HS. The size change of the SCO unit upon change of spin-state makes  $e_{--} > e_{++}$ . It is thus the value of  $e_{-+}$  which decides the nature (sign) of the effective elastic interaction. Following the work by K. Boukheddaden et al., [60], and as also explicitly shown in the Appendix of Chapter 3, the effective elastic interaction between two neighbouring SCO sites is given by,

$$K = \frac{1}{8} \ln\left(\frac{e_{+-}^2}{e_{++} \times e_{--}}\right)$$

Thus the effective elastic interaction,  $K$  turns out to be of ferroelastic nature for  $e_{+-} > \sqrt{e_{++} \times e_{--}}$  and of antiferroelastic nature for  $e_{+-} < \sqrt{e_{++} \times e_{--}}$ . It was demonstrated [47] that for ferro type elastic interaction, the magnetic interaction becomes operative only in qualitative manner, in terms of enhancing the hysteresis width, while for antiferro nature of elastic interaction, the magnetic exchange is the sole driving force in setting up the hysteresis.

In order to have a microscopic understanding of the observed hysteresis in M-P plot of the studied formate frameworks and its dependence on the choice of the amine cation, we thus first calculated the spin-state dependent elastic interactions for the two compounds. To do so, we adopted the same procedure as in Chapter 3 [47]. Electronic structure of the optimized crystal structure data shows that the LS state is obtained at a high pressure phase for an average Fe-O bond length of 1.9 Å or less, while the HS state is obtained at an ambient pressure phase for an average Fe-O bond length of 2.1 Å or more. Keeping this in mind, we constructed crystal structures setting the average Fe-O bond length at 1.9 and 2.1 Å to emulate the LS and HS states of neighbouring Fe-O<sub>6</sub> octahedra, respectively. To simulate the LS-HS situation, structure with alternating arrangements of Fe-O<sub>6</sub> octahedra having average Fe-O bond lengths of 1.9 and 2.2 Å was constructed. Considering the three model structures with

Material	$E_{elastic}$	$J_{magnetic}$	Relative strength
DMAFeF	3.52K	3.19K	$E \approx J$
HAFeF	8.93K	2.85K	$E > J$

Table 4.1: Table summarising the elastic and magnetic exchanges.

HS-HS, LS-LS and LS-HS arrangements of neighbouring Fe-O<sub>6</sub> octahedra, the Fe-O bond lengths were varied by small amounts ( $\approx 0.02 - 0.06 \text{ \AA}$ ) within the harmonic oscillation limit around the equilibrium bond lengths. The obtained energy versus bond length variation for the three cases for both the compounds are shown in Figures 4.8 top and bottom panel. A parabolic fit of the data points provides the estimates of the spin-dependent elastic interactions. DMAFeF is found to be weakly ferroelastic with  $e_{+-} \simeq \sqrt{e_{++} \times e_{--}}$  while HAFeF is found to be strongly ferroelastic with  $e_{+-} > \sqrt{e_{++} \times e_{--}}$ , having effective elastic constant of 3.52 K for DMAFeF compared to a substantially larger effective elastic constant of 8.93K for HAFeF.

We next turn our attention to the magnetic super-exchange coupling between neighbouring Fe(II) centers in HS state. To estimate their values we calculated the total energies of ferromagnetic and antiferromagnetic Fe<sup>2+</sup> spin configurations, and mapped on to the spin Hamiltonian,

$$\mathcal{H}_{magnetic} = -JS_iS_j,$$

where,  $J$  is the magnetic exchange between nearest neighbour Fe<sup>2+</sup> spins,  $S_i$  and  $S_j$ . The difference of the ferromagnetic and antiferromagnetic energies provides the estimate of  $J$ . The calculated  $J$ -s turned out to be of negative signs which indicate antiferromagnetic nature of magnetic exchanges, and of values 3.19K and 2.85K for DMAFeF and HAFeF, respectively. A summary of the elastic and magnetic exchanges is given in Table 4.1. This leads us to conclude that while the magnetic exchanges in the two compounds are of same sign and of similar strengths, the spin-dependent elastic interactions are of ferroelastic nature with significantly larger strength for HAFeF compared to DMAFeF. Following the work from the previous chapter [47] we also conclude that the primary responsible factor in driving cooperativity in these formate frameworks is the spin-dependent lattice effect, wherein the magnetic exchange only plays a role in quantitatively increasing the width of the hysteresis region in the system. This is different from the case of coordination polymer compounds discussed in Chapter 3 in which it was found to be entirely driven by the magnetic super-exchanges. [47, 61] The change of amine cation, leads to the change in cross-linking hydrogen bonding, and thus to the rigidity of the lattices. Interestingly, the change of amine molecule is also found to affect the spin-phonon coupling, thereby producing a profound effect on the cooperativity. This also demonstrates that the cooperativity may be tuned by chemical means and hence with the huge plethora of organic A cations

available one might simply choose a suitable organic amine cation to tailor the cooperativity according to device requirements.

## 4.8 Conclusions

In conclusion, we show that apart from exhibiting interesting multiferroic properties transition metal formate based hybrid perovskites are also potential candidates for exhibiting spin-switching upon application of external stimuli. We demonstrated this through rigorous first-principles calculations, considering two formate based hybrid perovskite compounds, DMAFeF and HAFeF under hydrostatic pressure. We found that dense framework structures of these compounds help in building up cooperativity in spin-switching, making the phenomena a spin-state transition with appreciable hysteresis effect. The spin-switching is reflected in associated changes in electronic, magnetic and also possible changes in optical properties. This opens up several novel potential applications of these materials, for example, as pressure sensors, as active elements of various types of displays, and in information storage and retrieval - an aspect which has remained unexplored so far. Our computed values of pressure needed to drive the spin-state transition is found to be in the range of about 2-6 GPa, which should be readily achievable in a laboratory set-up of a low to medium pressure diamond anvil cell (DAC). The appreciable hysteresis effect of 2-5 GPa associated with these spin-state transitions would make them functional in memory devices for a reasonably wide range of pressure. Interestingly, taking the advantage of flexibility of these MOF perovskites to undergo substantial change in mechanical properties upon tuning of hydrogen bonds, both the pressure required from the transition, as well as the hysteresis-width are found to be tunable by choice of appropriate amine cation. Microscopic investigation shows elastic properties are vastly different between the two studied compounds, lending support to our observation.

It is worth mentioning that all the calculations, reported here, have been carried out within the scheme of  $T = 0$  K DFT calculations. The magnetic exchange interactions being a few K, the magnetic ordering temperature is expected to be few tens of K, for *e.g.* considering  $S = 2$  state of Fe and using simple mean field formula, it turns out to be about 40 K. However, following the analysis, as presented above, the effective elastic interaction is of ferroelastic nature, in which case the magnetic interaction becomes operative only in qualitative manner, in terms of enhancing the hysteresis width. [47] We thus expect the pressure induced spin-state transition and the related hysteresis effect, reported in the present study, to be observable even at high temperature. It is to be noted, however, our study has been carried out considering the experimental ordered phases of the compounds. The order-disorder transition of H bonds in such compounds

is estimated to be around 160 - 180 K, [28] so the chosen temperature should be less than that.

## 4.9 Appendix

This section contains the calculated crystallographic information files for the materials DMAFeF and HAFeF.

## DMAFeF crystal structure

```

_symmetry_space_group_name_H-M 'C 1 c 1'
_symmetry_Int_Tables_number 9

_cell_length_a      14.46400
_cell_length_b      8.35500
_cell_length_c      8.95700
_cell_angle_alpha   90.00000
_cell_angle_beta    60.18700
_cell_angle_gamma   90.00000

loop_
_space_group_symop_operation_xyz
x, y, z
x, -y, z+1/2
x+1/2, y+1/2, z
x+1/2, -y+1/2, z+1/2

loop_
_atom_site_label
_atom_site_type_symbol
_atom_site_fract_x
_atom_site_fract_y
_atom_site_fract_z
_atom_site_occupancy
O1  O    0.27159  0.15661  0.05081  1.00000
O2  O    0.47828  0.15765  0.07709  1.00000
O3  O    0.09216  0.14556  0.22589  1.00000
O4  O    0.39211  0.47004  0.01879  1.00000
O5  O    0.38977  0.34418  -0.29461  1.00000
O6  O    0.47669  0.03717  -0.24522  1.00000
C1  C    0.18090  0.22292  0.14297  1.00000
C2  C   -0.05175  0.47988  -0.34926  1.00000
C3  C    0.39319  0.48875  -0.34331  1.00000
C4  C   -0.27549  0.28335  0.00204  1.00000
C5  C   -0.38388  0.24360  0.31647  1.00000
H1  H    0.17680  0.35512  0.15385  1.00000
H2  H    0.39543  0.05261  -0.37837  1.00000
H3  H   -0.10231  0.08507  -0.26232  1.00000
H4  H   -0.27752  0.33557  -0.10826  1.00000
H5  H   -0.26267  0.15388  -0.01455  1.00000
H6  H   -0.21151  0.33871  0.01545  1.00000
H7  H   -0.45910  0.27831  0.42956  1.00000
H8  H   -0.31598  0.28773  0.32682  1.00000
H9  H   -0.38008  0.11312  0.30377  1.00000
H10 H  -0.43932  0.26334  0.14182  1.00000
H11 H  -0.39143  0.43915  0.17943  1.00000
N1  N   -0.37896  0.31410  0.16028  1.00000
Fe1 Fe   0.42884  0.25345  -0.10893  1.00000

```

## HAFeF crystal structure

```

_symmetry_space_group_name_H-M 'P 21 21 21'
_symmetry_Int_Tables_number 19

_cell_length_a      13.17300
_cell_length_b      7.96100
_cell_length_c      7.81200
_cell_angle_alpha   90.00000
_cell_angle_beta    90.00000
_cell_angle_gamma   90.00000

loop_
_space_group_symop_operation_xyz
x,y,z
x+1/2,-y+1/2,-z
-x,y+1/2,-z+1/2
-x+1/2,-y,z+1/2

loop_
_atom_site_label
_atom_site_type_symbol
_atom_site_fract_x
_atom_site_fract_y
_atom_site_fract_z
_atom_site_occupancy
C1 C      0.48884  0.47466  0.32430  1.00000
C2 C      0.27581  0.03028  0.44373  1.00000
C3 C      0.21338 -0.47823  0.43689  1.00000
H1 H      0.47608  0.41745  0.19745  1.00000
H2 H      0.21106  0.06248  0.35958  1.00000
H3 H      0.27811 -0.45705 -0.47562  1.00000
H4 H      0.46763 -0.30367 -0.46015  1.00000
H5 H     -0.47400  0.49361 -0.33621  1.00000
H6 H      0.45976 -0.43134 -0.15999  1.00000
H7 H     -0.41267 -0.38603 -0.18872  1.00000
O1 O      0.44306 -0.38681  0.35490  1.00000
O2 O     -0.45280  0.40100  0.42968  1.00000
O3 O      0.33480 -0.08681  0.39931  1.00000
O4 O      0.28665  0.11672 -0.41936  1.00000
O5 O      0.21253 -0.40948  0.29153  1.00000
O6 O      0.14201  0.42551  0.49073  1.00000
O7 O      0.48946 -0.26020 -0.34294  1.00000
N1 N     -0.48250 -0.40671 -0.25040  1.00000
Fe1 Fe    0.33354 -0.25627  0.19514  1.00000

```

# Bibliography

- [1] Kieslich, G.; Sun, S.; Cheetham, A. K. *Chem. Sci.*, **2014**, 5, 4712.
- [2] Shekhah, O.; Liu, J.; Fischer, R. A.; Wöll, *Chem. Soc. Rev.*, **2011**, 40, 1081-1106.
- [3] Cheetham, A. K.; Rao, C. N. R.; *Science*, **2007**, 318, 58-59.
- [4] Maczka, M.; Kadlubanski, P.; Freire, P. T. C.; Macalik, B.; Paraguassu, W.; Hermanowicz, K.; Hanuza, J. *Inorg. Chem.*, **2014**, 53, 9615-9624.
- [5] Wang, X. Y.; Gan, L.; Zhang, S. W.; Gao, S. *Inorg. Chem.*, **2004**, 43, 4615-4625.
- [6] Li, B.; Wen, H. M.; Zhou, W.; Chen, B. *J. Phys. Chem. Lett.*, **2014**, 5, 3468-3479.
- [7] Kreno, L. E.; Leong, K.; Farha, O. K.; Allendorf, M.; van Duyne, R. P.; Hupp, J. T. *Chem. Rev.*, **2012**, 112, 1105-1125.
- [8] Ranocchiari, M.; van Bokhoven, J. A. *Phys. Chem. Chem. Phys.*, **2011**, 13, 6388-6396.
- [9] Horcajada, P.; Chalati, T.; Serre, C.; Gillet, B.; Sebrie, C.; Baati, T.; Eubank, J.F.; Heurtaux, D.; Clayette, P.; Kreuz, C.; Chang, J.S.; Hwang, Y.K.; Marsaud, V.; Bories, P.N.; Cynober, L.; Gil, S.; Ferey, G.; Couvreur, P.; Gref, R. *Nat Mater* **2010**, 9, 172-178.
- [10] Tejuca, L.; Fierro, J. *Properties and Applications of Perovskite-Type Oxides*, CRC Press, New York, 1993.
- [11] Yin, W-J.; Yang, J-H.; Kang, J.; Yan, Y.; Wei, S-H. *J. Mater. Chem. A*, **2015**, 3, 8926.
- [12] Kojima, A.; Teshima, K.; Shirai, Y.; Miyasaka, T. *Journal of the American Chemical Society* **2009**, 131, 6050-6051,

- [13] Zhou, H.; Chen, Q.; Li, G.; Luo, S.; Song, T.b.; Duan, H.S.; Hong, Z.; You, J.; Liu, Y.; Yang, Y. *Science* **2014**, *345*, 542–546,
- [14] Heo, J.H.; Song, D.H.; Han, H.J.; Kim, S.Y.; Kim, J.H.; Kim, D.; Shin, H.W.; Ahn, T.K.; Wolf, C.; Lee, T.W.; Im, S.H. *Advanced Materials* **2015**, *27*, 3424–3430.
- [15] *Nature Nanotechnology*, *9*, 687, 2014
- [16] *Advanced Materials*, *27*, 1248, 2015.
- [17] *Nature Physics*, *11*, 427, 2015;
- [18] *ACS Nano*, *9*, 11557, 2015;
- [19] *JPC Letter*, *5*, 3335, 2015
- [20] Burschka, J.; Pellet, N.; Moon, S.J.; Humphry-Baker, R.; Gao, P.; Nazeeruddin, M.K.; Gratzel, M. *Nature* **2013**, *499*, 316–319. Letter.
- [21] Liu, M.; Johnston, M.B.; Snaith, H.J. *Nature* **2013**, *501*, 395–398. Letter.
- [22] Tian, Y.; Stroppa, A; C, Yisheng; Yan, L.; Wang, S.; Barone, P; Picozzi, S.; Sun, Y. *Sci. Rep.* **2014**, *4*, 6062.
- [23] Tian, Y., Cong, J., Shen, S., Chai, Y., Yan, L., Wang, S. and Sun, Y. *Phys. Status Solidi RRL* **2014**, *8*, 91-94.
- [24] Di Sante, D.; Stroppa, A.; Jain, P.; Picozzi, S. *J. Am. Chem. Soc.*, **2013**, *135*, 18126-18130.
- [25] Jain, P.; Dalal, N.; Toby, B.; Kroto, H.; Cheetham, A. K.; *J. Am. Chem. Soc.*, **2008**, *130*, 10450-10451.
- [26] Stroppa, A.; Barone, P.; Jain, P.; Perez-Mato, J. M.; Picozzi, S. *Adv. Mater.*, **2013**, *25*, 2284-2290.
- [27] Stroppa, A.; Jain, P.; Barone, P.; Marsman, M.; Perez-Mato, J. M.; Cheetham, A. K.; Kroto, H. W.; Picozzi, S. *Angew. Chem. Int. Ed.*, **2011**, *50*, 5847-5850.
- [28] Jain, P.; Ramachandran, V.; Clark, R. J.; Zhou, H. D., Toby, B. H.; Dalal, N. S.; Kroto, H. W.; Cheetham, A. K. *J. Am. Chem. Soc.* **2009**, *131*, 13625-13627.
- [29] Jain, P.; Dalal, N.S.; Toby, B.H.; Kroto, H.W.; Cheetham, A.K. *Journal of the American Chemical Society* **2008**, *130*, 10450–10451,

- [30] Jain, P.; Ramachandran, V.; Clark, R.J.; Zhou, H.D.; Toby, B.H.; Dalal, N.S.; Kroto, H.W.; Cheetham, A.K. *Journal of the American Chemical Society* **2009**, *131*, 13625–13627,
- [31] Weng, D.F.; Wang, Z.M.; Gao, S. *Chem. Soc. Rev.* **2011**, *40*, 3157–3181.
- [32] Stroppa, A.; Jain, P.; Barone, P.; Marsman, M.; Perez-Mato, J.M.; Cheetham, A.K.; Kroto, H.W.; Picozzi, S. *Angewandte Chemie International Edition* **2011**, *50*, 5847–5850.
- [33] Di Sante, D.; Stroppa, A.; Jain, P.; Picozzi, S. *Journal of the American Chemical Society* **2013**, *135*, 18126–18130,
- [34] Stroppa, A.; Barone, P.; Jain, P.; Perez-Mato, J.M.; Picozzi, S. *Advanced Materials* **2013**, *25*, 2284–2290.
- [35] Jain, P.; Stroppa, A.; Nabok, D.; Marino, A.; Rubano, A.; Paparo, D.; Matsubara, M.; Nakotte, H.; Fiebig, M.; Picozzi, S.; Choi, E.S.; Cheetham, A.K.; Draxl, C.; Dalal, N.S.; Zapf, V.S. **2016**. *1*, 16012 EP –. Article.
- [36] Tian, Y.; Stroppa, A.; Chai, Y.; Yan, L.; Wang, S.; Barone, P.; Picozzi, S.; Sun, Y. **2014**. *4*, 6062 EP –. Article.
- [37] Tian, Y.; Stroppa, A.; Chai, Y.S.; Barone, P.; Perez-Mato, M.; Picozzi, S.; Sun, Y. *physica status solidi (RRL) Rapid Research Letters* **2015**, *9*, 62–67.
- [38] Zhao, W.P.; Shi, C.; Stroppa, A.; Di Sante, D.; Cimpoesu, F.; Zhang, W. *Inorganic Chemistry* **2016**, *55*, 10337–10342,
- [39] Gmez-Aguirre, L.C.; Pato-Doldán, B.; Stroppa, A.; Yez-Vilar, S.; Bayarjargal, L.; Winkler, B.; Castro-García, S.; Mira, J.; Sánchez-Andújar, M.; Señarís-Rodríguez, M.A. *Inorganic Chemistry* **2015**, *54*, 2109–2116,
- [40] Kamminga, M.E.; Stroppa, A.; Picozzi, S.; Chislov, M.; Zvereva, I.A.; Baas, J.; Meetsma, A.; Blake, G.R.; Palstra, T.T.M. *Inorganic Chemistry* **2017**, *56*, 33–41,
- [41] Ptak, M.; Maczka, M.; Gagor, A.; Sieradzki, A.; Stroppa, A.; Di Sante, D.; Perez-Mato, J.M.; Macalik, L. *Dalton Trans.* **2016**, *45*, 2574–2583.
- [42] Ghosh, S.; Di Sante, D.; Stroppa, A. *The Journal of Physical Chemistry Letters* **2015**, *6*, 4553–4559,
- [43] Mazzuca, L.; Cañadillas-Delgado, L.; Rodríguez-Velamazán, J.A.; Fabelo, O.; Scarrozza, M.; Stroppa, A.; Picozzi, S.; Zhao, J.P.; Bu, X.H.; Rodríguez-Carvajal, J. *Inorganic Chemistry* **2017**, *56*, 197–207,

- [44] B. Kundys, A. Lappas, M. Viret, V. Kapustianyk, V. Rudyk, S. Semak, Ch. Simon, and I. Bakaimi, *Phys Rev B*, **81**, 224434 (2010)
- [45] Liu, S.; Cohen. R. E. *J. Phys. Chem. C*, **2016**, 120, 17274-17281.
- [46] Li, W.; Thirumurugan, A.; Barton, P. T.; Lin, Z.; Henke, S.; Yeung, H. H-M.; Wharmby, M. T.; Bithell, E. G.; Howard, C. J.; Cheetham, A. K. *J. Am. Chem. Soc.*, **2014**, 136, 7801-7804.
- [47] Banerjee, H.; Kumar, M.; Saha-Dasgupta, T. *Phys. Rev B.*, **2014**, 90, 174433.
- [48] Kahn, O.; Kröber, J.; Jay. C. *Adv. Mat.*, **1992**, 4, 718-728.
- [49] Kahn, O.; Martinez, C. J. *Science*, **1998**, 279, 44-48.
- [50] Gregor Kieslich, Shijing Suna and Anthony K. Cheetham, *Chemical Science*, 5, 4712, 2014.
- [51] Li, N.; Manoun, B.; Tang, L.; Ke, F.; Liu, F.; Dong, H.; Lazor, P.; Yang, W. *Inorg. Chem.*, **2016**, 55, 6770-6775
- [52] Kresse, G.; Hafner, J. *Phys. Rev. B (R)*, **1993**, 47, 558.
- [53] Kresse, G.; Furthmuller, J. *Phys. Rev. B*, **1996**, 54, 11169.
- [54] Blöchl, P. E. *Phys. Rev. B*, **1994**, 50, 17953.
- [55] Perdew, J. P.; Burke, K.; Ernzerhof, *Phys. Rev. Lett.*, **1996**, 77, 3865.
- [56] Liechtenstein, A.I.; Anisimov, V. I.; Zaanen, J. *Phys. Rev. B (R)*, **1995**, 52, R5467.
- [57] Murnaghan, F. D.; *Proceedings of the National Academy of Sciences of the United States of America*, **1944**, 30, 244-247.
- [58] Sanchez-Andujar, M.; Presedo, S.; Yanez-Vilar, S.; Castro-Garcia, S.; Shamir, J.; Senaris-Rodriguez, M.A. *Inorganic Chemistry*, **2010**, 49, 1510-1516.
- [59] Liu, B.; Shang, R.; Hu, K-L.; Wang, Z-M.; Gao, S. *Inorg. Chem.*, **2012**, 51, 13363-13372.
- [60] Boukheddaden, K.; Miyashita, S.; Nishino, M. *Phys. Rev. B*, **2007**, 75, 094112.

- 
- [61] Jeschke, H. O.; Salguero, L. A.; Rahaman, B.; Buchsbaum, C.; Pashchenko, V.; Schmidt, M. U.; Saha-Dasgupta, T.; Valenti, R. *New Journal of Physics*, **2007**, 9, 448.
- [62] Gütlich, Philipp; Gaspar, Ana. B; Garcia, Yann. *Beilstein J. Org. Chem.*, **2013**, 9, 342.

# Chapter 5

## Electronic Structure of Oxide Interfaces: A Comparative Analysis of $\text{GdTiO}_3/\text{SrTiO}_3$ and $\text{LaAlO}_3/\text{SrTiO}_3$ Interfaces

### 5.1 Introduction

Metal oxide perovskites constitute one of the largest classes of oxide materials. A general discussion of perovskite metal oxide materials along with some introduction to the possible distortions in the perovskite lattice has been given in Chapter 1. In this section we discuss further details of the distortions in the perovskite lattice and in particular how it may affect the heterostructure systems we intend to study.

One of the primary types of distortions in perovskite materials is gadolinium ferrite  $\text{GdFeO}_3$  type distortion. Owing to this distortion the corner shared  $\angle\text{B-O-B}$  deviates from the ideal value of  $180^\circ$  as shown in right panel of Figure 5.1, in comparison to a perfect cubic perovskite structure shown in the left panel. Primarily this distortion arises due to mismatch between A site and B site ionic radii. It is the  $\text{GdFeO}_3$  distortion which reduces the symmetry of the perfectly cubic perovskite to lower symmetries like orthorhombic, or tetragonal symmetries. This is intrinsic to the entire series of rare earth orthogallates and is responsible for reducing the  $d$  band width of the B site which is driven by the B-O-B covalency.

---

This chapter is based on "Electronic Structure of Oxide Interfaces: A Comparative Analysis of  $\text{GdTiO}_3/\text{SrTiO}_3$  and  $\text{LaAlO}_3/\text{SrTiO}_3$  interfaces", *Hrishit Banerjee*, Sumilan Banerjee, Mohit Randeria, Tanusri Saha-Dasgupta **Scientific Reports** **5**, 18647 (2015)

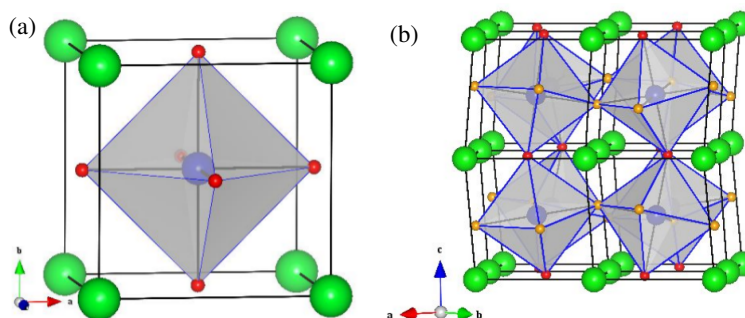


Figure 5.1: Cubic and distorted perovskites. Figure (a) on the left panel shows a perfectly cubic perovskite structure with no distortion as found for example in SrTiO<sub>3</sub>. Figure (b) on the right panel shows a perovskite structure with what is known as GdFeO<sub>3</sub> type distortion where there is rotation of the octahedra in plane and tilt of the octahedra out of plane.

This GdFeO<sub>3</sub> distortion will have particular bearing on our further discussion of the crystal structure of perovskite heterostructures in a later section.

Another type of distortion which is particularly important in case of perovskites is the Jahn-Teller distortion [1]. In Chapter 1 the Jahn Teller breathing modes have already been defined. In this section we discuss how the Jahn Teller distortion affects the splitting of the  $d$  energy levels of the B site in a perovskite structure. The Jahn-Teller theorem in its most general form states that any non-linear molecule with a spatially degenerate electronic ground state will undergo a geometric distortion that removes that degeneracy, because the distortion helps in lowering the overall energy of the species. In case of perovskites, this occurs in the form of contraction or elongation of the metal-oxygen octahedra. In absence of any Jahn-Teller effect we have the usual crystal field splitting of the degenerate  $d$  orbitals into  $t_{2g}$  orbitals comprising of  $d_{xy}$ ,  $d_{yz}$ ,  $d_{zx}$  orbitals and  $e_g$  orbitals comprising of  $d_{z^2}$ ,  $d_{x^2-y^2}$  orbitals, shown in left panel of Figure 5.2. Compression of octahedra results in a Jahn-Teller distortion which lifts the degeneracy by the stabilization of the  $d$  orbitals without a  $z$  component, while the orbitals with a  $z$  component are destabilized as shown in middle panel of Figure 5.2. This is due to the  $z$ -component  $d$  orbitals having greater overlap with the ligand orbitals, resulting in the orbitals being higher in energy. Since the  $d_{z^2}$  orbital is antibonding, it is expected to increase in energy due to compression. The  $d_{xz}$  and  $d_{yz}$  orbitals are nonbonding, but these are destabilized due to the interactions. Elongation of octahedra results in a type of Jahn-Teller distortion in which the degeneracy is broken by the stabilization (lowering in energy) of the  $d$  orbitals with a  $z$  component, while the orbitals without a  $z$  component are destabilized (higher in energy) as shown in the right panel of Figure 5.2. This is due to the  $d_{xy}$  and  $d_{x^2-y^2}$  orbitals having greater overlap with the ligand orbitals, resulting

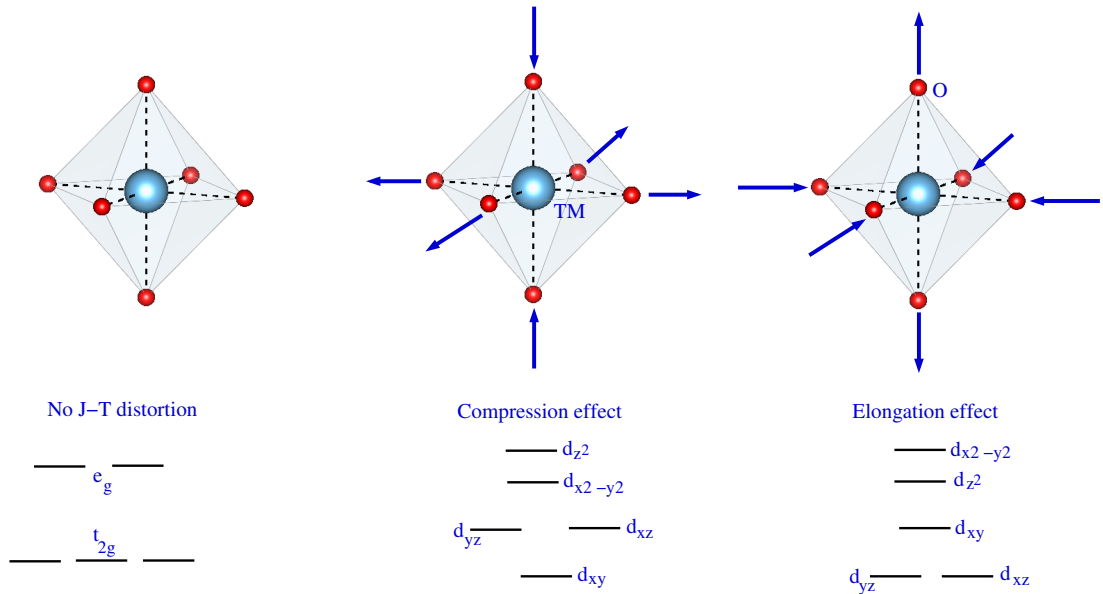


Figure 5.2: Schematic diagram showing tetragonal distortion (compression/elongation) for an octahedral complex. The top panel shows the compression and elongation effects. The bottom panel shows the effect of compression or elongation on the distribution of orbitals and the lift of degeneracy in energy of the orbitals.

in the orbitals being higher in energy. Since the  $d_{x^2-y^2}$  orbital is antibonding, it is expected to increase in energy due to elongation. The  $d_{xy}$  orbital is nonbonding, however it is destabilized due to the interactions.

### 5.1.1 Different kinds of Insulators

In this chapter we shall discuss the interfaces between different kinds of perovskite oxide insulators. Let us thus first discuss the various kinds of insulators, the insulating properties being driven by different mechanisms.

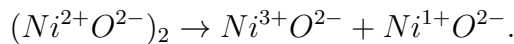
Based on the mechanism we primarily identify five different kinds of insulators:

1. Band insulator (band structure driven)
2. Mott insulator (correlation driven)
3. Charge transfer insulator (charge transfer process driven)
4. Anderson insulator (disorder driven)
5. Jahn Teller insulator (geometry driven)

**Band insulators:** These are insulators by virtue of their basic band structure and form the most common class of insulators that are found in nature. A band insulator fits all the standard one-electron criteria of being an insulator, i.e. it possesses an even number of valence electrons per unit cell, has an integral number

of filled bands, and a band gap.

**Mott insulators:** A class of insulators that should conduct electricity under conventional band theories, but are insulators when measured experimentally (particularly at low temperatures). Although the band theory of solids has been very successful in describing various electrical properties of materials, in 1937 Jan Hendrik de Boer and Evert Johannes Willem Verwey pointed out that a variety of transition metal oxides predicted to be conductors by band theory (because they have an odd number of electrons per unit cell) are insulators. Neville Mott and Rudolf Peierls [2] then (also in 1937) predicted that this anomaly can be explained by including interactions between electrons. In 1949, in particular, Mott proposed a model for NiO as an insulator, where conduction is based on the formula



Circumstanced as such, the formation of an energy gap preventing conduction can be understood as the competition between the Coulomb potential  $U$  between  $3d$  electrons and the transfer integral  $t$  of  $3d$  electrons between neighbouring atoms (the transfer integral is a part of the tight-binding approximation). The energy gap is then

$$E_{gap} = U - 2zt,$$

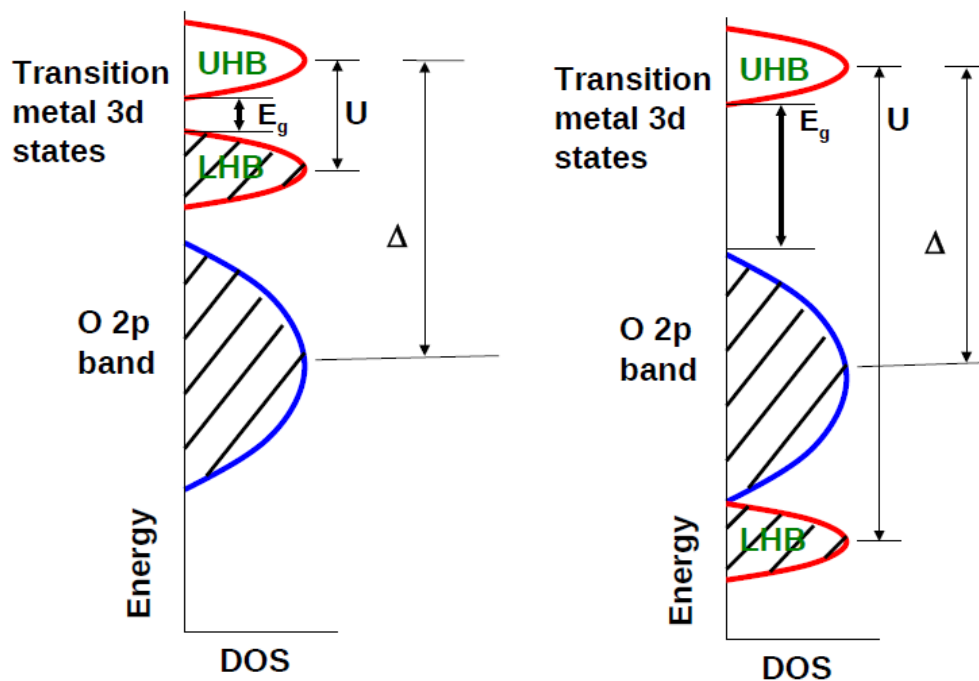
where  $z$  is the number of nearest-neighbour atoms. In general, Mott insulators occur when the repulsive Coulomb potential  $U$  is large enough to create an energy gap. One of the simplest theories of Mott insulators is the 1963 Hubbard model.

**Charge-transfer insulators:** These are also a class of materials predicted to be conductors following conventional band theory, but which are in fact insulators due to a charge-transfer process. Unlike Mott insulators, where the insulating properties arise from electrons hopping between unit cells, the electrons in charge-transfer insulators move between atoms within the unit cell [3]. In the Mott-Hubbard case, it is far more convenient for electrons to transfer between two adjacent metal sites (on-site Coulomb interaction  $U$ ); in the charge-transfer case, however it's easier to facilitate a transfer from the anion to the metal (charge-transfer energy  $\Delta$ ).  $U$  is determined by repulsive/exchange effects between the cation valence electrons.  $\Delta$  is tuned by the chemistry between the cation and anion. Determining the size of the on-site Coulomb interactions  $U$  is quite complicated. A hand waving approximation is that it's the energy for two metals  $M^{m+}$  to go to  $M^{(m+1)+}$  and  $M^{(m-1)+}$ . The Lower Hubbard Band (LHB) therefore reflects the metal electron energy in the former configuration and the Upper Hubbard Band (UHB) reflects the metal electron energy in the latter configuration. So a rough intuitive estimate for  $U$  is the difference between the metal's ionization potential and electron affinity. The charge-transfer gap is defined as the electronegativity difference between the cation and anion in the crystal lattice - which is quite different from atomic electronegativity, although

similar in certain respects. Anions are naturally unstable in vacuum. In contrast to cations, they require the surrounding crystal lattice to stabilize their electronic energy, which alters their electronegativity. The electrostatic potential of the surrounding ions (the Madelung potential) reduces their electron energy and increases their electronegativity. This is what makes the  $p$  states lower in energy than the metal's  $d$  states to begin with. However, the Madelung potential destabilizes the transition metal's  $d$  states, raising them in energy: the cations are surrounded by negatively charged anions, making it more difficult for electrons to occupy those states. Thus, one may be able to tune the size of the charge-transfer gap  $\Delta$  by making use of the Madelung potential, the electronegativity of the cation, and the electronegativity of the anion. Based on trends in ionization potentials/electron affinities and the estimates described above, we can thus see that late transition metals or transition metals with high oxidation states will have higher  $U$  and smaller  $\Delta$ , resulting in the LHB lying below the anion  $p$ -band. On the other hand, early transition metals or transition metals with low oxidation states will have lower  $U$  and larger  $\Delta$ , which is consistent with Mott-Hubbard behaviour. The covalency between the transition metal and anion also plays an extremely important role in this case. A comparison of Mott Hubbard insulator with the charge transfer insulator has been shown schematically in Figure 5.3. Here we see how the band structures of the two types of closely related insulators differ from each other, and the relations of  $U$  and  $\Delta$  as described above.

**Anderson insulators:** These insulators are driven by the presence of disorder in the system. These are the result of Anderson localisation, which is defined as the absence of diffusion of waves in a disordered medium. Named after the American Nobel laureate P. W. Anderson, who suggested that electron localization is possible in a lattice potential, provided that the degree of disorder in the lattice is sufficiently large, as is often seen in experiments for example in a semiconductor with impurities or defects. This localization theory suggests that a disorder-induced metal-insulator transition (MIT) exists for a system of non-interacting electrons in 3D systems at zero magnetic field and in the absence of spin-orbit coupling. In 1D and 2D systems, the same theory shows that there are no extended states and thus no MIT. However, since 2D is the lower critical dimension of the localization problem, the 2D case is in certain senses close to 3D: the states are only marginally localized for weak disorder and a small spin-orbit coupling can lead to the existence of extended states and thus a MIT. Consequently, the correlation lengths of a 2D system with potential-disorder can be quite large so that in numerical approaches one may find a localization-delocalization transition when either decreasing system size for fixed disorder or increasing disorder for fixed system sizes.

**Jahn Teller Insulators:** These materials become insulating due to the presence of Jahn Teller distortions in the system. If the TM-O octahedra is either elongated or compressed in the perovskite oxide classes of materials that we shall



Mott-Hubbard insulator:  $\Delta > U > U_c$  Charge-transfer insulator:  $U > \Delta > \Delta_c$

Figure 5.3: A schematic diagram showing the difference in band structure between the two closely related systems of Mott insulators and charge transfer insulators. The left panel shows a schematic density of states (DOS) for a Mott insulator with the various energy scales marked and the right panel shows a similar schematic for that of a charge transfer insulator.

primarily be considering, as we have pointed out before there occurs a breakdown of the degeneracy in the  $t_{2g}$  and  $e_g$  orbitals which causes the system to become insulating. If the Jahn Teller distortions in the system are reduced due to some geometrical effects, one may find these systems to show a transition from an insulating to a metallic state.

### 5.1.2 Oxide Heterostructures

A heterostructure of two compounds forms the interface that occurs between two layers or regions of dissimilar crystalline semiconductors or in our case perovskite oxides. Heterostructure fabrication generally requires the use of molecular beam epitaxy (MBE), chemical vapor deposition (CVD), or pulsed laser deposition (PLD) techniques in order to precisely control the deposition thickness and create a sharp lattice-matched abrupt interface.

Heterostructures have found use in a variety of specialized applications where their unique characteristics are critical:

1. Lasers: Using heterojunctions in lasers was first proposed in 1963 when Herbert Kroemer, who famously proclaimed in this Nobel lecture "Interface is the device", suggested that population inversion could be greatly enhanced by heterostructures. By incorporating a smaller direct band gap material like GaAs between two larger band gap layers like AlAs, carriers can be confined so that lasing can occur at room temperature with low threshold currents.

2. Junction transistors: When a heterostructure is used as the base-emitter junction of a bipolar junction transistor, an extremely high forward gain and low reverse gain result. This results in excellent frequency operation and very meagre leakage currents. This device is called a heterojunction bipolar transistor (HBT).

3. Field effect transistors: Heterostructures are also used in high electron mobility transistors (HEMT) which work at extremely high frequencies. The proper band alignment gives rise to extremely high electron mobilities by creating a 2 dimensional electron gas (2DEG) within a dopant free region where very little scattering can occur.

As mentioned in the previous section the metal oxide perovskite family, includes a huge number of different types of structures, and at the same time different elements of the periodic table, giving rise to wide variety of physical properties. In this chapter we are interested in heterostructures arises out of layered combination of different types of insulating transition metal oxides. The perovskite oxides  $ABO_3$  may be thought of as alternating AO and  $BO_2$  layers. Here we have considered layered heterostructure interface between a Mott Insulator and a band insulator and studied it in contrast to an interface between two band insulators and demonstrated the effect of correlation in these types of systems. Carefully controlled interfaces between two materials can give rise to novel physical phenomena and functionalities not exhibited by either of the

constituent materials alone. Modern synthesis methods have yielded heterostructures and superlattices of oxide materials with competing quantum many-body states. In order to explore new correlation-driven interface phenomena, we try to understand and manipulate spin, charge and orbital order at oxide interfaces.

Oxide heterostructures span a wide range of combinations of complex oxides and play host to an incredible variety of physical phenomena. High dielectric permittivities, piezo-, pyro-, and ferroelectricity are just a few of the functionalities offered by this class of materials, while the potential for applications of the more exotic properties like high temperature superconductivity and colossal magnetoresistance is still waiting to be fully exploited. With recent advances in deposition techniques, the structural quality of oxide heterostructures now rivals that of the best conventional semiconductors, taking oxide electronics to a new level. Such heterostructures have enabled the fabrication of artificial multifunctional materials. At the same time they have exposed a wealth of phenomena at the boundaries where compounds with different structural instabilities and electronic properties meet, giving unprecedented access to new physics emerging at oxide interfaces.

Following the pioneering work by Ohtomo and Hwang [4] on LAO/STO, there has been much effort in understanding the interface between two different insulating  $ABO_3$  perovskites. The [001] stacking consists of AO and  $BO_2$  layers, which are charge neutral in one of the oxides like the  $(SrO)^0$  and  $(TiO_2)^0$  layers in STO, but have charge +1/-1 in the other oxides, like LaO and  $AlO_2$  in LAO. This creates a polar discontinuity at the interface of the two types of oxides and a build up of electrostatic potential, which can only be averted by a transfer of charge to the interface. The 2DEG that results from this simple *polar catastrophe* (described in subsequent section) picture should lead to an interface carrier density of  $0.5e^-/IF$ , corresponding to  $\sim 3.3 \times 10^{14} cm^{-2}$ , much larger than that achieved in conventional semiconductor hetero-junctions.

### 5.1.3 Polar catastrophe hypothesis

Polar catastrophe or divergence catastrophe hypothesis was the first and most successful mechanism used to explain the conductivity at  $LaAlO_3/SrTiO_3$  interfaces. It postulates that  $LaAlO_3$ , which is polar in the 001 direction (with alternating sheets of positive and negative charges), act as an electrostatic gate on the insulating  $SrTiO_3$ . It is an allusion to the scenario where a sudden jump in potential occurs from charge neutral SrO and  $TiO_2$  layers to the charged LaO and  $AlO_2$  layers which have charges of +1 and -1 respectively. Due to this jump in charge as shown in Figure 5.4 there is a corresponding jump in electric field and the voltage in the  $LaAlO_3$  section builds up forever and diverges eventually. Thus this hypothesis has also been called the divergence catastrophe hypothesis. Of course it is highly unlikely that such a divergence in potential can exist in nature

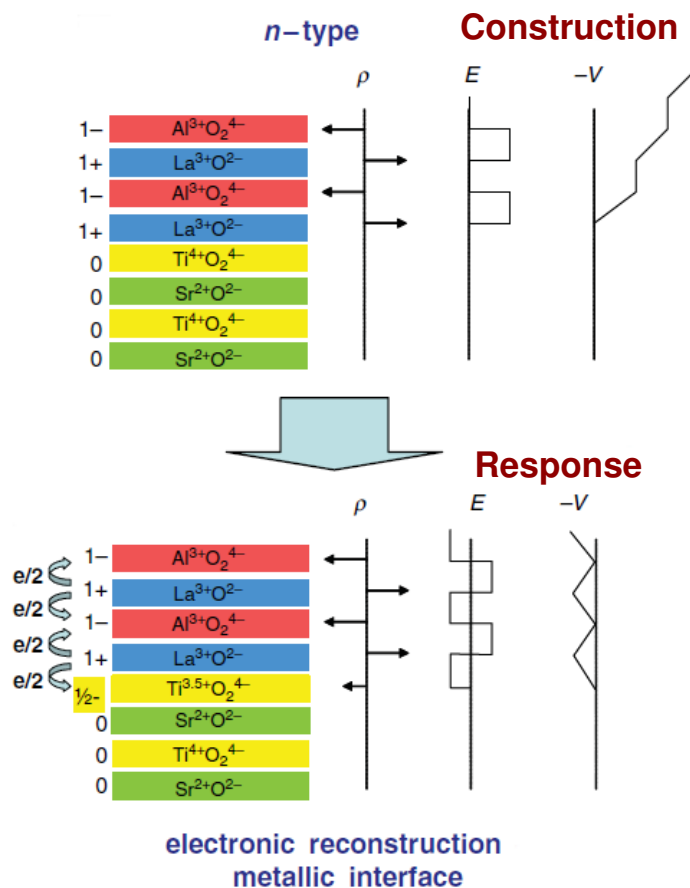


Figure 5.4: Diagram demonstrating the polar catastrophe hypothesis and the associated electronic reconstruction in an *n*-type interface. Figure adapted from J. Mannhart et al, MRS Bull. 33 1027 (2008)

and hence it is avoided by means of an electronic reconstruction, where, half an electron per unit cell is transferred to the interface  $\text{TiO}_2$  layer and consequently half a hole is transferred to the surface  $\text{AlO}_2$  layer. This is how the origin of half an electron charge at the interface of two insulators have been explained. This has also been called electron reconstruction hypothesis highlighting the fact that electrons, not ions, move to compensate the potential buildup.

#### 5.1.4 Existing studies on Oxide heterostructures

The *n*-type interface in LAO/STO heterostructures is the most studied of all oxide interfaces. [5–8] It exhibits gate-tunable superconductivity and in addition shows signatures of local moments and possible ferromagnetism [9–12] coexisting with the superconductivity. The density of itinerant carriers, however, is consis-

tently found to be an order of magnitude smaller [13–15] than  $0.5e^-/\text{interface}$ , the value expected from the polar catastrophe model. In addition, the interfaces are insulating, rather than being metallic, below a certain critical thickness of LAO layers. [15]

A more recent development is the study of the  $n$ -type interface between the Mott insulator GTO and the band insulator STO grown by molecular beam epitaxy. [16–18] Remarkably, the GTO/STO samples give rise to 2DEGs with carrier densities of  $0.5e^-/\text{interface}$ , exactly as expected from the ideal polar catastrophe scenario. Furthermore, the GTO/STO interface is found to be conducting irrespective of layer thickness of GTO, and hence there is no thickness threshold for metallic behavior. In both these respects GTO/STO seems to be qualitatively different from LAO/STO.

The GTO/STO interface also shows many other interesting properties. Quantum oscillation experiments have corroborated the presence of confined 2DEG and revealed the possibility of a sub-band structure different from LAO/STO. [16–18] Below a certain STO thickness, the interface has been found to exhibit signs of ferromagnetism, which might be an intrinsic property induced by electronic correlations in the high-density 2DEG, rather than induced by the proximity to ferromagnetic GTO layer. [19] The signatures of strong electronic correlations have also been observed in transport measurements [20] and this has led to the theoretical proposal of dimer Mott insulator for single SrO layer sandwiched between GTO layers. [21]

An extremely striking result for the 2DEG at the interface between another strongly correlated Mott insulator  $\text{LaTiO}_3$  (LTO) and  $\text{SrTiO}_3$  has been the observation of a 2D superconducting state [22]. The mechanism responsible for the onset of superconductivity is debatable. The effect of correlations in this Mott insulator is yet to be clarified. It has been shown that in spite of STO being a band insulator and the expected electronic correlations being present in LTO, the  $\text{LaTiO}_3/\text{SrTiO}_3$  interface 2DEG undergo a superconducting transition at a critical temperature  $T_c \sim 300\text{mK}$ . It was also found that the superconducting electron gas is confined over several layers of thickness of 12 nm and is located as usual on the STO substrate.

Another highly interesting case of conductivity and magnetism at oxide heterointerface arises at an interface between  $\text{LaMnO}_3$  (LMO) and  $\text{SrMnO}_3$  (SMO) [23]. Individually, both these oxides are antiferromagnetic insulators in their bulk ground state, however at their interface, a double-exchange ferromagnetism arises in analogy to the behavior of their bulk solid solution, the famous colossal magnetoresistance manganites. Here, the interface charge reconstruction has been experimentally observed by resonant x-ray scattering [24], providing another intriguing instance of novel two-dimensional states that may be induced by manipulating oxide heterostructures.

Motivated by all these observations, we present here a detailed electronic

structure study of the GTO/STO interface which is a Mott insulator/band insulator interface and contrast our results with those obtained for LAO/STO which is an interface between two band insulators. While the LAO/STO interface has been thoroughly studied by electronic structure calculations, [25–27] much less is known about GTO/STO. The specific problem of single SrO layer in a GTO matrix in the superlattice geometry has been studied [21, 28, 29] by a variety of techniques, first-principles, model Hamiltonian as well as combined density functional theory (DFT) and dynamical mean field theory (DMFT). There have been some suggestions [30] about the origin of the differences between the LAO/STO and GTO/STO systems, but to the best of our knowledge, no first principles electronic structure study exists which compares the LAO/STO and GTO/STO interfaces on same footing in different heterostructure geometries. Gaining insight into GTO/STO and into the differences and similarities with LAO/STO is very important for further advancement in the field of oxide interfaces.

## 5.2 Computational details

Our first-principles calculations are based on plane wave basis as implemented in the Vienna Ab-initio Simulation Package (VASP) [31,32] with projector-augmented wave (PAW) potential. [33] The exchange-correlation functional is chosen to be that given by generalized gradient approximation (GGA). [34] Since we are not interested in the magnetism of Gd spins in the present study, in the plane-wave calculations for the results reported here, the Gd f electrons are considered to be part of the core orbitals. The correlation effect beyond GGA is taken into account through supplemented on-site Hubbard  $U$  correction in form of GGA+ $U$ . [35] The use of GGA+ $U$  turn out to be crucial for the correct description of the Mott insulating behavior of GTO. A  $U$  value of 7eV at Ti site is found adequate to describe the insulating solution. The Hunds coupling parameter  $J_H$  is chosen to be 1 eV. We have thus consistently used  $U = 7$  eV and  $J_H = 1$  eV on Ti d states throughout our calculations. We found a smaller  $U$  value ( $\approx 4$  eV) within the linear muffin tin orbital (LMTO) basis calculation to be sufficient to drive bulk GTO insulating, a value more consistent with spectroscopic considerations. The fact that different  $U$  values are needed in different basis set implementations of DFT has been appreciated in the literature [36]. We found in our LMTO calculations of bulk GTO that taking into account the effect of  $U$  on both Ti d and Gd f states, with choice of  $U_{Ti} = 4$  eV and  $U_{Gd} = 9$  eV, and  $J_H = 1$  eV, resulted in a ferrimagnetic ground state with antiparallel alignment of the Ti and Gd spins, consistent with experiment.

The in-plane lattice constants of the simulation cells are fixed at the experimental lattice constant of STO with a value of 3.91 Å, while the out-of-plane lattice constant is allowed to relax. The consideration of tilt and rotation of

metal-oxygen octahedra becomes rather important for GTO with significant orthorhombic distortion. In order to take that into account, the in-plane dimension of the simulation cell is expanded by  $\sqrt{2} \times \sqrt{2}$ . Internal positions of the atoms are allowed to relax until the forces become less than  $0.01 \text{ eV}/\text{\AA}$ .

For the calculations carried out on thin film geometry, the thickness of vacuum layer is chosen to be  $16 \text{ \AA}$ . The effect of the artificial electric field in vacuum due to periodic boundary condition is taken into account through dipole correction, as implemented in VASP. The effect of this artificial electric field is however small, as shown in the detailed calculation by Chen et al. [27] in Appendix B1 of their paper. Considering the dielectric constants of STO and that of LAO and GTO, as shown by Chen et al. [27] the field in STO is found to be only about 0.3% of that in LAO or GTO for a vacuum thickness of  $16 \text{ \AA}$ . Further to establish the convergence of our calculations in terms of vacuum layer thickness, we have carried out additional calculations considering an increased thickness of vacuum layer ( $30 \text{ \AA}$ ). We found from our conclusions concerning the carrier density, minimum thickness of conductivity to remain unchanged, justifying physical soundness of our calculations. The situation becomes different in presence of external electric field which is not considered in the present study.

### 5.3 Heterostructure Geometries

A study of both experimental and theoretical literature [4–6, 16–18, 37–39] shows that the oxide interfaces have been investigated in two different geometries, (i) superlattice geometry with periodic repetition of alternating layers of STO and, LAO or GTO, and (ii) thin overlayer of LAO or GTO grown on a STO (001) substrate. Most experimental study on LAO/STO is carried out on overlayer geometry, the opposite being true for GTO/STO. Since we would like to have a comparative study of the two systems with an aim to arrive at a common understanding, in the present study we consider both the geometries, as shown in Figure 5.5. Following the experimental literature on GTO/STO, [16–18] we consider only the  $n$ -type IFs, *i.e.* that formed between GdO layer from GTO and  $\text{TiO}_2$  layer from STO in GTO/STO, and IFs formed between LaO and  $\text{TiO}_2$  in LAO/STO. Within the superlattice geometry, two symmetric  $n$ -type interfaces in the cell are considered which resulted in non-stoichiometric supercells with additional  $\text{TiO}_2$  layer in STO and an additional GdO (LaO) layer in GTO (LAO). This resulted in general formula of the superlattices being  $(\text{LAO})_{p.5}/(\text{STO})_{q.5}$  or  $(\text{GTO})_{p.5}/(\text{STO})_{q.5}$ . Calculations are carried out for choices of  $p = 1, 2, 3, 4$  and  $q = 4$  and  $9$ .

The adopted geometry of thin film-substrate, as shown in bottom panel of Figure 5.5, creates a single  $n$ -type interface and a surface of  $\text{TiO}_2$  (in case GTO/STO) or  $\text{AlO}_2$  (in case of LAO/STO) facing the vacuum. The general formula of the

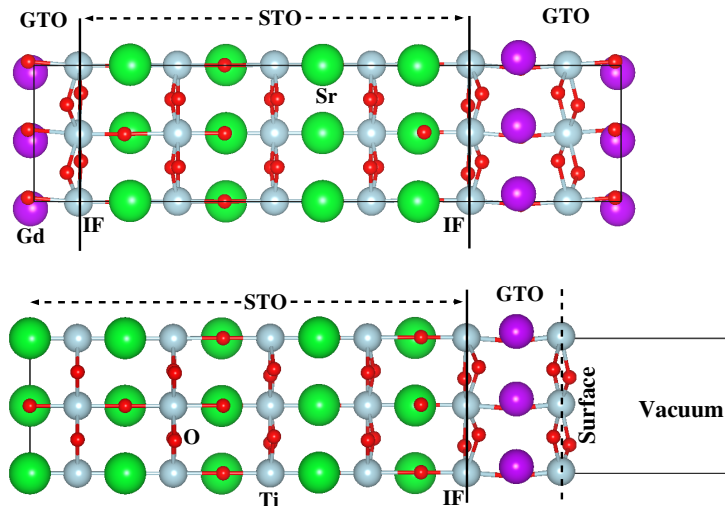


Figure 5.5: The two geometries used in the present study, the superlattice (upper panel) and the thin film-substrate (lower panel) geometry. Shown are the representative cases of  $(\text{GTO})_{1.5}/(\text{STO})_{4.5}$  superlattice and  $(\text{GTO})_1/(\text{STO})_5$  thin film-substrate geometry, projected onto the  $ac$  plane. The large, medium and small balls represent Sr/Gd, Ti and O atoms, respectively. The interfaces, formed between GdO from GTO and  $\text{TiO}_2$  layers from STO, are marked.

thin film-substrate systems is  $(\text{LAO})_p/(\text{STO})_q$  or  $(\text{GTO})_p/(\text{STO})_q$ . Calculations are carried out for choices of  $p = 1, 2, 3, 4, 5$  and  $q = 9$ .

The inplane dimensions of the simulation cell is expanded by  $\sqrt{2} \times \sqrt{2}$  creating two Ti or Al atoms in the  $\text{BO}_2$  layers in the unit cell to take into account the  $\text{GdFeO}_3$ -type orthorhombic distortion characterized by tilt and rotation of the  $\text{TiO}_6/\text{AlO}_6$  octahedra. This becomes specially important for the GTO/STO system, as we will see in the following sections.

## 5.4 Structure

We first start with discussion of the structural properties of the studied heterostructures. As mentioned already, the presence of  $\text{GdFeO}_3$ -type orthorhombic distortion forms an important structural aspect of GTO. This distortion in bulk GTO makes the structural properties of the optimized GTO/STO systems rather different compared to that of LAO/STO. Structural distortions observed include the tilt and rotation of the metal (M) - oxygen(O) octahedra as well as the compression or elongation of the individual  $\text{MO}_6$  octahedra. Figure 5.6 shows the plots of the deviation of M-O-M bondangle from  $180^\circ$ , as well as the difference between out-of-plane and in-plane M-O bondlengths. The former quantifies the

tilt/rotation of  $\text{MO}_6$  octahedra, while the latter quantifies the compression (for negative sign) or elongation (for positive sign) of  $\text{MO}_6$  octahedra. The top panels of the figure show the result for the superlattice geometry while the bottom panels are for the thin film-substrate geometry. The qualitative behavior is similar between the two geometries.

For the GTO/STO systems, the deviation of the Ti-O-Ti bond angle from  $180^\circ$  is as high as  $30^\circ$  or so in the GTO side. This decreases systematically and reaches a value of about  $10^\circ - 5^\circ$  within the interior of STO block. For thin film-substrate geometry the tilt/rotation attains a constant value within the interior of STO, which is found to be substantial for rotation. At the interfaces, the tilt angles become highly asymmetric with two different out-of-plane tilt angles varying between about  $15^\circ$  and about  $25-30^\circ$ . The in-plane and out-of-plane M-O bondlengths become unequal in GTO layers, with maximum difference of  $0.1 - 0.2 \text{ \AA}$ , indicating distortion of the  $\text{TiO}_6$  octahedra. This distortion becomes smaller at IF and inside the STO block it attains a value of  $\approx 0.1 \text{ \AA}$  or smaller. The  $\text{MO}_6$  octahedra are compressed in GTO layers, and are elongated in STO block. For the thin film-substrate geometry, the distortion of  $\text{TiO}_6$  attains more or less a small constant value inside the interior of STO block.

In comparison, in LAO/STO, the deviation of M-O-M bond angle from  $180^\circ$  occurs only for rotation, which is much smaller in magnitude compared to GTO/STO. The rotation angles are only significant at the IFs or close to them with values of about  $5-9^\circ$ . The tilt angles are found to be zero. Like in GTO/STO, the metal-oxygen octahedra are compressed in LAO side and elongated in STO side.

The structural differences between GTO/STO and LAO/STO, specially in terms of tilt and rotation of  $\text{MO}_6$  octahedra, has important bearing on the orbital character of the conducting electrons at different layers, as will be elaborated in the following section.

## 5.5 Electronic and Magnetic Structure

Electronic structure of the optimized GTO/STO and LAO/STO heterostructures in both superlattice and thin film-substrate geometry has been analyzed in terms of density of states, charge and orbital populations.

Figure 5.7 shows the layer-wise density of states (DOS) projected to Ti  $xy$ ,  $xz$  and  $yz$  states in  $(\text{GTO})_{1.5}/(\text{STO})_{4.5}$  and  $(\text{LAO})_{1.5}/(\text{STO})_{4.5}$  superlattices. Qualitatively similar results are obtained for  $(\text{GTO})_{1.5}$  or  $(\text{LAO})_{1.5}/(\text{STO})_{9.5}$  superlattices, proving the physics in the superlattice geometry is independent of the STO thickness. First of all, we find both GTO/STO and LAO/STO superlattices are metallic with non-zero density of states at the Fermi level ( $E_F$ ). Since the layer thickness of GTO or LAO of 1.5 layers is the minimum possible within the superlattice geometry, we conclude that for both LAO/STO and GTO/STO

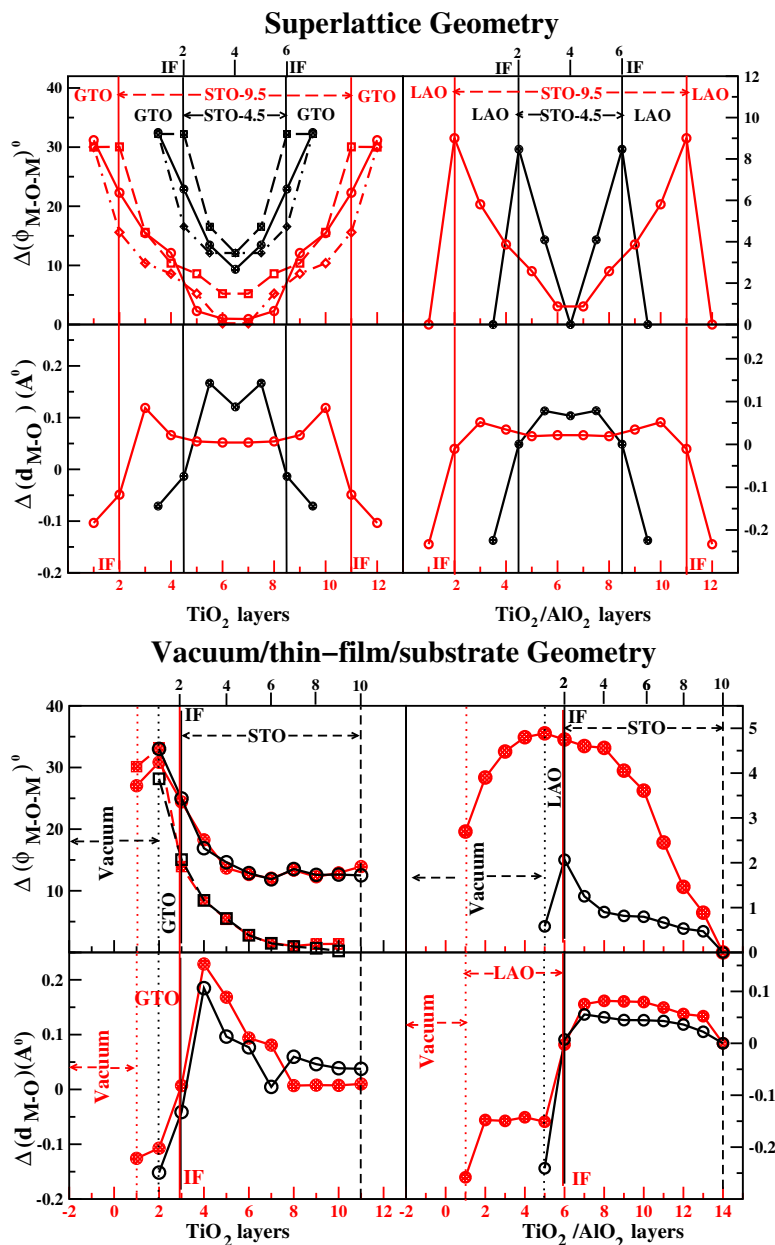


Figure 5.6: The deviation of M-O-M angles from  $180^\circ$ ,  $\Delta(\phi_{M-O-M})$  and the difference of M-O lengths in the out-of-plane and inplane directions,  $\Delta(d_{M-O})$  plotted as function of  $TiO_2$  layers, for LAO/STO (right panels) and GTO/STO (left panels) in superlattice and thin film-substrate geometries. Top left:  $\Delta(\phi_{M-O-M})$  for GTO/STO, top right:  $\Delta(\phi_{M-O-M})$  for LAO/STO. Bottom left:  $\Delta(d_{M-O})$  for GTO/STO, bottom right:  $\Delta(d_{M-O})$  for LAO/STO. In case of superlattices, results for two system sizes are shown,  $(LAO \text{ or } GTO)_{4.5}/(STO)_{1.5}$  (black symbols) and  $(LAO \text{ or } GTO)_{9.5}/(STO)_{1.5}$  (red symbols). In case of thin film-substrate geometries, results are shown for  $(GTO)_1/(STO)_9$  (black symbols),  $(GTO)_2/(STO)_9$  (red symbols), and  $(LAO)_1/(STO)_9$  (black symbols),  $(LAO)_5/(STO)_9$  (red symbols). For LAO/STO, only the rotation angles are shown as circles, the tilt angles being zero. The rotation and the asymmetric tilts in  $+c$  and  $-c$  directions in GTO/STO are shown as circles, squares and diamonds, respectively. The x-axis marked in red on normal side corresponds to layer numbering of the larger systems (shown in red symbols) while the x-axis marked in black on opposite side corresponds to layer numbering of the smaller systems (shown in black symbols).

superlattices, there is no critical thickness for conductivity. As expected, calculations with larger thickness of GTO and LAO (checked with thicknesses of 2.5, 3.5 and 4.5 unit cells), are also found to be metallic. We find in both superlattices, the conducting electronic charge is not strictly confined to the IF, and percolates to several layers in STO block, which is in agreement with experimental findings on LAO/STO. [40] Such behavior of LAO/STO superlattice has also been reported from theoretical calculations before. [41] It is interesting to note this is also the case for GTO/STO. Both superlattices, thus behave similarly as far as conduction goes. We, however, note the nature of the conduction electron is different in the two superlattices. Focusing on the DOS characters presented in Figure 5.7, we find that for both GTO/STO and LAO/STO, the carriers at the IFs are predominantly of  $xy$  character. The situation, however, is different in two systems in the other  $\text{TiO}_2$  layers in STO. The orbital characters of the carriers in these layers are rather mixed in case of GTO/STO, and mostly  $xz/yz$  in case of LAO/STO. This is also seen from the orbital occupancies shown in Figure 5.10 and charge density plots in Figure 5.11. This difference stems from the structural difference between GTO/STO and LAO/STO. To obtain the layer-wise contribution to the conduction electron, we integrate the layer projected DOS from 0.5 eV below  $E_F$  to  $E_F$ . For GTO/STO system this corresponds to integrating from the upper edge of the lower Hubbard band of Ti  $d$  in insulating GTO layer to  $E_F$ . The electron from  $\text{Ti}^{3+}$  ion in GTO layer in its  $d^1$  charge state occupies the localized lower Hubbard band and does not contribute to conduction. Table 5.1, shows the layer-wise contribution to the conduction electron for 1.5/4.5 as well as 1.5/9.5 superlattices. We find the total conduction charge in the LAO/STO as well as in GTO/STO superlattices to be  $1 e^-$  irrespective of the thickness of STO layers. This is fully consistent with the presence of two symmetric interfaces in the unit cell (u.c.), and a carrier density of  $0.5e^-$  per IF. Interestingly we find Ti  $d$  states at the IF of GTO and STO are spin-polarized, with Ti  $d$  states within STO layers adjacent to IF inheriting this spin-polarization, as shown in Figure 5.9. Moving further away from the IF, the spin-polarization decreases and finally vanishes deep inside the STO block.

The calculated magnetic moments at Ti sites are found to be  $\approx 0.15\mu_B$ ,  $\approx 0.12\mu_B$  in the STO layer next to IF,  $\approx 0.02\mu_B$  in the following layer, and vanishingly small in other layers. The Ti moments are found to be aligned in a ferromagnetic arrangement, consistent with experimental results.

A similar analysis in the thin film-substrate geometry shows dramatically different behavior. The left most and the middle panels in Figure 5.8, show the plot of the DOS in different  $\text{TiO}_2$  layers of LAO/STO in thin film-substrate geometry. The left and middle panels correspond to LAO/STO with two different thicknesses of LAO layers, 1 and 5 unit cells, respectively. We find the IF in 1 unit cell of LAO on STO is insulating with a large gap between the valence and conduction states, and zero states at  $E_F$ . On the other hand, 5 unit cell of LAO on

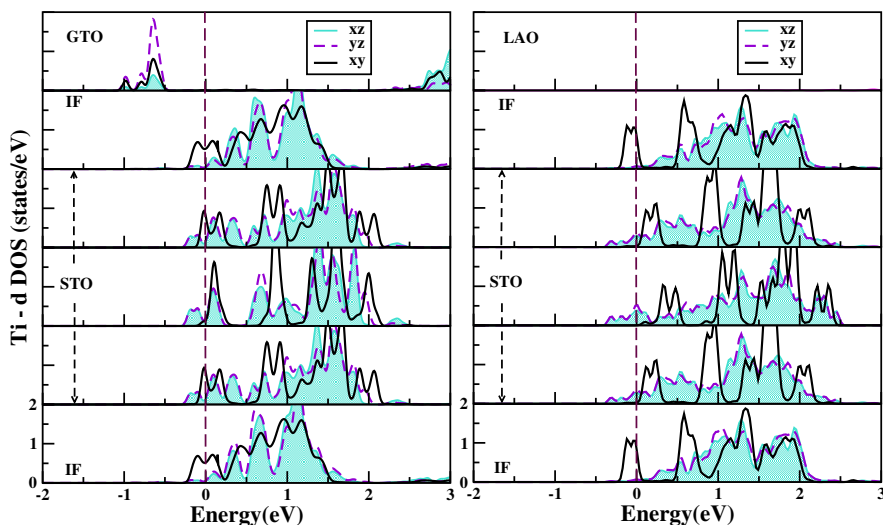


Figure 5.7: The density of states projected to  $xy$  (solid line),  $xz$  (shaded area),  $yz$  (dashed lines) orbitals of Ti, in different  $\text{TiO}_2$  layers of  $(\text{LAO})_{1.5}/(\text{STO})_{4.5}$  (right panels) and  $(\text{GTO})_{1.5}/(\text{STO})_{4.5}$  (left panels) superlattices. From top to bottom, different left panels refer to  $\text{TiO}_2$  in GTO,  $\text{TiO}_2$  at 1st IF, 1<sup>st</sup>, 2<sup>nd</sup> and 3<sup>rd</sup>  $\text{TiO}_2$  layers in STO block, and  $\text{TiO}_2$  at the 2nd IF in the cell. The cell is symmetric about the 2nd  $\text{TiO}_2$  layer in STO. Right hand panels refer to the same, except for the top most panel which refer to  $\text{AlO}_2$  layer in LAO, which shows no states in the chosen energy range. The zero of the energy is set at GGA+ $U$  Fermi energy.

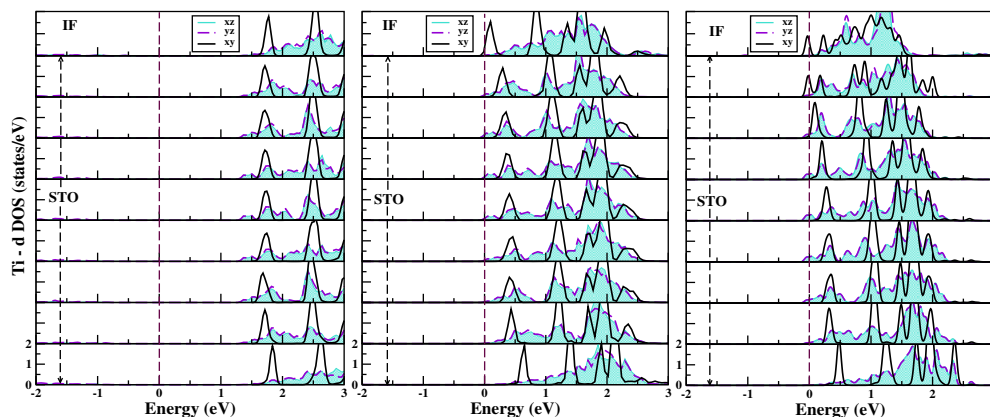


Figure 5.8: The density of states projected to  $xy$  (solid line),  $xz$  (shaded area),  $yz$  (dashed lines) orbitals of Ti, in different  $\text{TiO}_2$  layers of LAO/STO and GTO/STO in thin film-substrate geometry. The panels from left to right show results for  $(\text{LAO})_1/(\text{STO})_9$ ,  $(\text{LAO})_5/(\text{STO})_9$  and  $(\text{GTO})_1/(\text{STO})_9$ . From top to bottom, different panels refer to  $\text{TiO}_2$  at IF,  $\text{TiO}_2$  layers belonging to STO block. The zero of the energy is set at  $E_F$ .

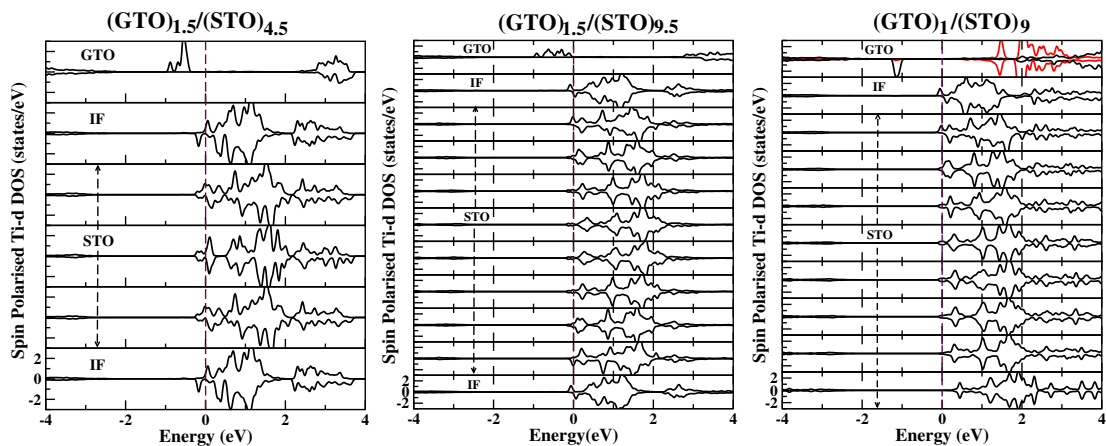


Figure 5.9: Spin-polarized DOS projected onto Ti d states for GTO/STO in superlattice (left and middle panels) and thin film-substrate geometry (right panel). For the thin film-substrate geometry, in the topmost TiO<sub>2</sub> layer, which is the surface layer of GTO, the projection to two charge disproportionate Ti d states are shown in black and red lines. The zero of the energy is set at Fermi level.

STO is barely metallic, setting a critical LAO thickness of 5 unit cell or so for the conductivity. This behavior is significantly different from that of LAO/STO in superlattice geometry for which IF's are found to be conducting for any thickness of LAO. This difference in conduction properties of LAO/STO, depending on the system geometry has been pointed out previously in literature. [26, 27] A markedly different picture is obtained for GTO/STO system. The right most panel of Figure 5.8, shows the plot of density of states of GTO/STO in thin film-substrate geometry with 1 unit cell thickness of GTO. We find the solution to be metallic even at the limit of 1 unit cell thickness of GTO. This is in sharp contrast to LAO/STO case, but in excellent agreement with experimental reports on GTO/STO. [16] The calculation of total conduction charge by integrating the layer wise density of states from  $-0.5$  eV below  $E_F$  to  $E_F$  gives a charge of  $0.5e^-$  (as seen from Table 5.1) for GTO/STO in thin film-substrate geometry with 1 unit cell thickness of GTO. This is in complete accordance with a single  $n$ -type interface in the unit cell, and the expectation from polar catastrophe model. On the contrary, the total conduction charge for the LAO/STO in thin film-substrate geometry with 5 unit cell thickness of LAO, which is at the critical thickness of metallicity, is found to be about  $0.14 e^-$ . This is about a factor of 4 smaller than that expected from polar catastrophe model. Increasing the LAO thickness beyond 5 u.c., the carrier concentration is found to slowly increase (for example for (LAO)<sub>6</sub>/(STO)<sub>9</sub> the conduction charge is found to be  $0.18 e^-$ ) which is expected to reach the asymptotic value of  $0.5 e^-$  for very large thickness of LAO.

The analysis of orbital population of the conduction electron, from right panel

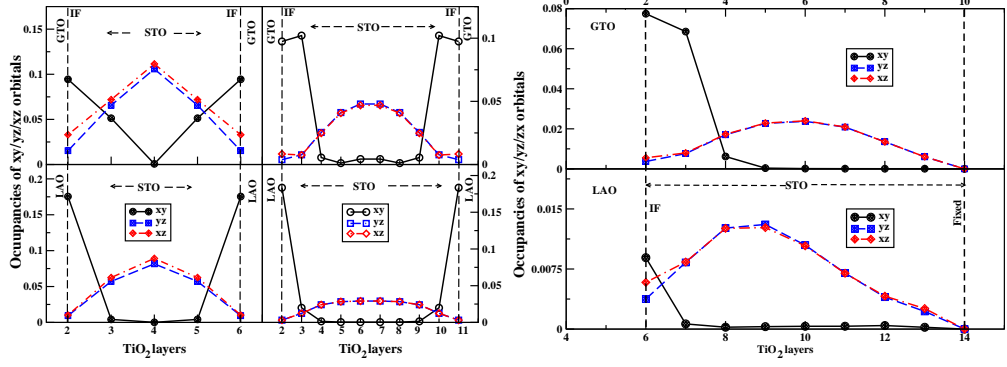


Figure 5.10: Plot of orbital occupancies with number of STO layers. The left panel shows the occupancies for the superlattice geometry and the right panel shows that for the thin-film/substrate geometry. The orbital characters are marked with different colours as shown in the legends. In the superlattice geometry both  $(\text{STO})_{4.5}$  and  $(\text{STO})_{9.5}$  blocks are shown. For the case of thin-films, only  $(\text{STO})_9$  substrates are shown.

of Figure 5.10 which shows the orbital occupancies plotted against number of layers in either the STO block, and also from Figure 5.11 which shows the charge density in the superlattice geometry, explicitly demonstrating the orbital character, and shows that the carriers at the IFs are predominantly of  $xy$  character, while that within the STO block are predominantly of  $yz/xz$  character in LAO/STO with LAO thickness beyond the critical thickness of conductivity. For GTO/STO, the IF is of significant  $xy$  character, the subsequent layers being of mixed character which converts to predominant  $yz/xz$  character in the interior of STO block. We thus find a similarity in the comparison of orbital character of LAO/STO and GTO/STO between the superlattice and the thin film-substrate geometry. This follows the expectation as the qualitative trend of the difference in structure between LAO/STO and GTO/STO systems are found to be similar in the superlattice and in the thin film-substrate geometry.

Another pertinent issue in the context of thin film-substrate geometry is the fate of the surface layer facing the vacuum, which is  $\text{AlO}_2$  in LAO, or  $\text{TiO}_2$  in GTO. By simple charge balance, the uppermost surface layer should be missing  $0.5 e^-$  which would bring the electric field and potential back to zero at the surface. This simple picture, of course, does not take into account the disordering effects like oxygen vacancy, cation disorder as well the effect of surface reconstruction, which are reported to be important in the context of LAO/STO. [42] Interestingly, our DFT calculation which allows for possible structural reconstruction only within the scope of  $\sqrt{(2)} \times \sqrt{(2)}$  cell, shows the topmost  $\text{AlO}_2$  surface in LAO to be metallic, while the topmost  $\text{TiO}_2$  surface in GTO to be insulating. This is seen in the plot of charge density contributed by a narrow energy window

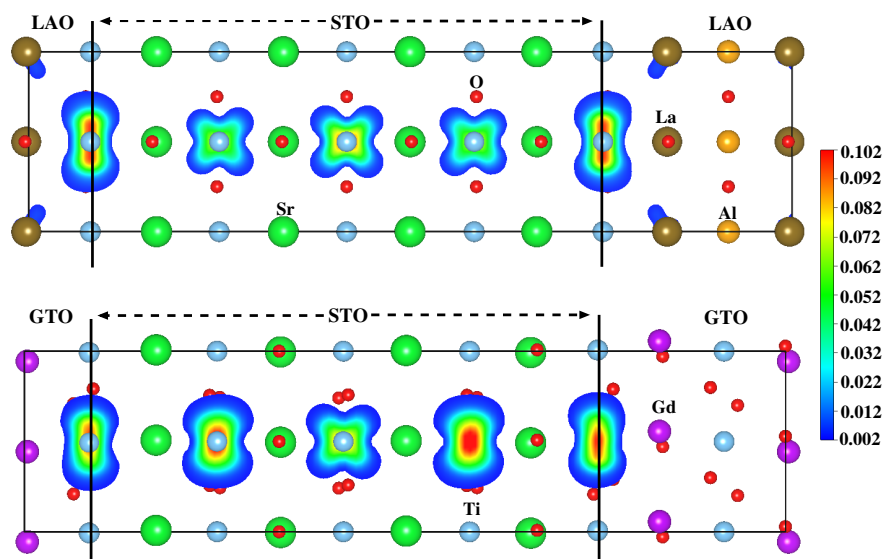


Figure 5.11: Conduction electron charge density plotted for  $(\text{LAO})_{1.5}/(\text{STO})_{4.5}$  (upper panel) and  $(\text{GTO})_{1.5}/(\text{STO})_{4.5}$  (lower panel) in the superlattice geometry, plotted for an energy window 0.5 eV below  $E_F$  to  $E_F$ . The colour coding of different contours are shown in side scale. The topmost  $\text{AlO}_2$  surface layer in LAO and the topmost  $\text{TiO}_2$  layer in GTO are both insulating.

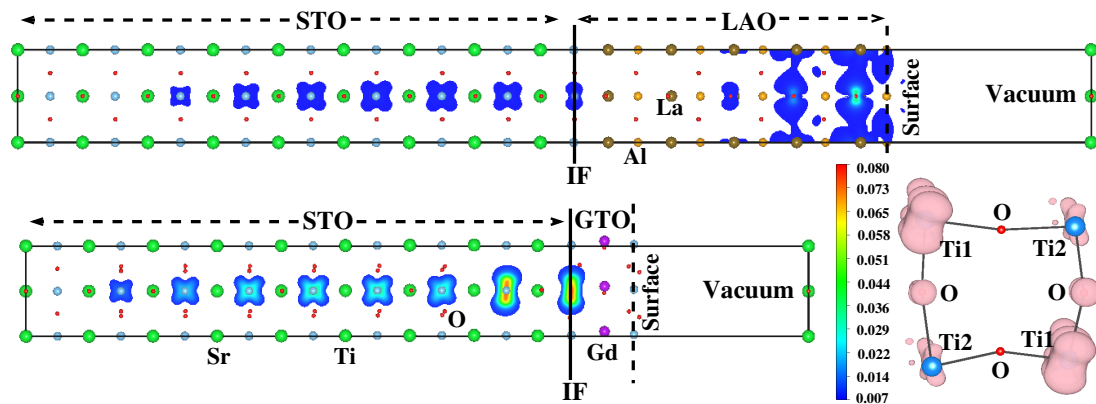


Figure 5.12: Conduction electron charge density plotted for  $(\text{LAO})_5/(\text{STO})_9$  (upper panel) and  $(\text{GTO})_1/(\text{STO})_9$  (lower panel) in thin film-substrate geometry, plotted for an energy window 0.5 eV below  $E_F$  to  $E_F$ . The colour coding of different contours are shown in side scale. The topmost  $\text{AlO}_2$  surface layer in LAO is metallic while the topmost  $\text{TiO}_2$  layer in GTO is insulating. The latter is driven by the charge disproportionation which happens between two Ti atoms in the unit cell in the topmost layer, shown as inset in the lower panel.

Table 5.1: The layer-wise contribution of the conduction electron in GTO/STO and LAO/STO in superlattice and thin film-substrate geometries. In case of superlattices, results for both (LAO or GTO)<sub>1.5</sub>/(STO)<sub>4.5</sub> and (LAO or GTO)<sub>1.5</sub>/(STO)<sub>9.5</sub> are shown. For thin film-substrate geometry, the results at minimum thickness of conductivity of LAO and GTO are shown, which are 5 u.c. and 1 u.c., respectively.

LAO/STO			GTO/STO		
Superlattice		Thin film-substrate	Superlattice		Thin film-substrate
<i>1.5-4.5</i>	<i>1.5-9.5</i>	<i>5-9</i>	<i>1.5-4.5</i>	<i>1.5-9.5</i>	<i>1-9</i>
Layer No.: Charge	Layer No.: Charge	Layer No.: Charge	Layer No.: Charge	Layer No.: Charge	Layer No.: Charge
2 : 0.185 (1 <sup>st</sup> IF)	2 : 0.200 (1 <sup>st</sup> IF)	6 : 0.062 (IF)	2 : 0.181 (1 <sup>st</sup> IF)	2 : 0.163 (1 <sup>st</sup> IF)	2 : 0.185 (IF)
3 : 0.184	3 : 0.104	7 : 0.050	3 : 0.203	3 : 0.101	3 : 0.108
4 : 0.260	4 : 0.070	8 : 0.006	4 : 0.231	4 : 0.058	4 : 0.034
5 : 0.184	5 : 0.066	9 : 0.007	5 : 0.203	5 : 0.082	5 : 0.045
6 : 0.185 (2 <sup>nd</sup> IF)	6 : 0.060	10 : 0.005	6 : 0.181 (2 <sup>nd</sup> IF)	6 : 0.096	6 : 0.049
	7 : 0.060	11 : 0.004		7 : 0.096	7 : 0.044
	8 : 0.066	12 : 0.002		8 : 0.082	8 : 0.029
	9 : 0.070	13 : 0.001		9 : 0.058	9 : 0.006
	10 : 0.104	14 : 0.000		10 : 0.101	10 : 0.000
	11 : 0.200 (2 <sup>nd</sup> IF)			11 : 0.163 (2 <sup>nd</sup> IF)	
Total Charge: 0.999	Total Charge: 1.000	Total Charge: 0.137	Total Charge: 0.999	Total Charge: 1.000	Total Charge: 0.500

around  $E_F$ , for (LAO)<sub>5</sub>/(STO)<sub>9</sub> and for (GTO)<sub>1</sub>/(STO)<sub>9</sub> (cf Figure 5.12). While the surface reconstruction in reality can be complex, which undoubtedly needs further exploration both from experimental and theoretical side, the stabilization of the insulating solution at the topmost TiO<sub>2</sub> surface layer of GTO doped with 0.5 hole is interesting. We find this to be triggered by charge disproportionation between two Ti atoms at the top layer. With the choice of  $U = 7$  eV applied on Ti atoms, [43, 44] this charge disproportionation becomes complete leading to insulating solution with nominal charge of  $d^1$  on one Ti atom and  $d^0$  on the other, maintaining an average charge of  $d^{0.5}$  per Ti at the top layer. This is evident from the charge density plot focused on the energy window around the occupied lower Hubbard band (LHB) of Ti  $d$  states (shown as inset in Figure 5.12), which shows significantly large charge on one set of Ti atoms and a significantly smaller on the other.

We find this to be triggered by the strong correlation effect which together with small differences in local environment of two Ti atoms, make the charges on two Ti's significantly different. The associated magnetic moments at two charge disproportionated Ti sites are found to be  $\approx 1\mu_B$  and  $\approx 0\mu_B$ , with spins of magnetic Ti ions ferromagnetically aligned. The spin polarised DOS for GTO/STO in film/substrate geometry is shown in rightmost panel of Figure 5.9. Our theoretical observation of charge disproportionation in top TiO<sub>2</sub> layer in GTO/STO in thin film-substrate geometry should be explored experimentally.

## 5.6 Electronic reconstruction

The above described DFT results lead to the following conclusions,

- (i) Both GTO/STO and LAO/STO show essentially similar behavior in the superlattice geometry, despite differences in details of the orbital character of the carriers due to differences in the structural distortions. The central result is that both GTO/STO and LAO/STO superlattices have the full interfacial charge density of  $0.5e^-/\text{IF}$ , and there is no critical thickness of GTO or LAO for conductivity.
- (ii) The behavior of the two systems is very different in the thin film-substrate geometry. We find that GTO/STO conducts even for GTO thickness of 1 unit cell with a carrier density of  $0.5e^-/\text{interface}$ , the minimum thickness possible, while LAO/STO conducts only beyond a critical thickness of 5 unit cells of LAO.

The obvious question is what causes this difference between two geometries and two systems? What are the driving mechanisms behind the similarity and contrast ?

The nonstoichiometry of GTO or LAO in the superlattice geometry, introduces a fixed carrier doping. The extra layer of GdO or LaO has a charge of +1, and thus an extra electron which is shared between the two symmetric interfaces. This results into doping of each interface by  $0.5e^-$  which, as pointed out Chen *et al.*, [27] exactly compensates the generated polar field. By construction, irrespective of the chosen thickness of LAO or GdO, the superlattice geometry behaves like ideal IF systems with infinite thickness of LAO or GTO and carrier density of  $0.5e^-$  per IF. It is therefore understandable that difference between LAO/STO and GTO/STO shows up only in thin film-substrate geometry with a single IF and a surface of  $\text{AlO}_2$  (for LAO) or  $\text{TiO}_2$  (for GTO) layer. In this context, the differences in band alignment, band bending and the electronic reconstruction between LAO/STO and GTO/STO systems appear to be crucial.

Figure 5.13 shows the DFT density of states plotted over a wide energy window, projected onto O  $p$ , Al  $p$ , Ti  $d$  and La/Ga  $d$  states for  $(\text{LAO})_5/(\text{STO})_9$  and  $(\text{GTO})_2/(\text{STO})_9$  in thin film-substrate geometry. This provides the picture after electronic reconstruction as given by DFT. From Figure 5.13, focusing on LAO/STO, we see that the upper edge of the oxygen valence band (VB) on the LAO side bends progressively towards  $E_F$  in moving from IF to surface, and matches with the lower edge of the Ti  $d$  band at the IF of the STO block which forms its conduction band (CB). In case of GTO/STO, keeping in mind the earlier discussed charge disproportionation scenario, projection to Ti  $d$  states is made separately to two charge disproportionated Ti atoms in a layer. We find a rather strong charge disproportionation at the topmost  $\text{TiO}_2$  layer which weakens in

moving towards IF and vanishes at IF and inside the STO block. We thus find the LHB of Ti  $d$  states at the top layer of GTO which otherwise would have been partially filled and matching with the lower edge of the Ti  $d$  band at the IF with the STO block, becomes split into occupied and unoccupied bands due to opening of charge gap. The band alignment before electronic reconstruction can be derived from the bulk band structure, shown schematically in upper panels in Figure 5.14. In case of LAO/STO, the valence band offset is small, and the valence band maxima of LAO and STO which is the upper edge of filled O- $p$  bands, are almost aligned. The experimentally measured bulk band gap of STO is 3.3 eV, while that of LAO is 5.6 eV. For conduction, therefore a large band bending with VB maxima of LAO aligning with conduction band minima of STO is needed, as observed in DFT results presented in Figure 5.13 and shown schematically in left lower panel of Figure 5.14. The necessary band bending is estimated to be about the same as band gap of STO *i.e.*, 3.3 eV. The bare potential shift of a 4-5 u.c. of LAO is about 80 - 90 eV. This is, however screened by the electronic and ionic polarization. Using the bulk dielectric constant of LAO,  $\epsilon = 24$ , the in-plane lattice constant of  $3.9 \text{ \AA}$ , the screened potential shift comes to be 3.4 - 3.5 eV, which is just sufficient to allow the necessary band bending of 3.3 eV, setting thus a critical thickness of about 4-5 u.c. For GTO/STO, on the other hand, the upper edges of VB of GTO and STO are misaligned. In case of GTO, it is the Ti  $d$  lower Hubbard band, which energetically lies far above the upper edge of the VB of STO which is the O  $p$  band, as shown in right upper panel in Figure 5.14. After electronic reconstruction, as given by DFT, in the topmost layer the Ti  $d$  LHB splits into two bands, due to charge disproportionation, requiring a small bending of  $\approx 0.5$  eV for the charge flow, shown in right lower panel in Figure 5.14. Using the estimate of the bulk dielectric constant of GTO as 30, and a similar analysis as in LAO/STO, it is found that a thickness of 1 u.c. of GTO would be sufficient to allow for the band bending and conduction. This would suggest the charge mismatch to be immediately accommodated at IF, independent of the thickness of the layers, justifying the DFT conclusion and the experimental observation.

The necessary band bending in LAO/STO is estimated to be about the same as band gap  $\Delta=3.3$  eV of STO. One can make a simple estimate of the critical thickness  $N_c$  of LAO layers for charge transfer from the surface to the interface as follows. The potential difference between the surface and interface is  $eE_{pol}N_c a$ , due to the polar field  $E_{pol} = 2\pi e/\epsilon a^2$  (where  $\epsilon$  is the dielectric constant of LAO arising from both electronic and ionic screening) should be equated to the gap  $\Delta$ . Using the bulk dielectric constant of LAO,  $\epsilon \simeq 24$ , and the in-plane lattice constant of  $a = 3.9 \text{ \AA}$ , the critical thickness could be estimated to be 4 layers, consistent with experiment and the DFT result. For thickness  $N \geq N_c$ , when an amount of charge  $q$  is transferred to the interface the potential difference  $(4\pi e/\epsilon a)(0.5e - q)N$  stays pinned at  $\Delta$ . This leads to an estimate of  $q(N) =$

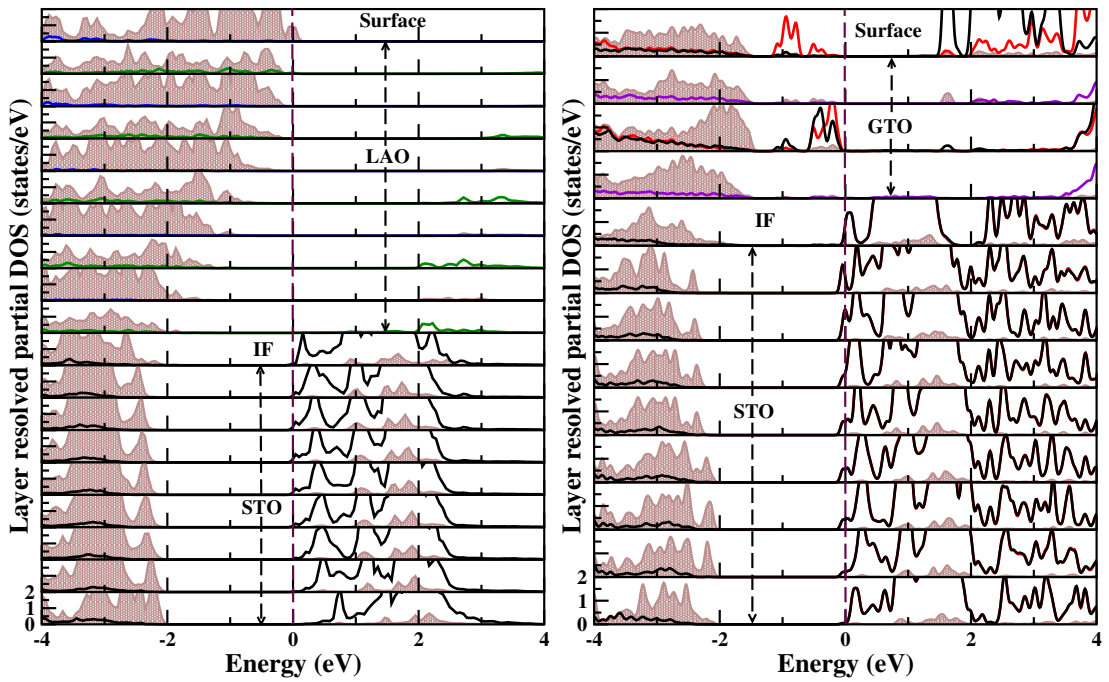


Figure 5.13: The layer decomposed DFT density of states for  $(\text{LAO})_5/(\text{STO})_9$  (left panel) and  $(\text{GTO})_2/(\text{STO})_9$  (right panel) in thin film-substrate geometry, projected onto O  $p$  (brown shaded), Al  $p$  (green line), Ti  $d$  (black/red line) and Ga  $d$  (magenta) and La  $d$  (blue line) states. For GTO/STO projection to two charge disproportionated Ti atoms are shown as black and red lines, respectively, while for LAO/STO projection to Ti  $d$  is shown as black line.  $E_F$  is set at zero. From top to bottom, various panels show the surface layer, the LAO or GTO block, the IF and the STO block.



in the superlattice set up, e.g. in terms of the total  $0.5 e^-/\text{Ti}$  transfer of charges to the interface, very different pictures emerge in case of thin film-substrate geometry due to the differences in electronic reconstructions in the two systems, even though, in both the cases, the reconstructions are driven by the same underlying electrostatic mechanism, namely the need to avert the polar catastrophe. We find a full  $0.5 e^-/\text{Ti}$  conducting charge at the interface even for 1 u.c. thick GTO on STO substrate, consistent with experiments. On the other hand, in case of LAO on STO, the transferred charge only increase gradually with thickness from a small value of  $\sim 0.14e^-/\text{Ti}$  above a critical thickness of about 4. Additionally, in the thin film-substrate case, we find the fate of the surface layers, which host the neutralizing charges for the interface carriers, to be quite distinct. The electronic states derived from O p orbitals at the surface LAO layer turn out to be metallic within DFT but are experimentally found to be localized, possibly due to disorder or surface imperfections like oxygen vacancies. On the other hand, the Ti d states at the top most layer of GTO/STO correspond to a doped Mott insulating layer of GTO and stays insulating by opening a charge gap via an interesting correlation driven charge disproportionation. Such a correlation induced phenomenon could be a robust feature, at least within a short length scale, even in the presence of surface disorder and, in principle, could be probed experimentally. This also pertains to the experimental verification of the polar catastrophe mechanism by detecting the counter charges at the surface of the heterostructure. The presence of conducting charges at the interface by itself does not unambiguously establish the polar catastrophe mechanism for the polar oxide interfaces as there could be other possible sources of interfacial charge carriers, e.g. oxygen vacancies.

# Bibliography

- [1] Jahn, H. A.; Teller, E. Proc. R. Soc. London A, 1937, 161, 220-235. DOI: 10.1098/rspa.1937.0142
- [2] Mott, N. F.; Peierls, R. (1937). Proceedings of the Physical Society. 49 (4S): 72
- [3] J. Zaanen, G. A. Sawatzky, and J. W. Allen, Phys. Rev. Lett. 55, 418 (1985)
- [4] Ohtomo, A. & Hwang, H. Y. **427**, 423-426 (2004).
- [5] Mannhart, J. et al. MRS Bull, **33**, 1027-1034 (2008).
- [6] Huijben, M. et al. Adv. Mater. **21**, 1665-1667 (2009).
- [7] Zubko, P. et al. Annu. Rev. Cond. Mat. Phys. **2**, 141-165 (2011).
- [8] Sulpizio, A., Ilani, S., Irvin, P. & Levy, J. Ann. Rev. of Mater. Res. **44**, 117-149 (2014).
- [9] Brinkman, A. et al, Nat. Mater. **6**, 493-496 (2007).
- [10] Reyren, N. et al. Science **317**, 1196-1199 (2007).
- [11] Bert, J. A. et al. Nature Phys. **7**, 767-771 (2011).
- [12] Li, L., Richter, C., Manhart, J. & Ashoori, R. C. Nat. Phys. **7**, 762-766 (2011).
- [13] Siemons, W. et al. Phys. Rev. Lett **98**, 196802 (2007).
- [14] Basletic, M. et al. Nat. Mater. **7**, 621-625 (2008).
- [15] Thiel, S. et al. Science **313**, 1942-1945 (2006).
- [16] Moetakef, P. et al. Appl. Phys. Lett. **99**, 232116 (2011).
- [17] Cain, T. A., Moetakef, P., Jackson C. A. & Stemmer, S. Appl. Phys. Lett. **101**, 111604 (2012).

- [18] Moetakef, P. et al. *Appl. Phys. Lett.* **101**, 151604 (2012).
- [19] Moetakef, P. et al. *Phys. Rev. X* **2**, 021014 (2012).
- [20] Moetakef, P. et al. *Phys. Rev. B* **86**, 201102 (R) (2012).
- [21] Chen, R., Lee, S. & Balents, L. Dimer, *Phys. Rev. B* **87**, 161119(R) (2013).
- [22] J. Biscaras, N. Bergeal, A. Kushwaha, T. Wolf, A. Rastogi, R.C. Budhani and J. Lesueur, *Nature Communications*, **1**, 89.
- [23] P.A. Salvador, A.-M. Haghiri-Gosnet, B. Mercey, M. Hervieu, B. Raveau, *Appl. Phys. Lett.* **75**, 2638 (1999).
- [24] S. Smadici, P. Abbamonte, A. Bhattacharya, X. Zhai, B. Jiang, A. Rusydi, J.N. Eckstein, S.D. Bader, J.-M. Zuo, *Phys. Rev. Lett.* **99**, 196404 (2007).
- [25] Zhong, Z. & Kelly, P. J. *Eur. Phys. Lett.* **84**, 27001 (2008).
- [26] Pentcheva, R. & Pickett, W. *Phys. Rev. Lett.* **102**, 107602 (2009).
- [27] Chen, H., Kolpak, A. & Ismail-Beigi, S. *Phys. Rev. B* **82**, 085430 (2010).
- [28] Bjaalie, L., Janotti, A., Himmetoglu, B., & Van de Walle, C. G. *Phys. Rev. B* **90**, 195117 (2014)
- [29] Lechermann, F., & Obermeyer, M. arXiv:1411.1637v2
- [30] Janotti, A., Bjaalie, L., Gordon, L. & Van de Walle, C. G. *Phys. Rev. B* **86**, 241108(R) (2012).
- [31] Kresse, G. & Hafner, J. *Phys. Rev. B* **47**, 558(R) (1993).
- [32] Kresse, G. & J. Furthmüller, *J. Phys. Rev. B* **54**, 11169 (1996).
- [33] Blöchl, P. E. *Phys. Rev. B* **50**, 17953 (1994).
- [34] Perdew, J. P., Burke, K. & Ernzerhof, M. *Phys. Rev. Lett.*, **77**, 3865 (1996).
- [35] Dudarev, S. L. et al. *Phys. Rev. B* **57**, 1505 (1998).
- [36] Zhang, Y., Jeschke, H. O. and Valenti, R. *Phys. Rev. B* **78**, 205104 (2008).
- [37] Kim, J.S. et al. *Phys. Rev. B* **82**, 201407(R) (2010)
- [38] Zhang, J. Y. et al. *Phys. Rev. B* **89**, 075140 (2014).
- [39] Zhang, J. Y. *Phys. Rev. Lett.* **110**, 256401 (2013).

- 
- [40] Dubroka, A. et al. Phys. Rev. Lett. **104**, 156807 (2010).
  - [41] Popovic, Z. S., Satpathy, S. & Martin, R. M. Phys. Rev. Lett, **101**, 256801 (2008).
  - [42] Huijben, M. et al. Adv. Mater. **21**, 1665-1677 (2009).
  - [43] Imada, M., Fujimori, A. & Tokura, Y. Rev. Mod. Phys. **70**, 1039 (1998)].
  - [44] Zhang, Y., Jeschke., H. O. & Valenti, R. Phys. Rev. B **78**, 205104 (2008).

# Chapter 6

## Understanding curious ferromagnetic insulating state of $\text{LaMnO}_3$ on $\text{SrTiO}_3$

### 6.1 Introduction

In recent times the study of interfaces formed between perovskite oxides have made a deep impact on the community engaged in both theoretical and experimental condensed matter research. The presence of the highly conducting 2 dimensional electron gas (2DEG) at the interface between oxide insulators have the possibility of many different device applications. In the previous chapter [1] it has been shown that the mechanism giving rise to the electron gas depends on polar catastrophe and band bending arguments and hence interfaces between band insulators and Mott insulators give rise to varying electronic effects. Among the various novel properties of heterostructures, a lot of effort has been devoted to control and utilize the magnetic properties of the interfaces for e.g. the magneto-electric coupling, the magnetic ordering modification, and the charge-transfer effect etc. In this context it is worthwhile to study the interface formed by heterostructures of  $\text{LaMnO}_3$ (LMO), which is a Jahn Teller insulator and  $\text{SrTiO}_3$ (STO), which is a band insulator.

LMO exhibits a very diverse phase diagram in the bulk state [2]. In undoped bulk LMO, orbital order due to Jahn-Teller (JT) distortions of the  $\text{MnO}_6$  octahedra sets in at reasonably high temperatures of  $\sim 750\text{K}$ . Subsequently, mag-

---

This chapter is based on "Understanding curious ferromagnetic insulating state of  $\text{LaMnO}_3$  on  $\text{SrTiO}_3$ " - *Hrishit Banerjee*, Oleg Janson, Karsten Held, and Tanusri Saha-Dasgupta, (under preparation)

netic exchange between  $\text{Mn}^{3+}$  ions leads to formation of A-type antiferromagnetic (AFM) insulating phase with Néel temperature of  $\sim 140\text{K}$  in which ferromagnetic (FM) planes are coupled in an antiferromagnetic manner. The primary characteristic of LMO is that the stoichiometric compound can be doped by cautiously controlling its stoichiometry. Doping La by Ca or tuning oxygen content, a phase transition can be triggered in bulk LMO from AFM insulating state to a FM metallic state. On the other hand, such a doping effect can also be a major disadvantage in identifying a system. The delicate effect of doping requires the careful characterization of LMO, especially when it is used in a heterostructure.

A lot of experiments have been done to identify the nature of the LMO/STO interfaces and the varied nature of the electronic structure of the LMO/STO interfaces have been reported ranging from ferromagnetic metal, antiferromagnetic insulator, ferromagnetic insulator and even superparamagnetism, depending on the relative thickness of LMO and STO and their geometry [3], [4], [5], [6], [7]. Following is a brief summary of experimental findings. LMO/STO has been studied experimentally in both superlattice and thin-films geometry. In the superlattice geometry, it has been reported that when LMO is much thicker than STO one obtains a ferromagnetic metal, however when LMO and STO have comparable thickness one obtains a ferromagnetic insulator. There is however no consistent satisfactory explanation of this FM insulating state! In the thin-film/substrate geometry for thickness of LMO  $\leq 5$  unit cells, LMO is AFM. However when thickness of LMO  $\geq 6$  unit cells, LMO is FM and in these cases FM state is usually accompanied with insulating behaviour above the critical thickness. One of the studies [7] have shown the emergence of an abrupt transition occurs from an AFM phase to a highly inhomogeneous magnetic state when more than five unit cells (u.c.) of LMO are epitaxially grown on STO. This experimental study claims to reveal well separated and weakly correlated superparamagnetic (SPM) islands. According to the study these nanoscale magnetic puddles account for the entire magnetization of the LMO/STO heterostructure as observed in global measurements. It is interpreted as electronic phase separation leading to the nucleation of metallic nanoscale ferromagnetic islands embedded in an insulating antiferromagnetic matrix which requires the polar discontinuity charge at the interface to reside on LMO side. No systematic microscopic study, ab-initio or otherwise to explain and/or verify all the above experimental results exist till date. There have been some theoretical calculations considering LMO films geometrically strained to an STO substrate which mostly fails to explain the FM insulating state [8] or considers symmetry broken structures to explain this behaviour [9].

In this chapter we aim to explain the origin of the elusive insulating FM ground state in LMO films strained to thick STO blocks from ab-initio approaches. We take into account the inadequacies which may be present in a DFT framework in the proper description of such strongly correlated systems.

## 6.2 Computational Details

Our first-principles calculations were carried out based on plane wave basis as implemented in the Vienna Ab-initio Simulation Package (VASP) [10, 11] with projector-augmented wave (PAW) potential. [12] The exchange-correlation functional was chosen to be that given by generalized gradient approximation (GGA), implemented following the Perdew Burke Ernzerhof (PBE) prescription. [13] The correlation effect beyond GGA was taken into account through supplemented on-site Hubbard  $U$  correction in form of GGA+ $U$ . [14] The value of  $U$  in the GGA+ $U$  scheme was varied from 2.5eV to 8eV. A  $U$  value of 3.5eV at Mn site was found to be adequate to describe the insulating A-AFM nature of bulk unstrained LaMnO<sub>3</sub> as found experimentally. The Hund's coupling parameter  $J_H$  was chosen be 0.9 eV. However it was found that band gap estimated from GGA+ $U$  calculated electronic density of states falls short of reproducing experimentally measured band gap. Note that the indirect or direct band gap obtained from GGA+ $U$  band structure provide a different estimate, than that obtained from density of states (DOS).

In order to have a better description of the system, we employed the hybrid functional based calculations. Hybrid functionals are a class of approximations to the exchange-correlation energy functional in density functional theory (DFT) that incorporate a portion of exact exchange from Hartree-Fock (HF) theory with the rest of the exchange-correlation energy estimated by DFT. The HSE (Heyd-Scuseria-Ernzerhof) [15] exchange-correlation functional uses an error function screened Coulomb potential to calculate the exchange portion of the energy in order to improve computational efficiency. The functional can be mathematically expressed as,

$$E_{XC}^{HSE}(\omega) = \alpha E_X^{HF,SR}(\omega) + (1 - \alpha) E_X^{PBE,SR}(\omega) + E_X^{PBE,LR}(\omega) + E_C^{PBE} \quad (6.1)$$

where  $\alpha$  is the mixing parameter and  $\omega$  is an adjustable parameter controlling the short-rangeness of the interaction. Here  $E_X^{HF,SR}$  denotes the short range HF exchange functional,  $E_X^{PBE,SR}$  denotes the short range PBE exchange functional,  $E_X^{PBE,LR}$  indicates the long range PBE exchange functional and  $E_C^{PBE}$  refers to the correlation functional as given by PBE. Standard value of  $\omega=0.2$  (referred to as HSE06) along with varying values of  $\alpha$  of 0.15, 0.20, 0.25, and 0.30 were used in our calculations. All calculations reported in this chapter are for a standard hybrid functional value of 25% exact HF exchange which is seen to reproduce very well the band gaps and magnetic exchanges for bulk unstrained LMO obtained experimentally.

## 6.3 Results

### 6.3.1 Bulk Calculations

#### Unstrained LMO

**Crystal Structure:** We start our discussion with the bulk unstrained LMO which forms in orthorhombic Pbnm crystal structure. Considering the experimental structure for LMO and using a  $\sqrt{2} \times \sqrt{2} \times 2$  perovskite supercell, a  $5 \times 5 \times 3$   $\Gamma$  centred k-point mesh, and a 500eV plane-wave cutoff were used for total-energy calculations and structural optimization. We relaxed both the lattice parameters and ionic positions considering A-AFM and FM magnetic states. The A-AFM state as defined previously consists of ferromagnetic planes of Mn atoms coupled antiferromagnetically.

Lattice constant	Experimental	FM (calc.)	A-AFM (calc.)
$a$ ( $\text{\AA}$ )	5.532	5.569	5.576
$b$ ( $\text{\AA}$ )	5.742	5.619	5.862
$c$ ( $\text{\AA}$ )	7.668	7.905	7.710
Volume ( $\text{\AA}^3$ )	243.572	247.365	252.013

Table 6.1: Lattice parameters ( $\text{\AA}$ ) of bulk  $\text{LaMnO}_3$  from experiment and GGA+ $U$  calculations

In Tables 6.1 and 6.2, we report the results of the first-principles calculations for the orthorhombic Pbnm bulk unstrained structure of LMO. Consistent with experiments and previous first-principles results [8], we find the ground state to be of A-AFM type. The structural parameters and other properties, including the magnitude of the Jahn-Teller distortions, the oxygen octahedral rotation angles, the local magnetic moment of Mn, the exchange coupling, and the direct band gap, are found to be in good agreement with previous first-principles studies. Table 6.1 shows the relaxed lattice parameters of unstrained LMO. In Table 6.2 we compare the structure and properties of the ground-state A-AFM-I phase, with the FM-M phase which is energetically close to the ground state being separated by a small energy difference of 9meV/fu. The most striking difference between the two phases is that the A-AFM phase is strongly orthorhombic, while the FM-M phase is nearly tetragonal. The degree of orthorhombicity is related to the magnitude of the JT distortions (c.f. Chapter 1 for definition of  $Q_3$ ), which is large in the A-AFM phase and almost negligible in the FM-M phase.

Another important point evident from Table 6.2 is that the energy difference between AFM and FM is small, and thus the FM phase may be stabilized by an appropriate perturbation. The large difference in orthorhombicity suggests that epitaxial growth on a square-lattice substrate could be effective. Matching to

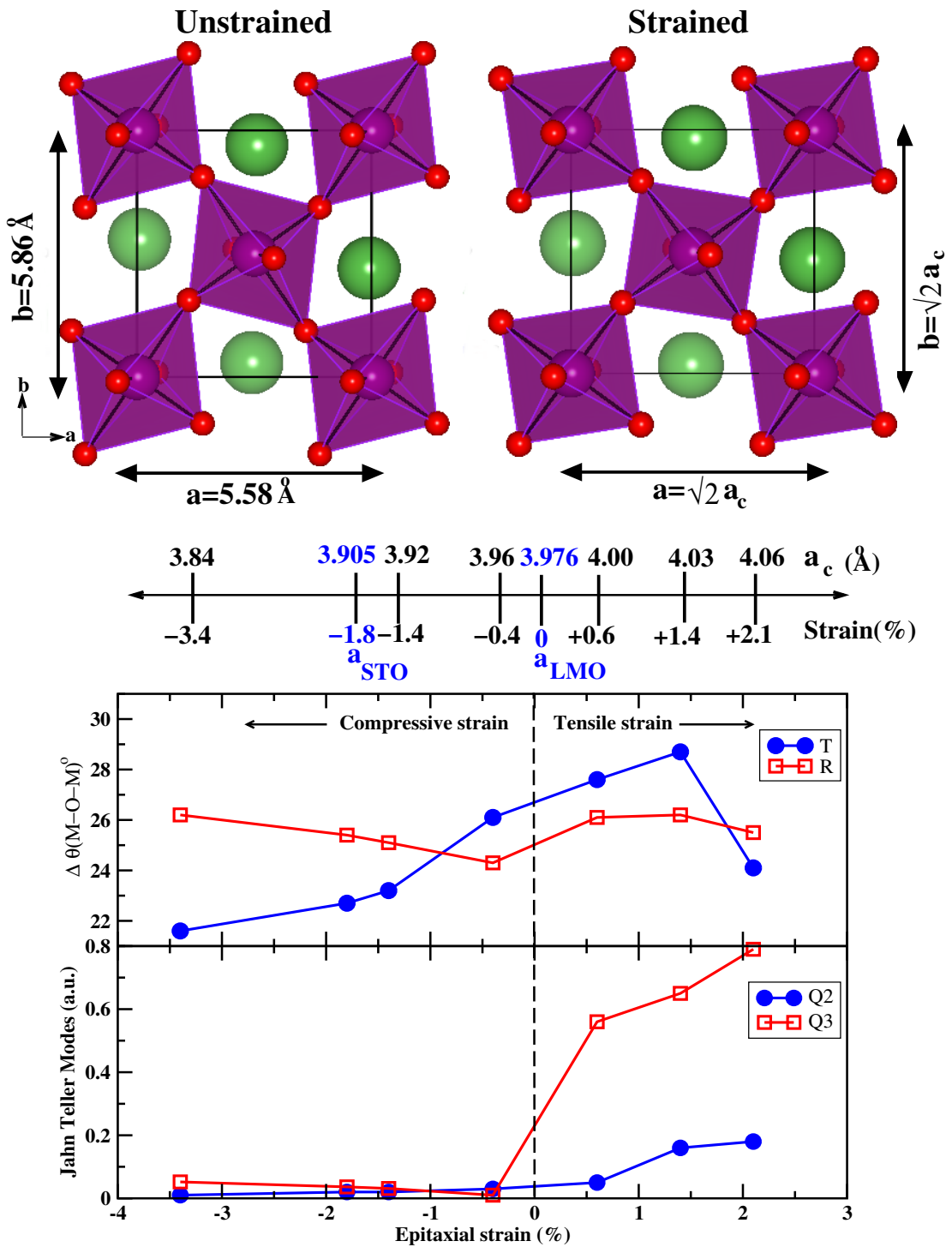


Figure 6.1: Figure showing the structures of unstrained and epitaxially strained LMO. The top panel shows how the LMO is strained to a square lattice. The middle panel shows the different epitaxial strains and corresponding values of the  $a$  lattice parameter. The bottom panel shows the rotation and tilt in the Mn-O octahedra and the corresponding Jahn Teller distortions at various values of strains.

Property measured	Bulk Phase	Alternate Phase
Magnetic order	A-AFM	FM
Relative Energy	0meV/fu	9.01meV/fu
Electronic property	insulating	half-metallic
JT magnitude ( $Q_3$ )	0.833au	0.031au
Rotation angles ( $\theta_R, \theta_T$ )	14.65°, 12.3°	12.16°, 8.16°
Volume/fu	63.003	61.841
Orthorhombicity( $b/a-1, c/\sqrt{2}a-1$ )	5.13%, -2.23%	0.897%, 0.37%

Table 6.2: Properties of the ground-state and low-energy competing bulk phases in LaMnO<sub>3</sub>

Quantity	Exptl.	GGA+U	HSE06
Band gap (from DOS)	1.7eV	0.75eV	1.72eV
Magnetic exchange $J_1$	1.85meV	2.19meV	2.46meV
Magnetic exchange $J_2$	-1.1meV	-1.14meV	-0.60meV

Table 6.3: Electronic properties of ground state bulk A-AFM insulating phase of LaMnO<sub>3</sub> using GGA+U and hybrid functionals in comparison to experimentally measured values.

a square lattice would force distortion of the orthorhombic AFM phase, costing elastic energy, while the nearly tetragonal FM phase can match to a square lattice with little elastic energy cost for the shape change. Furthermore, the FM phase, with a smaller volume per formula unit, will be favored by compressive strain.

**Electronic and Magnetic structure:** Next we discuss the basic electronic structure of unstrained bulk LMO from both GGA+U and HSE06 calculations, and find the ground state to be A-AFM insulating. Previous calculations by Spaldin et al [8] and Hou et al [9] both estimated band gaps from band structure and not DOS. Hou et al estimated a direct gap of 1.2eV, while Spaldin et al estimated a direct gap of 1.1eV and indirect gap of 0.83eV. Our calculation gives a direct band gap of 1.3eV from GGA+U bandstructure. The experimental band gap is measured to be 1.7eV [16]. From our HSE06 calculations using 25% HF exchange, we find a measured band gap of 1.72eV, which is a better agreement with experimental results than GGA+U, a fact that has been stressed upon by Munoz et al [17]. The magnetic interaction paths  $J_1$  and  $J_2$  are shown in figure 6.2. Here  $J_1$  is the in plane magnetic exchange in the ab plane and  $J_2$  is the out of plane magnetic exchange in the c direction. Our GGA+U calculation of magnetic exchanges gives  $J_1=2.19\text{meV}$ ,  $J_2=-1.14\text{meV}$ . Our hybrid calculation with HSE06, with 25% HF exchange gives,  $J_1=2.46\text{meV}$ ,  $J_2=-0.60\text{meV}$ , in comparison to experimentally measured values of  $J_1=1.85\text{meV}$ ,  $J_2=-1.1\text{meV}$ . [18]

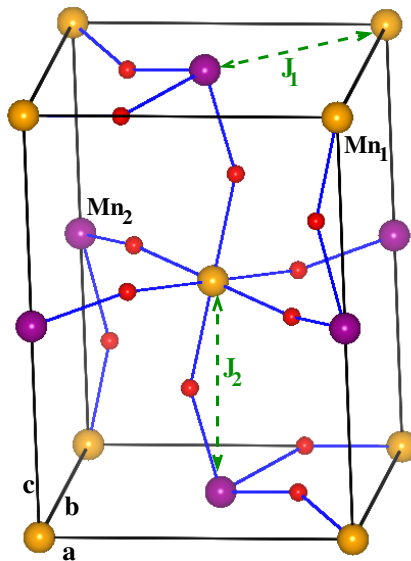


Figure 6.2: Figure showing the four Mn atoms in the unit cell, and the magnetic superexchange interactions  $J_1$  and  $J_2$  between them. The four Mn atoms are structurally equivalent, however they form two groups when treated within the regime of hybrid functional calculations, where each group is represented by Mn<sub>1</sub>(yellow) and Mn<sub>2</sub>(violet).

### Strained LMO

**Crystal Structure:** We next performed calculations on epitaxially strained LMO. Here epitaxial strain is defined as the in-plane strain produced by coherent matching of LMO to a square-lattice substrate with lattice parameter  $a_c$ , quantified as  $\frac{a_c - a_0}{a_0}$  with  $a_0 = 3.976 \text{ \AA}$ , the cube root of the computed volume per formula unit of the relaxed A-AFM Pbnm structure. To study the effect of such epitaxial strain, we first performed calculations of bulk LMO in its strained geometry, in which the structural parameters ( $c$  lattice, ionic positions) of the bulk periodic supercells ( $\sqrt{2} \times \sqrt{2} \times 2$  perovskite) were optimized subject to the constraint that the two in-plane lattice vectors which define the matching plane were fixed to produce the specified square lattice, of lattice parameter  $a_c$ . At each value of the strain, we considered FM, A-AFM, C-AFM, and G-AFM magnetic ordering for the epitaxially constrained Pbnm structure. Here C-AFM refers to antiferromagnetically arranged planes coupled ferromagnetically and G-AFM refers to antiferromagnetic alignment of Mn atoms both within the planes and in the out of plane directions.

The top panel of Figure 6.1 shows the structure of LMO both when unstrained and strained to a square substrate and viewed along the  $c$  direction. The  $a$  and  $b$  lattice parameters here are taken as  $\sqrt{2} \times a_c$ . The middle panel shows the  $a_c$  cubic lattice parameters which has been used to constrain the in plane lattice

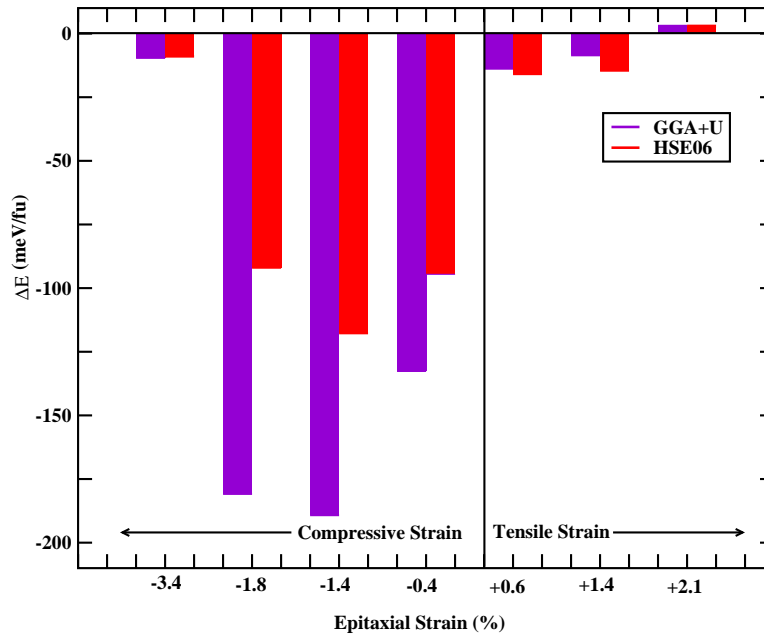


Figure 6.3: Energy differences  $\Delta E = E_{FM} - E_{AFM}$  between FM and A-AFM configurations at various square matching epitaxial strain values for both GGA+ $U$  and HSE06, showing that the trend in magnetic ground state for both GGA+ $U$  and HSE06 are the same.

constants of LMO to a square lattice. The lattice constant corresponding to both the special case of STO ( $=a_{STO}$ ) and unstrained LMO ( $a_{LMO} = a_0$ ) have been shown. All the different strain values corresponding to our chosen values of  $a_c$  are shown. The strained structures were relaxed considering relaxation of  $c$ -axis lattice parameters and ionic positions. The bottom panel shows the tilt ( $\angle T$ ) and rotation ( $\angle R$ ) of the Mn-O octahedra and also the Jahn Teller distortions ( $Q_2, Q_3$  as defined in Chapter 1) in the Mn-O octahedra, as a function of epitaxial strain. It is seen that the Jahn Teller distortion decreases significantly in the regime of compressive strain compared to unstrained or tensile strain cases. This particular behaviour was argued to favour FM ground state by Spaldin et al [8].

**Electronic and Magnetic structure:** Next we investigated the ground state electronic structure of orthorhombic LMO with its lattice parameters strained to different values of cubic lattice parameters including that of STO to emulate the effect of LMO/STO heterostructures. This leads to generation of both compressive and tensile strains on LMO. Depending on the values of compressive and tensile strains we identify three different ground states of LMO from our HSE06 calculations with 25% exact HF exchange. Comparison of these results with GGA+ $U$  results reveals that while the HSE06 results render a good description

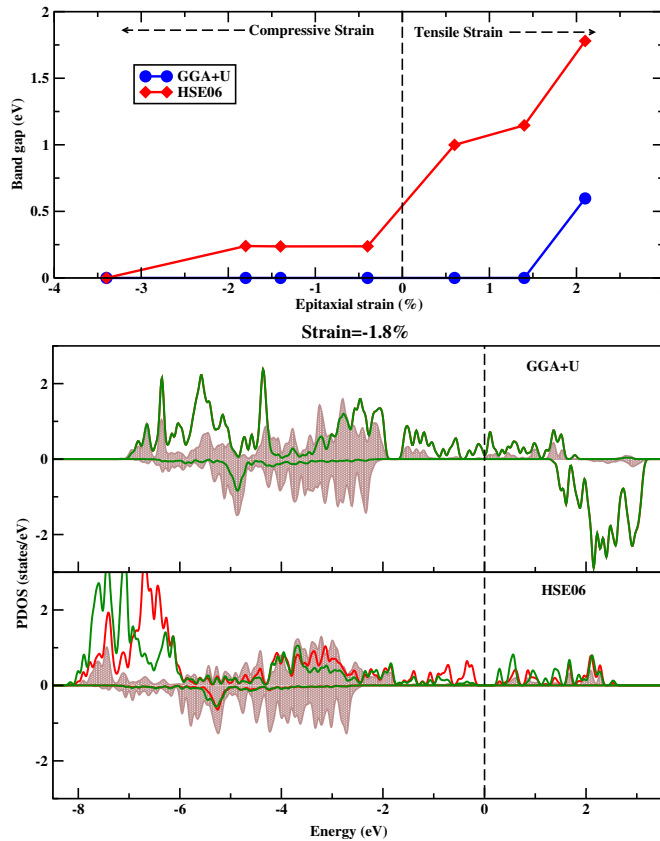


Figure 6.4: Projected Density of states (PDOS) for LMO strained to STO and band gaps for various epitaxial strains. The upper block shows the band gaps as calculated from both GGA+ $U$  (blue line) and HSE06 (red line) calculations. The lower block show PDOS using GGA+ $U$  and HSE06 at 25% HF exchange with  $Mn_1 - d$  (red),  $Mn_2 - d$  (green) and  $O - p$  (brown). The zero of energy is set to Fermi energy.

of the experimental scenario, the GGA+ $U$  do not.

Let us first consider the magnetic ground states of these strained structures. We find that the qualitative trend is same between GGA+ $U$  and HSE06, which is in agreement with experimental trend. As seen from the plot of  $\Delta E = E_{FM} - E_{AFM}$  presented in Figure 6.3 for large compressive strains of -3.4% both functionals show a FM state to be ground state though the energy differences are not very large. The energy differences increase as we decrease the compressive strain on the system and we find an increased propensity towards a FM ground state. This also corresponds to the reduction in JT distortion modes as indicated previously by Spaldin et al [8]. Moving to tensile strain values, for moderate tensile strains again the JT distortion increases and hence the relative stability

of the FM ground state is reduced, though the FM state continues to be lower in energy compared to A-AFM state. As we increase the tensile strain to +2.1%, we find the situation changes considerably and we find A-AFM state to be stabilized with respect to FM state, however the energy difference is quite small.

Following the discussion on magnetic state for which a good comparison is found between GGA+ $U$  and hybrid functionals, we move on to the comparison of electronic state. The upper panel of Figure 6.4 shows the variation of band gaps with epitaxial strain values as obtained in GGA+ $U$ , and HSE06. We find the ground state is metallic in GGA+ $U$  until a very large tensile strain, while HSE06 produces insulating ground states until a large value of compressive strain. We find that for GGA+ $U$  the band gaps for all strain values are zero except for the case of +2.1% tensile strain where an AFM ground state is gapped with a band gap of  $\sim 0.7\text{eV}$ ., while for HSE06 we find that band gap increases from 0eV at -3.4% compressive strain, which corresponds to a half metallic state, to a moderate value of  $\sim 0.4\text{eV}$  for moderate compressive strain values of -1.8%, -1.4% and remains more or less constant upto a small compressive strain value of -0.4%, and thus being a small band gap insulating state. When we move on to the regime of tensile strain we see an increase in band gap values upto 1.2-1.4eV at moderate tensile strain values of +0.6% and +1.4% and finally to a rather large band gap close to bulk band gap of  $\sim 1.8\text{eV}$  at +2.1% tensile strain.

The density of states projected to  $d$  states of four Mn atoms in the unit cell and the O- $p$  states is shown in the bottom panel of Figure 6.4 for the representative case of compressive strain of -1.8% which corresponds to matching to STO lattice parameters. We see that using GGA+ $U$ , the ground state turn out to be a ferromagnetic half metal. Even with a very high value of Hubbard  $U$  ( $U=8\text{eV}$ ), it is not possible within the framework of GGA+ $U$  calculations to drive the system towards an insulating state (not shown). The GGA+ $U$  calculation further shows identical PDOS for all the four Mn atoms in the unit cell with a large hybridization of O- $p$  states with Mn- $d$  states close to the Fermi energy. For the HSE06 calculation of the same situation we find the solution to be insulating. The four Mn atoms in the unit cell which are structurally equivalent, split up into two electronically inequivalent groups Mn<sub>1</sub> and Mn<sub>2</sub>, each group consisting of two Mn atoms, shown in Figure 6.2. The  $d$  states of Mn<sub>1</sub> and Mn<sub>2</sub> are found to differ substantially hinting towards a large charge disproportionation between Mn<sub>1</sub> and Mn<sub>2</sub>. This will be discussed in detail later. The oxygen  $p$  orbitals are plotted as average of all the oxygen  $p$  contributions in case of both GGA+ $U$  and HSE06. A shift in the O- $p$  band is seen away from the Fermi energy in case of HSE06 in comparison to the GGA+ $U$  case. A similar FM-I state, which arises due to the charge disproportionation in the system with HSE06 calculations, is also observed for -1.4% and -0.4% compressive strain values.

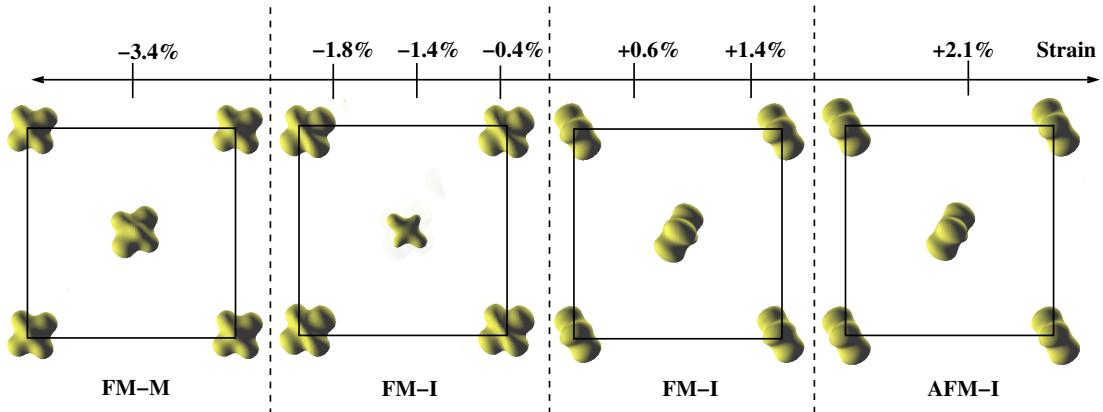


Figure 6.5: Charge density for various epitaxial strain values in the orthorhombic geometry, calculated using the HSE06 functional.

**Microscopic understanding:** In order to understand what gives rise to the curious FM-I behaviour in strained square lattice matched LMO, within a range of both compressive and tensile strain, we examine the charge density and hence the orbital character of the Mn atoms in the unit cell. For this purpose we plot the partial charge density for the orthorhombic unit cell taking an energy window from  $-0.5\text{eV}$  below Fermi energy upto the Fermi energy. Figure 6.5 shows charge density for various values of epitaxial strain. In this case we look at only the calculations with HSE06 functionals since GGA+ $U$  is unable to produce the FM-I solution in any case.

In case of large compressive strain values we see that a ferro type orbital ordering exists between the Mn atoms in the unit cell. This explains the FM-M behaviour at large compressive strains on LMO. When we move to moderate values of compressive strains we find that for strain values of  $-1.8\%$ ,  $-1.4\%$  and  $-0.4\%$  we find a similar ferro type ordering, albeit with a considerable charge disproportionation between the central Mn atom ( $\text{Mn}_2$ ) and the Mn atom at the corner ( $\text{Mn}_1$ ). Here it is the considerable charge disproportionation in this regime which gives rise to the FM insulating behaviour in this case.

The strong charge disproportionation between  $\text{Mn}_1$  and  $\text{Mn}_2$  atoms is reflected in large difference in magnetic moments between  $\text{Mn}_1$  and  $\text{Mn}_2$  atoms, as shown in Figure 6.6. Examining Figure 6.6 we see that there is no difference in moments for large compressive strains however as we decrease the compressive strains respectively to  $-1.8\%$ ,  $-1.4\%$  and  $-0.4\%$  we find a large moment difference of approximately  $0.16\text{-}0.18 \mu_B$ . When we move on to the case of tensile strains we find that both for moderate values of tensile strains of  $+0.6\%$  and  $+1.4\%$  and large tensile strain of  $+2.1\%$  there is hardly any charge disproportionation, however we find a strong anti-ferro alternating type orbital ordering of the kind

$d_{3x^2-r^2}/d_{3y^2-r^2}$ , as shown in Figure 6.5. Thus the FM I phase arises which has a type of three-dimensionally  $d_{3x^2-r^2}/d_{3y^2-r^2}$  alternated orbital order, in case of +0.6% and +1.4% and AFM I phase for a large strain of +2.1%, with the same ordering. As demonstrated in Figure 6.5 the alternating orbital ordering in case of tensile strain values gives rise to insulating behaviour in case of both FM and A-AFM cases.

We try to identify how this charge disproportionation arises in manganites. In  $\text{LaMnO}_3$ , Mn is in 3+ or  $d^4$  state. Compounds like  $\text{CaFeO}_3$  has Fe is 4+ or  $d^4$  state. Thus Mn in  $\text{LaMnO}_3$  and Fe in  $\text{CaFeO}_3$  are isoelectronic i.e. both in  $d^4, t_{2g}^3 e_g^1$  state. Fe  $d^4$ , in spite of their orbital-degenerate,  $t_{2g}^3 e_g^1$  configuration remain free from Jahn-Teller instabilities. They rather show charge-disproportionation (CD) transitions [19]. This has been understood as manganites prefer a JT distortion because the covalent character is weak in the Mn-O bond, while the Fe-based perovskites like  $\text{CaFeO}_3$  favor a CD distortion because the covalent character is stronger in the Fe-O bond [20]. Putting LMO on STO, causes -1.8% (compressive) strain on LMO, which in turn increases the Mn-O covalency thereby dis-favoring JT distortion and enhancing the tendency to CD. While this aspect is not captured by GGA+ $U$  owing to restriction on correlation being operative in one spin channel only for half metallic GGA+ $U$  solution, this is captured correctly in our hybrid HSE06 calculation. HSE06 shows the CD between Mn atoms in the unit cell, with two Mn atoms having  $4 + \delta$  charge and another two Mn atoms having  $4 - \delta$  charge. This in turn gives rise to an insulating solution.

This effect of both the alternating orbital ordering and charge disproportionation is seen arising purely as an electronic phenomena since all the Mn atoms in the unit cell are structurally equivalent in the orthorhombic geometry and there is no difference in either their environments or their JT distortions. Hence these phenomena can only arise as an electronically driven phenomena which is not captured by GGA+ $U$  however HSE06 having exact short range HF functional is well suited to capture this phenomena. The role of hybrid functionals in correctly capturing the electronic ground state of bulk unstrained LMO and similar oxide materials with complex band structures and strong hybridisation between Mn  $d$  and O  $p$  orbitals have been emphasized previously by Munoz et al. [17]

### 6.3.2 Superlattice Calculations

To understand exactly what happens when LMO is put next to STO in a superlattice where LMO and STO are of reasonable and comparable thickness, we finally performed both GGA+ $U$  and hybrid HSE06 calculations on  $(\text{LMO})_{4.5}/(\text{STO})_{4.5}$  in superlattice geometry. Experimentally similar systems have been studied which have been shown to be FM insulators. We placed LMO in orthorhombic geometry matched to cubic STO layers, where a  $\sqrt{2} \times \sqrt{2} \times c$  superlattice of both LMO and STO are allowed to tilt and rotate. This results in four structurally equiv-

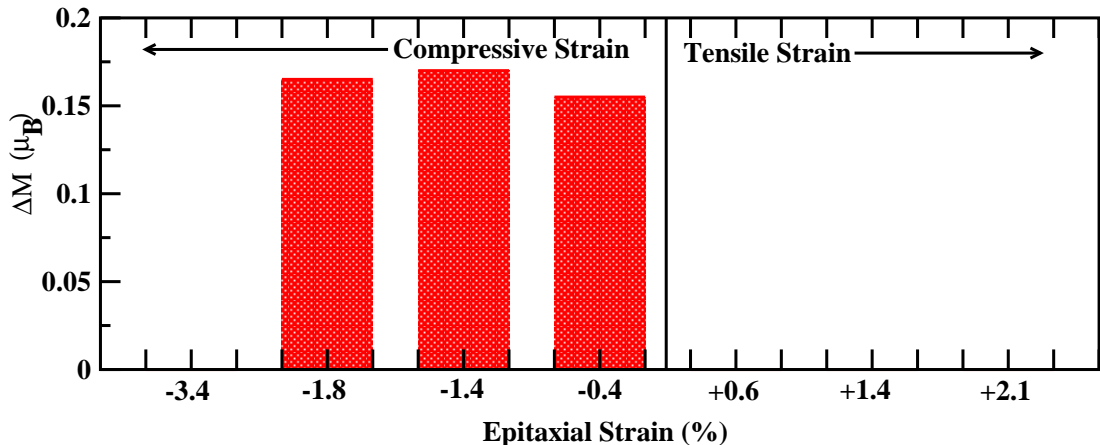


Figure 6.6: Charge disproportionation using HSE06 functionals for various epitaxial strain values in the orthorhombic geometry. The histograms are calculated by measuring the difference between the magnetic moments of the two Mn atoms, with change in epitaxial strain.

alent Mn and Ti atoms in each LMO and STO layer. The ionic positions and  $c$  lattice parameters were allowed to relax, keeping the  $a$  and  $b$  lattice parameters fixed, with  $a = b$ , thus generating a square matched epitaxial strain of -1.8%, as seen previously. We find a significant decrease in both Jahn Teller distortion and tilt and rotation angles in case of LMO, while some JT distortion and tilt and rotation is introduced in the STO layers due to its proximity to largely distorted LMO layers, as we have also seen before in Chapter 5 in case of GTO/STO. As we see from the left panel of Figure 6.7, the GGA+ $U$  PDOS gives a solution which is metallic and from comparison of energy of FM and AFM calculations we find the FM state to be lower in energy. Next HSE06 calculations were performed with 15%, 25% and 30% fraction of exact HF exchange. While the 15% HF exchange calculation gave rise to a FM metallic ground state similar to that found in GGA+ $U$  calculation, for 25% and 30% HF exchange a FM insulating ground state was obtained. We present in right panel of Figure 6.7 the PDOS for HF exact exchange of 25%. We find that the Mn layers are charge disproportionated, as seen from the PDOS, and that gives rise to the insulating behaviour in case of the LMO as was seen previously also in case of -1.8% strain. What is very interesting is that the electron gas generated due to polar catastrophe in the STO side is locally spin polarised and that causes a gap to arise at the Fermi level even in the STO block, thus turning the entire system towards an insulating ground state.

In case of GGA+ $U$  calculations, all the four structurally equivalent Mn atoms in each layer of LMO produce identical PDOS contributions, however in case of

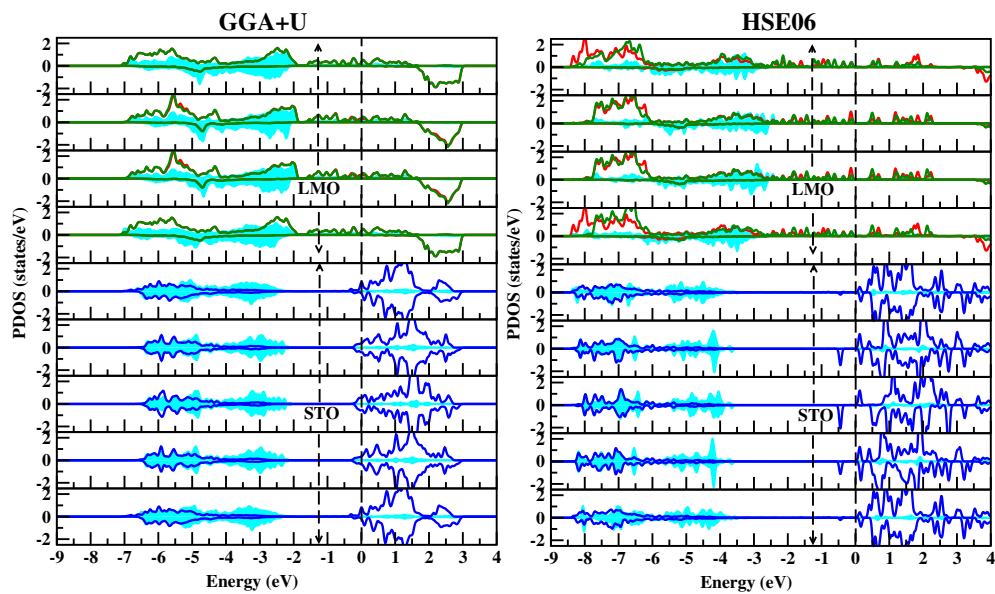


Figure 6.7: Layer projected Density of States for  $(\text{LMO})_{4.5}/\text{STO}_{4.5}$  superlattice with states projected to  $\text{Mn}_1 - d$  (red),  $\text{Mn}_2 - d$  (green),  $\text{Ti} d$  (blue), and  $\text{O} p$  (cyan). The left panel shows the layer resolved DOS with the GGA+ $U$  functional compared to the right panel which shows the layer resolved DOS with HSE06 hybrid functional. The zero of energy is to Fermi energy.

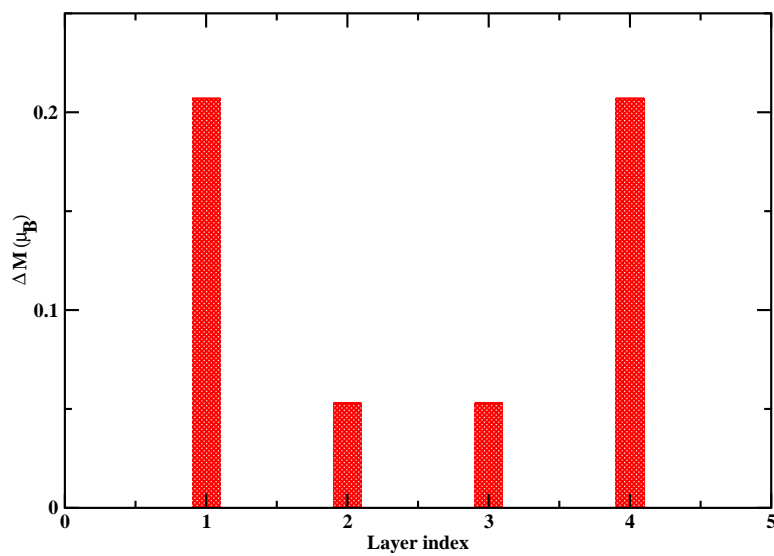


Figure 6.8: Layerwise charge disproportionation for  $(\text{LMO})_{4.5}/\text{STO}_{4.5}$  superlattice calculated being taking difference in magnetic moment between  $\text{Mn}_1 d$  and  $\text{Mn}_2 d$  in each layer.

HSE06 calculations, two of the Mn atoms in each layer form electronically inequivalent groups of two Mn atoms each and hence produce different contributions to the PDOS. To estimate the charge disproportionation quantitatively in the LMO block we plot here the difference in magnetic moments between the two electronically inequivalent Mn atoms, as indicated in the PDOS by red and green lines, in each  $\text{MnO}_2$  layer in Figure 6.8. We find that in this case the layers 1 and 4 which are the IF layers have maximum charge disproportionation while the middle layers 2 and 3 have a lesser amount of charge disproportionation, however considerable enough to cause the LMO block emerge as an insulator.

## 6.4 Conclusion

In this chapter we have shown that the ferromagnetic insulating phase in orthorhombic LMO strained to an STO substrate arises from the charge disproportionation as obtained within the formulation of hybrid functionals. Though it has been suggested in previous studies that an orbital ordering arises due to an intrinsic difference in the JT distortions in the LMO unit cell arising due to a slight monoclinicity in the unit cell it however seems unlikely to happen in the experimental case where LMO thin films are put over thick STO substrates which plausibly forces LMO to conform to the symmetry of the substrate which is tetragonal in nature. This is also the case with other moderate values of compressive strain by charge ordering gives rise to FM insulating behaviour over a wide range of compressive strain values. For tensile strain values we find FM-I state to be driven by an alternate orbital ordering. For large values of tensile strain an AFM-I phase is stabilised which is also the ground state for bulk unstrained LMO where the LMO in plane lattice parameters are not fitted to that of a square lattice. Thus we find that not only strain but also matching the lattice parameters to a square lattice plays an important role in this case.

We have also investigated the case of superlattice structure with comparable thicknesses of LMO and STO and we find that we can qualitatively reproduce the experimental result of a ferromagnetic insulating ground state. The microscopic analysis of our results reveals that LMO block becomes insulating owing to the charge disproportionation which is again a purely electronic phenomena as was in the case of epitaxially strained LMO, while the STO layers become insulating due to spin polarisation in the system which makes the itinerant electron gas generated due to polar catastrophe model spin split and hence opens up a gap at Fermi level driving it insulating. It is also to be noted that unlike some previous suggestions [7] the electron gas in our calculations does not reside in LMO side, instead as in the cases of LAO/STO and GTO/STO heterostructures, it resides on the STO side.

# Bibliography

- [1] H. Banerjee, S. Banerjee, M Randeria, T. Saha Dasgupta, Scientific Reports 5, 18647, (2015)
- [2] S. Satpathy; et al. (1996). Physical Review Letters. 76: 960.
- [3] Barriocanal et al, Nat. Commun. 1:82 doi: 10.1038/ncomms1080 (2010).
- [4] Barriocanal et al, Adv. Mater. 22, 627-632 (2010)
- [5] Choi et al, Phys. Rev. B 83, 195113 (2011)
- [6] Liu et al, J. App. Phys 113, 17D902 (2013)
- [7] Y. Anahory, L. Embon, C. J. Li, S. Banerjee, A. Meltzer, H. R. Naren, A. Yakovenko, J. Cuppens, Y. Myasoedov, M. L. Rappaport, M. E. Huber, K. Michaeli, T. Venkatesan, Ariando & E. Zeldov, Nature Communications 7, 12566 (2016).
- [8] Jun Hee Lee, Kris T. Delaney, Eric Bousquet, Nicola A. Spaldin, and Karin M. Rabe Phys. Rev. B 88, 174426 (2013)
- [9] Y. S. Hou, H. J. Xiang, and X. G. Gong, Phys. Rev. B 89, 064415 (2014)
- [10] Kresse, G. & Hafner, J. Phys. Rev. B **47**, 558(R) (1993).
- [11] Kresse, G. & J. Furthmüller, J. Phys. Rev. B **54**, 11169 (1996).
- [12] Blöchl, P. E. Projector augmented-wave method. Phys. Rev. B **50**, 17953 (1994).
- [13] Perdew, J. P., Burke, K. & Ernzerhof, M. Phys. Rev. Lett., **77**, 3865 (1996).
- [14] Dudarev, S. L. et al. Phys. Rev. B **57**, 1505 (1998).
- [15] Jochen Heyd; Gustavo E. Scuseria; Matthias Ernzerhof (2003). J. Chem. Phys. 118 (18): 8207.

- 
- [16] T. Saitoh, A. E. Bocquet, T. Mizokawa, H. Namatame, A. Fujimori, M. Abbate, Y. Takeda, and M. Takano, *Phys. Rev. B* 51, 13942 (1995)
- [17] D. Munoz, N. M. Harrison, and F. Illas, *Phys. Rev. B* 69, 085115 (2004)
- [18] R. J. McQueeney, J.-Q. Yan, S. Chang, and J. Ma, *Phys. Rev. B* 78, 184417 (2008)
- [19] T. Saha-Dasgupta, Z. S. Popovic, and S. Satpathy, *PRB* 72, 045143, 2005
- [20] M.-H. Whangbo, H.-J. Koo, A. Villesuzanne, and M. Pouchard, *Inorg. Chem.* 41, 1920, 2002

# Chapter 7

## Conclusion

The aim of the studies undertaken in the current thesis is to investigate the microscopic origin of various exciting and intriguing physical properties of different complex and novel materials, employing primarily ab-initio electronic structure techniques coupled with many body and model Hamiltonian methods as and when deemed necessary. In particular, both zero temperature and finite temperature first principles electronic structure calculations have been performed within the framework of Density Functional Theory (DFT) and Ab Initio Molecular Dynamics (AIMD). In addition to first principles study, classical model Hamiltonians have been studied and solved using techniques like classical Monte Carlo simulation. Applications of these computational techniques have been used in studying, understanding and designing novel properties in inorganic oxide compounds as well as hybrid materials.

In chapters 3 to 6 we have considered two different novel phenomena arising in two different classes of materials including both organic and inorganic complexes. In the present chapter we summarize the primary findings described in the previous chapters that emerge out of our study. We then discuss the future directions.

### 7.1 Summary

#### 7.1.1 Summary of Chapter 3

This chapter emphasized the microscopic role of magnetic superexchange in cooperativity and bistability in the class of Fe-triazole Spin crossover (SCO) linear coordination polymers.

Our Monte Carlo study based on model Hamiltonian vehemently established the important role of magnetic super-exchange interaction acting between the transition metal (TM) ion centers in the cooperativity in spin transition in coordination polymers. They turned out to be equally important as the elastic

interaction, the latter being generally accepted as the main cause of cooperativity in polymeric SCO systems. Depending on the nature of the spin-dependent elastic interaction, which is decided by the nature of the spin-phonon coupling, the magnetic interaction was thought to contribute to the development of cooperativity in a quantitative or a qualitative manner. In case of ferro type elastic interaction, the magnetic interaction helps enhancing the hysteresis effect, developed already by the elastic interaction, thus being important in a quantitative manner. In case of antiferro nature of elastic interaction, the magnetic interaction play a decisive role in driving the hysteresis in the system. Considering linear coordination polymer, Fe triazole, which was found to belong to the latter category we demonstrated the existence of bistability in this compound through Ab-initio Molecular Dynamics simulation. This established the capability of ab-initio technique to capture the bistability accurately. The observed bistability in this system, was found to be totally driven by the magnetic exchange interaction. The computed transition temperature, and the width of the hysteresis was found to be in excellent agreement with that of the measured susceptibility reported for the similar compound.

### 7.1.2 Summary of Chapter 4

This chapter was devoted to designing spin crossover properties in transition metal hybrid perovskites, which have been explored so far in context of multiferroic properties.

We demonstrated that these hybrid perovskites can also undergo spin crossover using rigorous first-principles calculations, and considering two formate based hybrid perovskite compounds, Dimethylammonium Iron Formate and Hydroxylammonium Iron Formate under hydrostatic pressure. We found that dense framework structures of these compounds help in building up cooperativity in spin-switching, making the phenomena a spin-state transition with appreciable hysteresis effect. The spin-switching is reflected in associated changes in electronic, magnetic and also possible changes in optical properties. This opens up several novel potential applications of these materials, for example, as pressure sensors, as active elements of various types of displays, and in information storage and retrieval - an aspect which has remained unexplored so far in this class of materials. Our computed values of critical transition pressure required to drive the spin-state transition was found to be in the range of about 2-6 GPa, which should be readily achievable in any standard laboratory set-up. The appreciable hysteresis effect of 2-5 GPa associated with these spin-state transitions would make them functional in memory devices for a reasonably wide range of pressure. It was also seen that unlike the previous class of materials studied in Chapter 3, hybrid perovskites considered in this chapter are ferroelastic materials and in this case elastic interaction is the driving element behind cooperativity and magnetic

superexchange having only quantitative effect. Taking the advantage of flexibility of these MOF perovskites to undergo substantial change in mechanical properties upon tuning of hydrogen bonds, both the pressure required for the transition, as well as the hysteresis-width are found to be tunable by choice of appropriate amine cation.

### 7.1.3 Summary of Chapter 5

In this chapter we considered the oxide interfaces formed between two band insulators like Lanthanum Aluminate (LAO) and Strontium Titanate (STO) and between a band insulator and a Mott insulator like STO and Gadolinium Titanate (GTO). Our study provided a microscopic understanding of the essential similarities and dissimilarities between these two classes as observed experimentally.

While the two systems were found to behave quite similarly in the superlattice set up, viz. in terms of the total  $0.5 e^-/\text{Ti}$  transfer of charges to the interface, very different pictures emerged in case of thin film-substrate geometry due to the differences in electronic reconstructions in the two systems, even though, in both the cases, the reconstructions are driven by the same underlying electrostatic mechanism, namely the need to avert the polar catastrophe. We found a full  $0.5 e^-/\text{Ti}$  conducting charge at the interface even for 1 unit cell thick GTO on STO substrate, consistent with experiments. On the other hand, in case of LAO on STO, the transferred charge only increase gradually with thickness from a small value of  $\sim 0.14e^-/\text{Ti}$  above a critical thickness of about 4-5 unit cells. Additionally, in the thin film-substrate case, we found the fate of the surface layers, which host the neutralizing charges for the interface carriers, to be quite distinct. The electronic states derived from O  $p$  orbitals at the surface LAO layer turn out to be metallic within band theory but are experimentally found to be insulating, which have been suggested to be due to disorder or surface imperfections like oxygen vacancies. On the other hand, we found the Ti  $d$  states at the topmost layer of GTO/STO correspond to a doped Mott insulating layer of GTO and stays insulating by opening a charge gap via an interesting electronic correlation driven charge disproportionation. Such a correlation induced phenomenon is expected to be a robust feature, at least within a short length scale, and may be probed experimentally.

### 7.1.4 Summary of Chapter 6

In this chapter we studied the origin of the elusive ferromagnetic insulating phase in some cases of LMO/STO interfaces. The effect of square planar strain which is induced by matching of LMO lattice constants to cubic STO lattice constants is the crucial issue here. The electronic and magnetic properties of epitaxially

strained LMO and LMO/STO superlattices have been studied with different techniques and with varying degree of sophistication in handling electron-electron correlation and exchange effects like GGA+U and hybrid functionals. This multi pronged approach reveals the curious state of ferromagnetic insulator of LMO, as observed experimentally arises owing to a correlation driven charge disproportionation which is found to be captured by the hybrid functional calculations.

## 7.2 Outlook

### 7.2.1 Metal-organic Complexes

The present thesis focused primarily on theoretical studies of temperature and pressure induced cooperative SCO. A much less studied and worth exploring area from theoretical point of view would be study of cooperativity in light induced spin state trapping (LIESST). While empirical theories have been proposed within the non-adiabatic multiphonon framework [1] for mononuclear compounds in terms of  $\Delta E_{HL}^0$ , the energy difference between the lowest vibrational levels of HS and LS states, and the change of metal-ligand bond length  $\Delta r_{HL}$ , the ab-initio description of the complete process is lacking, apart from very few quantum-chemical calculations [2, 3] studying the electronic structure of excited state geometries. More importantly, extension to multinuclear systems with possible cooperative effect is non-existent. The study by Létard et al. [4] through irradiation of the sample at low temperature with laser coupled to an optical fiber within a SQUID cavity showed that the temperature dependence of the photomagnetic properties of mononuclear and multinuclear systems to be very different. To the best of our knowledge no microscopic theory has been developed to explain this difference. This thesis also focused on Fe(II) based systems, which are so far the most popular ones. However, in addition to Fe or Co based systems, there are few examples of SCO in Mn(III) [5, 6]. Mn(III) is a particularly interesting candidate for SCO as it should exhibit a significant Jahn-Teller effect in its HS state. It is an interesting question to ask how the Jahn-Teller distortion affects the phononic contribution to cooperativity in terms of influencing the spin-lattice coupling. This may result in different profiles of SCO, like double transition, compared to those observed for Fe(II). This issue demands future attention. Finally, hybrid perovskites which are new candidates proposed for observing cooperative SCO effect, should be also explored for LIESST effect both from experimental and theoretical point of view. Given the observation of multiferroicity, already reported in literature for hybrid perovskites, it will be also worth to investigate any exotic magnetic ordering of HS Fe(II)s leading to breaking of inversion symmetry, and thus resulting in magneto-electric coupling.

Moreover related to the formate linked hybrid perovskites that we have studied there is another class of halide linked hybrid perovskites which have very

similar properties to the formate based hybrids. Some similar halide based class of materials have been shown to form very interesting 2D ferromagnets in two recent studies. Our conjecture is that the halide based hybrid perovskites may be cleaved to form similar 2D compounds with ferromagnetic properties which shall have immense binding on theoretical studies of these materials and shall diversify immensely the application possibilities of these materials. I intend to investigate this extremely interesting aspect of metal organic complexes as a part of my future research endeavours.

### 7.2.2 Inorganic Oxide heterostructures

A few interesting future directions in this section for theoretical study would be to investigate in detail the sub-band structures, that is relevant for quantum oscillation measurements, and spin-orbit coupling in the GTO/STO interface. Our structural analysis indicates substantially larger polar distortions of the Ti-O-Ti bonds at the GTO/STO interface compared to that in LAO/STO. This could potentially lead to much larger Rashba spin-orbit coupling for GTO/STO heterostructure. The magnetic property of the interface 2DEG in GTO/STO should also be investigated by DFT. As demonstrated in Chapter 5, GTO/STO shows signature of ferromagnetism that could be an intrinsic correlation driven phenomenon, independent of the proximity to magnetic GTO layer. Calculation of magnetic superexchanges and building a model for the magnetic ground state of these heterostructures can shed further light on the understanding of the magnetic structure of these materials.

There are a plethora of hetero-interfaces which have been known experimentally and interfaces between Samarium Titanate  $\text{SmTiO}_3$  (SmTO) and STO have been shown to be extremely interesting and I would like to investigate such materials. Also a very interesting case of study would be an interface between two Mott insulators, since we have mostly considered interfaces of Mott insulators with band insulators and we have found that the band structure of the heterostructures influences to a great extent the type of interface formed and its properties. In this content an interface between GTO and LTO might be an extremely interesting case to study both of them being Mott insulators.

# Bibliography

- [1] Buhks, E.; Navon, G.; Bixon, M.; Jortner, J. *J. Am. Chem. Soc.* 1980, 102, 2918-2923.
- [2] Hauser, A.; Guetlich, P.; Spiering, H. *Inorg. Chem.* 1986, 25, 4245-4248.
- [3] Létard, J.F.; Guionneau, P.; Rabardel, L.; Howard, J.A.K.; Goeta, A.E.; Chasseau, D.; Kahn, O. *Inorg. Chem.* 1998, 37, 4432-4441.
- [4] Létard, J.F.; Capes, L.; Chastanet, G.; Moliner, N.; Létard, S.; Real, J.A.; Kahn, O. *Chem. Phys. Lett.* 1999, 313, 115-120.
- [5] Morgan, G.G.; Murnaghan, K.D.; Muller-Bunz, H.; McKee, V.; Harding, C.J. *Angew. Chem.* 2006, 118, 7350-7353.
- [6] Martinho, P.N.; Gildea, B.; Harris, M.M.; Lemma, T.; Naik, A.D.; Müller-Bunz, H.; Keyes, T.E.; Garcia, Y.; Morgan, G.G. Cooperative Spin Transition in a Mononuclear Manganese(III) Complex. *Angew. Chem.* 2012, 124, 12765-12769.